Automated parametric Rietveld refinement and its application to two-dimensional X-ray powder diffraction experiments

Rajiv Paneerselvam

Institut für Geophysik
Universität Stuttgart

Max-Planck-Institut für
Festkörperforschung
Stuttgart

Dissertation an der Universität Stuttgart
Stuttgart, 2011

Automated parametric Rietveld refinement and its application to two-dimensional X-ray powder diffraction experiments

Von der Fakultät für Bau- und Umweltingenieurwissenschaften der Universität Stuttgart zur Erlangung der Würde eines Doktor-Ingenieurs (Dr.-Ing.) genehmigte Abhandlung

Vorgelegt von
Rajiv Paneerselvam
geboren in Madurai (Indien)

Hauptberichter:	Prof. Dr. M. Joswig
Mitberichter:	Prof. Dr. R.E. Dinnebier
Mitberichter:	Prof. Dr. H-W. Reinhardt

Tag der Einreichung: 01.03.2011
Tag der mündlichen Prüfung: 25.05.2011

Institut für Geophysik,
Universität Stuttgart

Max-Planck-Institut für
Festkörperforschung, Stuttgart

2011

Contents

Chapter 1

Introduction

1.1 Introduction

X-ray powder diffraction[1] (XRPD) is a well-established analytical method for the characterization of crystalline materials used extensively in the fields of mineralogy, crystallography, chemistry, geology, petrology, material science, natural sciences and pharmaceutical industry. Earlier, the applications of XRPD was confined mostly to the areas of qualitative phase[2] analysis (e.g., the identification of new or unknown crystalline phases), to 'conventional' applications such as the determination of unit-cell parameters (Langford and Louër, 1996) and to the micro-structural[3] analysis of materials using the diffracted 'line profiles' (Figure 1.1) (Scardi *et al*., 2001; Audebrand and Louër, 2004; Kapoor *et al*., 2004; Dinnebier and Billinge, 2008; Scardi and Dinnebier 2010).

In the year 1967, Rietveld method (Rietveld, 1967; 1969) was introduced as a structural refinement method to be used originally for powder data collected using neutron sources (Albinati and Willis, 1982). Later, the method evolved into a general structural refinement method that can be applied to both X-ray and neutron powder data collected in various categories of experiments (Albinati and Willis, 1982). As the complete measured powder pattern rather than the 'line profiles' could be used in Rietveld refinement, the method opened the possibility to extract the maximum amount of structural information of materials from powder diffraction experiments (Young, 1991; Langford and Louër, 1996). Such information was formerly acquired mainly using single crystal X-ray diffraction

[1] Debye and Scherrer, 1916.
[2] Throughout the thesis the convention '*phase*' (italics) is used to represent the phase of an interfering wave; 'phase' (regular style) is used to denote a crystalline phase (chapter 3 is an exception).
[3] Crystallite size and lattice strain.

(XRD), which provided reliable-higher dimensional experimental data in comparison to powder experiments but was limited by the availability of high quality single crystals of suitable size.

The advent and development of Rietveld method between 1967 and 1970 had drastically increased the application of powder method to many standard structural refinements. The renaissance in instrumentation and the introduction of high speed computers to XRPD-data analysis after mid 1970s have further extended the use of Rietveld method to many complex structural refinements, to applications based on 'quantitative phase analysis' (Bish and Howard, 1988; Monecke *et al.*, 2001; Winburn, 2003), and to other applications beyond structural refinement (some of them are explained in detail in Evans and Evans, 2004)[4].

The important and widely recognized applications of Rietveld method in structural science is the direct exploration of structural phase transitions and the study of the physical/chemical properties of crystalline phases at non-ambient conditions. The state-of-the-art prospects of *in situ* investigation of crystalline solids at non-ambient conditions have been improved significantly due to the advancements in the brightness (Parise *et al.*, 2000) and collimation of modern (3rd generation) synchrotron light sources (Bilderback *et al.*, 2005; Fitch, 2007). The usage of 2D detectors with minimal read out times (Dickerson *et al.*, 2002) in contemporary time-resolved powder diffraction experiments[5] has allowed the rapid collection of hundreds and even thousands of high-resolution synchrotron powder diffraction patterns (Hinrichsen, 2008) in dependence on external variables. Frequently, the external variables used in these experiments are time[6], temperature[7] or pressure. An example of an angle resolved synchrotron powder data of AgNCO (Schmidt *et al.*, 2009) collected as a function of temperature is plotted in Figure 1.1.

The key properties studied in such 2D XRPD experiments are often the chemical reaction kinetics (Kennedy and Clark 1996), the thermal, electrical and mechanical properties of the crystalline specimen. Typically during the 2D XRPD data analysis, these parameters are retrieved by the sequential[8] application (Stinton and Evans, 2007) of whole powder pattern fitting (WPPF) methods (LeBail, 2005) to the powder data collected at each time step of

[4] Applications of Rietveld method in earth sciences, mineralogy and petrology are presented in literatures e.g.: Hill *et al.*, 1993, Liang & Hawthorne, 1994, Gonzalez *et al.*, 2003, Monecke *et al.*, 2001 and Raudsepp *et al.*, 2002. Most of these applications concern with the determination of relative amount of phases in mixed compounds (e.g., the relative abundance of the minerals that constitute rocks).

[5] These experiments will be called as 2D X-ray powder diffraction experiments. The powder patterns collected in these experiments will be called as 2D data.

[6] Constant temperature or isothermal experiments.

[7] Variable temperature (non-isothermal experiments).

[8] The name convention 'sequential refinements' or 'sequential WPPF' will be used repeatedly in this thesis to represent the consecutive refinements/decomposition of powder patterns collected in 2D experiments.

the experiment. The WPPF methods comprise the whole powder pattern decomposition (WPPD) methods (LeBail and Pawley algorithms) and also the whole powder pattern refinement method (WPPR) (Rietveld refinement method). In general, these methods calculate an approximate 'trial' powder pattern of the crystalline specimen by mixing several model parameters and functions (e.g., the incident wavelength, approximate lattice parameters, background parameters, etc.) that contribute to the diffracted intensities and their positions. The model parameters are then refined by minimizing the squared difference between the calculated 'trial' powder pattern and the experimentally measured powder pattern using the method of non linear least squares (Detailed explanations are provided in chapter 2, sections 2.3 and 2.4).

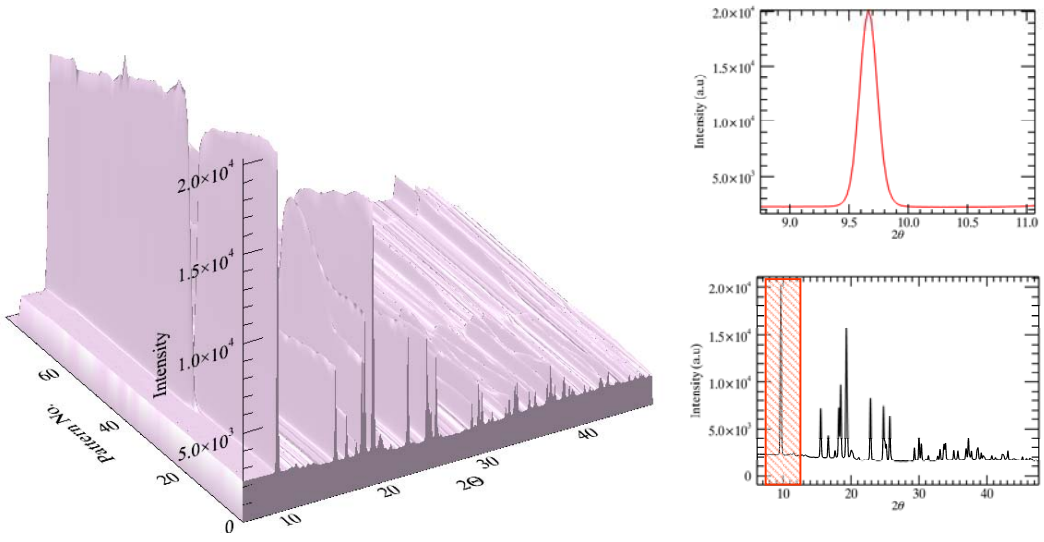

Figure 1.1 Synchrotron 2D powder data of silver isocyanate (AgNCO) (Schmidt *et al*., 2009) measured in dependence on temperature (Pattern No.) is presented. The powder pattern collected at room temperature (bottom right) and one of its line profiles (top right) are highlighted. The pictures are drawn with the help of the program 'Powder 3D' (Hinrichsen *et al*., 2006).

A simple application of sequential refinement is the estimation of the linear thermal expansion coefficient (Hammond *et al*., 2005; Jagtap *et al*., 2005; Schorr and Geandier, 2006; Hummer *et al*., 2007) of a crystalline material from its temperature dependent powder diffraction data. The low temperature lattice parameter (e.g., the parameter '*a*') of the compound can be refined using either WPPD or WPPR method. The refined value of the parameter '*a*' can be passed in as a starting input value to calculate[9] the succeeding

[9] And refine the model parameters.

'trial' powder pattern that corresponds to the next temperature step and so on for the higher temperatures. An array of lattice parameters refined at each temperature will be obtained; from its derivative, the thermal expansion coefficient of the compound can be determined (e.g., Jagtap *et al*., 2005). Other information that can be retrieved from *in situ* 2D powder diffraction experiments are stated in the literatures Norby *et al*., 1996; Evans and Evans, 2004 and Stinton and Evans, 2007.

In the example stated above, instead of subjecting each measured powder pattern to independent sequential WPPF, if one overall WPPF is performed using many powder patterns collected in the experiment, high quality and/or additional physical/chemical information of the crystalline phase can be acquired from the 2D data. This approach was named 'parametric Rietveld refinement'[10], and was introduced first in crystallography by J.S.O. Evans in the year 2007 (Stinton and Evans, 2007). As 'parametric Rietveld refinement' method involves simultaneous refinements of multiple powder patterns, the method unveils the possibility to introduce a model or a constraint of a crystallographic variable that changes with temperature (or time) into the refinement. In doing so, the convergence of the refinement can be directed more towards the correct minima, provided the model used is correct.

As a practical example the parameterization of 'zero-point-error' versus temperature in a high temperature laboratory experiment using Bragg-Brentano[11] geometry can be considered (Figure 1.2). 'Zero-point-error' is the systematic shift in the angular position of a measured powder pattern with respect to the center (or origin) of the detector. In a high temperature experiment, this parameter is expected to be a constant throughout the experiment.

However during a heating experiment, in addition to the sample the flat metallic holder on which the powder sample is placed will also be heated up. The thermal expansion of the metal sample holder will cause slight increase in the vertical position of the sample relative to the incident X-ray beam. As a consequence, the Bragg peaks in the recorded powder pattern shift continually from their expected position with the increase in temperature (Figure 1.2). The refinement of other variables that are dependent on the peak positions (e.g., the lattice parameters) will eventually be biased due to the continual shift of the origin of the powder patterns.

[10] 'Parametric Rietveld refinement': Also called as 2D refinement or surface refinement.

[11] Bragg-Brentano geometry (also called 'flat plate reflection geometry') is the common experimental set up used in powder diffraction experiments. In this setup, the powder sample to be probed by X-rays is spread on a flat sample holder (Figure 1.2), in contrast to the 'capillary mode' where the sample to be probed is filled in a narrow glass capillary.

In order to minimize this effect, the variation of 'zero-point-error' with temperature can be assigned an appropriate model (e.g., a quadratic function). The coefficients of this model can be refined simultaneously from multiple powder patterns and they can be fed back as a constraint or a correction term to other refinable variables that are the functions of Bragg peak positions (e.g., the lattice parameters).

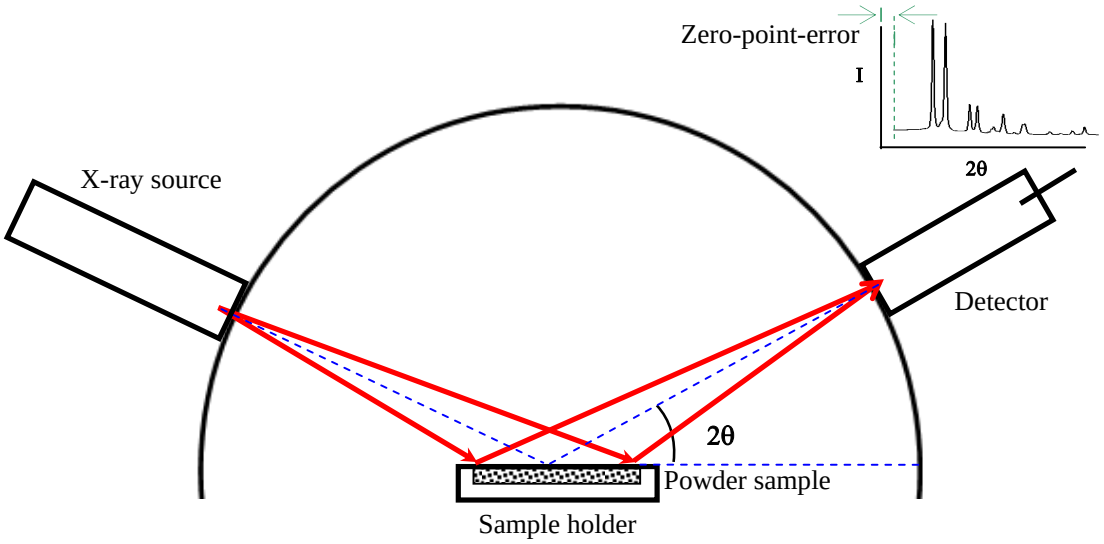

Figure 1.2 A simple schematic of Bragg-Brentano flat plate powder diffraction geometry is presented. For clarity, the divergence slits, primary and secondary Soller slits, and the receiving slits are not shown. In a laboratory experiment, these components are placed along the path of the X-ray beam to control its divergence along the two axes. (Top): A measured powder pattern (schematic), Bragg peaks and zero-point-error.

Instead of using a general model, if a realistic physical model of a variable is introduced into the refinement, additional information of the material can also be derived from 2D powder data. For example, in the isothermal studies related to the chemical kinetics, the solid state phase transitions are often described by the well known JMAK or Avrami's relation[12] (Avrami, 1939; Avrami, 1941). This relation can be substituted as a physical model of the continually growing crystalline phase fraction with respect to time (as explained in Müller *et al.*, 2009). Using Avrami's relation in the simultaneous Rietveld refinement allows for the otherwise unfeasible direct refinement of the rate constant of chemical reaction from the 2D XRPD data (see also chapter 6).

[12] A function of the reaction rate constant and reaction order.

Besides the general examples explained above, 'parametric Rietveld refinement' has variety of applications including the studies related to the extraction of vibrational frequencies of materials from their thermal expansion coefficients, refinement of non-crystallographic parameters, etc. More information about the method can be found in Stinton and Evans, 2007. The scope of the method has been explained in Evans and Evans, 2004, some applications are presented in the literatures Evans and Evans, 2004, Müller *et al*., 2010a and in Halasz *et al*., 2010.

One of the fundamental requirements for the evaluation of 2D XRPD data using sequential or parametric WPPF methods is a robust software that can perform fast and automated (or semi-automated) refinements of hundreds of powder patterns collected in 2D experiments. Major challenges in the accomplishment of a 'sequential/parametric WPPF software' exist in the development of a module that automates the preparation of data for the refinements, that manipulates the considerable number of variables used in the simultaneous/multiple refinements, that organizes the refined output variables and that provides possibility to easily re-do bulk refinements with various models of variables. The construction and the implementation of the 'math' routines required for the refinements are trivial, as there are many least squares minimization packages available for open use that can be interfaced with the new sequential/parametric refinement software.

A computer program 'Powder 3D Parametric' (chapter 3) has been developed during the course of this work as an attempt to meet the requirements mentioned in the previous paragraph. The developed program provides space to load, visualize and handle bulk 2D powder data (chapter 3) and to perform fast and semi-automated sequential and parametric WPPF by interacting with the launch mode kernel of the powder pattern analysis program Topas® (Coelho, 2007). The launch mode kernel of Topas simplifies the massive tasks of sequential and parametric refinements through its unique macro language and by the use of input and output command files[13]. Using these provisions, the set of instructions necessary to perform refinements can be passed in (**.inp*) and the refined parameters can be easily retrieved (**.out*). The example illustrated before (parameterization of 'zero-point-error') can be easily realized by introducing the 'zero-point-error' model equation in the input file and executing it in the Topas launch mode. Powder 3D Parametric provides facility (a text editor set up) for easier preparation and execution of input files (chapter 3) and many other graphical interface tools for analyzing the refined results.

In a 2D experiment, if the crystalline sample to be analyzed is measured under non-isothermal conditions (or the sample shows reconstructive[14] type of phase transitions) then,

[13] The '**.inp*' and '**.out*' files respectively.
[14] Refer chapter 4 footnote 2.

additional demands arise in analyzing and handling the data and in doing independent refinements of various reconstructive structural phases that the compound exists in. In such circumstances, the separation, organization and classification of the powder patterns belonging to identical phases, prior to the refinements becomes crucial.

The problem of classification/grouping of powder patterns belonging to various reconstructive (or non isothermal) phases has also been considered in the developed program. The powder pattern classification has been automated using a simple and robust algorithm based on the Pearson's correlations coefficients (chapter 4) of the powder pattern intensities collected in successive instants[15] of the external variables. The developed routine for its improved efficiency demanded a method for normalizing the powder patterns. Alongside the development of the main classification method, a robust 'squared standard score' normalization method has been developed, which significantly improved the efficiency of the presented classification procedure (section 4.6.3). Other analytical and statistical methods useful for the pattern classifications were also developed and their efficiencies were summarized in chapter 4 (section 4.3).

On the applications part of the work, the chemical reaction kinetics of copper phthalocyanine (CuPC) polymorphs[16] (Müller *et al*., 2009) has been studied from several isothermal experimental data using parametric Rietveld refinement method[17], assisted by the developed program. The use of the program has considerably simplified the general difficulties that are faced otherwise in doing sequential and parametric refinements of bulk 2D powder data. A comparison between the kinetics of CuPC obtained from the Arrhenius relation (IUPAC, 1997; Kennedy and Clark 1996) and those obtained from parametric Rietveld refinement has also been made; the reasons for the discrepancies of results between the two methods are briefly discussed.

The second application concerns with the parametrization of the crystallite size with respect to the annealing time and temperature. Some data used in the parametric kinetic analysis of CuPC polymorphs and the temperature dependent nano-crystalline titanium dioxide-Anatase (TiO_2) data were used in this analysis (TiO_2: Horn *et al*., 1972). The variation of the crystallite size (~1/ FWHM[18]) with respect to time for some selected data samples could be parameterized by a general 3rd order polynomial.

[15] Steps of temperature, pressure or time
[16] Some additives were also added to the polymorphs to study their influence (Müller *et al*., 2010b).
[17] Will be called 'parametric kinetic analysis'.
[18] Full Width at Half Maximum.

1.2 Thesis outline

The thesis is divided into two parts. The first part consists of the required scientific theory, the analytical part of the work, the description of the sequential/parametric WPPF software, and its scientific applications to XRPD data. The second part of the thesis provides the tutorials for performing sequential and parametric WPPF etc., and also gives a detailed reference manual for the graphical user interfaces of the program.

Chapter 2 begins with the explanation of the basic physics behind diffraction and Bragg's law and a general overview of the powder diffraction method, full pattern decomposition methods and the fundamentals of Rietveld method etc. (More information can be acquired elsewhere from the well known literature Cullity and Stock, 2001. The elementary principles of powder diffraction are explained well in a simple and comprehendible language in Pecharsky and Zavalij, 2003. Advanced theory and applications of powder diffraction methods are summarized in Dinnebier and Billinge, 2008).

Chapter 3 gives a practical explanation of the program 'Powder 3D Parametric' interfaced with 'Topas launch mode' and a basic demonstration of the preparation and execution of Topas input files required for sequential and parametric WPPF.

In chapter 4, methods used for the determination of phase transition points in *in situ* XRPD data are presented. Applications of one of the developed methods to several temperature dependent 2D data are presented in chapter 5. Chapter 6 presents the application of parametric Rietveld refinement to extract the reaction kinetic information of CuPC at various temperatures. In chapter 7, the parameterization of the crystallite size versus annealing time and temperature has been explained with CuPC and TiO_2 sample data.

Chapter 2

Theory

2.1 Basics of X-ray diffraction

The foundation of XRD is laid on the classical phenomenon of wave interference, where two or more parallel-monochromatic electro magnetic (EM) waves superimpose to produce a resultant wave whose amplitude is a function of the relative *phases*[1] (or path difference) of the original interacting waves. The amplitude of the resultant wave increases (constructive interference) if the path difference between the interfering waves is an integer multiple of the incident wavelength; the amplitude decreases (destructive interference) if the path difference is odd-half integer multiple (1/2, 3/2, 5/2, etc.) of the incident wavelength. Diffraction is observed when the constructively interfering parallel-monochromatic waves are scattered by an object or by a set of periodically placed objects.

The atoms are arranged periodically in a 'theoretically' infinite crystal. Therefore the atoms[2] diffract[3] the incident X-rays allowing them to form unique symmetrical reflection patterns on a detector placed in the inverted frequency or reciprocal space.

The positions and the magnitudes of intensities[4] formed on the detector are governed by the wavelength and geometrical conditions imposed by Bragg's law (Equation 2.1) (Bragg, 1913).

$$2d_{hkl}\sin\theta_{hkl} = n\lambda \tag{2.1}$$

[1] The relative *phase* (φ) is proportional to the difference in the path travelled (Δx) by the waves and the incident wavelength (λ): $\varphi = (2\pi/\lambda).\ \Delta x$.
[2] More precisely the clouds of electrons diffract X-rays.
[3] The phenomenon is called Thompson's or inelastic scattering.
[4] Amplitude squared.

where,
θ_{hkl} - Diffraction angle
λ - Wavelength of the incident X-ray beam
n - Diffraction order
$\{hkl\}$ - Indices of reflection in the reciprocal space (Miller indices)
d_{hkl} - d-spacing.

Bragg's law thus permits only certain waves incident at the angles θ_{hkl} on the fictitious atomic planes (with spacings - d_{hkl}) to be diffracted. Furthermore, the atoms in the crystal lattice diffract the incident X-rays as the inter-atomic spacings are of the same order of magnitude as the wavelength of incident X-ray beam (Pecharsky *et al*., 2003).

The intensities (I_{hkl}) of the waves diffracted by a crystal lattice at Bragg angles (θ_{hkl}) and their corresponding (relative) *phases* are unique for each diffracted wave. Apparently these properties (the magnitude (I_{hkl}), direction (θ_{hkl}) and relative *phases*) of the diffracted waves carry the information about the atomic co-ordinates, the unit cell dimensions and symmetry of the diffracting crystal (together called the crystal structure). Out of the three properties, only the magnitudes (intensities) of the waves diffracted in the directions (θ_{hkl}) are directly measurable from X-ray diffraction experiments. The relative *phases* of the diffracted waves, which are the basic requirement for the reconstruction of real space electron density (or crystal structure) are not directly obtainable from the experiment. (Typically, in an X-ray diffraction experiment the diffractometer provides a long list of Bragg intensities (I_{hkl}) diffracted in the directions θ_{hkl}).

A major part of X-ray crystallography concerns with the reconstruction of the real space crystal structure of the diffracting material using a set of experimentally measured intensities (I_{hkl}) reflected in the directions θ_{hkl}, assisted by various methods that can find/assign suitable *phases* to the measured wave amplitudes (I^2_{hkl}).

2.2 Powder diffraction

In an X-ray diffraction experiment, the crystalline specimen to be probed can either be of a 'single crystal' of suitable size and quality or of a powder consisting of small randomly oriented crystallites. Obviously, the diffraction patterns observed also vary according to the form of the crystalline sample (a single crystal or a powder sample) used in the experiment. X-rays incident on a 'single crystal' are diffracted as lines, which when obstructed by a 2D detector form well resolved 'spots' of Bragg intensities on the detector plane (Figure 2.1).

If the sample is polycrystalline (a powder sample), the incident X-rays are diffracted as cones in the directions (h,k) whose projection on the 2D detector plane are confocal ellipses

(Figure 2.1). As the number of quasi crystallites in the powder sample tends towards infinity their orientations in space (Pecharsky *et al.*, 2003) becomes completely random, the spots that constitute the elliptical base of the cones smear out to form circles (or ellipses) called Debye rings whose intensities are almost uniform[5]. The set of Debye rings formed on the detector plane in various directions (*h,k*) diffracted by fewer crystallites and by many crystallites are shown schematically in Figure 2.1.

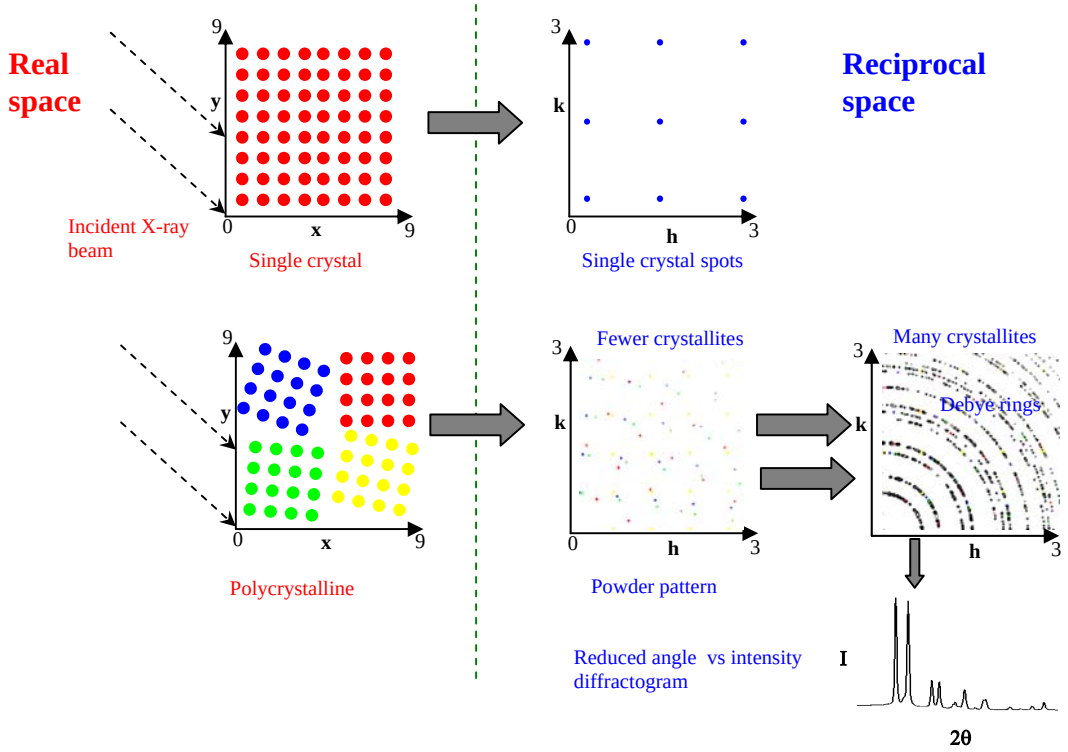

Figure 2.1 The intensities observed (schematic) from XRD experiments performed using a single crystal and powder sample are projected in the 2D reciprocal space. Intensity 'spots' are formed if the diffracting material is in the form of a single crystal. (Debye) 'Rings' are formed if the diffracting material is an ideal powder.

In an angle resolved powder diffraction experiment, the Debye rings formed are reduced and represented typically as a one dimensional angle (direction) versus intensity diffractogram (I vs 2θ) as shown in Figure 2.1. Depending on the nature of the experiment and the dimensionality of the detector used, there are some data preprocessing steps (e.g., experimental calibration, integration of the Debye rings, etc.) involved before generating the 1D angle versus intensity diffractogram. The preprocessed angle versus intensity

[5] The spots/patterns formed on the detector plane are the pictorial representations of the wave intensities I_{hkl} diffracted in the directions θ_{hkl}, as counted by the detector set up.

diffractogram (equivalent to a list of diffracted Intensity along θ_{hkl} in single crystal XRD) obtained is used for further analysis and in the extraction of the structural information of the crystalline sample under study.

In the following sections the focus will be mainly given to the analysis and the extraction of the structural information from 1D powder diffractograms.

2.3 Pattern decomposition methods

As mentioned at the end of section 2.1, the reconstruction of structural information of a crystalline material from diffraction methods requires a list of experimental Bragg intensities (I_{hkl}) diffracted at various angles (θ_{hkl}). In powder diffraction, the restoration of the Bragg intensities (I_{hkl}) (so also the atomic structural information) from a diffractogram is not as straightforward, as compared to the single crystal XRD, since the reciprocal space dimension of the former has been reduced[6] from 3 to 1.

As a consequence, the measured diffractogram (or observed powder patterns) often consists of several overlapped Bragg peaks due to systematic and accidental effects (Massüger, 2007; Rius *et al*., 1999). The magnitudes of the individual Bragg intensities are only proportional to the height of the peaks in the observed histogram; their actual values must be determined by integrating the area under the observed peaks.

The automated separation of overlapped Bragg peaks and the extraction of the integrated Bragg intensities (I_{hkl}) (proportional to squared intensities of structure factors[7]) become significant when the problem of *ab-initio* structural solution from powder data is of concern (Mukherjee, 2007). The Whole Powder Pattern Decomposition methods (WPPD) are used for the purpose of partition and extraction of the integrated intensities from the observed diffractograms. Apparently, the (approximate) positions of the Bragg peaks and space group information must be known a priori for applying the WPPD methods. In other words, the powder pattern must be 'indexed', (Chernychev, 2001) prior to its decomposition.

The WPPD methods generally refine (or derive) the intensities by minimizing the difference between a (theoretical) powder pattern calculated from a model and the experimentally observed powder pattern in a least squared sense (Harris *et al*., 1996). The theoretical powder pattern is calculated mainly from the lattice parameters, space group information, the profile parameters and background parameters[8].

The most commonly used WPPD methods are the Pawley (Pawley, 1981) and the LeBail (LeBail *et al*., 1988) algorithms. Both the procedures extract the integrated intensities from

[6] See Figure 2.1 for the dimensionality reduction from 3 to 2 to 1 (crystal to Debye rings to diffractogram).
[7] Diffraction (amplitude and phase) of a unit cell.
[8] Only the major parameters are mentioned here.

the powder pattern, independent of the structural model[9] of the compound (Toraya, 1989). The lattice parameters, profile parameters, along with the background parameters are refined during the pattern decomposition.

LeBail method calculates the intensities by iterating the Rietveld decomposition formula (Equation 2.3), which was originally used in the refinement of the crystal structures. Analogous to the Rietveld method, the observed (experimental) intensity ($(y_{obs})_i$) is partitioned among all the peaks (p in Equation 2.2), proportional to their calculated peak intensities. Except that a set of arbitrary starting values (e.g. 1 or 1000) are assigned to the calculated peak intensities in the first iteration of the LeBail extraction.

$$\left(I_{obs}\right)_1 = \sum_{i=0}^{n-1}\left[\left(y_{obs}\right)_i \cdot \left(\frac{\left(y_{calc}\right)_{i1}}{\sum_{j=0}^{p-1}\left(y_{calc}\right)_{ij}}\right)\right] \tag{2.2}$$

where,

i - The data points that contribute to the peak
$(y_{obs})_i$ - Experimentally observed intensity
$(y_{calc})_{i1}$ - The calculated intensity of peak '1'
$(I_{obs})_1$ - The 'observed' intensity of peak '1'.

Equation 2.2 calculates the 'observed' intensity $(I_{obs})_1$ of a particular peak '1' of a powder pattern using the total experimentally observed intensity $(y_{obs})_i$ and the ratio of the calculated intensity of peak '1' $(y_{calc})_{i1}$ to the total calculated intensity of all the peaks $\Sigma_j(y_{calc})_{ij}$. The 'observed' intensities calculated from Equation 2.2 will be used as an alternative for the calculated intensities in the Rietveld decomposition formula for the 1st iteration cycle (Equation 2.3).

After the first iteration, the lattice, background and profile parameters etc., will be refined. The set of refined lattice, background and profile parameters will be used for calculating a new set of I_{obs}. The new set of I_{obs} obtained will be updated in the succeeding refinement cycle to refine the lattice, background and profile parameters again. This process is iterated until good agreement between the observed and calculated powder pattern and also physically meaningful values for lattice parameters are attained.

Pawley's method is a full profile non-linear refinement method similar to LeBail method; the important difference in this method is that the intensities are treated as individual refinable least squares variables along with the profile, lattice and background parameters. The process is much slower than LeBail as the speed of the convergence depends on the

[9] The atomic coordinates, (x, y, z) the site occupancies and temperature factors.

number of independent refinable variables present in the least squares minimization equation (Equation 2.4). Handling of non physical 'negative' intensities resulting from the least squares fit is an additional drawback of Pawley's method.

2.4 Rietveld method

The Rietveld method (Rietveld, 1967 and1969) is a Whole Powder Pattern structural Refinement method (WPPR) and it is not meant for the extraction of integrated intensities from the observed powder pattern only, as the other WPPD methods explained in section 2.3. In fact the algorithm used by LeBail (section 2.3) was originally used by Rietveld for structural refinement; the difference in Rietveld method is that the structure factors calculated from an approximate model are supplied to the calculation of intensities ($y_{i(calc)}$ in Equation 2.3) from the first iteration onwards. Along with a list of parameters, (Equation 2.3) the atomic coordinates and temperature factor of the atoms are also refined in the Rietveld method.

$$\left(y_{calc}\right)_i = \sum_l \left[S_l \sum_{lk} \left(M_{lk} A_{lk}(2\theta_i) P_{lk} \left| \left(F_{calc}\right)_{lk} \right|^2 LP(2\theta_i) \Phi_{lk}(2\theta_i) \right) \right] + \left(b_{obs}\right)_i \qquad (2.3)$$

where,

$(y_{calc})_i$ - Calculated intensity of i^{th} data point of a powder pattern that comprises of l phases

$\sum_{lk}$ - Sum over all reflections k of the phase l

S_l - Scale factor of the phase l

M_{lk} - Multiplicity

$A_{lk}(2\theta_i)$ - Absorption factor

P_{lk} - Preferred orientation factor

$(F_{calc})_{lk}$ - Structure factor

$LP(2\theta_i)$ - Lorentz-Polarization factor

$\Phi_{lk}(2\theta_i)$ - Profile function

$(b_{obs})_i$ - Background intensity of i^{th} data point.

} $C_0, C_1, C_2, C_3, \ldots, C_{(R-1)}$

In Equation 2.3, a step scan intensity ($(y_{calc})_i$) is calculated using some basic functions that describe the background intensities, peak profile, atomic coordinates, instrumental and sample aberrations and other corrections parameters. The experimentally observed powder profile is an outcome of the combination of many such step scan intensities that are calculated using these math functions and correction terms.

The Rietveld method uses the non linear least squares method and minimizes the difference between the observed powder pattern and the calculated pattern (using Equation

2.3) by refining the model parameters. In other words, the Rietveld method refines a crystal structure and also gives a numerical account of the aberrations in the experimentally observed powder pattern using the non linear least squares minimization method.

2.5 Basic math in the Rietveld method

In the Rietveld method (as mentioned in section 2.4), the starting values for the structure factors are calculated from a known approximate structural model of the specimen to be analyzed. The other parameters ($(C_0 C_1, C_2, ..., C_{(R-1)})$ in Equation 2.3) that contribute to the observed powder pattern position, shape and intensities must be given some sensible starting values (or functions that describe their variation along the abscissa) at the onset of the refinement. The least squares solution for Equation 2.3 can be obtained mathematically by minimizing the squared difference (E) between the calculated powder pattern ($f(\boldsymbol{x}_D, C_0 C_1, C_2, ..., C_{(R-1)})$)[10] and the experimentally observed pattern ($\boldsymbol{p}_D$) (Equation 2.4).

$$E = \sum_j (\boldsymbol{p}_D - f(\boldsymbol{x}_D, C_0 C_1, C_2, ..., C_{(R-1)}))^2 \qquad (2.4)$$

where,

$f(x_D, C_{0,1,..,(R-1)})$	-	Calculated powder pattern ($\boldsymbol{x}_D$ are the independent variables)
$\{C\}_{0,1,2,...,R-1}$	-	Set of refinable parameters/functions described in Equation 2.3
E	-	Difference squared between the observed and calculated powder patterns
$\boldsymbol{p}_D$	-	A single powder pattern $\boldsymbol{p}_D = \{y_0, y_1, y_2, ..., y_{(D-1)}\}$ with D data points.

The squared difference 'E' in Equation 2.4 must be minimized with respect to every refinable variable ($C_{0,1,2,...,(R-1)}$ or $\{C\}_{i=0,1,...,(R-1)}$) in the Rietveld decomposition formula (Equation 2.3). Mathematically, the minima of these variables can be determined by finding the partial derivatives of E with respect to individual variables and equating them to zero. The minima of an arbitrary refinable variable C_p can be written as Equation 2.5, where C_p could be S_l in Equation 2.3.

$$\frac{\partial E}{\partial C_p} = 0 \qquad (2.5)$$

[10] Conventions: In all the equations used in this thesis, the upper case subscripts (e.g. D) denotes the vector dimensions and the lower case subscripts (e.g., i,j) are used as running indices. The bold lower case letters represent a vector (e.g., $\boldsymbol{v}$) and the bold upper case letters represent a matrix (e.g., $\boldsymbol{A}$).
e.g., $\boldsymbol{p}_{D:}$ is a vector $\boldsymbol{p}$ with D elements. $\boldsymbol{p}_i$ is the ith element of vector $\boldsymbol{p}$. $(\boldsymbol{p_D})_i$ is the ith vector $\boldsymbol{p_D}$ in an array of vectors. $\boldsymbol{Q_{N,D}}$ is a matrix of N rows and D columns.

where,
C_p - A refinable Rietveld variable.

A set of non-linear equations (as Equation 2.5) corresponding to the minima of all '*R*' refinable variable ($\{C\}_{i=0,1,2,...,(R-1)}$) described in Equation 2.3 can be obtained in a similar manner. The total number of the equations (*R*) obtained (called the normal equations) will now be equal to the total number of unknown Rietveld variables. The normal equations so obtained prepare the way to solve the least squares problem of approximating the 'overdetermined' system of equations. These (normal) equations can be represented in a compact matrix form as Equation 2.6.

$$\boldsymbol{A}\boldsymbol{v} = \boldsymbol{b} \tag{2.6}$$

where,
$\boldsymbol{A}$ - A matrix containing the independent variables $\boldsymbol{x_D}$
$\boldsymbol{v}$ - A column vector of the refinable parameters $\{C\}_{i=0,1,2,...,(R-1)}$
$\boldsymbol{b}$ - A column vector whose elements are functions of the independent variables $\boldsymbol{x_D}$ and $\boldsymbol{p}_D$.

The variables $\boldsymbol{A}$ and $\boldsymbol{b}$ in Equation 2.6 are respectively a matrix of independent variables ($\boldsymbol{x_D}$) and a vector whose elements are several functions of the dependent ($\boldsymbol{p}_D$) and independent variables ($\boldsymbol{x_D}$) derived from the original normal equations. The important variable in Equation 2.6 is $\boldsymbol{v}$, which is a column vector of the unknown Rietveld variables$\{C\}_{i=0,1,2,...,(R-1)}$. The vector of unknown variables $\boldsymbol{v}$ can be evaluated by finding the transpose of the matrix $\boldsymbol{A}$ ($\boldsymbol{A}^{-T}$) and pre multiplying $\boldsymbol{A}^{-T}$ in Equation 2.6[11].

The least squares minimization can be improved by assigning suitable statistical significance factors to the refinable variables. This can be accomplished by introducing a matrix of weight ($\boldsymbol{W}$) in Equation 2.6. The weight matrix that contains the normalized (0 and 1) significance of the variables (representing how well and/or under what experimental conditions the variables are measured) must be pre-multiplied to the coefficients of the minimization equation as in Equation 2.7a. The weighted least squares fit can be implemented by pre multiplying the variables $\boldsymbol{A}$ and $\boldsymbol{B}$ by $\boldsymbol{A}^{-T}$ (Equation 2.7b) and evaluating the unknown variable $\boldsymbol{v}$.

$$\left.\begin{aligned} \boldsymbol{W}\boldsymbol{A}\boldsymbol{v} &= \boldsymbol{W}\boldsymbol{b} \qquad (2.7a)\\ (\boldsymbol{A}^T\boldsymbol{W}\boldsymbol{A})\boldsymbol{v} &= (\boldsymbol{A}^T\boldsymbol{W})\boldsymbol{b} \qquad (2.7b) \end{aligned}\right\}$$

where,
$\boldsymbol{W}$ - Weight matrix.

[11] i.e., the least squares solution to Equation 2.6.

The vector ***v*** refined using the steps explained so far in section 2.5 corresponds to the set of parameters obtained in one cycle of the least squares refinement. To assure that the refined variables are physically sensible and they correspond exactly to the global minima of *E*, the new values refined in the first cycle must be updated in the Rietveld decomposition formula (Equation 2.3) and the complete procedure described in this section must be repeated. Usually, many numbers of iterations (depending on the starting values of the parameters and/or the precision of the structural model etc.) are required until the 'expected' physically meaningful values of the variables are attained.

The convergence of Rietveld refinement can be inspected with the help of several statistical agreement factors available in literature. Most of the agreement factors are based on the difference or the squared difference between the observed and the calculated powder patterns. A widely used reliability factor is the weighted residual profile factor (R_{wp}) (Equation 2.8). The weighted residual profile factor (Equation 2.8) calculates the squared difference between the observed and calculated powder patterns with the weights of the observed pattern included in the calculation

$$R_{wp} = \sqrt{\frac{\sum_{i=0}^{D-1} w_i (y_{i(obs)} - y_{i(calc)})^2}{\sum_{i=0}^{D-1} w_i y^2_{i(obs)}}} \qquad (2.8)$$

where,
R_{wp} - Weighted residual profile factor
$y_{i(obs)}$ - Observed powder pattern
W_i - Weights of the observed intensities
$y_{i(calc)}$ - Calculated powder pattern.

It is worth to mention that a high background in the observed powder pattern (if present) must be subtracted before calculating the residuals; else the calculated weighted residuals (R_{wp}) will be biased by the background, consequently ending up in physically non-reliable agreement factors (The background subtracted '*R_wp*' is conventionally written as '*R_wp_dash'* (Coelho, 2007)).

2.6 Parametric Rietveld method

'Parametric Rietveld refinement' method concerns with the simultaneous refinement of variables (or its model coefficients) that change with time,[12] using multiple powder patterns (N in Equation 2.9) collected in the 2D XRPD experiment. The math involved in 'Parametric Rietveld method' is similar to that explained in section 2.5 but the least squares minimization involves finding the squared difference between observed and calculated 2D data (sets of powder patterns); it involves the inclusion of one more dimension to Equation 2.4. The minimization equation (similar to Equation 2.4) for parametric refinement method is given as follows.

$$E = \left[\left(\boldsymbol{Q}_{obs} \right)_{N,D} - \left(\boldsymbol{Q}_{calc} \right)_{N,D} \right]^2 \tag{2.9}$$

where,
$(\boldsymbol{Q}_{obs})_{N,D}$ - A matrix of N observed powder patterns $\boldsymbol{p}_D$ with D data points (2D data)
$(\boldsymbol{Q}_{calc})_{N,D}$ - A matrix of N calculated powder patterns $\boldsymbol{p}_D$ with D data points (2D data calculated from Equation 2.3)
E - Squared difference between observed and calculated 2D data

In Equation 2.9, the terms $(\boldsymbol{Q}_{obs})_{N,D}$ and $(\boldsymbol{Q}_{calc})_{N,D}$ are the observed and calculated 2D data; each of them contain an array of powder patterns ($\boldsymbol{p}_D$) collected at subsequent time steps. The terms $(\boldsymbol{Q}_{obs})_{N,D}$ and $(\boldsymbol{Q}_{calc})_{N,D}$ are expanded in Equations 2.10a to 2.10c.

$$\left(\boldsymbol{Q}_{obs} \right)_{N,D} = \left\{ \left(\boldsymbol{p}_D \right)_i \right\}_{i=0,1,2,...,(N-1)} \tag{2.10a}$$

$$\left(\boldsymbol{p}_D \right)_i = \left\{ y_0, y_1, y_2, ..., y_{D-1} \right\}_i \tag{2.10b}$$

$$\left(Q_{calc} \right)_{N,D} = \begin{Bmatrix} f_0(\boldsymbol{x}_D, C_{00}, C_{01}, ..., C_{0(R-1)}), \\ f_1(\boldsymbol{x}_D, C_{10}, C_{11}, ..., C_{1(R-1)}), \\ ..., \\ ..., \\ f_{(N-1)}(\boldsymbol{x}_D, C_{(N-1)0}, C_{(N-1)1}, ..., C_{(N-1)(R-1)}) \end{Bmatrix} \tag{2.10c}$$

[12] For clear description the external variable 'time' is considered throughout this section, in general the external variables can be time, temperature, pressure etc.

where,

$(\boldsymbol{p}_D)_i$ - A powder pattern (with D data points) measured at i^{th} time step

$f_i(\boldsymbol{x}_D, C_{00}, C_{01}, .., C_{0(R-1)})$ - Calculated i^{th} powder pattern ($\boldsymbol{x}_D$ are the independent variables)

C_{ij} - j^{th} refinable parameter of the i^{th} calculated powder pattern.

N - Number of powder patterns in the 2D data.

The set of parameters (C_{00}, C_{10}, C_{20},..., $C_{(N-1)0}$) (in shortened form: $\{C\}_{i,0}$) in Equation 2.10b, represents a single refinable Rietveld variable measured at different time steps (e.g., the weight fraction 'w' that varies with time). The procedure to parameterize one set of a variable with respect to time is described below.

Consider a Rietveld variable $\{C\}_{i,1}$ with the time index (i) of '*0* to N' and variable index (j) of '*1*' to be parameterized by a second order polynomial equation ($a_0+a_1T+a_2T^2$). The set of variables $\{C\}_{i,1}$ to be refined at various instants listed in Equation 2.10b must be replaced by its polynomial model as shown in Equation 2.11.

$$\left(Q_{calc}\right)_{N,D} = \left\{ \begin{array}{l} f_0(\boldsymbol{x}_D, C_{00}, (a_0 + a_1T + a_2T^2), ..., C_{0(R-1)}), \\ f_1(\boldsymbol{x}_D, C_{10}, (a_0 + a_1T + a_2T^2), ..., C_{1(R-1)}), \\ ..., \\ ..., \\ f_{(N-1)}(\boldsymbol{x}_D, C_{(N-1)0}, (a_0 + a_1T + a_2T^2), ..., C_{(N-1)(R-1)}) \end{array} \right\} \tag{2.11}$$

where,

$a_0+a_1T+a_2T^2$ - A polynomial describing the evolution of variable $\{C\}_{i,1}$ with time T

a_0, a_1, a_2 - The coefficients of the polynomial refined from multiple powder patterns.

The coefficients of the polynomial a_0, a_1, and a_2 in the parametric equation for $(\boldsymbol{Q}_{calc})_{N,D}$ (Equation 2.11) are common and are refined from all the powder patterns that constitutes the 2D data. In order to arrive at the least squares solution for parametric refinement (similar to section 2.5), the equation for $(\boldsymbol{Q}_{calc})_{N,D}$ (Equation 2.11) must be substituted for $(\boldsymbol{Q}_{calc})_{N,D}$ in the least squares minimization equation (Equation 2.9).

As explained in section 2.5, Equation 2.9 must be minimized with respect to all the parameters ($\{C\}_{i,j}$) including the new global parameters and (a_0, a_1 and a_2) arrayed in Equation 2.11. A least squares matrix equation similar to Equation 2.6 must be constructed and solved for the set of unknown parameters $\boldsymbol{V}$. The unknown variable $\boldsymbol{V}$ (similar to $\boldsymbol{v}$ in Equation 2.6) for parametric refinement is expanded in Equation 2.12.

$$\boldsymbol{V} = \begin{bmatrix} \{C_{00}, (a_0 + a_1T + a_2T^2), C_{02}, ..., C_{0(R-1)}\} \\ \{C_{10}, (a_0 + a_1T + a_2T^2), C_{12}, ..., C_{1(R-1)}\} \\ .. \\ .. \\ .. \\ \{C_{N0}, (a_0 + a_1T + a_2T^2), C_{N2}, ..., C_{N(R-1)}\} \end{bmatrix} \tag{2.12}$$

where,

$\boldsymbol{V}$ - A matrix of unknowns of N rows and R columns (N - number of patterns, R - number of refinable Rietveld variables in each pattern)

C_{ij} - j^{th} parameter in the i^{th} powder pattern.

The obvious difference between the variable $\boldsymbol{v}$ in Equation 2.6 and $\boldsymbol{V}$ in Equation 2.12 is that it is no more a column vector as in case of a single powder pattern but rather a matrix of N rows and R columns. R is the number of refinable variables per pattern and N is the total number of patterns used in the simultaneous (parametric) refinement (Equation 2.12). The corresponding $\boldsymbol{A}$ and $\boldsymbol{B}$ matrices (analogous to Equation 2.6) for parametric Rietveld refinement are complicated and have many dimensions; they are not expanded here.

One of the intrinsic advantages of parametric Rietveld refinement in 2D XRPD is the reduction of correlations between variables that are mutually dependent. Parameterizing one of the variables is equivalent to separating (or fixing) the variable during the refinement but allowing it to refine independently within the constraints imposed by its physical model. The chance of the refinement to fall into false minima is reduced if the known model of the variable is used rather than the variable itself.

The basic mathematical procedure involved in parametric Rietveld refinement (explained so far in sections 2.5 and 2.6) has been implemented in many existing refinement programs (e.g. Topas). For implementing the ‘graphics’ part and the ‘analysis’ part of parametric refinement, the interface program ‘Powder 3D Parametric’ has been developed.

Chapter 3

A program for sequential and parametric Rietveld refinements using Topas[1]

3.1 Introduction

The computer program 'Powder 3D Parametric' has been developed during the course of the work to realize fast and automated sequential/parametric WPPF of large number of 2D XRPD data. The developed program interacts with the full pattern analysis software suite Topas (Coelho, 2007) to perform the refinements. In this chapter, some of the essential features and applications of the developed program are presented.

3.2 Topas launch mode and 'Powder 3D Parametric' interface

The software suite 'Topas' can be executed (Coelho, 2007) in two operation modes; the GUI mode and the launch mode. Most of the features of Topas are accessible in its powerful launch mode with its flexible macro language and the input command text file (*.*inp* file). In Topas launch mode, a specific task[2] can be accomplished by entering the set of necessary Topas statements in the *.*inp* file and passing the file to the Topas kernel for execution. An important feature of Topas launch mode is that it provides way for complex variable models to be introduced into the refinement through the *.*inp* file, (Stinton and Evans, 2007) with which almost any refinable variable can easily be parameterized. The

[1] Part of the contents of this chapter has been published in Rajiv *et al.,* 2010.
[2] e.g., performing a WPPF.

developed program 'Powder 3D Parametric' provides space for easier and quicker preparation and/or execution of the Topas *.*inp* files required for sequential and parametric WPPFs and also supports the graphics related to sequential/parametric WPPFs. Topas is used by 'Powder 3D Parametric' only as a kernel where the refinements (minimizations) are performed.

At various instants, 'Powder 3D Parametric' interacts with Topas kernel through the prepared *.*inp* files and the refined output files (*.*out*) with which all the information necessary to perform the refinements[3] are exchanged. A block diagram portraying the exchange of information at various instants between Topas and 'Powder 3D Parametric' is presented in Figure 3.1.

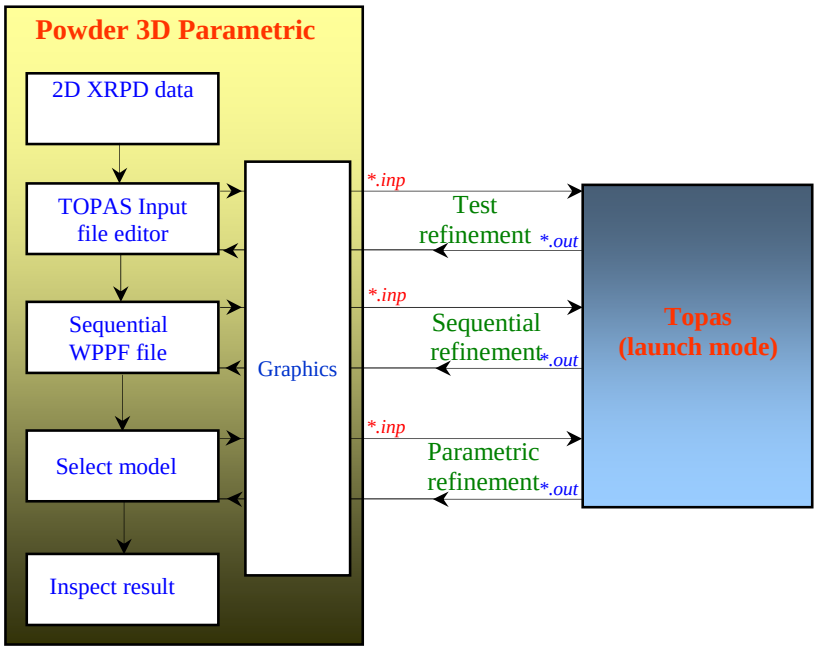

Figure 3.1 The information flow between 'Powder 3D Parametric' and Topas at various instants (during test, sequential and parametric refinements) is shown. The required input files are prepared within 'Powder 3D Parametric'. Topas launch mode kernel is used only for performing the minimizations.

3.3 Description of 'Powder 3D Parametric'

The program consists of three major functional components. It has a graphics interface ('Powder 3D Parametric' graphics interface) to load and visualize 2D powder diffraction data (Figure 3.2), a plain text editor setup (Figure 3.3) used for building Topas input files and a spreadsheet (chapter 6, Figure 6.5) to view, analyze and parameterize the variables.

[3] The so called 'test' refinement, sequential/parametric refinements (explained later in this chapter, and also in the Users manual).

The important features of these components will be briefly described in the following sections.

3.3.1 Graphics interface

The graphics interface[4] (Figure 3.2) is meant essentially for powerful, high quality 2D and 3D graphical representations of 2D XRPD data (Hinrichsen *et al*., 2006).

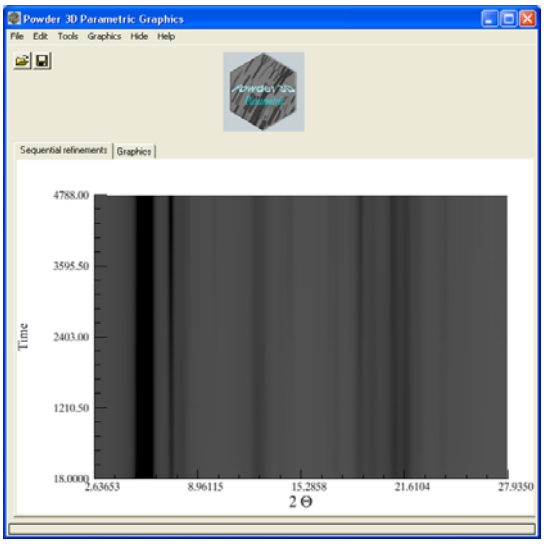

Figure 3.2 The graphics interface of the program 'Powder 3D Parametric' is shown. A 2D simulated heating Guinier plot of CuPC synchrotron data measured at 230°C (Müller, *et al*., 2010b) in dependence on time (isothermally measured) is loaded.

It is also used for visualizing the 'phase transition points' graphics (Rajiv *et al*., 2009) and the graphics related to the sequential and parametric WPPFs. Detailed description of the graphics interface is given in the Users manual section F2.

3.3.2 Text editor interface

The text editor interface consists of several tab windows with the titles: *Control/Macros* tab, *Pattern* tab, *Background* tab, *Phase* tab, etc (Figure 3.3) and plain text editors associated with them. Each of these tabs consists of many widget gadgets that hold the tags of the Topas keywords, reserved parameter names or macro commands. These gadgets are grouped to their respective tabs according to the functions/properties of Topas statements[5].

[4] Same as 'Powder 3D Parametric' graphics interface explained in the Users manual.
[5] e.g., the Topas keywords '*start_X*' and '*finish_X*' are related to a powder pattern. Therefore they are grouped to the '*pattern*' tab of the text editor interface.

The required Topas statements can be placed in the text editor by prompting the respective gadgets. Various modules of the input file (e.g., **.ctrl*, **.patt*, **.bkg*, **.phs*) can be built in their respective tabs by activating these gadgets.

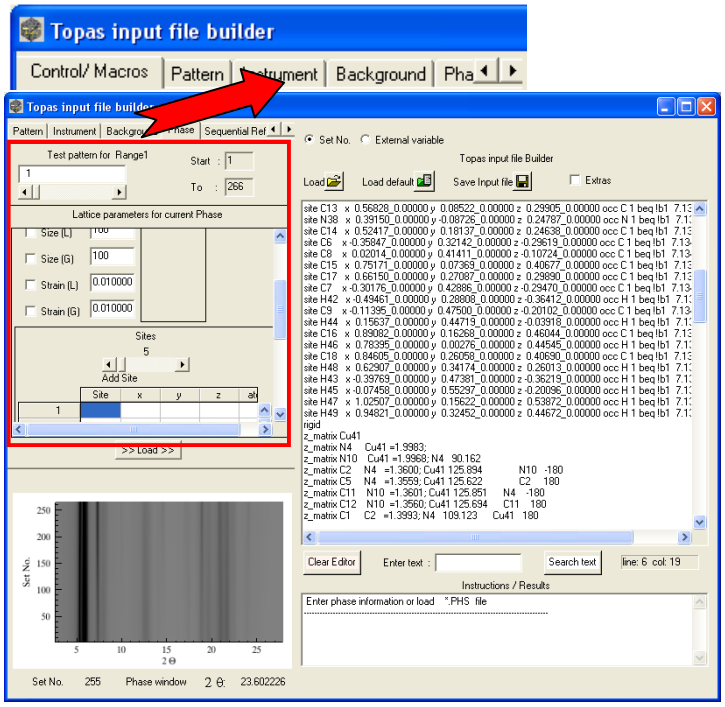

Figure 3.3 The text editor interface setup of 'Powder 3D Parametric' is shown. Various widget gadgets used for loading the Topas keywords and macro commands to the editor (right) are highlighted by the red frame. These gadgets are grouped in different tab windows (zoomed and indicated by a red dart). The '*Phase* tab' is focused in this figure. The set of commands that comprise the '**.phs*' (structure) part of the input file is gathered and placed on the text editor.

In Figure 3.3, the function of one of the tab windows (*phase* tab) is highlighted, where the necessary macro templates and the Topas keywords associated with a structural phase (e.g., '*Strain_L*', '*site*' respectively) can be selected by the user by activating the widget gadget provided in '*phase* tab'. The program automatically converts the selected information into a series of 'Topas readable' input commands and prepares the '**.phs*' part[6] of the input file and places it in the respective text editor. In a similar manner, the set of Topas statements required to describe the background of a powder pattern (e.g., '*bkg*', '*One_on_X*' etc.) and the statements that are related to the control of the refinements ('*iters*', '*do_errors*', etc.) can be combined and placed in the respective editors as '**.bkg*' and '**.ctrl*' parts of the input file respectively.

Splitting up of input file into its component parts (**.patt*, **.bkg*, **.phs*, etc.) is flexible in analyzing high temperature data with many reconstructive (Chung *et al.*, 1993) or non-

[6] There are also provisions in this tab to read the structure data directly from a Crystallographic Information File (CIF) file and to convert the read CIF data to a set of commands recognizable by the Topas kernel (as in the Topas GUI).

isothermal structural phase transitions. The independent quantitative phase analyses of such data often require that the powder patterns that belong to identical phases are grouped together (Figure 3.4). The program offers routines for graphical determination of phase transition points (explained in detail in chapters 4 and 5).

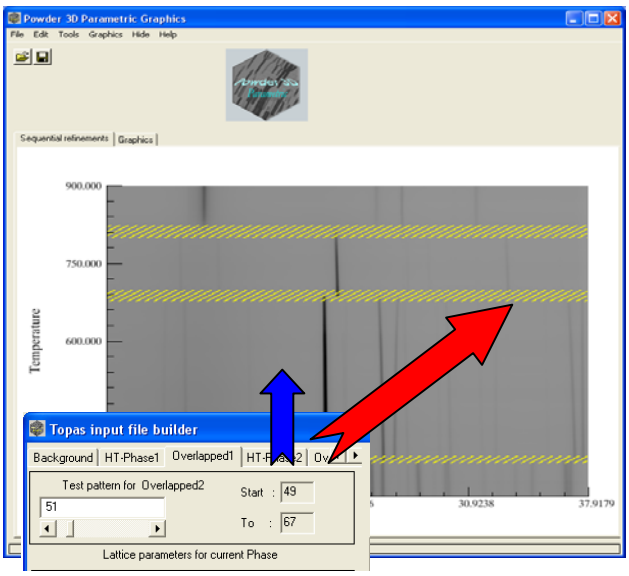

Figure 3.4 The phase transition points found by the program are displayed as dashed lines (yellow hatches). The editor interface window divides itself into tabs each representing an identified phase (shown by arrow colored blue) and overlapped part (shown by arrow colored red). Phase (structure) information (**.phs* file) can be built separately and independently for all the identified phases and overlapped parts in these tabs.

Once the reconstructive phase transition points in the data are determined, the relevant Topas phase commands (**.phs* file) for all the identified phases (when required, also for the overlapped parts) can be built independently in the respective editors (Figure 3.3). The auxiliary sections of the input file (**.patt*, **.inst*, **.ctrl*, etc) mostly contain the variables (e.g. diffractometer radii '*Rp*', '*Rs*') that are independent of the external variable. Therefore these parts of the file will be treated common for all the determined phases and they will be affixed to the '**.phs*' file associated with a particular phase at the onset of the refinement.

As an example, the three phases[7] of Ag_3VO_4 (Dinnebier *et al.*, 2007) observed in a high temperature experiment, analyzed independently with sequential LeBail fits with the help of the program (Figure 3.5) is presented. The sets of sequentially refined lattice parameters for all three phases (as obtained from the program) are plotted simultaneously against the temperature in Figure 3.5. Any evolving parameter (e.g., the lattice parameters) belonging to any of the identified phases can be chosen from the spreadsheet (chapter 6, Figure 6.5) and can be parameterized with a physical/user defined model.

[7] Details of phase transitions are in chapter 5 section 5.1.1.

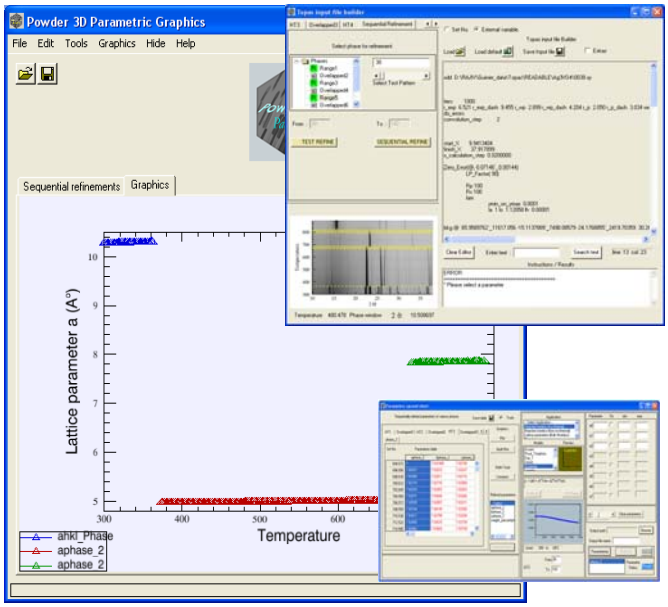

Figure 3.5 Lattice parameter (*a*) refined sequentially for three different phases of Ag_3VO_4 (Dinnebier *et al.*, 2007) are plotted in the graphics window. The high temperature phases and overlapped parts in the data can be selected (see also Figure 3.6) and refined independently (right up). All the parameters refined sequentially are displayed in a separate spreadsheet (right down) (see also Figure 6.5).

The program thus allows for the identification of the non-isothermal and reconstructive type phase transitions and also provides way for the convenient and independent analysis of the identified reconstructive structural phases using the WPPF methods.

3.3.3 Test refinement

The sub parts of the input files (**.patt*, **.inst*, **.ctrl*, etc) built in their respective tabs and the '*.*phs*' part are combined into a single Topas **.inp* file in the '*Sequential Refinement*' tab (Figure 3.6). Here, the user must select a phase from a list of identified phases to start a test refinement. The Topas **.out* file obtained in the test refinement is passed back to 'Powder 3D Parametric' for graphical visualization and for the inspection of the results (Figure 3.6, inner picture).

At the end of the successful test refinement, the user is directed by the program to store the Topas output file and to proceed with the sequential refinements. The program reads the stored output file and scans all the 'Topas' keywords and macro variables which are set refinable by the user and automatically builds the input files necessary for every succeeding refinements.

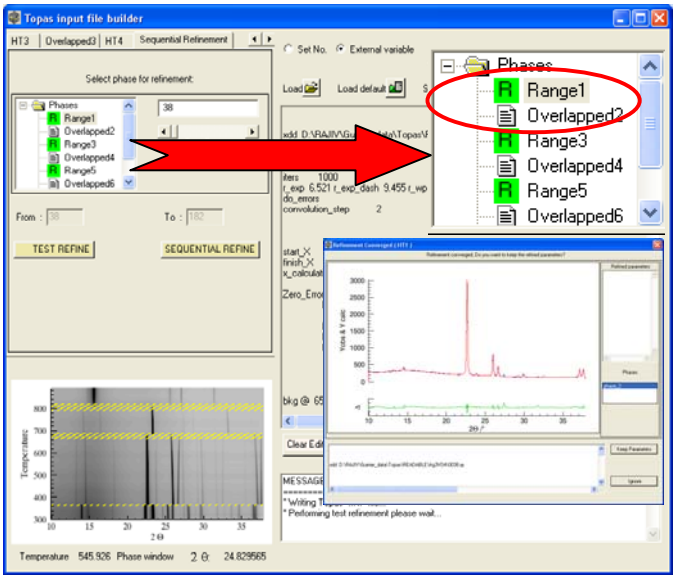

Figure 3.6 The '*Sequential Refinement*' tab is shown (left). Various parts of the file (**.patt*, **.inst*, etc) are gathered as a single Topas **.inp* file in this tab. The user is required to perform a 'test WPPF' in this tab for the desired phase (zoomed and pointed by the arrow colored red). '*Range1*', '*Range2*' etc, are the default names of the identified phases. The result of the test refinement, the Topas '**.out*' file and the refined parameters are displayed in a separate window (inner picture).

3.3.4 Parameters spread sheet

The third graphical component of the program is the parameters spreadsheet which pops up automatically once the sequential refinements are completed. All variables refined in sequential WPPF will be collected, sorted according to their phases and displayed in this spreadsheet. The evolution of any set of refined variables or a group of variables can be inspected, by plotting them simultaneously against their time/temperature axis. Any refined variable can be parameterized after assigning a suitable physical model to it (right part of the GUI in Figure 6.5) from a list provided by the program. (Detailed explanation of this component is provided in chapter 6, Figure 6.5).

3.4 Operation modes

Powder 3D Parametric provides a general base to perform sequential refinements of the loaded 2D data and also provides space to do parametric refinements of any refinable variable associated with the prepared 'test' input file. In addition, the program also supplies various application packages (e.g., '*Reaction kinetics*', '*Micro structure*' etc) to accomplish a specific scientific task. Some of these modules are demonstrated in chapters 6 and 7 using some test data samples.

3.5 Technical details

As all the refinements are performed in the Topas launch mode kernel, the program requires the user license dongle for Topas academic version 4 or higher. For better performance of the program, usage of a computer with at least 2GB of virtual memory is advised. All routines of Powder3D Parametric work only on the Windows® operating system. This software has been developed with the Interactive Data Language (IDL®) (ITT, 2009). To be able to run this software, the IDL virtual machine (IDL^{VM} version 6.4) has to be installed from the ITT website[8] (free of charge).

3.6 Summary

The basic functionalities of the sequential/parametric WPPF program 'Powder 3D Parametric' have been explained in this chapter. 'Powder 3D Parametric' is capable of refining large number of powder patterns collected in the 2D experiments, with least manual effort and in minimum time. The program could successfully read and comprehend most forms of the 'test' input files prepared by the user[9]. The applications of parametric Rietveld refinement to some datasets, assisted by the developed software are presented in chapters 6 and 7.

The analytical part of the work that has been carried out towards the goal of grouping the powder patterns to their phases (section 3.3.2) in high temperature experiments (non-isothermal measurements) is described from chapters 4 to 5.

[8] http://www.ittvis.com/ProductServices/IDL/VirtualMachine.aspx.

[9] The simplicity in the organization of the Topas commands in the 'test input files' is an important factor that determines the success of sequential and parametric refinements (see exceptions in section T7 in the user's manual).

Chapter 4

Automatic determination of phase transition points[1]

4.1 Introduction

Automatic classification of powder patterns is crucial for fast and independent sequential and/or parametric WPPF of 2D XRPD data. In particular, the crystalline materials measured in dependence on temperature[2] demand that the powder patterns in the 2D data are grouped to their relevant phases prior to the application of WPPF methods.

Often in 2D powder diffraction, the patterns are grouped to their phases by means of general data clustering algorithms (e.g., in Barr *et al*., 2004), where the like patterns are grouped together by minimizing the distance or the squared distance between the patterns and the predefined cluster centroids. The groups or clusters so formed can be used in qualitative analysis for identifying unknown phases (Barr *et al*., 2004) and in quantitative applications such as sequential/parametric WPPF. Data clustering is also used in applications such as polymorph screening in pharmaceutical science for rapid sorting of large amounts of powder patterns (Xua *et al*., 2007).

Numerous search match algorithms for the general classification of multi dimensional data are available in literature. Jain *et al.* (2000) presented a general overview of the available strategies for data clustering. Horn *et al.* (2002) proposed an algorithm based on quantum

[1] Part of the contents of this chapter has been published in Rajiv *et al.,* 2009.

[2] The compounds that undergo reconstructive structural phase transitions (Chung *et al*., 1993) also demand that the powder patterns are grouped to their respective phases. The reconstructive structural phase transitions involve the extensive rearrangement of atoms in the unit cell. These rearrangements are reflected in the 2D datasets as the discontinuities, shift and disappearance of the parent phase peaks in the newly formed phase (Figures 5.1 to 5.4 in chapter 5).

mechanics for the classification of multivariate data. In crystallography, Barr *et al.* (2004) used agglomerative hierarchical clustering to match the *in situ* powder patterns to their respective phases.

In this chapter an analytical method that automatically determines the phase transition points[3] of compounds from their 2D data has been presented. The method uses the Pearson's correlation coefficients[4] (Press *et al.*, 2002) of the powder pattern (intensities) measured in succession, for identifying the phase transition points. The transition points found are used as spatial constraints for grouping the powder patterns together that belong to like phases. The sequential organization of the powder patterns in the temperature dependent data and their recognizable data structure has prevented the usage of compound methods such as neural networks for grouping the powder patterns.

The proposed routine and other analytical methods which were attempted for the phase transition points determination will be discussed in detail in the following sections (sections 4.3, 4.4 and 4.7).

4.2 Preprocessing

Data normalization is an essential preprocessing step in analyses involving comparison of variables arising from various classes of data. In particular, normalization prepares the powder patterns for precise statistical analysis and for the unbiased measure of correlations between them. Each observed powder pattern in the 2D data is normalized by converting the pattern to its array of modified[5] squared standard scores[6] ($\boldsymbol{z_D}$ in Equation 4.1).

Standard scores are a general representation of measured variables in terms of their squared distances from the mean (in the present case it is median) of their population distribution. The distances are typically expressed in units of standard deviations of the individual data points.

A set of modified, squared standard scores for a single powder pattern $\boldsymbol{p_{Di}} = \{y_0, y_1, \ldots, y_{(D-1)}\}_i$ measured at a time step i is calculated by Equation 4.1.

$$\boldsymbol{z}_D = \left\{ \left\{ \frac{D}{\sigma_i^2} \left(y_j - m_i \right)^2 \right\}_{j=0,1,2,\ldots,(D-1)} \right\}_i \tag{4.1}$$

where,

$\boldsymbol{z}_D$ - An array of squared standard scores of a powder pattern $\left(\boldsymbol{p_D} \right)_i = \{ y_0, y_1, y_2, \ldots, y_{D-1} \}_i$ measured

[3] The phase transition temperature/time/pressure, depending upon the external variable upon which the experiment is performed.

[4] Also called Pearson's '*r*'.

[5] Median of individual powder pattern is used for calculating its array of standard scores.

[6] Also called standardization.

at a time step i

D - Number of data points of the pattern $(\boldsymbol{p_D})_i$

y_j - Observed intensities of the powder pattern $(\boldsymbol{p_D})_i$

σ_i - Sample standard deviation of the powder pattern $(\boldsymbol{p_D})_i$

m_i - Median of the powder pattern $(\boldsymbol{p_D})_i$

i - runs from *0* to *N-1,* with *N* being the number of powder patterns in the 2D data.

In Equation 4.1, the median rather than mean of the individual powder pattern is used for finding the standard scores. The median of the powder pattern provides reliable estimates of standard scores, as most powder pattern intensity distributions are centered near the medians.

The deviations of the background and the low intense data points from their median are very small when compared to those of the high intense Bragg peaks. The squared standard normalization therefore suppresses most of the insignificant low and background intensities of the original powder pattern and serves as a background filter.

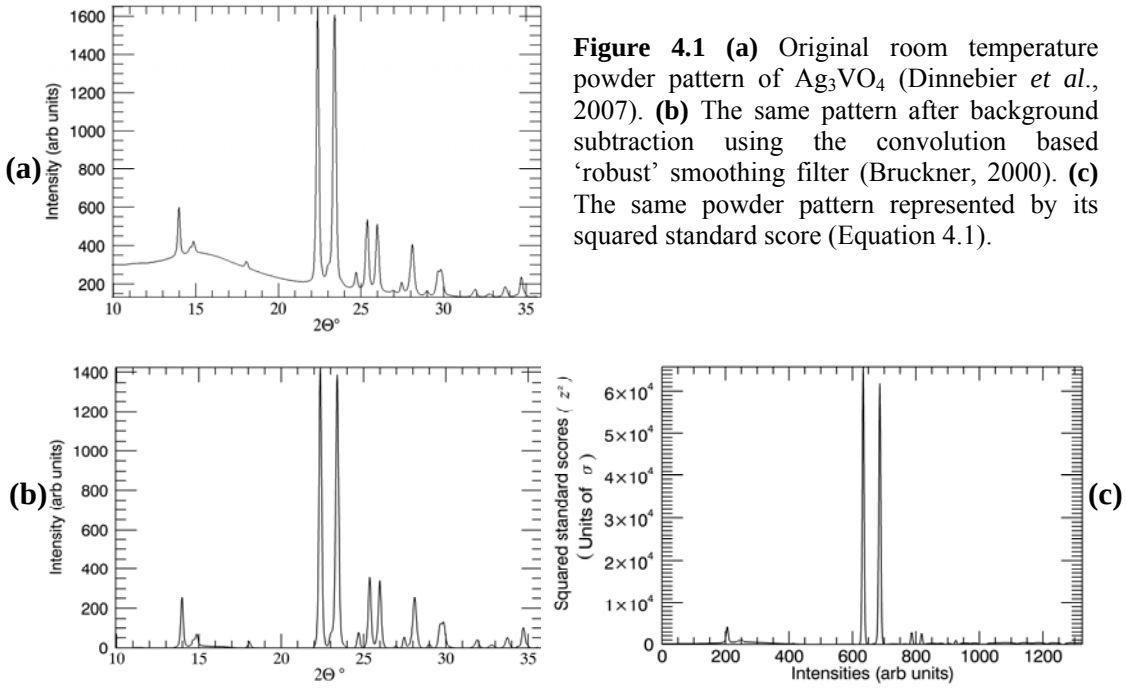

Figure 4.1 (a) Original room temperature powder pattern of Ag_3VO_4 (Dinnebier *et al.*, 2007). **(b)** The same pattern after background subtraction using the convolution based 'robust' smoothing filter (Bruckner, 2000). **(c)** The same powder pattern represented by its squared standard score (Equation 4.1).

The room temperature powder pattern of Ag_3VO_4 (Dinnebier *et al.*, 2007) whose background is removed by a convolution based smoothing filter (Bruckner, 2000) and the same pattern represented by its standard scores are shown in Figures 4.1 (a), (b) and (c).

In Figure 4.1 (c), many low intense Bragg reflections were removed and the high intense Bragg peaks were augmented as a result of squared standard-normalization. The physical significances of the peaks are lost after the application of the standard-normalization procedure. Nevertheless, the loss of information doesn't bias the calculation correlation coefficients (section 4.4) or either the statistical methods described in the following section (see explanation in section 4.6).

4.3 Statistical analysis

The statistical analysis described in this section is an outcome of an attempt to automatically group similar powder patterns in the 2D data using the parameters of a mathematical function that describes the powder pattern intensity histogram[7].

To understand the frequency distribution of powder pattern intensities, some of the powder patterns belonging to two different structural phases of Ag_3VO_4 were converted into histograms (Figure 4.2).

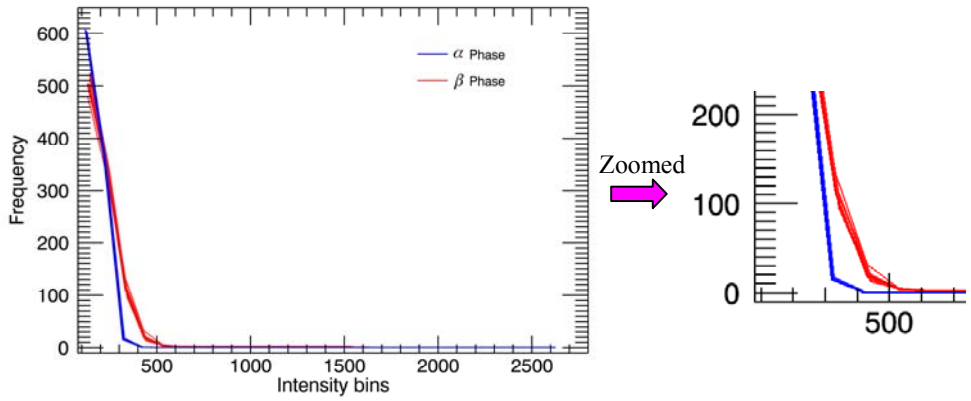

Figure 4.2 Each curve in the picture represents a histogram of a powder pattern intensities that belongs to α-Ag_3VO_4 (blue) or β-Ag_3VO_4 (red) (Dinnebier *et al.*, 2007). (Only limited numbers of powder patterns belonging to α and β phases of Ag_3VO_4 are used). 'Intensity bins' in the abscissa denotes the intervals of measured intensities. 'Frequency' in the ordinate denotes the number of counts in the pattern intensity histogram. The height and tail lengths of the curves (zoomed picture) allow for the clear distinction of patterns belonging to two phases. The high discrepancies in asymmetry and peakedness of curves are due to the continuous appearance and disappearance of Bragg reflections indicating a phase transition.

The shapes of the distribution functions can be described roughly by asymmetric Gaussian function with higher skewness or more precisely by a skew normal distribution function

[7] Powder pattern intensity histogram: The theoretical frequency distribution function of a powder pattern.

(Azzalini, 1985). The huge asymmetry in the intensity distribution curves in Figure 4.2 is due to high number of background data points as compared to the number of Bragg reflections.

In Figure 4.2, the difference in tail lengths of the curves (Figure 4.2, zoomed) and the difference in their peakedness/flatness are the properties that allow for clear distinction of patterns belonging to different phases. The 3rd and 4th central moments, (Press *et al.*, 2000) skewness and kurtosis (Equations 4.2 and 4.3) measure the symmetry and the peakedness of the powder pattern distribution respectively.

$$s = \frac{1}{D}\sum_{j=0}^{D-1}\left[\frac{(y_j - \bar{y})}{\sigma}\right]^3 \tag{4.2}$$

$$k = \left(\frac{1}{D}\sum_{j=0}^{D-1}\left[\frac{(y_j - \bar{y})}{\sigma}\right]^4\right) - 3 \tag{4.3}$$

where,
s - Skewness of a distribution
k - Kurtosis of a distribution
y_j - The data points (samples)
D - Number of samples
$\bar{y}$ - Sample mean of the distribution
σ - Sample standard deviation.

As both the parameters (s and k) contribute to the distortion of the normal curve, a function involving the two parameters could be a better discriminator of the powder patterns belonging to different phases. The relation used in the so called 'Jarque-Bera statistical test'[8] (Jarque and Bera, 1980) (Equation 4.4) was used for representing/discriminating the powder patterns.

$$\boldsymbol{j}_N = \frac{(N-1)}{6}\left\{s_i^{\,2} + \frac{(k-3)_i^{\,2}}{4}\right\}_{i=0,1,2,\ldots,(N-1)} \tag{4.4}$$

where,
$\boldsymbol{j}_N$ - A function of s and k
s - Skewness of the powder pattern $(\boldsymbol{p_D})_i = \{y_1, y_2, \ldots, y_D\}_i$ measured at the time step i
k - Kurtosis of the powder pattern $(\boldsymbol{p_D})_i$ measured at the time step i
N - Number of powder patterns in the 2D data.

[8] The Jarque-Bera method describes the deviation of a distribution from normality. There are several methods available in literature for quantifying the normality of a distribution (Öztuna *et al*., 2006).

$\boldsymbol{J}_N$ in Equation 4.4 represents all the N powder patterns in the 2D data in terms of their kurtosis and skewness. Equation 4.4 was tested with three different data samples: Ag_3VO_4, $Rb_2[C_2O_4]$ (Dinnebier *et al*., 2005) and $MgCl_2.6H_2O$ (Sugimoto *et al.,* 2007). The results obtained from two samples are plotted in the Figures 4.3 (a) and 4.3 (b), where the higher variations of normality of the powder patterns residing near the transition points are revealed as peaks[9].

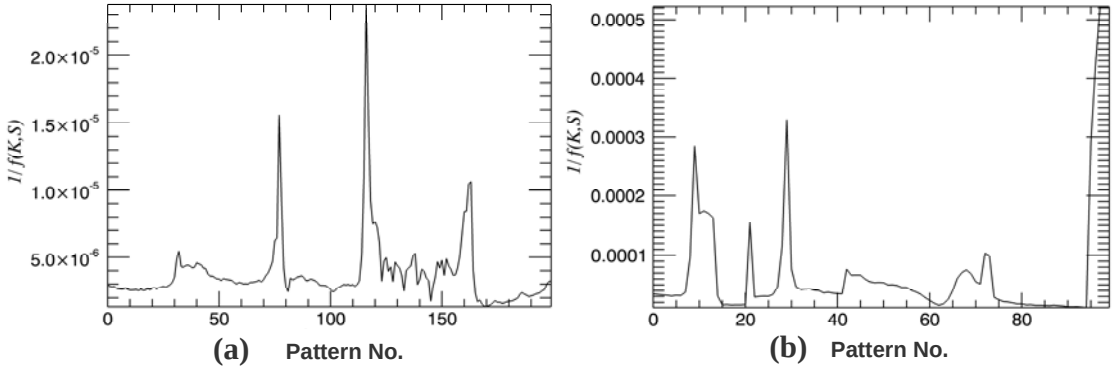

Figure 4.3 The reciprocal of the right-hand side of Equation 4.4 (Jarque *et al*., 1980) after applying it to two different data samples are plotted. **(a)** $Rb_2C_2O_4$ & Rb_2CO_3 in a heating/cooling experimental cycle (Dinnebier *et al*., 2005). **(b)** $MgCl_2.6H_2O$ (bischofite) in a high temperature experiment (Sugimoto *et al*., 2007). The abscissa is the time axis, where the 'Pattern No.' corresponds to different experimental temperatures. The sharp peaks in the plots represent the phase transition points. The reciprocal of Equation 4.4 are plotted to reveal the phase transition points as peaks.

Feasible ways to automatically determine the phase transition points would be to find the maxima of $1/\boldsymbol{j}_N$ (in Figures 4.3 (a) and (b)) or by imposing a suitable threshold to the calculated curves to separate the phase transition peaks from the background.

The procedure described in this section to determine the phase transition points suffers from several intrinsic drawbacks as the patterns in the data are represented only by the frequency of occurrences of individual intensities and their positional information is disregarded. The formation of transition peaks depends strongly on the speed of the phase transition; the transition peaks are sharp and clearly recognizable for the phases that transform slowly and are smeared out for quickly transforming phases. Therefore this method cannot be considered as a universal method to determine the transition points, as its efficiency depends strongly on the quality of the data used.

The outcome of Jarque-Bera statistical test nevertheless allows us to make a sensible assumption that the powder pattern intensities follow a family of normal distribution.

[9] These peaks will be called 'transition peaks' or 'phase transition peaks' throughout this thesis.

Moreover, the statistical analysis has unveiled the fact that the higher statistical moments of the powder pattern distributions are the better representatives of their features.

4.4 Correlation coefficients

In general, the classification of powder patterns involves the construction of a matrix of correlations (or similarities) between the patterns in the 2D data followed by the application of clustering algorithms to this matrix for grouping the patterns to their respective phases.

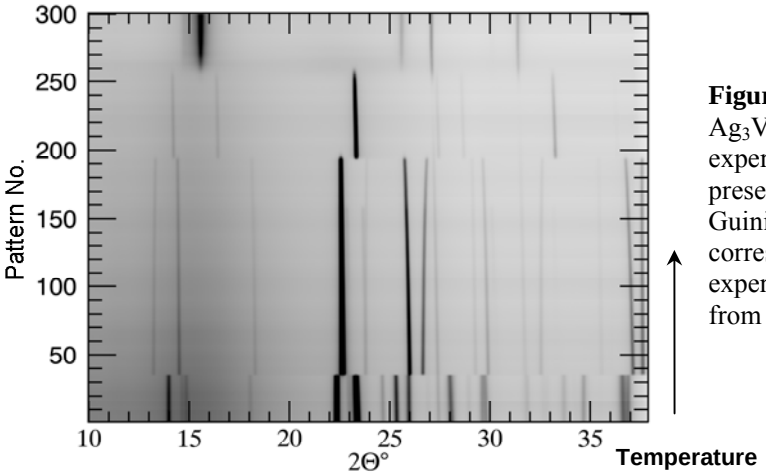

Figure 4.4 The phase transitions of Ag_3VO_4 in a high temperature experiment (Dinnebier *et al*., 2007) are presented as a simulated heating-Guinier-film plot. The 'Pattern No.' corresponds to the different experimental temperatures, starting from room temperature to 893 K.

Representing the high temperature 2D data as a simulated heating Guinier-film plot as in Figure 4.4 avoids the construction of the compound correlation matrix and creates new possibilities of applying uncomplicated methods for associating the powder patterns in the 2D data. Figure 4.4 clearly portrays the strong linear associations between the successive powder patterns in the data that belong to the phases. The weak relationships between the phase patterns[10] and the successive boundary[11] patterns manifest themselves as phase transition points in the image.

An array of correlations coefficients calculated for successive powder patterns[12] in the 2D data extracts of both strong and weak relationships of patterns in the 2D data whilst maintaining a high level of separability between the coefficients. This array (sequential

[10] The terms 'phase pattern' and 'boundary pattern' will be used to denote respectively the powder pattern that belongs to a phase and the powder pattern representing the phase transition or phase decomposition.
[11] The patterns that reveal the transition peaks.
[12] Will be called as 'sequential correlations vector' throughout the thesis.

correlations vector[13]) resides in a line parallel and adjacent to the leading diagonal of the correlations matrix (indicated in Figure 4.5 as a line colored blue).

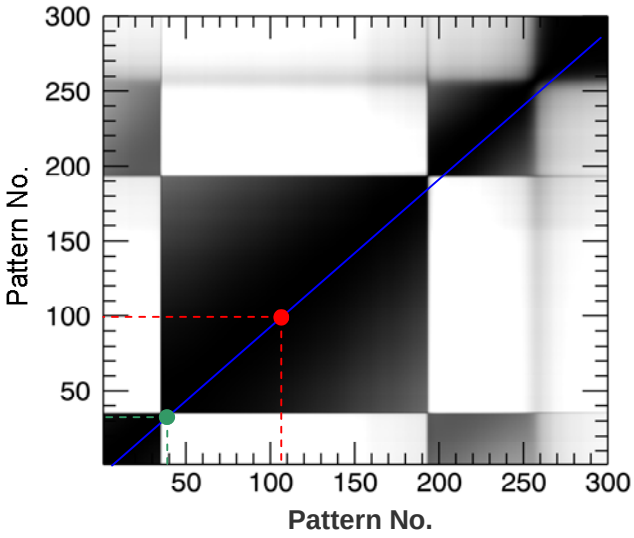

Figure 4.5 The Pearson's correlation matrix of the 300 powder patterns of Ag_3VO_4 (Dinnebier *et al.*, 2007) is displayed as a grey scaled image. The dark and bright regions in the image correspond respectively to strong and weak correlations of the powder patterns The blue line adjacent to the leading diagonal is drawn to mimic the array of correlations between successive powder patterns (sequential correlations vector). The green and red dots (exaggerated for clarity) represent the weak and strong correlations coefficients contained in this array.

The plot of the sequential correlations vector is shown in Figure 4.6, where the strong correlation coefficients between phase patterns gather along a line parallel to the abscissa and the weak correlations representing the phase transition points are revealed as outliers. A threshold of about 0.98 times the median of the sequential correlations vector separates its outliers from the rest of the coefficients. The pattern numbers corresponding to the separated outliers represent the determined phase transition points.

The powder patterns belonging to various phases can be grouped easily by accumulating the pattern indices separately in a simple looping routine constrained by the detected phase transition points. In rare circumstances, closely spaced multiple outliers representing a single-phase transition point may appear in the sequential correlations vector. They can be constrained by their relative magnitudes and by their distances from the origin of the correlations matrix.

[13] The sequential correlations vector contains wide magnitudes of coefficients in the order of approximately 0.1 to 0.98 (indicated by green and red dots in Figure 4.5).

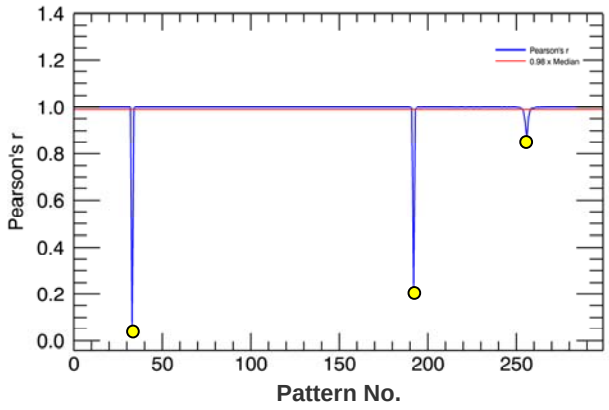

Figure 4.6 The sequential correlations vector (colored blue) of Ag_3VO_4 (Dinnebier *et al.*, 2007) is plotted. The line colored red represents a threshold of about 0.98 times the median of the sequential correlations vector. This line is used to extract the outliers (yellow dots) or phase transition points automatically.

4.5 Parametric and non-parametric correlation coefficients

There are numerous statistical methods available in literature for studying the correlations of multivariate data. Based on the knowledge of the parent distribution, these statistics are broadly classified as parametric and non-parametric methods. Some of these methods (Pearson's *r*, Spearman's rank order coefficient, etc.) and their applications in classifying the powder patterns are explained in Gilmore *et al.* (2004). Gilmore *et al.* have used parametric as well as non-parametric statistical methods for representing the powder patterns in the data. Gilmore *et al.* have matched the powder patterns using a linear combination of Pearson's coefficients, Spearman's rank order coefficients and the Kolmogorov-Smirnow two-sample test applied only to the Bragg peaks present in the powder patterns.

The performances of parametric statistic (Pearson's *r*) and non-parametric statistics (Spearman's rank order coefficient (ρ) and Kendall (τ) rank correlation coefficient) have been tested in the presented 'phase transition points' determination algorithm. The three methods were tested on three different sample data. It was found that (as will be discussed below) the parametric Pearson's correlation coefficients ($\boldsymbol{r}_N$) worked efficiently for the determination of phase transition points, independent of the nature of the data used. The Pearson's coefficients ($\boldsymbol{r}_N$) are calculated by the following relation.

$$\boldsymbol{r}_N = \left\{ \frac{\left(\boldsymbol{p}_D - \boldsymbol{m}_D\right)_i \cdot \left(\boldsymbol{p}_D - \boldsymbol{m}_D\right)^T_{i+1}}{\sigma_i \sigma_{i+1}} \right\}_{i=0,1,2,\ldots,(N-1)} \tag{4.5}$$

where,

$\boldsymbol{r}_N$ - An array of correlations coefficients calculated between powder patterns measured at successive time steps i and i+1

N - Total number of measured powder patterns[14]

$\left(\boldsymbol{p}_D\right)_{i\vee(i+1)} = \left\{y_0, y_1, y_2, ..., y_{(D-1)}\right\}_{i\vee(i+1)}$ is a powder pattern measured at the time step i or i+1

D - Total number of data points per powder pattern

$\left(\boldsymbol{m}_D\right)_{i\vee(i+1)} = \left\{m_0, m_1, m_2, ..., m_{(D-1)}\right\}_{i\vee(i+1)}$ is a vector of D elements, with all the elements equal to the median of $\left(\boldsymbol{p}_D\right)_{i\vee(i+1)}$

$\sigma_{i\vee(i+1)}$ - Sample standard deviation of $\left(\boldsymbol{p}_D\right)_{i\vee(i+1)}$: $\sigma_{i\vee i+1} = \left(\sqrt{\sum_{j=0}^{D-1}(y_j - m_j)^2}\right)_{iv(i+1)}$

The correlations coefficients calculated between successive powder patterns from parametric and non-parametric methods are compared in Figure 4.7. It is clearly observed that the dissimilarity between the phase patterns and the boundary patterns are not completely resolved by both Spearman's rank order coefficients and Kendall tau rank correlation coefficients.

High fluctuations of the coefficients calculated from the two non-parametric methods restrict the selection of a sensible threshold that separates the outliers (or phase transition points) from the rest of the coefficients. In contrast, the higher separability of Pearson's coefficients in Figure 4.7 allows one to choose a definite threshold which eases the automatic extraction of phase transition points.

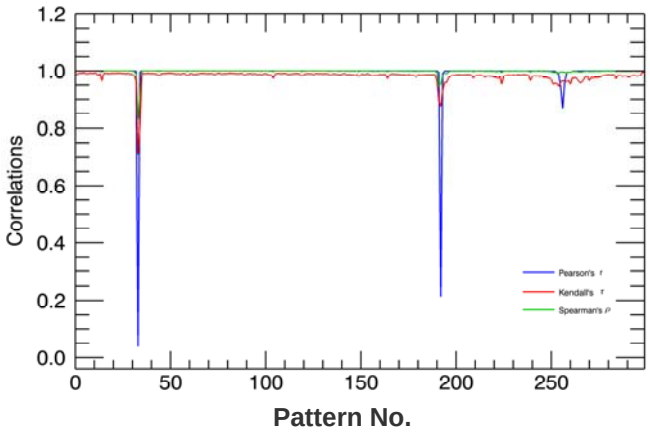

Figure 4.7 Comparison of the sequential correlations vectors obtained using Pearson's r (blue colored), Spearman's ρ and Kendall's τ (green and red colored plots respectively) in the determination of phase transition points. The 2D data of Ag_3VO_4 (Dinnebier *et al*., 2007) is used in this example.

[14] The index i in Equation 4.5 (also in Equations 4.4 and 4.6 to 4.8) runs from 0 to N-1 rather than from 0 to N-2.The last pattern measured ((N-1)th pattern) has no successor N^{th} pattern to correlate with. The non existing N^{th} pattern was synthesized by averaging the two preceding powder patterns ((N-1)th and (N-2)nd) in the dataset and padded to the dataset as the N^{th} pattern. Padding (Smith, 2003) is often used to address the problem of the 'end effect' in the design of convolution filters in digital signal processing.

One of the practical reasons for the superior performance of Pearson's method in the 'phase transitions points' determination is its intrinsic response to the outliers present in the data. Pearson's coefficients are generally considered to be weaker estimators of the linear relationship (Abdullah, 1990) between the variables when the data is contaminated with a higher level of statistical noise. The Pearson's correlations calculated between successive powder patterns in the 2D data enable the treatment of the powder patterns lying near the phase transitions as random fluctuations. The high sensitivity of Pearson's coefficients to these fluctuations causes the correlations of patterns near the transition points to move further away from the median of the coefficients (Figure 4.7). Practically, the large separation of outliers from the rest of the coefficients eases the automatic determination of phase transition points.

4.6 Improvements in the determination of correlations coefficients

The efficiency of Pearson's coefficients in the determination of phase transition points has been improved considerably by introduction of the image segmentation method (Seul *et al*., 2000; Rajiv *et al*., 2007) and also by the application of the robust standardization procedure (section 4.2). The outcome of the application of these two methods in the determination of phase transition points will be discussed in the following sections.

4.6.1 Image segmentation

Image segmentation is one of the practical analysis methods used to study the statistics of different parts of an image generated by non-stationary processes. To study the influence of image segmentation in the determination of phase transition points, the 2D data (simulated heating-Guinier-film plot in Figure 4.4) was segmented (Smith, 2003) into three angular (2θ) regions along its abscissa in the ratio 3:19:3. The sequential correlations vectors for each of these segments were calculated separately[15] and are compared in Figure 4.8.

As expected, the coefficients calculated for the central part image (colored blue in Figure 4.8) show wide separability[16], which favors the automatic extraction of phase transition points from the rest of the coefficients. The large fluctuations in the coefficients calculated

[15] Similar analyses were carried out for the high temperature datasets ($Rb_2[C_2O_4]$ and $MgCl_2.6H_2O$).

[16] Consistent results were obtained in the analyses carried out for $Rb_2[C_2O_4]$ and $MgCl_2.6H_2O$ sample datasets.

from the first and last 12% of the image (colored red and green in Figure 4.8) suggest that these two parts can be ignored in the calculation of correlation coefficients.

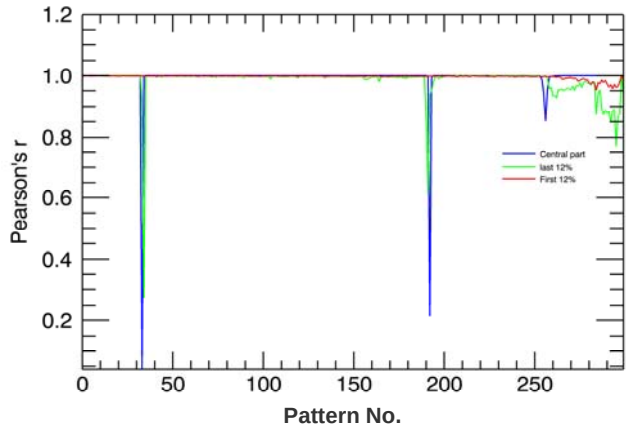

Figure 4.8. The Sequential correlations vectors calculated for the three different segments of Ag_3VO_4 dataset are compared. The coefficients obtained from the central part of the image (colored blue) show higher separability. The coefficients obtained from the first and the last 12% of the image (colored red and green respectively) do not contain reliable information required for the determination of phase transition points.

To numerically substantiate the reason for the reliability of correlation coefficients in the central segment of the image, the statistics of the three segments of the Ag_3VO_4 image were analyzed individually (Table 4.1, also in Table 4.2 for $Rb_2[C_2O_4]$). Kurtosis of the patterns rather than the variance was used in to study the statistics of the data (Figure 4.9 (b)), as kurtosis clearly revealed the distinctness of each powder pattern (also the phase transitions) (Figure 4.9 (a)).

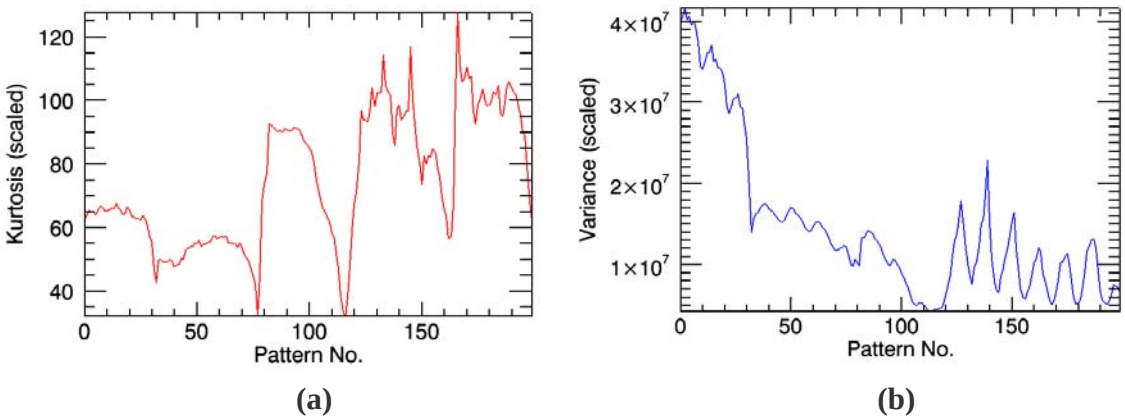

Figure 4.9 (a) kurtosis and **(b)** variance of $Rb_2[C_2O_4]$ 2D data along the temperature axis (Pattern No.) are plotted. The phase transitions are revealed better in the kurtosis array than the 'noisy' variance array.

The vectors of kurtosis for the three images segmented in the ratio 3:19:3 were calculated independently (the calculated vector for whole image is shown in Figure 4.9). The ranges of kurtosis (i.e., the maximum and minimum value of the kurtosis array) for each of these

kurtosis vectors, were found and are presented in Tables 4.1 and 4.2 (fourth column). The medians of each kurtosis arrays are calculated separately and presented in Tables 4.1 and 4.2. The slopes obtained in the linear fits performed on each array of kurtosis are listed as 'variations of kurtosis in Tables 4.1 and 4.2.

Table 4.1 Statistics of three different angular segments of Ag_3VO_4 image (Dinnebier *et al*., 2007) are presented. Each angular segment is represented by an array of kurtosis (as in Figure 4.9 (a)). Their medians are listed in second column. 'Variation of kurtosis' in the third column represents the residue of linear fit to the array of kurtosis. Range of kurtosis represents the maximum and minimum values in the array of kurtosis.

Image segments Ag_3VO_4	Median of kurtosis	Variation of kurtosis	Range of kurtosis	
First 12%	0.007	0.001	-0.14	7.25
Central part 76%	170.4	0.007	20.53	180.7
Last 12%	11.14	0.001	-0.46	17.04

The statistics of the three segments of the Ag_3VO_4 data in Table 4.1 implies that the central part of the image contains relatively higher maximum range and higher variation of kurtosis. The results obtained for the rubidium oxalate ($Rb_2[C_2O_4]$) (Dinnebier *et al*., 2005) and bischofite ($MgCl_2.6H_2O$) data sample (Sugimoto *et al.,* 2007)the Ag_3VO_4 data sample are consistent with those obtained from Ag_3VO_4.

Table 4.2 Statistics of three different angular segments of the $Rb_2[C_2O_4]$ image (Dinnebier *et al*., 2005) are presented. Each angular segment is represented by an array of kurtosis. Their medians are listed in second column. 'Variation of kurtosis' in third column represents the residue of linear fit to the array of kurtosis. Range of kurtosis represents the maximum and minimum values in the array of kurtosis.

Image segments $Rb_2[C_2O_4]$	Median of kurtosis	Variation of kurtosis	Range of kurtosis	
First 12%	0.00407038	0.0013	-1.24	20.04
Central part 76%	0.0252537	0.015	51.6	223.8790
Last 12%	-0.00518897	0.0012	-1.43	28.30

As inferred from Tables 4.1 and 4.2, the reliability of the determination of phase transition points is related to the maximum range and highest variation kurtosis of the powder

patterns in each segment of the image. The values presented in Tables 4.1 and 4.2 (e.g., the range of kurtosis, its median and variation) can be used as a representative of the data. These values can be used to automatically understand or interpret the data.

4.6.2 Robustness of the standard normalization procedure

The standard normalization routine explained in section 4.2 results in an enormous amount of information loss, since the majority of the low intense and background data points are suppressed during the normalization. To assure that the loss of information has no negative effect on the calculation of correlations coefficients, the 'phase transition points' routine is tested on three different forms of the rubidium oxalate sample data (Dinnebier *et al*., 2005).

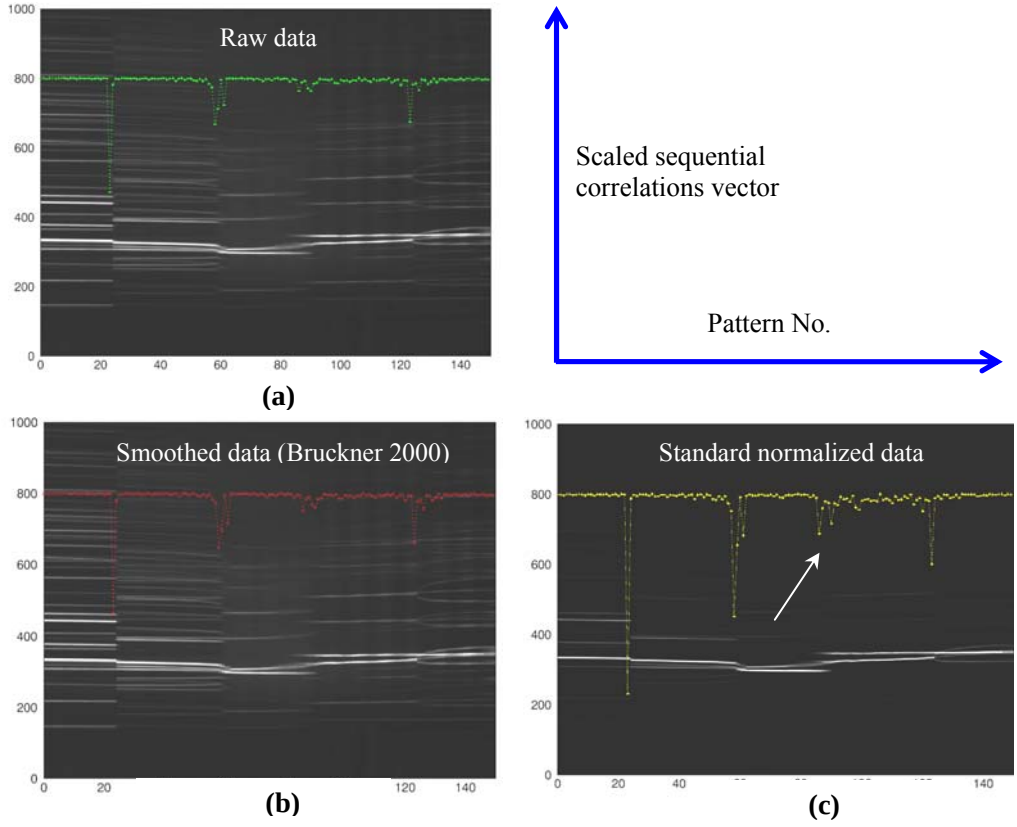

Figure 4.10 The scaled sequential correlations vectors calculated from the three forms of $Rb_2[C_2O_4]$ data are plotted over their respective inverted images. **(a)** The sequential correlations vectors obtained from the raw data (without background subtraction) is colored green. **(b)** The sequential correlations vector obtained from the data whose background intensities are eliminated by the 'robust smoothing method' is colored red. **(c)** The sequential correlations vectors calculated from the standard normalized data are colored yellow. One of the enhanced transition peaks is indicated by the arrow.

The routine was first applied to the original (raw) data of rubidium oxalate, then to the data whose background intensities are subtracted using the 'robust smoothing' procedure (explained in Bruckner, 2000) and finally to the standard normalized data. The sequential correlations vectors obtained in the three cases are plotted over their respective simulated heating Guinier film plots in Figure 4.10. For convenience, the reduced image[17] of the rubidium oxalate data has been used throughout this analysis. (The intensities of the simulated Guinier film plots are inverted in Figures 4.10 (a) to (c) for clear graphical presentation).

As observed in the (inverted) heating Guinier film plot in Figure 4.10 (b), the application of the 'robust' smoothing filter to the data enhances some weak Bragg reflections of the original image. There is no considerable difference in the sequential correlations vector calculated using the original and the smoothed image (Figure 4.10 (a) and (b)).

In contrast to Figures 4.10 (a) and (b), the loss of Bragg reflections is clearly observed in the image produced after the application of the standard normalization procedure (Figure 4.10 (c)). Only the major reflections that contribute to the phase transitions are preserved in Figure 4.10 (c). Nevertheless, significant improvements in the separability of transition peaks are observed in Figure 4.10 (c). The 'transition peaks' (e.g., near the pattern number~80 and 100, indicated by the arrows) were suppressed in Figures 4.10 (a) and (b) were augmented in Figure 4.10 (c) after the standard normalization. The augmentation of the suppressed transition peaks eases the selection of suitable threshold for sequential correlations vectors and improves the overall efficiency of the 'phase transitions points' method.

It is worth mentioning that the suppression of some background intensities in the due to the application of standard normalization procedure does not produce any significant effects in the correlation analysis of the data. Standard normalization procedure in fact enables the direct comparison of standard deviations of different pattern intensities, which is considered to be a robust approach to characterize the maximum dissimilarities between the patterns.

The application of the standardization procedure to 2D powder data also improves the precision of the other routines suggested in this chapter for 'phase transition points' determination.

[17] Original dimension of rubidium oxalate dataset (200 x 2300) is reduced to 150 x 2300.

4.6.3 Enhancement of correlations matrix elements by the application of standard normalization procedure

The Pearson's correlation matrices calculated from the raw data and from the standardized data of Ag_3VO_4 (Dinnebier *et al*., 2007), AgNCO (Schmidt *et al*., 2009), $MgCl_2.6H_2O$ (Sugimoto *et al*., 2007) and $MgBr_2.H_2O$ (Dinnebier, 2007) are plotted as images in Figures 4.11 and 4.12.

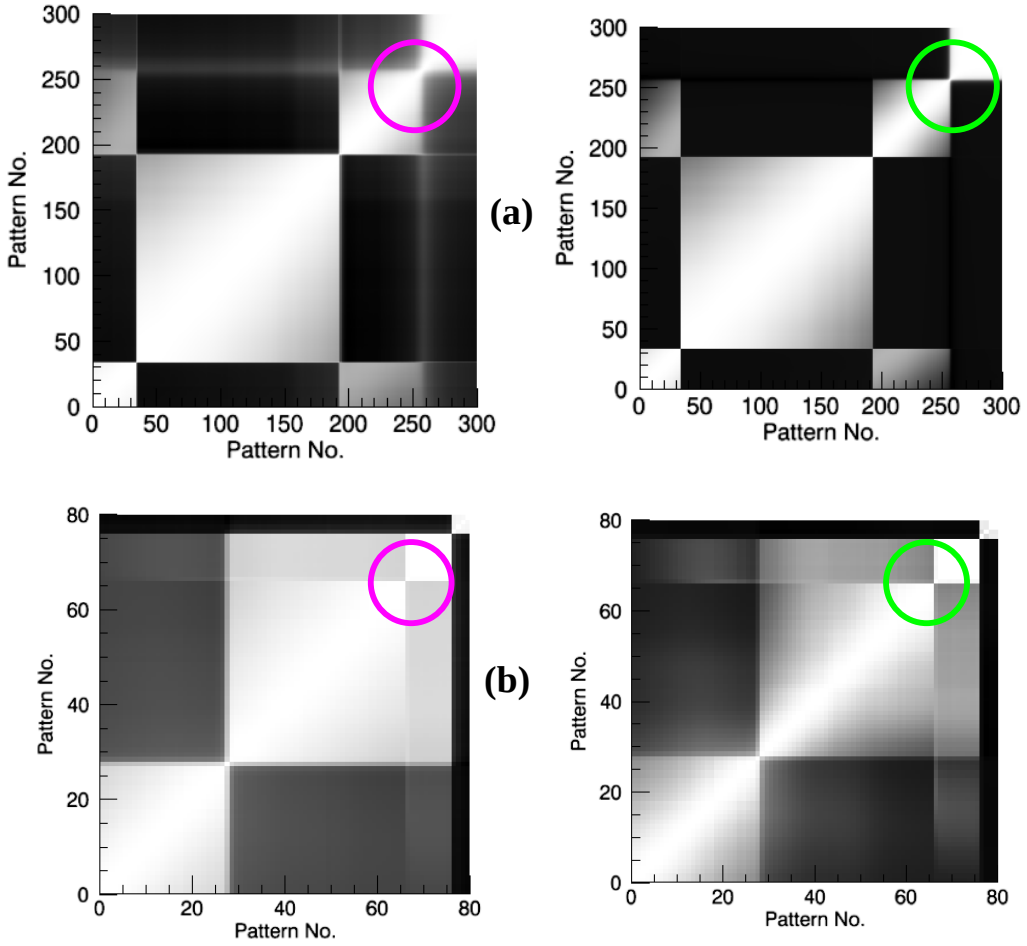

Figure 4.11 Pearson's correlation matrices calculated from the raw data (left) and from the standardized data (right) are displayed as images. **(a)** Pearson's correlation matrix of Ag_3VO_4 (Dinnebier *et al*., 2007). **(b)** Pearson's correlation matrix of AgNCO (Schmidt *et al*., 2009). The circles indicate the parts of the correlation matrices that are enhanced after the application of the standardization procedure.

The application of the standardization procedure to these data has made some of the hazy parts of the correlation matrices (indicated by circles in Figure 4.11 and Figure 4.12) clear and sharp, making the correlations matrices more suitable for grouping/classification.

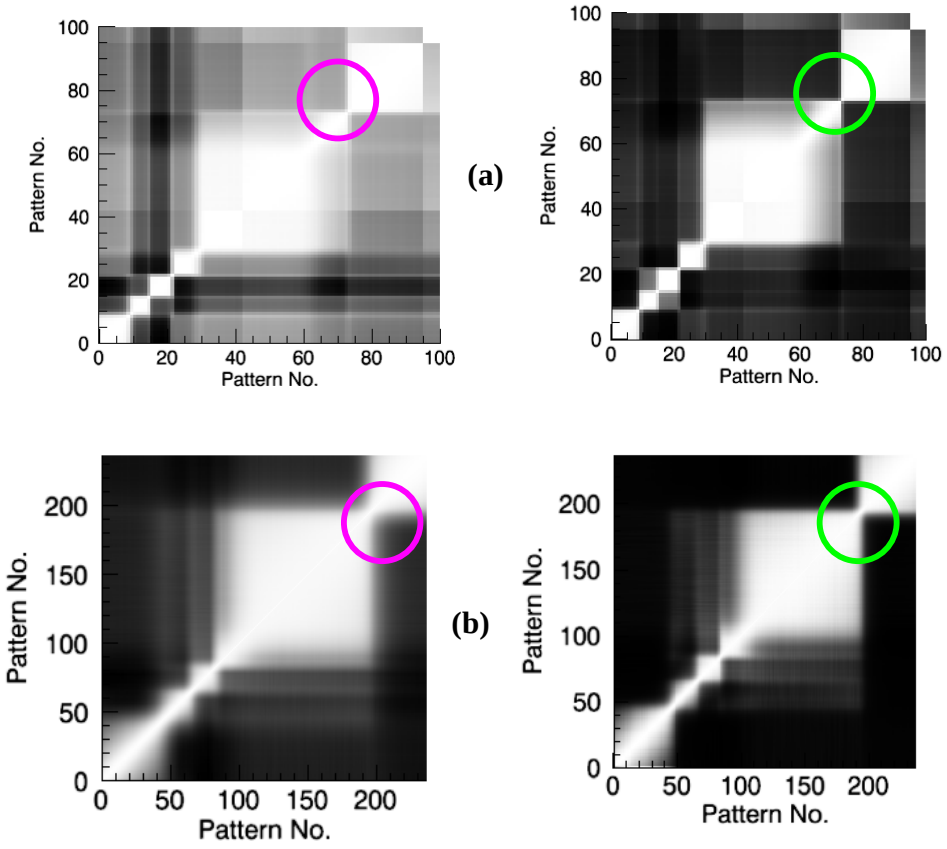

Figure 4.12 Pearson's correlation matrices calculated from the raw data (left) and from the standardized data (right) are displayed as images **(a)** Pearson's correlations matrix of ($MgCl_2.6H_2O$) (Sugimoto *et al*., 2007). **(b)** Pearson's correlation matrix of $MgBr_2.H_2O$ (Dinnebier, 2007). The circles indicate some of the parts of the correlation matrices that are enhanced after the application of the standardization procedure. (The quality of these two data is relatively lower than those plotted in Figure 4.11).

The standardization method is much more efficient when applied to low quality data (as in Figure 4.12). The application of the method widens the intensity range of the data and considerably enhances and sharpens the image edges lying near phase transition points.

4.7 Other methods used for the determination of phase transition points

Besides the methods explained in sections 4.3 and 4.4, (Jarque-Bera relation and Pearson's '*r*') some additional methods to support the automatic determination of phase transition points were initially attempted during the course of this work. The efficiencies of these methods (Equations 4.6 to 4.8) are illustrated briefly in this section using the rubidium oxalate data sample (Dinnebier *et al*., 2005).

These methods (Equations 4.6 to 4.8) are based purely on the Euclidean distances ($\boldsymbol{d}_N$) between the intensities of powder patterns measured at subsequent temperature/pressure or time.

$$\boldsymbol{d}_N = \left\{ \left| (\boldsymbol{p}_D)_i - (\boldsymbol{p}_D)_{i+1} \right|^2 \right\}_{i=0,1,2,\ldots,N} \tag{4.6}$$

$$\boldsymbol{d}_N = \left\{ \left((\boldsymbol{p}_D)_i - (\boldsymbol{p}_D)_{i+1} \right)^2 \right\}_{i=0,1,2,\ldots,N} \tag{4.7}$$

$$\boldsymbol{d}_N = \sqrt{\frac{1}{N} \left\{ \frac{\left((\boldsymbol{p}_D)_i - (\boldsymbol{p}_D)_{i+1} \right)}{0.5\left((\boldsymbol{p}_D)_i + (\boldsymbol{p}_D)_{i+1} \right)} \right\}_{i=0,1,2,\ldots,N}} \tag{4.8}$$

where,

$\boldsymbol{d}_N$ -An array of the Euclidean distances calculated between powder patterns measured at successive time steps i and i+1 (using Equations 4.6 to 4.8)

$(\boldsymbol{p}_D)_{i\vee(i+1)} = \{y_0, y_1, y_2, \ldots, y_{D-1}\}_{i\vee(i+1)}$ wder pattern measured at the time step i or i+1

D - Total number of intensities measured per powder pattern

N - Total number of measured powder patterns in the 2D data[18].

The Euclidean distances ($\boldsymbol{d}_N$) calculated between the neighboring powder patterns (as in section 4.4) using the Equations 4.6 to 4.8 are plotted in Figure 4.13.

[18] See foot note 1

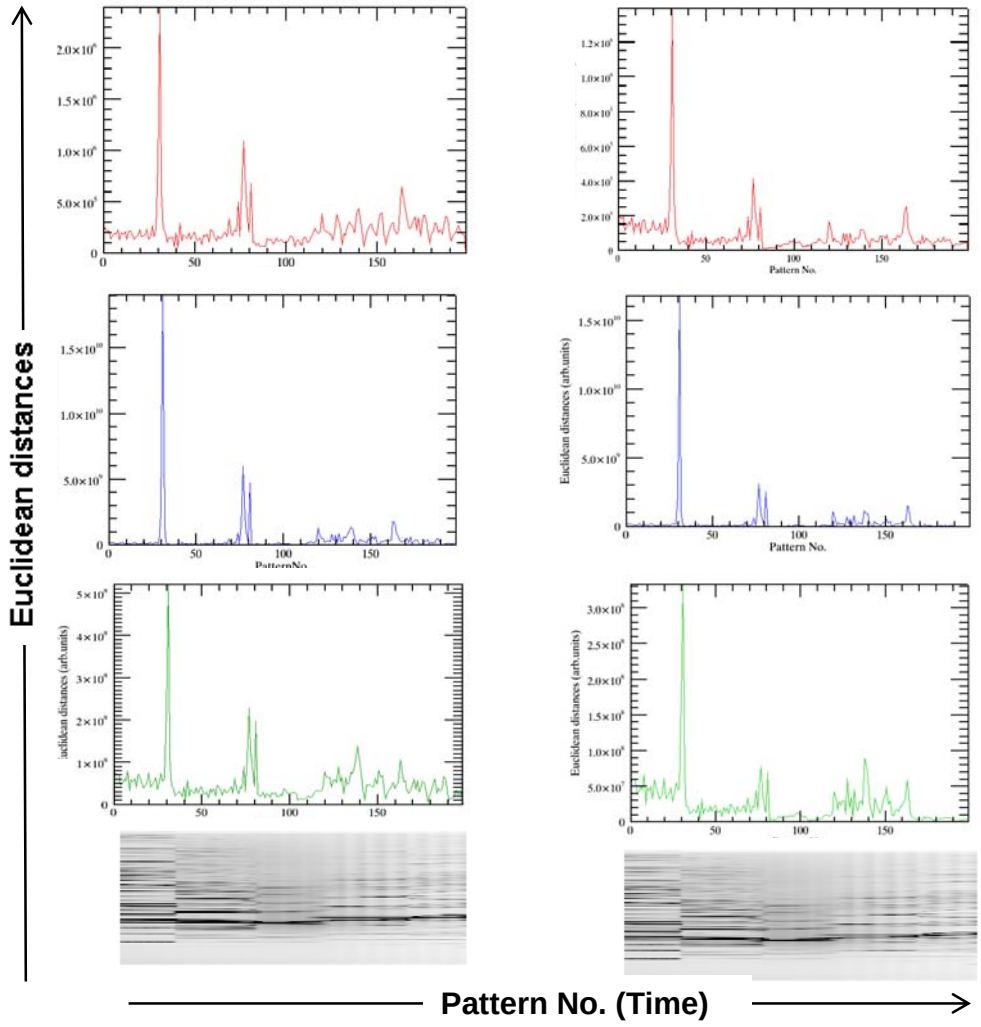

(a) **(b)**

Figure 4.13 The Euclidean distances obtained from Equations 4.6, 4.7 and 4.8 are colored red, blue and green respectively. **(a)** The distances found without background subtraction are shown. **(b)** The distances calculated after the subtraction of background intensities are plotted. The sharp peaks (phase transition peaks) represent the phase transition temperatures of the compound. The 'heating Guinier film plot' of $Rb_2[C_2O_4]$ is presented at the bottom for comparison.

The sharp peaks in Figures 4.13 (a) and 4.13 (b) represent the phase transition temperatures of rubidium oxalate. They can be automatically extracted by imposing a suitable distance constrain (as described in section 4.3) to the distance arrays plotted in Figures 4.13 (a) and (b).

When the Equations 4.6 to 4.8 were applied to the powder patterns after eliminating their background intensities, the fluctuations in the distance plots are significantly reduced. In

Figure 4.13, the distance arrays ($\boldsymbol{d}_N$) calculated using the original data (Figures 4.13 (a)) and those calculated after background subtraction (Figure 4.13 (b)) are compared.

The background subtraction for each powder pattern is accomplished by imposing a median constraint[19] of the intensities. The data points that fail to meet the constraint are considered as background intensities and are replaced by a smooth baseline of magnitude ~1.5 times the median of the pattern.

The classification methods described in this section are very basic; their success depends mainly on the quality of the data used. Among the methods explained from Equations 4.6 to 4.8, the squared Euclidean distances (calculated using Equation 4.7) worked best for the automatic determination of the phase transitions points.

4.8 Summary

A simple and effective method using the Pearson's correlation coefficients to determine the phase transition points in *in situ* powder diffraction data has been presented in this chapter. The efficiency of this method has improved considerably when accompanied by the robust standard score normalization technique. The performances of parametric and non-parametric statistics were examined for several 2D powder diffraction data and the supremacy of parametric statistics in the determination of phase transition points was revealed. The representation of data as image and the application of practical image segmentation method have simplified the classification procedure and have improved the accuracy of estimation of phase transition points in 2D data. It was also observed that the higher statistical moments play an important role in governing the powder pattern intensity distributions.

In the following chapter, the applications of the routine to some *in situ* powder data measured in dependence on temperature are presented.

[19] All the intensities less than ~1.5 times the median of the powder pattern intensity are treated as background.

Chapter 5

Applications of the algorithm that determines the phase transition points[1]

5.1 Sample data

In this chapter the applications of the 'phase transition points algorithm' to various *in situ* 2D powder diffraction data collected as a function of temperature will be demonstrated. The performance of the routine was tested with four different data: Silver vanadate (Ag_3VO_4) (Dinnebier *et al*., 2007), rubidium oxalate ($Rb_2[C_2O_4]$) (Dinnebier *et al*., 2005), bischofite ($MgCl_2.6H_2O$) (Sugimoto *et al.,* 2007) and silver isocyanate (AgNCO) (Schmidt *et al*., 2009). All these data were collected using image plate detectors at various synchrotron sources.

5.1.1 Polymorphism of silver vanadate

Polymorphism of silver vanadate (Ag_3VO_4) was studied by Dinnebier *et al*., 2007 using the high temperature XRPD method. Three hundred powder patterns were collected in the temperature range of 300 K up to 893 K at a synchrotron radiation source (ANKA) in Karlsruhe, Germany. The phase transitions of Ag_3VO_4 at different temperatures are displayed as a heating-Guinier-film plot in Figure 5.1 (Hinrichsen *et al*., 2006).

Silver vanadate undergoes two structural phase transitions at the temperatures 365 K and 687 K (pattern Numbers 36 and 192) and decomposes at approximately 803 K (pattern No

[1] Some of the contents of this chapter have been published in Rajiv *et al.,* 2009.

258). The sequential correlations vector[2] calculated from the algorithm is plotted on top of the simulated heating-Guinier-film plot of Ag_3VO_4 in Figure 5.1.

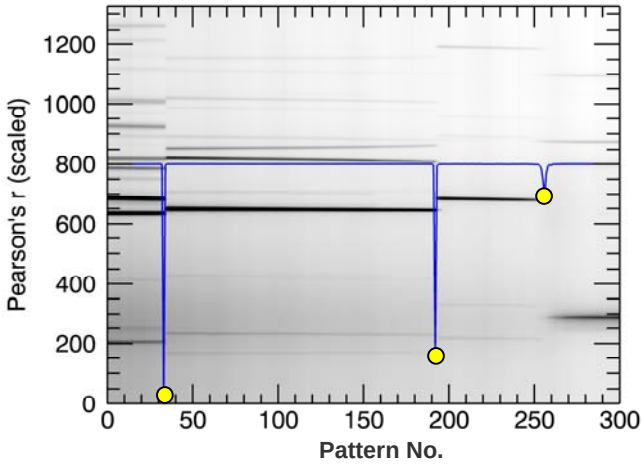

Figure 5.1 Sequential correlations vector (blue colored) is plotted over the simulated 'heating-Guinier-film' plot of Ag_3VO_4. Phase transition points determined from the proposed method are denoted by the yellow dots. 'Pattern No' in abscissa denotes different experimental temperatures.

The phase transition points determined by the method correspond precisely to the pattern numbers shown as yellow colored dots in Figure 5.1. The relatively smooth decomposition of the specimen that occurs near the pattern number 255 has also been determined by the program.

5.1.2 Phase transitions and decomposition products of rubidium oxalate

The phase transitions and decomposition of alkali metal oxides ($K_2[C_2O_4]$, $Rb_2[C_2O_4]$ and $Cs_2[C_2O_4]$) were studied (Dinnebier *et al*., 2005) using *in situ* XRPD method. The powder patterns of $Rb_2[C_2O_4]$ and its decomposition product $Rb_2[CO_3]$ collected as a function of temperature are used to test the 'phase transition points' routine.

The experiment was performed in dependence on temperature in a heating-cycle (298 K to 898 K at a rate of 2.4 K /min) and subsequent cooling-cycle (898 K-298 K at a rate of 4.8 K/min.). Totally 7 phases were observed in this experiment; three phase transitions of $Rb_2[C_2O_4]$ occurred upon heating and two phase transitions of the decomposition product ($Rb_2[CO_3]$) occurred after cooling. Some details of the phase transitions are tabulated below (Table 5.1).

[2] The coefficients of the sequential correlations vector in Figures 5.1 to 5.4 are scaled by a factor of about 800 for clear presentation.

Table 5.1 Phase transitions of $Rb_2[C_2O_4]$ and $Rb_2[CO_3]$ in a heating /cooling cycle (Dinnebier *et al.*, 2005). The phase transition temperatures and the corresponding pattern numbers are listed in first and second columns respectively.

Temperature (K)	Pattern No.	Transition from	Transition to
436	33	δ-$Rb_2[C_2O_4]$	γ-$Rb_2[C_2O_4]$
638	79	γ-$Rb_2[C_2O_4]$	β-$Rb_2[C_2O_4]$
648	82	β-$Rb_2[C_2O_4]$	α-$Rb_2[C_2O_4]$
760	109	α-$Rb_2[C_2O_4]$	β-$Rb_2[CO_3]$
838	118	β-$Rb_2[CO_3]$	α-$Rb_2[CO_3]$
838	125	α-$Rb_2[CO_3]$	β-$Rb_2[CO_3]$
600	165	β-$Rb_2[CO_3]$	γ-$Rb_2[CO_3]$

The 200 powder patterns collected in this experiment are shown as a simulated 'heating-Guinier-film' plot in Figure 5.2. The program could correctly identify[3] all the phase transitions observed in Figure 5.2. Even the weak phase transition from α-$Rb_2[CO_3]$ to β-$Rb_2[CO_3]$ upon cooling near the temperature of 838 K (pattern number ~125 in Figure 5.2) could be detected by the program.

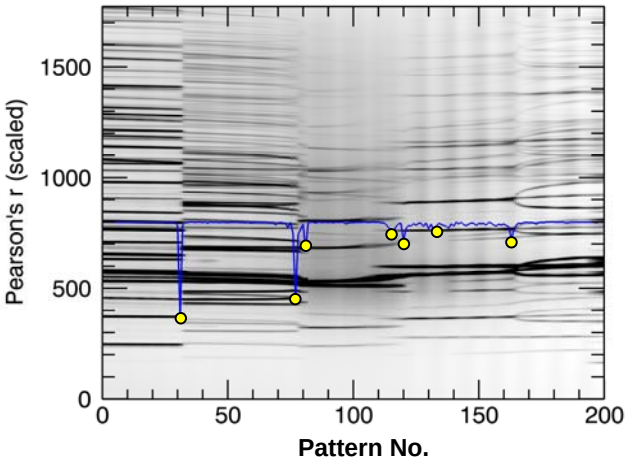

Figure 5.2 Sequential correlations vector (blue colored) are overlaid on the simulated heating-Guinier-film plot of the $Rb_2[C_2O_4]$ & $Rb_2[CO_3]$ data. Phase transition points determined from the program are indicated by the yellow dots.

However, some of the phase transition points (e.g. near pattern numbers 119, 125) determined by the program are slightly shifted from their ideal positions due to the higher width and smoothness of the boundaries between the phases (see explanation in section

[3] The phase transition points detected by the program correspond to the pattern numbers 30, 80, 84, 110, 119, 125 and 165.

5.2). To compensate such deficiencies, the program provides options to manually (by eye) shift the phase transition points to their ideal locations (section T3.1 in Users manual).

5.1.3 Decomposition products of Bischofite

The decomposition products of bischofite ($MgCl_2.6H_2O$) were studied (Sugimoto *et al.*, 2007) in the temperature range from 298 K to 873 K using *in situ* XRPD. For this experiment, 100 powder patterns were collected at a synchrotron source; they are shown in Figure 5.3 as a simulated 'heating-Guinier-film' plot.

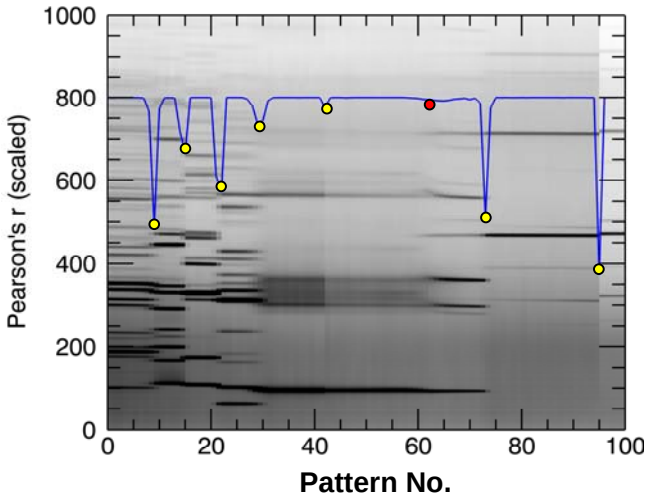

Figure 5.3 Sequential correlations vector (blue colored) is overlaid on the simulated heating-Guinier-film plot of the bischofite data ($MgCl_2.6.H_2O$). The yellow dots represent the estimated phase transition points. The red dot denotes the weak transition that could not be detected by the program in its automatic mode.

In total eight phases were identified manually (Sugimoto *et al.*, 2007) for the bischofite data. The program could correctly identify only 6 phase transition temperatures. The weak phase transition corresponding to the pattern number 63 (shown as a red dot in Figure 5.3) could not be identified by the program. The program allows for manual adding of phase transition points (identification by human eye) if the automatic mode fails to identify a phase transition point (see also the explanation in section 5.2 and section T3.1 in Users manual).

5.1.4 Thermal behavior of silver isocyanate

The thermal behavior of the compound silver isocyanate (AgNCO) was studied using high temperature *in situ* XRPD method (Schmidt *et al.*, 2009). About eighty powder patterns, starting from the room temperature to 523 K were collected at a synchrotron source.

AgNCO undergoes a structural phase transition at the temperature of 393.15 K (pattern number ~29), which remains stable until its decomposition at 523 K (~pattern number 62). During the experiment, the sample is quenched at this temperature (523 K) to obtain another modification of AgNCO (quenched-AgNCO or q-AgNCO). The patterns collected in the heating experiment and also from quenching are gathered and shown in Figure 5.4 as a heating-Guinier-film plot.

The program could successfully determine the phase transition and decomposition points of AgNCO at the temperatures 393.15 K and 523 K (corresponds to the pattern numbers 29 and 62).

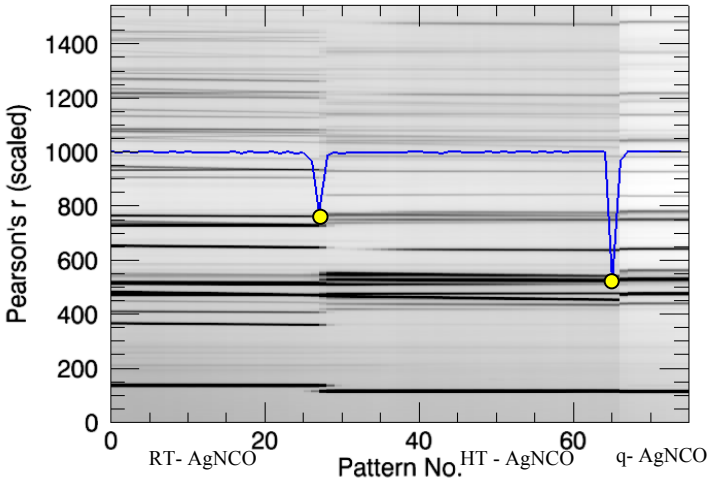

Figure 5.4 Sequential correlations vector (blue colored plot) is overlaid on the simulated heating-Guinier-film plot of AgNCO. The yellow dots represent the estimated phase transition and decomposition points.

5.2 Some interpretations about the position, width and multiplicity of the correlations peaks

In most of the applications presented in section 5.1, the phase transition peaks (see Figures 5.1 to 5.4) found by the program were shifted slightly from their expected positions towards the region of lower temperature/time. Furthermore the sequential correlations vector calculated for some data e.g., rubidium oxalate[4] (section 5.1.2) show many non resolvable multiple transition peaks/fluctuations in some regions where there are actually no phase transitions (e.g., near the pattern number 100 to 160 in Figure 5.2). In the bischofite data sample, the shifts in transition peaks[5] and also the smearing out of transition

[4] Also for Bischofite dataset near Pattern No. 60.
[5] See also Figure 5.4.

peaks near the pattern number 60 are observed (Figure 5.3). These effects cause some difficulties in the automatic determination of transition points.

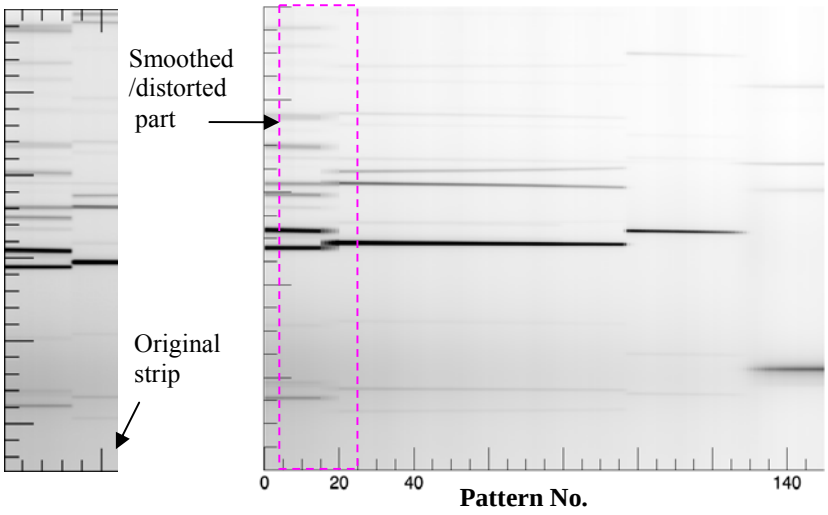

Figure 5.5. **(a)** The strip of the Ag_3VO_4 data to which the filter was applied is shown. **(b)** The Ag_3VO_4 data obtained after applying the smoothing filter (8 data points width) is shown. The distorted part is highlighted by a dashed rectangle colored pink. Overlapping and smoothing of high intense Bragg peaks are observed inside the region enclosed by the pink dashed rectangle.

The reason for these discrepancies is the presence of the quickly varying (or highly volatile) Bragg intensities near the phase transition points (e.g., in the bischofite data). In this section, the cause for the shift in the positions and multiplicity of transition peaks near the boundaries will be substantiated. In order to reckon the effect of the volatility of Bragg intensities (near the transition points) on the multiplicity and shift of transition peaks, the algorithm was tested in two deformed images of the Ag_3VO_4 data[6]. A narrow strip (along the time axis) of the Ag_3VO_4 data in the vicinity to a phase transition point was smoothed using a moving average convolution filter (ITT, 2009). Filters of widths 6-data points and 8-data points were applied separately on this part of the dataset to create two images with different levels of distortion. One of them (obtained with the 8-data points smoothing filter) is shown in Figure 5.5.

[6] Silver vanadate dataset was preferred for this particular analysis, as the quality of the dataset (Figure 5.1) was higher than other data tested in section 5.1.

The 'phase transition points' algorithm was applied to the original image and to other two images distorted by filters of widths 6-data points and 8-data points. The sequential correlations vectors obtained for these three cases are compared in Figure 5.6.

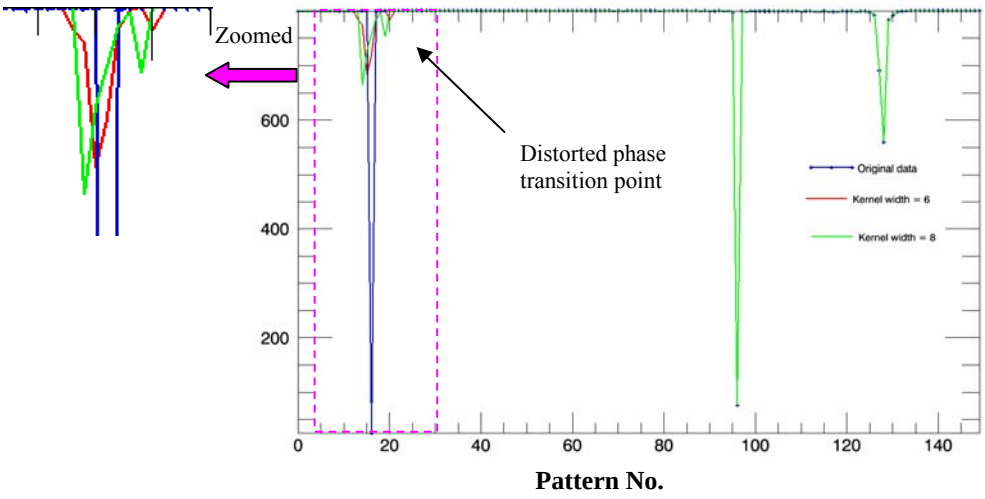

Figure 5.6 The scaled sequential correlations vectors calculated from the original Ag_3VO_4 data (colored blue) and those calculated from the images distorted using the smoothing filters of widths 6 (green colored plot) and 8 (red colored plot) data points are compared (zoomed out on the left).

As seen in Figure 5.6, the phase transition peak (colored blue) obtained for the original image is high, sharp and distinct. After the application of the smoothing filter, the volatility of the intensities in the filtered region increases, causing the transition peaks to blunt, split and to shift towards the region of lower temperature (or pattern number). These effects are augmented when the width of the filter is altered (zoomed part in Figure 5.6). It is obvious from Figure 5.6 that distorting/smoothing of a dataset near a phase transition point causes drastic changes in the shape, position and multiplicity of the phase transition peaks The aberrations in the sequential correlation vectors (section 5.1.1 to 5.1.4) is only due to the nature of phase transition and the volatility of intensities near the phase transition points. It was also observed that the sharpness, width and the area under the phase transition peak are directly correlated to the speed and nature of the phase transition. As the time taken for a phase transition increases, the widths and areas of the phase transition peaks also increase.

5.3 Implementation

The 'phase transition points' routine is implemented in the program 'Powder 3D Parametric' in an interactive manner. The phase transition points can be determined and

displayed graphically by prompting a widget button provided by the graphical user interface of the program (shown by an arrow in Figure 5.7).

The detected phase transition points are displayed in the main graphics window of the program GUI as lines. These lines can be moved manually to fine tune the detected phase transition points. The phase transition points can be blown up to select the regions of multiple or mixed phases (More details are presented in the 'Users manual' section T3).

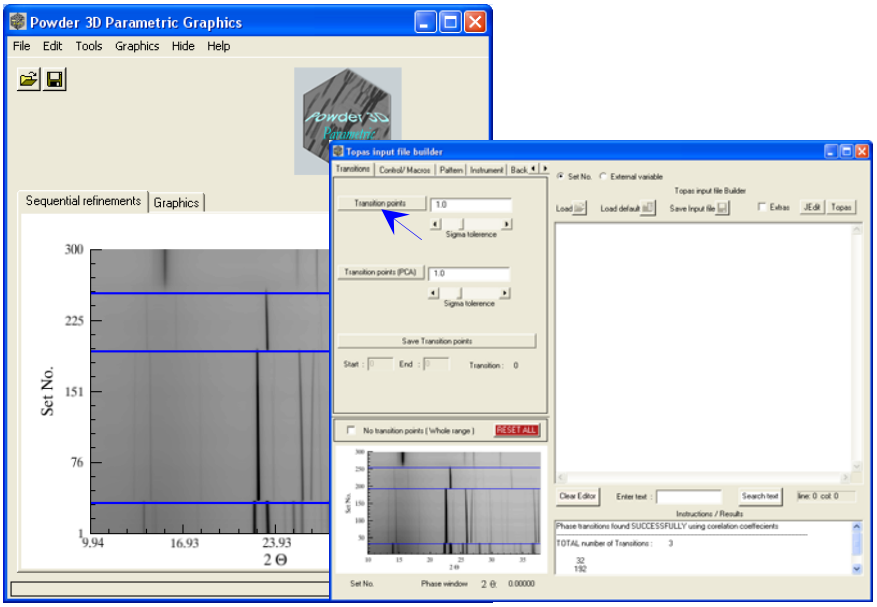

Figure 5.7 The implementation of the 'phase transition points' routine in the program 'Powder 3D Parametric' is shown. The arrow points to the button to be prompted to determine the phase transition points. The horizontal lines (colored blue) drawn on the data are the determined phase transition points whose positions can be altered.

5.4 Summary

The overall efficiency of the presented algorithm is higher when applied to data collected continuously in high temperature experiments. The performance of the method is much more limited when applied to high-pressure data, where the steps between the measurements are often huge. As explained in section 5.2, to some extent the success of this method depends on the nature and speed of the phase transitions.

Chapter 6

Parametric Rietveld analysis of the kinetics of copper phthalocyanine

6.1 Introduction

This chapter demonstrates the application of 'parametric Rietveld refinement' method, assisted by 'Powder 3D Parametric' in the extraction of the reaction kinetic information[1] of crystalline materials from 2D XRPD data. Copper phthalocyanine (CuPC)[2] data measured in dependence on time are used in this demonstration. The kinetic parameters *k* and *n* of several reactions involving various polymorphs of CuPC (Table 6.1) are derived from the well known Johnson-Mehl-Avrami-Kolmogorov (JMAK) equation[3] (Avrami, 1939; Avrami, 1941; Farjas and Roura, 2006; Malek and Mitsuhashi, 2000), which is substituted[4] in place of the weight fraction (Hill and Howard, 1987) of one of the changing phases during the multi phase Rietveld refinement. The set of rate constants (*k*) derived from the Avrami's equation at various temperatures (Table 6.1) are used to estimate the activation energies of several CuPC polymorphs.

Similar analysis on CuPC was once carried out by M. Müller in the year 2009 (Müller *et al*., 2010b), in which the rate constants were determined manually from the slopes of linearized weight fractions obtained in the full quantitative sequential Rietveld refinements.

In this chapter, the rate constants and the activation energies derived from the Avrami model are compared with those obtained in sequential analysis (Müller *et al*., 2010b) and the discrepancies between the two results are briefly discussed.

---

[1] The reaction rate constant *k* and reaction order *n*.
[2] Some additives were also added to CUPC to study their influence (Müller *et al*., 2009).
[3] The exponent term $(1\text{-}Exp\ (-kt)^n)$ in Equation 6.1.
[4] As proposed in Müller *et al*., 2009.

6.2 Experimental details and parameterization

To be able to do the isothermal kinetic analysis of CuPC, individual time-dependent XRPD measurements at various temperatures[5] (Table 6.1), for all the polymorphs and polymorph-additive mixtures of CuPC were performed at a synchrotron source (ANKA). The samples were measured at temperatures ranging from 230°C to 340°C. (More details about the experiment and the compound are available in the literatures Müller *et al*., 2009 and Müller *et al*., 2010b; some required experimental information are reproduced from the literature Müller *et al*., 2010b in Table 6.1).

Table 6.1[6] CuPC samples used in the analysis, their initial phase concentrations and the measurement temperatures are listed. The time-dependent XRPD measurements of samples made at various temperatures are marked with the symbol 'x'.

Sample	Temperature [°C]						
	230	250	270	290	320	330	340
α-CuPC	x	x	x	x			
90 % α-CuPC + 10 % β-CuPC		x	x				
90 % α-CuPC + 10 % ε-CuPC		x	x				
90 % ε-CuPC + 10 % β-CuPC		x	x				
85.5 % α-CuPC + 9.5 % ε-CuPC + 5 % DMAM[7]	x	x					
85.5 % α-CuPC + 9.5 % ε-CuPC + 5 % NU[8]	x	x					
ε-CuPC		x			x		x
ε-CuPC (BlauEFL[9])					x	x	

All the samples measured at the temperatures indicated by 'x' in Table 6.1 are subjected to independent sequential and parametric Rietveld refinements. Sequential refinements were performed before starting the parametric refinements, as some data required that the sequentially refined scale factors to be used as constrains during parametric refinement

[5] The experiments were performed by M. Müller (Müller, *et al.*, 2009).
[6] This table is reproduced from the literature (Müller, *et al.*, 2010b) with the consent of the author.
[7] DMAM: CUPC derivative.
[8] NU: Naphthyl derivative.
[9] BlauEFL is the commercial form of ε-CUPC.

(Coelho, 2007). In doing so, the parametric refinements can be directed towards the global minima.

Equation 6.1 (Hill and Howard, 1987) relates the scale factors of a crystalline mixture that consists of two phases *a* and *b*. In Equation 6.1, the weight fraction of one of the phases (*a*) has been parameterized (Müller *et al*., 2009) with the JMAK equation[10].

$$S_a = \frac{-S_b * M_b * V_b * \left[Exp(-(kt)^n) \right]}{M_a * V_a * \left[Exp(-(kt)^n) - 1 \right]} \tag{6.1}$$

where,

k	-	Reaction rate constant
t	-	Experimental time
n	-	Avrami constant (reaction order)
(S, M, V) $_{a, b}$	-	The scale factors, unit cell mass and volumes of the (*a*) decaying and (*b*) emerging phases.

The exponent terms within the square brackets in Equation 6.1 are the JMAK equations, which originally were the weight fractions (W_a and W_b) of the two phases *a* and *b*. The Avrami parameter *k* required for the calculation of activation energy can be directly derived from Equation 6.1 during the refinement. The set of Topas macro language statements (Müller *et al.,* 2009) that corresponds to the parameterization of weight fraction (Equation 6.1) are appended in supplementary information section (Topas input files-E).

6.3 Program

For the kinetic analysis of CuPC, 19 sets of isothermal (time-dependent) powder data has to be treated with sequential and parametric Rietveld refinements; each set contains an average of about 60 powder patterns to be refined (Table 6.1). Handling of such bulk dataset and manual preparation of Topas input files required for the refinement of all the patterns listed in Table 6.1 is a tedious and time consuming process.

The aid of the program has considerably reduced the time to prepare and execute the input files and also to carryout the analysis. The program obliges the user to prepare only one input file per dataset, the files required for the succeeding sequential and parametric refinements are prepared and executed automatically by the program.

[10] The weight fraction of the other phase '*b*' is (1-(1-(*Exp (-kt)*^{n})) in the numerator.

6.4 A case study[11]

To begin with the kinetic analysis of CuPC, the sequential and parametric Rietveld analysis performed on the mixture of α-CuPC and β-CuPC (90% and 10% initial phase concentrations respectively measured at 270°C[12]) using the program will be demonstrated in this section.

6.4.1 A single refinement

The first step in the parametric kinetic analysis of CuPC is to prepare an input file to perform a refinement (or a WPPF) of a single powder pattern (will be called the 'test' refinement). The pattern used in the test refinement is usually the one measured at the lowest time step or the pattern from which the user wishes to begin the sequential refinements.

The Topas input file required for the test refinement can be prepared with the help of 'Topas input file builder' GUI provided by the program[13] (Figure 6.1).

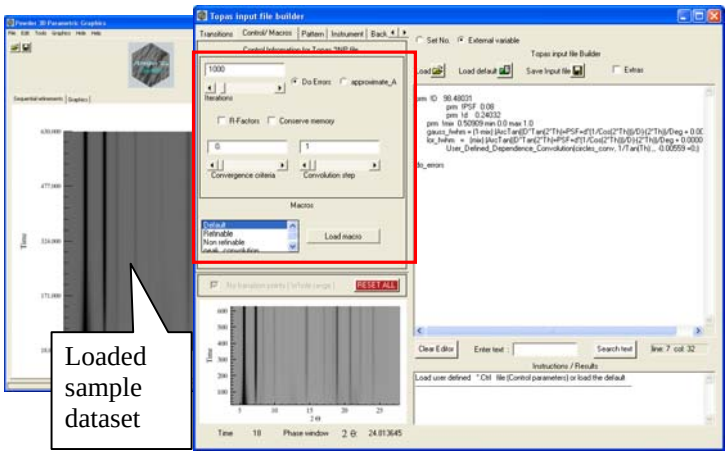

Figure 6.1 (a) The test data are plotted as simulated 'heating Guinier-film' plot in the '*main graphics window*' (see also in user's manual section F3). **(b)** The plain text editor of the '*Topas input file builder*' is at the right. Some widget tools are at the left of the editor (highlighted with a red frame), using them, the important 'Topas' statements that makes up the test input file can be entered into the editor.

The '*Topas input file builder*' offers many widget tools; using them the set of Topas statements that makes up the 'test input file' can be built. Once the test refinement has been performed successfully, the convergence plot, the Topas output file (*.*out*) received from

[11] Detailed procedures to do test, sequential and parametric refinements are provided in the Users manual - section T.5.
[12] Will be called the test data.
[13] More details are supplied in the 'Users manual'-section F3.

its kernel and the refined variables will be displayed in a separate window (Figure 6.2). The user is free to inspect and modify the **.out* file and to redo the test refinement until satisfactory convergence is achieved.

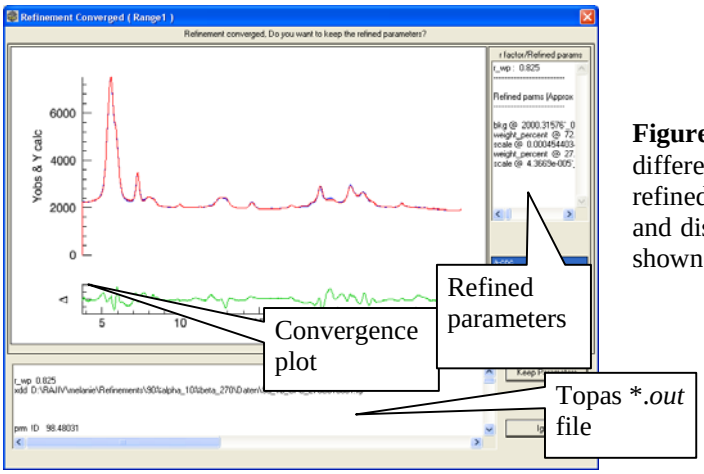

Figure 6.2. The observed calculated and difference plots are shown. The parameters refined in the test refinement are extracted and displayed (right). The Topas **.out* file is shown at the bottom of the convergence plot.

6.4.2 Sequential refinements

Prior to the beginning of the sequential refinements, the user is obliged to name all the parameters that are refined in the 'test' refinement and to set their refinement flags (Figure 6.3).

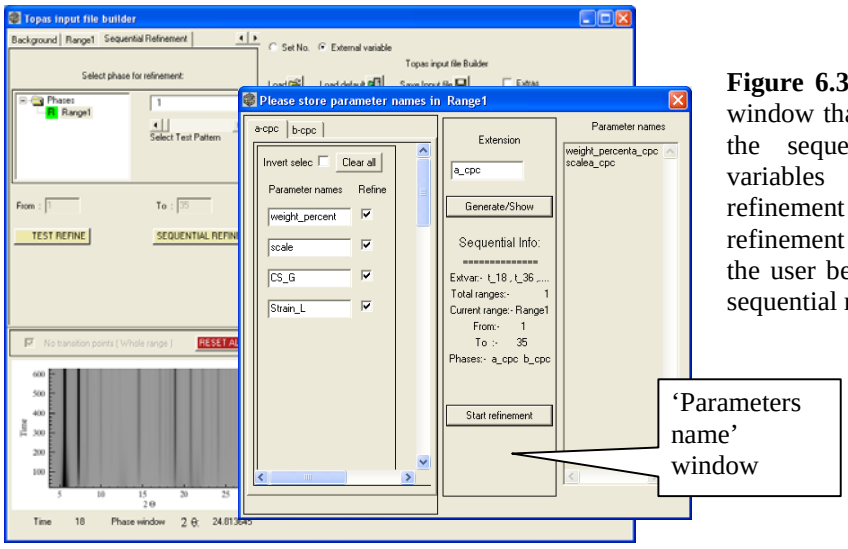

Figure 6.3 The '*Parameters name*' window that pops up before starting the sequential refinements. The variables refined in the test refinement are listed. Their refinement flags have to be set by the user before proceeding with the sequential refinements.

These names will be used by the program to identify the refinable variables while preparing the input files required for the parametric refinement. After the variables were

given valid names and their refinement flags were set by the user, the program automatically begins the sequential refinements by preparing and executing the input files using the '**.out*' file obtained from the test refinement. The results of the sequential Rietveld refinements of 35 powder patterns[14] of the sample dataset are shown in Figure 6.4.

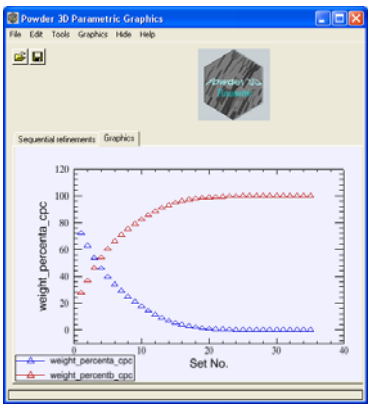

(a)

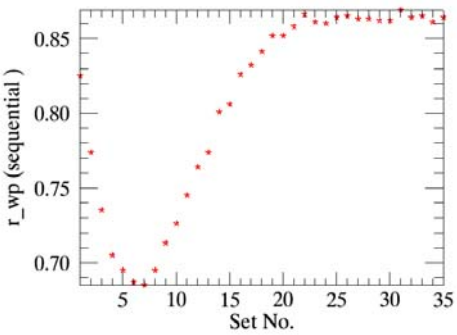

(b)

Figure 6.4 (a) The sequentially refined weight fractions of the decaying α-CuPC (blue) and the emerging β-CuPC (red) as obtained from the program are plotted. **(b)** The weighted residuals (*r_wp*) of the sequential refinements are plotted.

The weight fractions of α-CuPC (decaying phase) and β-CuPC (emerging phase) in sequential Rietveld refinements are simultaneously plotted against the time axis (Figure 6.4 (a)). The weighted residuals (*r_wp*) of consecutive refinements are also plotted in 6.4 (b), this plot helps the user to choose the optimal time-segment of the dataset to be used in the parametric refinement (section 6.5).

The refined values of the variables will be read from the corresponding **.out* files after each cycle of the sequential refinement. The read values will be sorted out and displayed in a separate worksheet as shown in Figure 6.5. This worksheet (Figure 6.5) provides options to study the evolution of all the refined variables with time and to parameterize them with the desired models.

6.4.3 Parametric refinement

Parametric Rietveld refinement related to the 'kinetic analysis' can be started after selecting the '*Reaction kinetics* (*Iso thermal*)' module and the '*Avrami*' model from their respective lists (Figure 6.5)[15].

[14] Totally 35 powder patterns collected to study the transformation from α-CuPC to β-CuPC at 270°C.
[15] For detailed explanations refer sections F4 and T 6.2 in the Users manual.

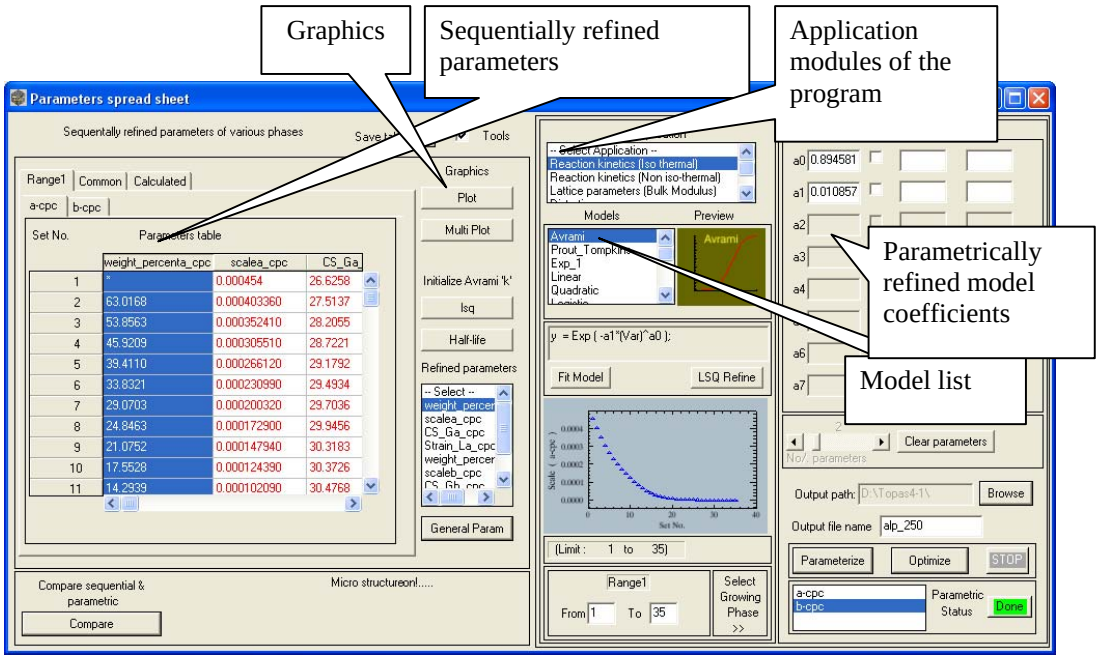

Figure 6.5 The 'parameters worksheet' is shown. The sequentially refined variables are sorted according to their phases and presented here. The parametric refinement can be started in this GUI, after selecting the number of patterns and after choosing an appropriate model.

The program makes use of the **.out* file of the test refinement and places Equation 6.1 or substitutes the keyword '*scale*' with Equation 6.1 in one of the 'phase' parts (e.g., in the phase α-Cu*PC*) of the file, as many number of times as the number of patterns selected by the user. The codes necessary to parameterize the weight percent with Avrami equation and all the other supporting statements are automatically generated by the program and written in the large input file and the file is executed in the Topas launch mode kernel.

After the completion of the refinement, the linearized weight fractions of the emerging phase (in this case β-CuPC) obtained from sequential refinements and the weight fractions refined form the model (Avrami) will be plotted together in the main graphics interface of the program (Figure T.28 in Users manual). The parameters *n* and *k* refined from the Avrami model will be read from output file returned by Topas and will be displayed in the parameters sheet (Figure 6.5).

6.5 Analysis

The Avrami parameters *n* and *k* of the test data obtained in sequential (Müller *et al.*, 2010b) and in parametric kinetic analyses are presented in Table 6.2. The values (*n* and *k*) from parametric refinement using all 35 patterns (Table 6.2 column 3) are close to those

obtained from literature (Table 6.2 column 2). The overall weighted residual for this fit is ~0.869.

Table 6.2 The Avrami parameters obtained from sequential refinements and the weighted residuals (second column) are compared with those obtained from parametric refinements (third column). In fourth column, the parameters refined in the optimal time-segment (linear region of weight fraction) of the data are listed.

Parameters	Literature (sequential)	Parametric refinement	
		All 35 patterns	Linear region
n	1.04	0.895	1.07
k	0.0087	0.011	0.0095
r_wp	~1.1	0.9	0.8

The aberrations in the parameters *n* and *k* in Table 6.2-column 2 and 3 is minimized when only the linear part of the weight fraction curve is used in the refinement. The region between the pattern numbers 7 and 15 (indicated by arrows in Figure 6.6) represents (roughly) the linear part of the weight fraction curve (also the '*r_wp*' curve).

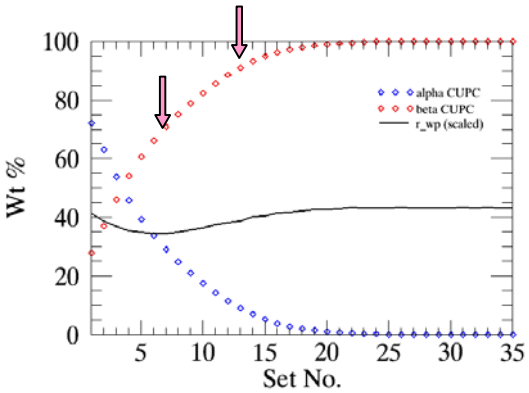

Figure 6.6 The weighted residuals (scaled, colored black) are overlaid on the weight fractions of α-CuPC (decaying phase) and β-CuPC (emerging phase). The two arrows indicate the approximate linear part of the weight fractions.

It is worth mentioning that the Avrami equation serves as the best linear approximation of the weight fraction that vary with respect to time. The overall weighted residual of parametric refinement is thus lowest (0.754) when the patterns that belong to this region alone are included in the refinement. The slight variation of *n* and *k* (in Table 6.2-column 4) from the expected values (in Table 6.2-column 2) is due to the exclusion of crystallite size effects in the original refinements from literature (Müller *et al*., 2010b).

The weight fractions obtained from parametric fits (using all the 35 patterns in the dataset and only the linear part of weight fraction curve) are compared with the respective weight fractions obtained in sequential refinements (Figure 6.7).

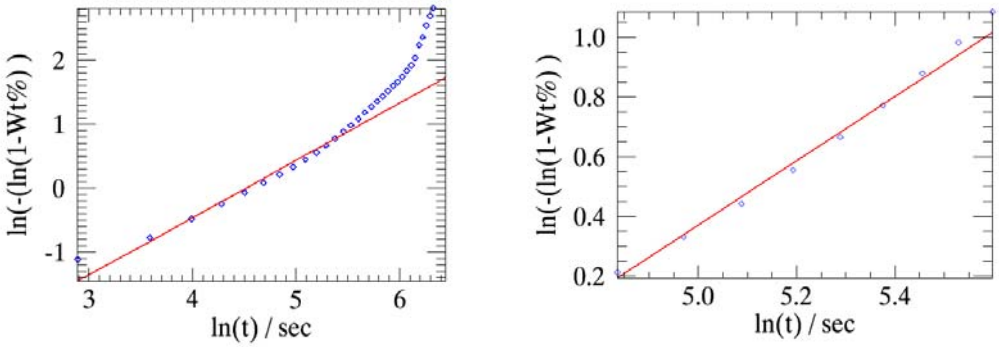

Figure 6.7 The linearized weight fractions of the emerging β-CuPC obtained in sequential refinements (colored blue) and the weight fractions obtained in parametric refinements (colored red) are compared. **(a)** All 35 patterns are included in parameterization. **(b)** Only the patterns from 7 and 15 are used in the parameterization (Figure 6.6).

The entire procedure described in sections 6.4 and 6.5 (preparation and execution of the input files and graphics handling etc.) was done with the help of the program. Similar analyses were carried out for all the time dependent data (listed in Table 6.1) collected in the experiment. The comparison of the rate constants and the activation energies determined from sequential and parametric refinements, and the explanations for the discrepancies between the results are presented in the following section.

6.6 Comparison of results and interpretation

A summary of the sequential and parametric reaction kinetics analysis performed on all the polymorphs of CuPC used in the analysis is presented in Table 6.3. The rate constants and activation energies of some selected groups of CuPC polymorphs as derived from parametric refinements are also individually interpreted in this section.

Table 6.3 The sequentially (blue lettered) and parametrically refined rate constants and the activation energies of all the polymorphs and polymorphs-additives mixtures of CuPC are listed. 'Optimal' (red lettered) denotes the rate constants and activation energies found from the linear region of the weight fraction of the vanishing phase (Figure 6.4 (b) and Figure 6.6). '-err-' indicates an unexpected refinement error from Topas. '-N.A-' indicates (not applicable) the failure of parametric refinement[16]. '-T.P-' indicates two parametric refinements performed. '-N.C-' indicates 'not the correct data'.

Sample - CuPC		Temperature [°C]	Avrami parameter *k* (rate constant) x 10^{-5}			E [kJ/mol]	
			Sequential	Parametric	Optimal	Sequential	Optimal
Pure α		230 250 270 290	4.7 41.0 255 2100	-err- 42.4 353 -err-	4.71 43.5 356.00 2260	241(2)	243.1
90 % *α*+10 % *β*		250 270	178 870	229 1100	215.6 950	187(6)	175.2
ε		320 340	0.026 83000	0.016 108900	0.0264 108253	2263(9)	2302
ε + BlauEFL		320 330	0.008 3.40	38.8 3.9	0.0069 14.97	1807(26)	2285
90%ε[17] + 10%*β*	0-16 %	250 270	6.714 95	-T.P.- -T.P.-	5.134 6.9	325(5)	34.9
	0-16 %						
	>16%	250 270	0.0721 0.0091	-T.P.- -T.P.-	2.247 3.7	-N.C.-	58.9
	>16%						
90 % *α* + 10 % ε		250 270	447 2700	-N.A.- -N.A.-	314.34 2272.63	213(6)	233
85.5 % *α* + 9.5 % ε + 5 % NU		230 250	297 1926	105.65 621.95	106 1108.3	205(13)	225
85.5 % *α* + 9.5 % ε + 5 % DMAM		230 250	8.7 377	-err- 48.36	7.85 243.15	413(5)	375

6.6.1 Pure α-CuPC

The kinetics of phase transition from pure α-CuPC (containing no additives) to β- CuPC has been studied using the time-dependent powder data collected at the temperatures 230 °C, 250°C, 270°C and 290°C (Table 6.3). For the data collected at 230°C, parametric Rietveld refinement did not successfully converge when all the 348 patterns collected in

[16] As observed from many datasets, parameterization was found to be successful incase where the compounds have higher reaction rates.

[17] The estimated standard deviation (ESD) for this parametric fit is large due to low reaction rate of the compound.

the experiment were used in the refinement. The convergence couldn't be reached even after providing sensible starting values (close to the 'expected' values) for the parameters *n* and *k*.

The weight fractions of the simultaneously decaying α-CuPC and emerging β-CuPC phases for this experiment as determined from sequential Rietveld refinement are plotted in Figure 6.8 (a). As observed in Figure 6.8 (a), the reaction of pure α-CuPC at 230°C is extremely slow until 18 min from the starting time of experiment (approximately up to pattern number 60). The stability of the parametric refinement is strongly biased, when large number of patterns with very low weight fractions is included in the refinement.

Using the patterns recorded after the initiation of the reaction (between pattern number 60 and 348) in the parametric refinement (shown in Figure 6.8 (b)) ended up with the rate constants comparable to the expected values. Reliable values of rate constant could also be obtained when the region between pattern number 200 and 348 (Figure 6.8 (c)) were used in parametric refinement.

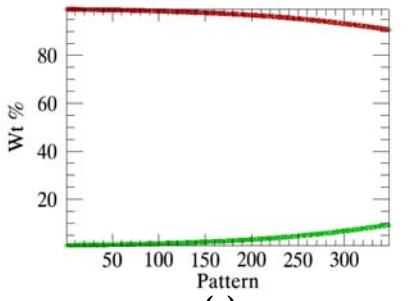

(a)

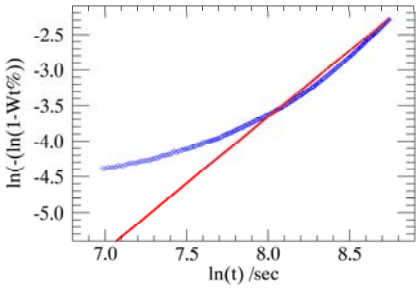

(b)

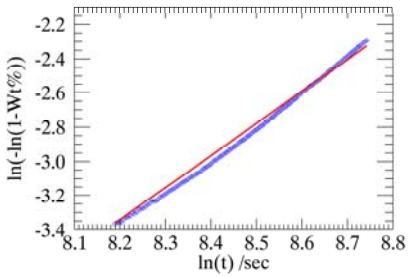

(c)

Figure 6.8 (a) The weight fractions of α-CuPC and the emerging β-CuPC at 230°C as obtained in sequential refinements (colored red and green) are plotted. **(b) & (c)** The weight fractions of the emerging β-CuPC in sequential refinements (colored blue) and the same obtained from parametric refinements (colored red) **(b)** for the region between pattern numbers 60 and 300 and **(c)** for the region between pattern numbers 200 and 300.

The parametric refinements of pure α-CuPC data samples measured at temperatures higher than 230°C produced more accurate results even without supplying sensible starting values for *k* and *n*. The weight fractions determined from parametric refinements of α-CuPC data measured at 250°C is shown in Figure 6.9. For the sample α-CuPC measured at 250°C, the linear region of the weight fraction (Figure 6.9 (b)) alone is sufficient to produce the parameters that are consistent with those found from the sequential refinements. The

overall weighted residual of the parametric refinement of the linear region is slightly lower (~0.94) than the weighted residual obtained when all the 224 patterns collected in the experiment are used (~1.01) in the refinement.

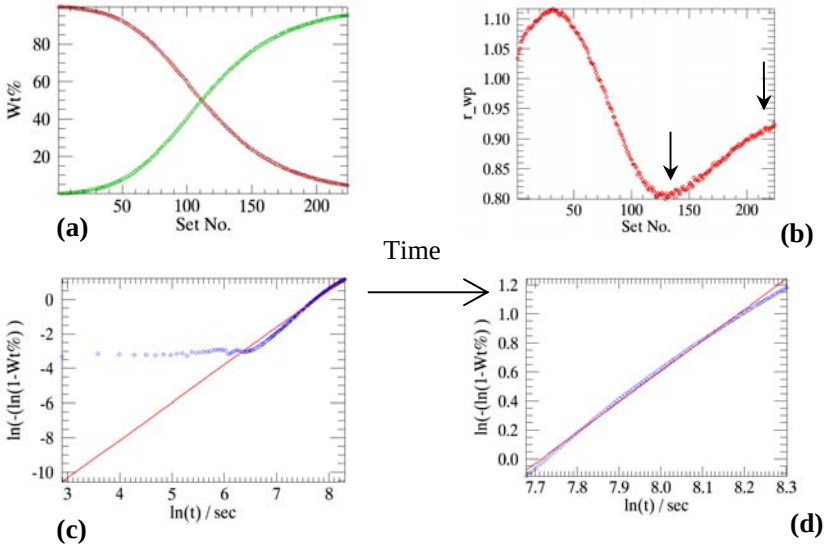

Figure 6.9 (a) The weight fractions of the decaying pure-α-CuPC (red) and emerging β-CuPC (green) from sequential refinements are plotted. **(b)** The weighted residuals of sequential refinements are plotted; the linear region is indicated by arrows. **(c)** The linearized weight fraction of the emerging β-CuPC (blue) in sequential refinements and parametric fit (red) using all the patterns collected (224). **(d)** The weight fractions of β-CuPC in sequential refinements and parametric refinements when only the linear region is used in the refinement (pattern numbers 120 to 224).

For the same sample (pure-α-CuPC) measured at 270°C, the linearized weight fractions of the emerging β-CuPC determined in sequential refinements and the weight fractions derived from parametric refinement are plotted in Figure 6.10.

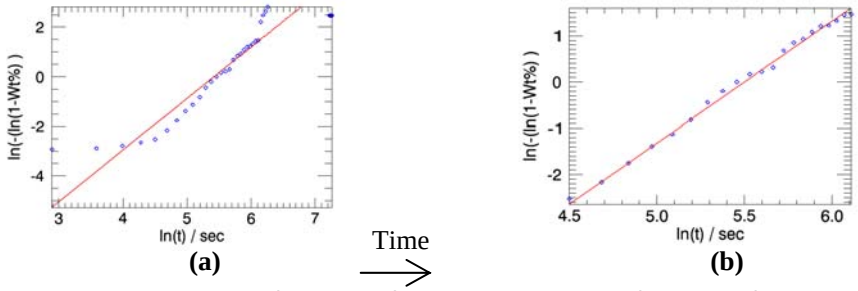

Figure 6.10 The linearized weight fractions of β- CuPC in the transformation from pure α- CuPC to β-CuPC at 270°C, in sequential (blue) and parametric refinements (red) are plotted. **(a)** All the 79 powder patterns collected in the experiment are used in the parametric refinement. **(b)** The powder patterns that correspond to the linear region of the weighted residual curve (~ pattern numbers 5 to 25) alone are used in the refinement.

The rate constants *k* derived from the Avrami model, in all the experiments involving the transformation of pure α-CuPC (from temperatures 230°C to 290°C) to β-CuPC are plotted as an Arrhenius type of plot (Iordanova *et al*., 2002) in Figure 6.11.

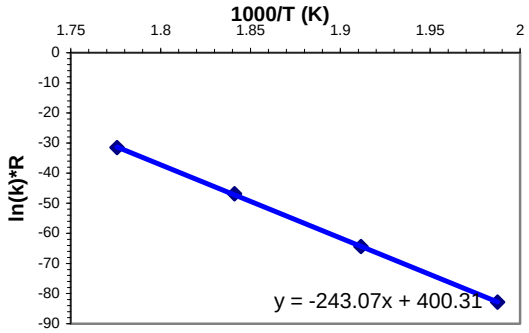

Figure 6.11 The rate constants of the reaction involving the transformation from pure α-CuPC to β-CuPC as derived from Avrami equation are plotted as an Arrhenius type plot. Linear fit has been made to these points. The slope of the regression line gives the activation energy of the reaction.

The slope of the regression line fitted to these rate constants gives the activation energy of the reaction. The activation energy of the reaction involving the transition from pure α-CuPC to β-CuPC, found from the parameterized rate constants is ~243 kJ/ mol (Table 6.3).

6.6.2 α-CuPC and β-CuPC

The kinetics of transformation of α and β CuPC mixture in the ratio 9:1 to β-CuPC was studied from their time-resolved datasets collected at temperatures of 250°C and 270°C. The weight fractions of β-CuPC determined from parametric refinements for one of these experiments (performed at 250°C) is plotted in Figure 6.12. (The weight fractions of the same sample measured at 270°C are plotted in Figures 6.7).

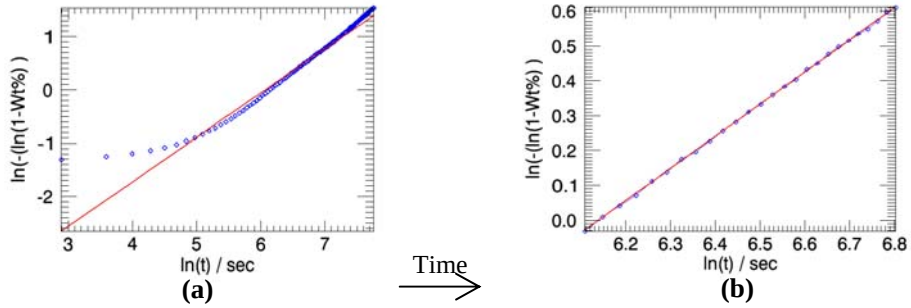

Figure 6.12 The linearized weight fractions of β-CuPC in the transformation of α-CuPC +β-CuPC mixture at 270°C, from sequential (blue) parametric refinements (red) are shown. **(a)** All the 130 powder patterns collected in the experiment are used in the parametric refinement. **(b)** Only the powder patterns that correspond to the linear region of the weighted residual curve (~ pattern numbers 25 to 50) alone are used in the refinement.

As inferred from Table 6.3, the addition of β-CuPC to pure α- CuPC has increased the rate constant *k* of the experiments performed at 250°C and 270°C by a factor of about 3 (Table 6.3). The activation energy of this reaction, derived from the parameterized rate constants is about 175 kJ/ mol, which is about 70 kJ/ mol smaller than the energy of the reactions involving pure α-CuPC.

6.6.3 α-CuPC ε-CuPC and additives

6.6.3.1. α-CuPC and ε-CuPC

The phase transition of α-CuPC+ε-CuPC mixture (in the ratio 9:1) to β-CuPC was studied from their time-resolved datasets collected at temperatures 250°C and 270°C. The weight fractions of the three phases involved in these experiments, determined from sequential refinements are plotted in Figure 6.13.

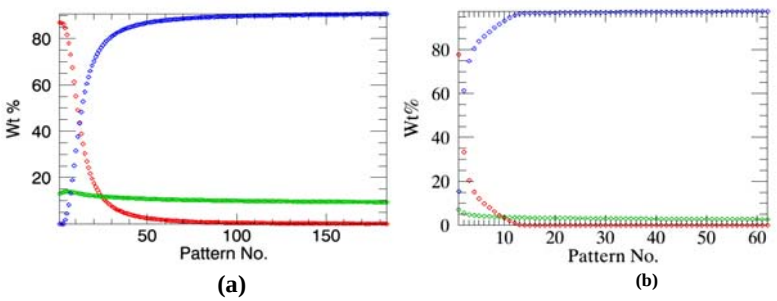

Figure 6.13 The weight fractions of the decaying α-CuPC (red) and the emerging β-CuPC (blue) and ε-CuPC (green) at 250°C and 270°C determined from sequential refinements are plotted in **(a)** & **(b)**.

Parametric refinement of α-CuPC+ε-CuPC mixture could be performed only for the data collected at the temperature 250°C. For this data, the powder patterns that correspond to the linear region of the weight fraction curve alone were used in the refinement (patterns 12 to 50 out of 184). The weight fractions of β-CuPC derived from parametric refinement are compared with the linearized weight fractions obtained in sequential refinements (Figure 6.14).

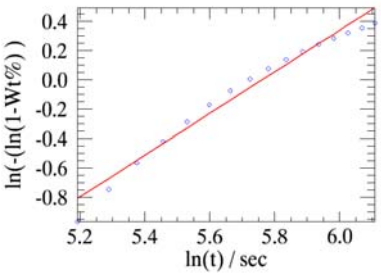

Figure 6.14 The weight fractions of β-CuPC in reaction involving the transformation of α-ε-mixture of CuPC to β-CuPC at 250°C from parametric refinement (red) are compared with the linearized weight fractions of β-CuPC determined from sequential refinements (blue). Only 38 out of 184 powder patterns were used in the parametric refinement.

For the data collected at the temperature 270 °C, parametric refinement ended up in results with large standard deviation (compared to the literature Müller *et al*., 2010), even after using the 'linear' powder patterns and after supplying sensible starting values for the variables *k* and *n*.

The α-CuPC present in the α-ε mixture was completely transformed into β-CuPC in approximately 3.6 min from the beginning of the experiment (Figure 6.13(b)). The high reactivity of α-CuPC+ε-CuPC mixture at the temperature 270°C has strongly influenced the convergence of parametric refinement.

The activation energy of this reaction determined using the Avrami model is ~233 kJ/ mol. The addition of ε-CuPC to α-CuPC has considerably increased the rate constants of this reaction.

6.6.3.2. α-CuPC ε-CuPC with NU

The kinetics of transition of the mixture α+ε-CuPC (85.5 % and 9.5% respectively) and the additive NU to β-CuPC was studied from their isothermal data collected at the temperatures 230°C and 250°C. The weight fractions of the three phases involved in the two experiments, determined from sequential refinements are plotted in Figure 6.15.

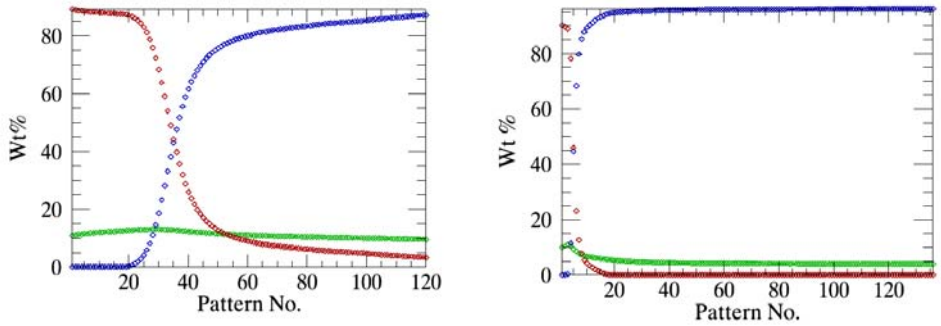

(a) **(b)**

Figure 6.15 The weight fractions of the decaying α-CuPC (red) and the emerging β-CuPC (blue) and ε-CuPC (green) in the experiment with α-CuPC, ε-CuPC and NU performed at 230°C and 250°C as determined from sequential refinements are plotted in **(a)** & **(b)**.

The weight fractions of the emerging β-Cu*PC* determined from parametric refinements for the two experiments involving the α-Cu*PC* +ε-Cu*PC* +NU mixture measured at 230°C and 250°C are plotted in Figure 6.16.

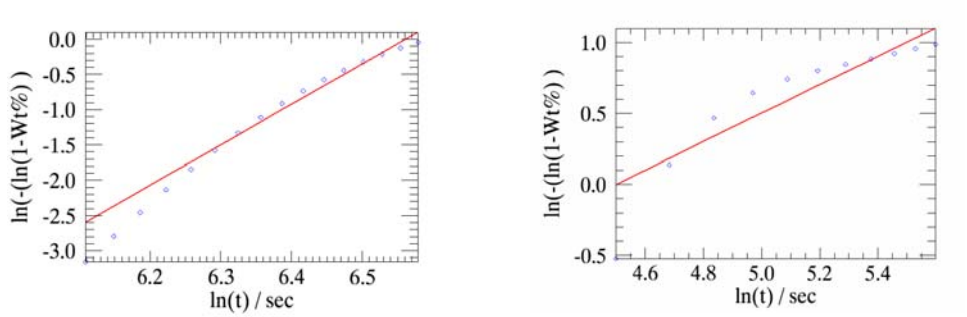

Figure 6.16 The weight fractions of β-CuPC in the transformation of α+ε-CuPC with NU studied at 230 °C **(a)** and 250°C **(b)** derived from parametric refinements (red) are compared with linearized weight fractions obtained from sequential refinements (blue). **(a)** Only 15 of 120 powder patterns (25 to 40) collected in the experiment are used in the parametric refinement. (b) Only 10 out of 136 powder patterns (5 to 15) that correspond to the linear region of the weighted residual curve are used in the refinement.

Similar to the α-CuPC+ε-CuPC mixture, the convergence of parametric refinements of the α-CuPC+ε-CuPC with NU required a sensible starting value for the variable *k*. Furthermore, the convergence of the refinement required only those powder patterns that were collected at the optimal (linear) time region (as in Figure 6.9(c)).

The compound 'NU' (Table 6.3) has decreased the rate constants of the reaction when added to the mixture containing α-CuPC and ε-CuPC phases.

6.6.3.3. α-CuPC ε-CuPC with DMAM

The results of the kinetic analysis carried out for the reactions involving the transformation of α+ε- CuPC and DMAM to β-CuPC are summarized in Figure 6.17. The addition of the compound 'DMAM' to the mixture of α-CuPC and ε-CuPC lead to a drastic decrease in the rate constant k of the reaction (Table 6.3). The activation energy of this reaction, found from the parameterized rate constants is about 375 kJ/mol.

The convergence of parametric refinements involving more than two phases (in all the cases in section 6.6.3) required a sensible starting value for the variable *k* and required only the powder patterns collected in the linear time region to be included in the refinement.

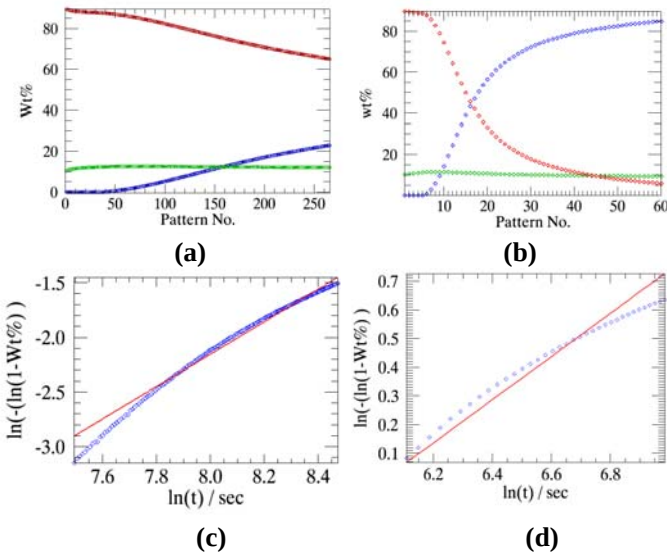

Figure 6.17 The weight fractions of α-CuPC (red) and β-CuPC (blue) and ε-CuPC (green) in the experiment with α+ε-CuPC and DMAM performed at 230°C and 250°C as determined from sequential refinements are plotted in **(a)** & **(b)**. The weight fractions of β-CuPC **(c)** at 230°C and that at 250°C **(d)** from parametric refinements (red) are plotted. **(c)** Only 180 of 230 powder patterns (50 to 230) collected in the experiment are used in the parametric refinement. **(d)** Only 35 of 60 powder patterns (25 to 60) that correspond to the linear region of the weighted residual curve are used in the refinement.

6.6.4 ε-CuPC and additives

6.6.4.1 ε-CuPC

The reaction involving the transformation of ε-CuPC to β-CuPC is slow at 320°C and at 330°C. Epsilon-CuPC starts reacting faster at 340°C. The results of sequential and parametric refinements of the reactions of ε-CuPC at temperatures 320°C and 340°C are shown in Figures 6.18 and 6.19 respectively.

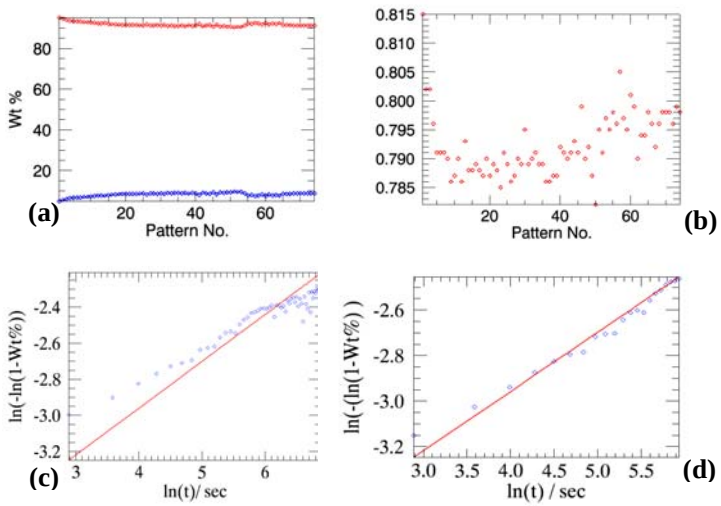

Figure 6.18 (a) The weight fractions of the decaying ε-CuPC (red) and the emerging β-CuPC (blue) obtained in sequential refinements. **(b)** The weighted residuals (fluctuating) in sequential refinements are plotted. The linearized weight fraction of the emerging β-CuPC (blue) in sequential and parametric refinements (red) **(c)** using all patterns and **(d)** using only for the patterns in the linear region (between 1 and 21) are plotted.

Large deviation between the parametrically refined weight fractions and the sequentially refined weight fractions is observed in Figure 6.18 (c). The convergence of parametric refinement could not be easily reached for the data collected at 320°C and 330°C, whereas the data collected at 340°C can be easily subjected to parametric fit, as the change of the weight fraction (β-CuPC) of the growing phase at the temperature 340 °C is considerably higher (Figure 6.19).

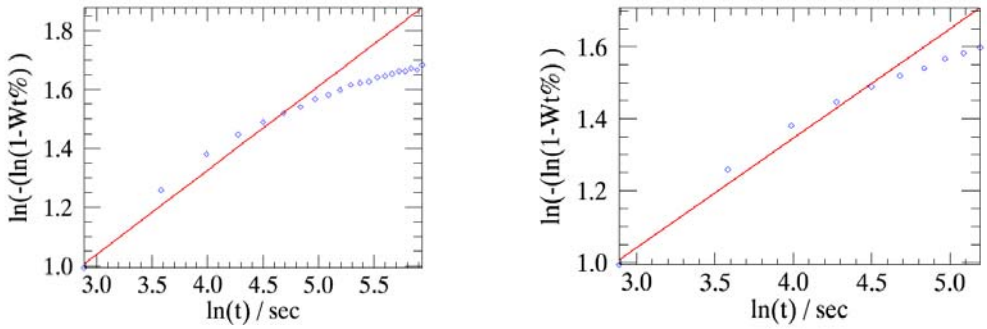

Figure 6.19 The linerarized weight fractions of β-Cu*PC* in the transformation of ε-Cu*PC* to β-Cu*PC* at 340°C, as determined from sequential refinements (blue) are compared with weight fractions obtained from parametric refinements (red). (a) All the 21 powder patterns collected in the experiment are used in the parametric refinement. (b) The powder patterns that correspond to the linear region of the weighted residual curve (~ pattern numbers 1to 10) alone are used in the refinement.

6.6.4.2 ε-CuPC and β-CuPC

To study the transformation of a mixture of ε-CuPC (90%) and β-CuPC (90%) to β-CuPC, about 700 powder patterns were collected in total at the two different temperatures 250°C and 270°C. As the order of this reaction changes after about 16% of the experimental starting time (Müller *et al*., 2010), two independent sets of parametric refinements were performed on these samples (measured at the two temperatures).

The first refinement comprises the patterns collected from the starting time up to 16% of the experimental time whilst the second refinement comprises the patterns collected after 16% of the experimental time to the end of experiment.

Parametric refinements could be performed on both the segments of the dataset (<16% and > 16%) collected at the two temperatures only after supplying a sensible starting value for the parameter. The deviations of the fit in both regions (at the temperatures 250°C and 270°C) were however extremely large (Table 6.3), since the reactivity of the specimen is extremely low on the order of ~ E-8. The weight fractions of the decaying ε-CuPC and emerging β-CuPC at the two temperatures are plotted in Figure 6.20.

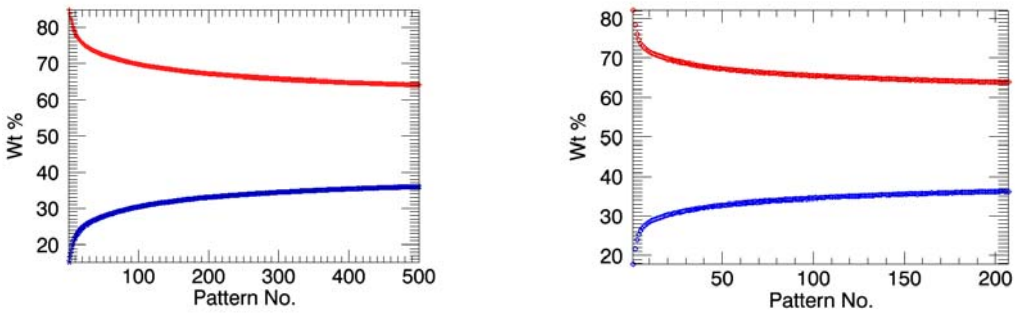

Figure 6.20 The weight fractions of the transformation of (red) ε-Cu*PC* +β-Cu*PC* to β-Cu*PC* (blue) studied at 250°C (a) and 270°C (b) respectively, determined from sequential refinements are presented.

6.6.4.3 ε-CuPC and BlauEFL

The results of the kinetic analysis carried out for the reactions involving the transformation of ε- CuPC +BlauEFL to β-CuPC are summarized in Figure 6.21. ε-CuPC and BlauEFL datasets collected at 320°C and 330°C could be parameterized only after supplying a sensible initial value of *k*. Like most other reactions, the convergence of parametric refinements of ε-CuPC+BlauEFL data also required that only the powder patterns collected at the linear time region are included in the refinement.

The addition of BlauEFL to the ε-CuPC sample has decreased the rate constants of the reaction by a factor of ~10. The activation energy determined from the (parameterized) rate constants is about ~ 2285 kJ/ mol.

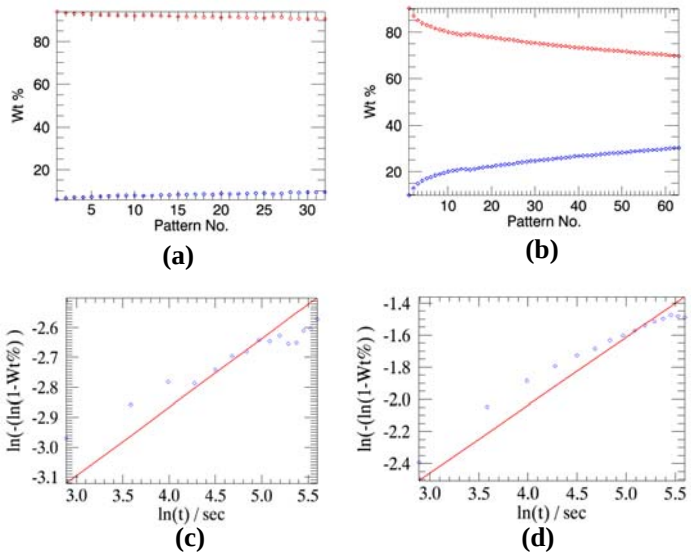

Figure 6.21 (a) and **(b)** The weight fractions of the transformation from (red) ε-Cu*PC*+BlauEFL to β-Cu*PC* (blue) studied at 320°C and 330°C respectively determined from sequential refinements are presented. **(c)** and **(d)** the parameterized (red) and sequentially refined (blue) weight fractions of β-Cu*PC* data measured at 320°C and 330°C are plotted.

The success of parametric refinement for the transformations involving ε-CuPC and BlauEFL and also the other measurements involving the transition of most ε-CuPC samples with additives and the reaction involving three phases of CuPC (e.g., α+ε-CuPC to β-CuPC) depend strongly on a physically sensible starting value of the rate constant (*k*). In most of these cases (dependent on the reaction order), the starting value for the parameter k was approximated from the half-life decay equation of a first order reaction (Equation 6.2).

$$k = \frac{0.693}{t_{1/2}} \tag{6.2}$$

where,

$t_{1/2}$ - Half-life of decay of a vanishing phase in a first order reaction

k - Reaction rate constant.

Equation 6.2 gave the correct order of magnitude of the rate constant (*k*), which when used as a starting value of *k* in the parametric refinement resulted in the convergence of most of the data used in this analysis. This equation was included in the program along with a least squared refinement routine; both were used to initialize the rate constant *k*.

6.7 Summary

The sequential and parametric kinetic analysis of various forms of CuPC and some CuPC-additive mixtures were performed with the help of the program 'Powder 3D Parametric'. The use of the program in the kinetic analysis of CuPC has considerably speeded up the sequential refinements and also eased the preparation of input files required for the parametric refinements of data measured between specific time intervals. Most CuPC datasets used in this analysis also demanded that only certain time-segments of the data are used in parametric refinement.

On the whole, kinetic analysis of CuPC using parametric refinement could be successfully performed for most CuPC data samples, except that the stability of refinement for many data samples showed a dependence on the reactivity of the polymorphs. The CuPC samples with low reactivity could also be analyzed using parametric refinement, however the precision of the refined variables in these trials were relatively lower. The success of parametric refinements of the 'low reactive' polymorphs also depended to some extent on the number of measurements made, and on the quality of the data. The strong dependence of the convergence of refinement on the starting values of the variable *k* is noticed in most of the samples. Significant improvements with respect to activation energies can only be achieved by performing more measurements at different temperatures.

Chapter 7

Parameterization of crystallite size against annealing time/temperature

7.1 Introduction

In this chapter, a general procedure to parameterize the crystallite size variation of materials with respect to the annealing time/temperature is presented. Some of the isothermal data used in the kinetic analysis of CuPC (chapter 6) and the nano-crystalline titanium dioxide (TiO_2) (Horn *et al*., 1972) data measured in dependence on temperature are used as examples. This application is considered a case study to prove that the parameterization of the crystallite size (inversely proportional to the FWHM of the phase peaks) versus time/temperature is feasible.

All the input files required for this analysis were prepared with the help of the program 'Powder 3D Parametric'[1].

7.2 Crystallite size

The major sources of peak broadening in XRPD are the micro-structure of the material (crystallite size and lattice strain) and the instrumental aberrations. In Rietveld analysis, the instrumental contributions to the peak broadening are handled by various physical and mathematical models. Once, the Caglioti relation was mainly used for this purpose (Caglioti *et al*., 1958; David *et al*., 2010).

The angle dependent (θ_k) X-ray powder peak broadening due to crystallite size can be modelled best by functions that are convolutions of Gaussian and Lorentzian functions

[1] As explained in chapter 6 and in Users manual section A2.

(Coelho, 2007; Balzar *et al*., 1999). In a similar way, the lattice strain contribution to X-ray powder peak broadening can be modelled by convoluting the Gaussian and Lorentzian functions.

Altogether, the micro-structural contribution to X-ray peak broadening can be satisfactorily explained by a set of four equations that are dependent on one another (Equations 7.1 to 7.4). Depending upon the necessity, some of these equations can be introduced as micro-structural convolution models of the material during the Rietveld refinement.

$$(\beta_{sz})_{gauss} = \frac{\lambda}{S_{gauss} Cos(\theta_k)} \tag{7.1}$$

$$(\beta_{sr})_{gauss} = 4\varepsilon_{gauss} Tan(\theta_k) \tag{7.2}$$

$$(\beta_{sz})_{lor} = \frac{\lambda}{S_{lor} Cos(\theta_k)} \tag{7.3}$$

$$(\beta_{sr})_{lor} = 4\varepsilon_{lor} Tan(\theta_k) \tag{7.4}$$

where,

$(\beta_{sz})_{gauss}$ and $(\beta_{sz})_{lor}$ - Gaussian and Lorentzian related FWHM of the size broadened phase peak
$(\beta_{sr})_{gauss}$ and $(\beta_{sr})_{lor}$ - Gaussian and Lorentzian related FWHM of the strain broadened phase peak
$(S)_{gauss}$ and $(S)_{lor}$ - Gaussian and Lorentzian related crystallite size of the material
$(\varepsilon)_{gauss}$ and $(\varepsilon)_{lor}$ - Gaussian and Lorentzian related lattice strain of the material
λ - Wavelength of the incident X-ray beam
θ_k - Phase peak positions

Topas launch mode offers a simple way to introduce these models (Equations 7.1 to 7.4) during the Rietveld refinement using its built-in macros *CS_G*, *CS_L*, *Strain_G*, and *Size_G*. These macros can be introduced into the input file to directly refine the Gaussian and/or Lorentzian related crystallite size (or lattice strain) of the material.

Parameterization of one of these equations with respect to time/temperature can be easily accomplished by modifying and rewriting the contents of these macros in the prepared input file. For instance, the parameterization of Gaussian related crystallite size versus time/temperature with a quadratic equation (Equation 7.5) can be accomplished by

replacing the respective FWHM (Equation. 7.1) by the model equation and rewriting the size term (S_{gauss}) and the FWHM term $(\beta_{sz})_{gauss}$, as in Equation 7.6.

$$y = (a_0 + a_1 T + a_2 T^2) \tag{7.5}$$

$$S_{gauss} = \frac{\lambda}{(a_0 + a_1 T + a_2 T^2) Cos(\theta_k)} \tag{7.6}$$

where,

y	-	Dependent variable
a_0 , a_1, a_2	-	Refinable (global) model coefficients
T	-	Time (or other external variable)

The Topas macro language statements analogous to Equations 7.5 to 7.6 are appended in the supplementary section 'Topas input files'-F. The program automatically generates these statements and writes them in the appropriate locations in the 'phase' parts of the input file before its execution.

In the following sections, some examples of parameterization of the Gaussian related crystallite size versus time/temperature (similar to Equation 7.6) will be explained.

7.3 Gaussian crystallite size of CuPC

In the sequential and kinetic analysis of the phase transitions of CuPC (chapter 6), the Gaussian-crystallite sizes of the emerging β-CuPC in most of the experiments are found to increase uniformly with respect to the annealing time.

The evolution of the sequentially refined Gaussian FWHM of β-CuPC in one of the reactions involving the transition of a α+β-CuPC mixture (in the ratio 9:1) to β-CuPC measured at 270 °C (the test-data in chapter 6) is plotted in Figure 7.1.

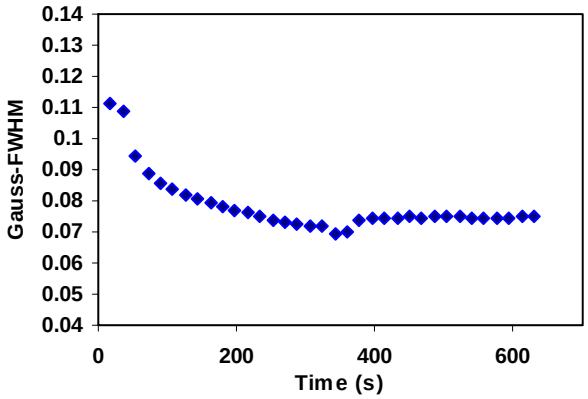

Figure 7.1 The sequentially Rietveld refined Gaussian FWHM of β-CuPC versus the measurement time of the test-data (chapter 6) is plotted.

Some basic mathematical functions have been attempted to model the variation of size-related Gaussian FWHM broadening of β-CuPC. A 3rd order polynomial (cubic function) gave a satisfactory description of the variation of Gaussian FWHMs versus time. The Gaussian FWHM and the crystallite size derived from the cubic model are compared in Figure 7.2 along with those determined from the sequential refinements.

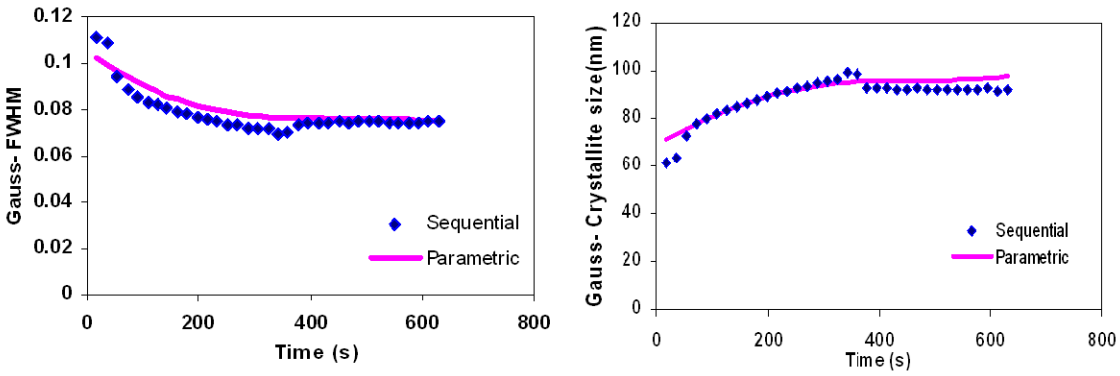

Figure 7.2 The Gaussian FWHM and crystallite sizes of β-Cu*PC* obtained in sequential (blue) and parametric refinements (pink) of the test-data sample are compared. A cubic function is used to model the evolution of Gaussian-FWHM versus time.

The coefficients of the cubic model determined from parametric refinement are provided in Table 7.1.

Table7.1 The coefficients of cubic function and their estimated standard deviations obtained in the parametric refinement of the test-data are presented.

Model	a_0	a_1	a_2	a_3
Cubic	0.1057 (48)	-0.00019 (5)	0.000000412 (95)	-29 e-10 (1)

The parameterization of Gaussian-FWHM with the cubic function has also (slightly) smoothed the refined scale factors of β-CuPC (Figure 7.3).

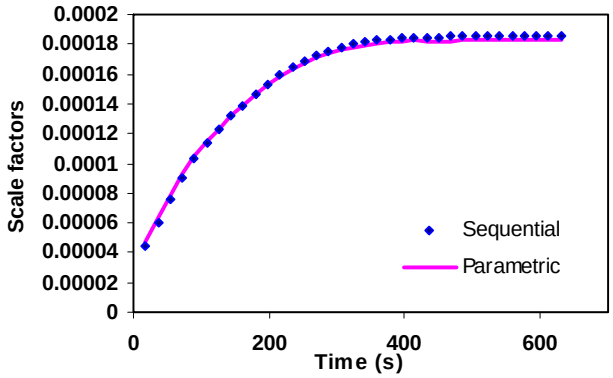

Figure 7.3 The Rietveld scale factors of β-CuPC obtained in sequential refinements (blue) and in parametric refinements (with a cubic function) (pink) of the test-data are plotted.

Higher order polynomials (e.g. quintic function) were also attempted to model the variation of Gaussian-crystallite sizes with time. The parametric refinements of Gaussian crystallite size with the functions other than cubic resulted in larger estimated standard deviations of the model coefficients.

7.4 Simultaneous parameterization of crystallite size and scale factor

Using the data measured at 320°C to study the transformation from ε-CuPC to β-CuPC, the size-related Gaussian-FWHMs of both phases (ε-CuPC and β-CuPC) were parameterized with a cubic function. In addition to the crystallite size, the weight fraction of β-CuPC was parameterized with the Avrami equation (as explained in chapter 6). The weight fractions of the growing β-CuPC after the parameterization with three variables and

that obtained after the parameterization of only the weight fraction (as in chapter 6) are compared in Figure 7.4.

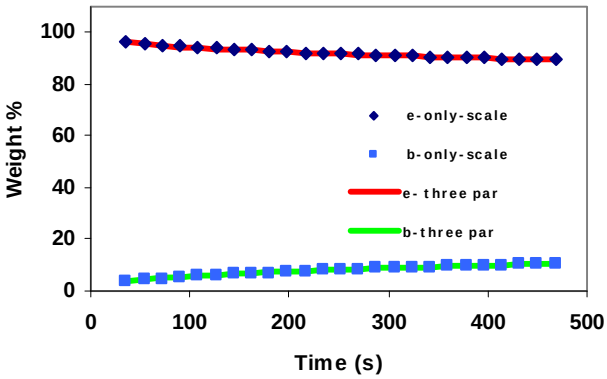

Figure 7.4 The weight fractions of β-CuPC obtained after parameterizing only the scale factors of β-CuPC with Avrami relation. (blue diamonds and squares) and the same obtained after parameterizing Gaussian crystallite sizes of the two phases (ε-CuPC and β-CuPC) and scale factors of β-CuPC (red and green lines) are presented.

The coefficients of the three models obtained in these refinements are summarized in Table 7.2.

Table 7.2 The coefficients of the three models used in the parametric refinement of ε-CuPC +β-CuPC data are presented. The estimated standard deviations of the coefficients a_1 to a_3 of the cubic functions (2nd and 3rd row) are relatively large due to strong correlations between the variables in parametric refinement.

Parameter	Model	$a_0(n)$	$a_1(k)$	a_2	a_3
Scale factor β- Cu*PC*	Avrami[2]	0.407 (8)	0.000011386 (2097)	-	-
Gauss-size β- Cu*PC*	Cubic	0.131 (1)	-0.00000056 (201)	5.5 e-10 (7783)	0.009 e-10 (104)
Gauss-size ε- Cu*PC*	Cubic	0.233 (17)	-0.000099 (244)	0.000000019 (982)	-0.345 e-10 (12772)

7.5 Gaussian crystallite size of TiO_2-anatase

The phase transition of the nano-crystalline TiO_2 from its anatase to rutile form was studied using *in situ* XRPD data collected at a synchrotron source. In total, ninety powder

[2] The accuracy of the Avrami parameter '*k*' is lower than the expected value. The parameterization of the weight fraction with Avrami equation was influenced strongly by the quality of the data used (Table 6.3) in this analysis.

diffraction patterns in dependence on temperature were collected for this analysis (from 298 K to 1123 K, with a heating rate of 6.875 K/min).

The anatase to rutile transition occurs approximately at a temperature of 700 K (Figure 7.5). Full quantitative sequential Rietveld analysis was performed on all the patterns (for the two phases) collected in the experiment (Dinnebier, 2010).

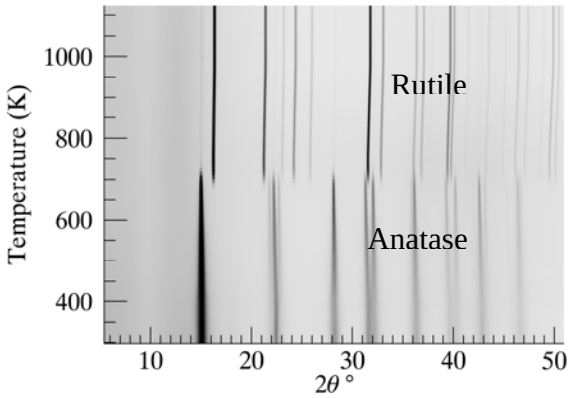

Figure 7.5 The anatase to rutile phase transformation of TiO_2 is shown as a simulated 'heating Guinier film plot'. The phase transition occurs approximately at the temperature of 700 K.

The Gaussian-FWHMs of the phase peaks of TiO_2-anatase, determined from the sequential refinements are plotted in Figure 7.6.

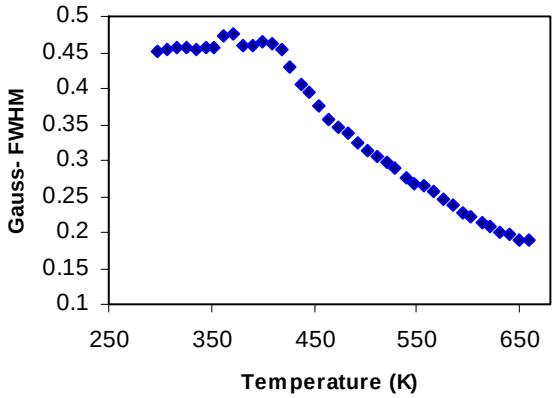

Figure 7.6 The Gaussian FWHMs of the phase peaks of TiO_2-anatase obtained in sequential refinements are presented.

As an initial attempt, the cubic function was used to model the Gaussian crystallite size variation with temperature. The Gaussian FWHM and crystallite size determined from sequential refinements and those derived from the cubic model are compared in Figure 7.7.

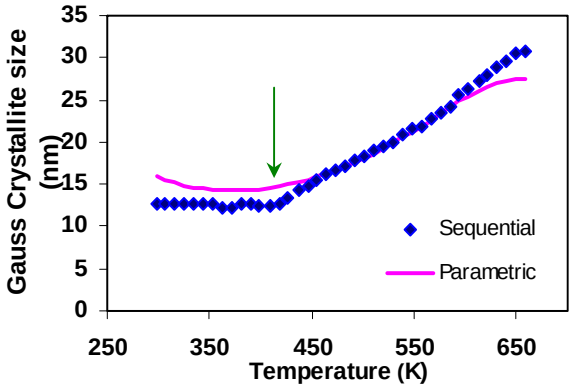

Figure 7.7 The Gaussian crystallite size of TiO_2-anatase obtained in sequential refinements (blue diamonds) and parametric refinements (pink lines) using cubic model are compared.

As seen from Figure 7.7, the cubic function was unable to describe the variation of crystallite size versus temperature correctly. In particular the deviation of the fit is large in the lower temperature region (roughly from experimental temperature 298 K to 409 K).

The crystallite size curve was therefore divided into two different temperature regions and the patterns that belong to the two regions are independently parameterized with two functions. The crystallite size of TiO_2 anatase remains approximately constant from room temperature up to 409 K. This region was parameterized with a linear function.

The region from 418 K to 659 K, which corresponds to the growing stage of TiO_2 anatase phase was parameterized by a cubic function. The parametrically derived crystallite sizes of both temperature regions are plotted in Figure 7.8; the model coefficients obtained in the two independent parametric refinements are summarized in Table 7.3.

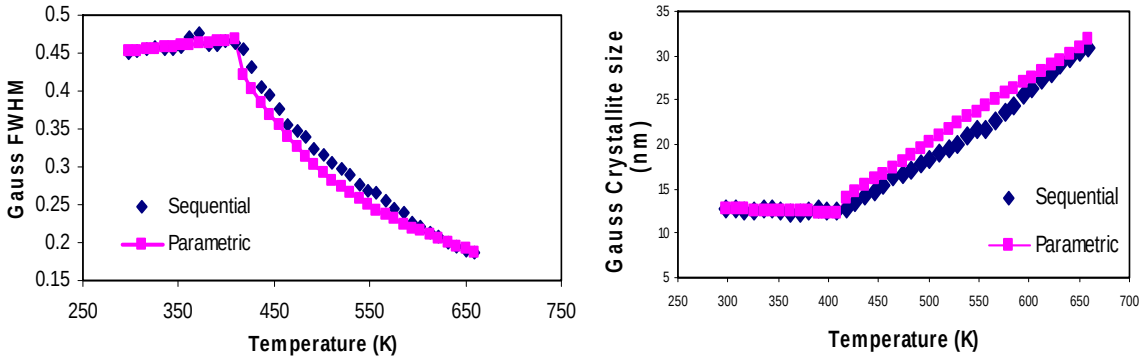

Figure 7.8 The Gaussian related FWHM (left) and Gaussian crystallite size (right) of TiO_2-anatase obtained in sequential refinements (blue diamonds) and parametric refinements (pink) using the linear function (298 K 409 K) to cubic function (418 K to 659 K) are compared.

The relatively smooth high temperature region (from temperatures 418 K to 659 K) of the 'crystallite size curve' could be conveniently parameterized by a cubic function. The

parameterization of the low temperature region (298 K to 409 K) with the linear model resulted in coefficients with lower statistical significance, as the growth of the crystallite in this temperature region is non-uniform and the rate is negligibly small.

Table 7.3 The coefficients of the linear and cubic functions obtained in the independent parametric refinements of two growth regions of TiO_2-anatase are presented.

Temperature range (K)	Model	a_0	a_1	a_2	a_3
298 – 409	Linear	0.4136	0.00013133	-	-
418 – 659	Cubic	3.2697	-0.0134195	0.00002011	-0.000000011

7.6 Summary

The feasibility of parameterization of micro structural variables (Gaussian crystallite size) has been verified using three different data samples. The input files required in several trials of parametric refinements with various crystallite size models and various time segments were prepared quickly and conveniently using the options provided by the program. The variation of Gaussian crystallite size against time/temperature for the selected datasets (section 7.3 and 7.4 and the growing part of TiO_2 anatase) could be successfully parameterized with a higher order polynomial, nevertheless the convergences of these refinements demanded physically sensible starting values of the model coefficients. The coefficients obtained in the non-linear least squares fit of the sequentially refined Gaussian crystallite sizes were used as the starting values of the model coefficients in the refinements. The dependence of the convergence of parametric refinement on the smoothness of variation of the crystallite size with respect to temperature and on the data quality was also observed in all these trials.

The parameterization of micro structural variables with time/temperature as introduced in this chapter is only a basic application. As such it can be used only to stabilize other refinable variables during parametric refinement, provided that the model used is appropriate. The slight smoothening of the scale factor of β-CuPC because of the

parameterization of Gaussian crystallite size of β-CuPC with a higher order polynomial has already been demonstrated in section 7.3.

Chapter 8

Précis

The conventional approach to quantitatively evaluate the XRPD data collected in dependence on an external variable is the sequential application of the WPPF to the individual powder patterns. The introduction of 'Parametric Rietveld refinement' method (Stinton and Evans, 2007) has opened new possibilities to collectively evaluate the powder patterns and also to introduce models of the evolving variables during the refinement; in this manner, additional information of crystalline specimen can be directly derived from the XRPD data. 'Parametric Rietveld refinement' has also other advantages over the sequential refinement method in relation to the precision of the refined parameters.

The basic necessity for the realization of sequential/parametric WPPF in 2D XRPD is a software that is capable of handling and performing sequential/parametric WPPF of bulk data. This concern has been primarily addressed in this thesis with the help of the software 'Powder 3D Parametric'- interfaced with the total powder pattern analysis software Topas. The developed software could considerably speedup the sequential/parametric quantitative analysis of large number of XRPD patterns collected in dependence on external variable, which was otherwise considered a monotonous and time consuming task.

Two practical scientific applications of parametric Rietveld refinement method have been demonstrated with the assistance of the developed program. The first application has presented the results of kinetic analysis performed on several polymorphs and polymorphs-additives mixtures of CuPC using parametric refinement method. The kinetic information (the reaction rate constant and the reaction order) was directly extracted from the isothermal experimental data by introducing the Johnson-Mehl-Avrami-Kolmogorov relation as a physical model for the variation of the weight fraction with time (Müller *et al*., 2009).

Parameterization of the weight fractions could be successfully done on most of the data of the CuPC collected in the experiment. For most of the data samples used in the analysis, the reaction rate constants and the activation energies derived from the Avrami's model are

close to those determined from conventional sequential methods (Müller *et al*., 2010b). In many cases, the precision of the refined parameters has improved considerably when the optimal time segment of the data alone is used in the refinement. The overall stability of parameterization depended to a large extent on the speed and completeness of the chemical reaction and also on the physical sensibility of the starting values of the model coefficients.

The second application has illustrated the feasibility of the parameterization of crystallite size with respect to the annealing time/temperature. A 3rd order polynomial has described satisfactorily the evolution the crystallite size with time/temperature of some of the test data samples used in the analysis (the polymorphs of CuPC). For this application, the success of parametric refinement depended strongly on the quality of the data used, on the uniformity of the variation of the crystallite size with time/temperature and also on the correctness of the model that describes the crystallite size variation with time/temperature.

Besides the implementation of sequential/Parametric WPPF software and the demonstrations of the applications of parametric Rietveld refinement, the analytical methods that were developed during the course of the work have shown a high potential of being used in general non-quantitative XRPD applications. The simple and robust method developed to determine the phase transitions points using the Pearson's correlations coefficients has worked effectively on most of the sample data. The application of the developed routine to selected 2D data has revealed that the rate of phase transitions and the nature of phase transitions near the transition boundaries are related directly to the correlations coefficients calculated between the successive powder patterns collected in the experiment (the so called correlations peak). In addition to the Pearson's correlation coefficients, other non-parametric statistical methods (Spearman's rank order coefficient-ρ and the Kendall-τ) were also attempted in the determination of phase transition points. The applications of these methods to several data samples have revealed the superiority of parametric (Pearson's coefficients) method over the non-parametric (ρ and τ) methods in the determination of phase transition points.

An effort has been made to represent the powder patterns as their squared standard scores (or standard-normalization), calculated using the medians of the pattern intensities. The 'phase transition points' routine when applied to the standard-normalized data could work with improved efficiency, as the standard-normalization increases the distinctness of the powder patterns belonging to different phases. Although, many low-intense Bragg reflections of the powder patterns were suppressed after the application of the standard-normalization method, the essential features of the pattern required for its classification has been preserved.

The application of standard-normalization procedure to low quality data has resulted in the sharpening of some hazy/obscure parts of their correlation matrices (Figure 4.11 and 4.12); making the data suitable to be treated with the general classification procedures. This

method when accompanied as a data preprocessing or a normalization procedure with the conventional data clustering algorithms hasn't affected their performances.

The presented work has aided the quicker quantitative evaluation of bulk time-resolved XRPD data collected in dependence of external variables. The quantitative applications of parametric Rietveld refinement that have been illustrated in this thesis are simple when compared to practical uses of parametric Rietveld refinement method. The scope of the work and parametric Rietveld refinement method can be always expanded to other new scientific applications. The accuracy of parameterization of variables could be improved further by incorporating suitable weights to the refinable variables (weighted parametric fit). Improvements in the developed program can be conveniently made by adding in new routines that support parameterization of new variables. Future improvements in the program will include the parameterization of the temperature dependence of the reaction order parameter of structural phase transitions in accordance with the Landau theory (Müller *et al*., 2011).

Zusammenfassung

Der herkömmliche Ansatz XRPD (X-ray Powder Diffraction) Datensätze, die in Abhängigkeit einer externen Variablen gemessen wurden, zu analysieren, ist die sequentielle Anwendung von WPPF (Whole Powder Profile Fit) Methoden auf die individuellen Pulverdiffraktogramme. Die Einführung der parametrischen Rietveldverfeinerung (Stinton and Evans, 2007) eröffnete Möglichkeiten zur gemeinsamen Auswertung von Pulverdiffraktogrammen sowie zur Einführung physikalischer Modelle verfeinerbarer Variablen; auf diese Weise können zusätzliche Informationen über kristalline Materialien direkt aus XRPD Datensätzen erhalten werden. Parametrische Rietveldverfeinerung bietet auch zusätzliche Vorteile im Vergleich mit der sequentiellen Verfeinerung bezüglich der Qualität der verfeinerten Parameter.

Eine Grundvoraussetzung für die quantitative Auswertung von 2D Röntgenpulverdiffraktogrammen, unter Verwendung von sequentiellen und parametrischen WPPF Methoden ist ein Programm, welches die Datensätze bewältigt und dazu beiträgt, Informationen schneller aus den Datensätzen zu gewinnen. Die vorliegende Arbeit befasst sich mit diesem Problem. Das entwickelte Programm beschleunigt die sequentielle und parametrische quantitative Analyse von 2D XRPD Datensätzen deutlich, was zuvor zeitaufwändig und umständlich war.

An zwei Beispielen wurde die parametrische Rietveldverfeinerung mit Hilfe des Programms demonstriert. Im ersten Beispiel wurde die Reaktionskinetik verschiedener Polymorphe von Kupferphthalocyaninpigmenten (CuPC) zusammen mit Additiven parametrisch analysiert. Dabei wurden, durch Verwenden der Johnson-Mehl-Avrami-Kolmogorov-Gleichung als physikalisches Modell für die Phasenanteile in der Verfeinerung (Müller *et al*., 2009), die Reaktionskonstanten und Reaktionsordnungen der Proben direkt aus den Messdaten ermittelt. Die durch die Parametrisierung ermittelten Werte für Reaktionskonstanten und Aktivierungsenergien stimmen gut mit den sequentiell bestimmten überein. Parametrische Rietveldverfeinerungen konnten erfolgreich für die meisten CuPC-Datensätze durchgeführt werden, wobei die Präzision der verfeinerten Parameter, durch die Verwendung des optimalen Zeitsegments für die Parametrisierung, verbessert wurde. Dennoch hängt die Stabilität der Verfeinerung stark von

Geschwindigkeit und Vollständigkeit der Reaktion sowie von der Wahl geeigneter Startwerte ab.

Die zweite Anwendung umfasst die Parametrisierung der Kristallitgröße in Abhängigkeit der Dauer/Temperatur eines Tempervorgangs und zeigt die Möglichkeit dieser. Ein Polynom dritter Ordnung (kubische Funktion) konnte die Entwicklung der Kristallitgröße (~1/FWHM) (Full Width at Half Maximum) der Phasen mit der Zeit für einige der Testbeispiele (CuPC-Polymorphe und nanokristallines TiO_2) am besten beschreiben. In dieser Anwendung hängt der Erfolg der Parametrisierung stark von der Qualität der verwendeten Datensätze und der Entwicklung der Parameter mit der Zeit/Temperatur ab.

Neben der Einführung des sequentiellen und parametrischen WPPF Programms und dessen quantitativen Anwendungen, zeigten die in dieser Arbeit entwickelten Methoden auch großes Potential in der Anwendung auf nicht quantitative XRPD Problemstellungen. Die einfache und robuste Methode, die zur Bestimmung des Phasenumwandlungspunkts mit Hilfe des Pearson- Korrelationskoeffizienten entwickelt wurde, funktionierte für die meisten Datensätze. Ihre Anwendung auf verschiedene 2D Datensätze zeigt, dass die Geschwindigkeit und Art der Phasenumwandlung in der Nähe der Umwandlungsgrenzen direkt mit dem Korrelationskoeffizienten, der zwischen den einzelnen Pulverdiagrammen berechnet wurde, zusammenhängen. Neben dem Pearsons-Korrelationskoeffizienten wurden auch andere nichtparametrische statistische Methoden (Spearmans Rangkorrelationskoeffizient (ρ) und Kendall (τ)) zur Bestimmung des Phasenumwandlungspunkts getestet. Nach Anwendung der Methoden auf mehrere Beispiele zeigte sich die parametrische (Pearsons-Korrelation) Methode den Spearmans Rangkorrelationskoeffizient (ρ) und Kendall (τ) Methoden in der Bestimmung der Phasenübergangspunkte überlegen.

Zusätzlich wurden die 2D Datensätze als ihre „squared 'median' standard scores“ dargestellt. Dieses Verfahren ist für qualitative Anwendungen bestimmt und hat die Effektivität der Routine zur Bestimmung des Phasenumwandlungspunkts deutlich erhöht, da es die Trennbarkeit der Daten, die zu unterschiedlichen Phasen gehören, erhöht. Obwohl viele wenig intensive Braggreflexe nach Anwendung unterdrückt wurden, werden verlässliche Ergebnisse erzielt, da die für die Darstellung nötigen Anteile des Datensatzes, erhalten werden. Die Anwendung der standard-normalization Methode auf Datensätze niedriger Qualität resultierte in einer Schärfung einiger unklarer Bereiche ihrer Korrelationsmatrizen (Abbildungen 4.11 und 4.12), wodurch es möglich wird auf die Datensätze weitere Klassifizierungsmethoden anzuwenden. Die Standard-normalization Methode hat keinen Einfluss auf die konventionellen Datenclustering-Algorithmen, wenn sie vor Verarbeitung oder Normalisierung der Daten genutzt wird.

Die vorliegende Arbeit hat zur schnelleren Auswertung zeitaufgelöster XRPD Datensätzen in Abhängigkeit externer Variablen beigetragen. Die in dieser Arbeit gezeigten

quantitativen Anwendungen der parametrischen Rietveldverfeinerung sind grundlegend. Die Anwendungsbereiche des entwickelten Programms und der parametrischen Rietveldverfeinerung können auf andere wissenschaftliche Problemstellungen ausgeweitet werden. Die Genauigkeit der Parametrisierung der Variablen kann durch Einführung geeigneter Gewichtungen für die verfeinerbaren Variablen weiter verbessert werden. Durch Hinzufügen neuer Routinen, die die Parametrisierung weiterer Variablen ermöglichen, kann das entwickelte Programm ausgebaut werden. Eine zukünftige Erweiterung des Programms wird die Parametrisierung der Temperaturabhängigkeit des Ordnungsparameters nach der Landau-Theorie in strukturellen Phasenübergängen sein (Müller *et al.*, 2011).

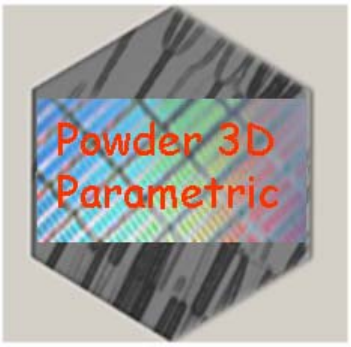

'Powder 3D Parametric' Users manual

The ‘users manual’ section is divided into three parts. The first part **(Part I)** provides the stepwise instructions for starting up the program, the tutorials related to the phase transition points determination (chapters 4 and 5), the general procedures for performing sequential and parametric refinements (WPPF) and a practical demonstration of the application module ‘Reaction kinetics’.

The second part **(Part II)** of the manual describes the functionalities of some important gadgets and graphical user interface (GUI) tools of the program. The third part **(Part III)** of the manual describes recent routines that have been included in the main program.

Some conventions used in this manual

The words typed in bold letters (e.g., **‘Powder 3D Parametric Graphics**’ GUI, ‘**File**’ menu ‘**Load**’ button etc.) represent widget tools used in the GUIs of the program. The words typed in italics (e.g., **‘***iters*’, ‘*ctrl*’, ‘*convolution_step*’, ‘*scale’*) represent the keywords associated with Topas macro language.

Part I

Tutorials

T1. Starting up instructions

1 Unpack the file 'Powder3DParametric.zip' and extract the contents to a separate folder.

2 To execute the program, double click the icon 'IDL Virtual Machine 6.4'  . Click on 'Click to continue' and select the file 'Powder 3D Parametric.sav'. The '**Powder 3D Parametric Graphics**' interface (Figure T.1) of the program will popup. (More explanations of this interface are given in section F2.1 and in Figures F.1 to F.4).

T2. Loading files

T2.1. Select files (Step 1)

1 In the '**Powder 3D Parametric Graphics'** interface, click on the '**File**' menu (Figure T.1), select the '**Import**' option and click on the corresponding experimental file format. The program supports the following data file formats:

*.chi: 2θ vs I list (angle versus intensity with some description of data location and detector type)

*.xy: 2θ vs I list

*.xye: 'DASH' files (David *et al.*, 2006)

*.gda: 'GSAS' files (Larson and Von Dreele, 1994)

*.dat: 'Fullprof' files (Rodriguez-Carvajal, 1990)

*.uxd: Files generated by some Bruker machines (Bruker-Axs, 1960)

*.cpi: Files generated by Sietronics machines (Sietronics, 1978)

2 The multiple data files to be refined can be selected and loaded (Figure T.1)

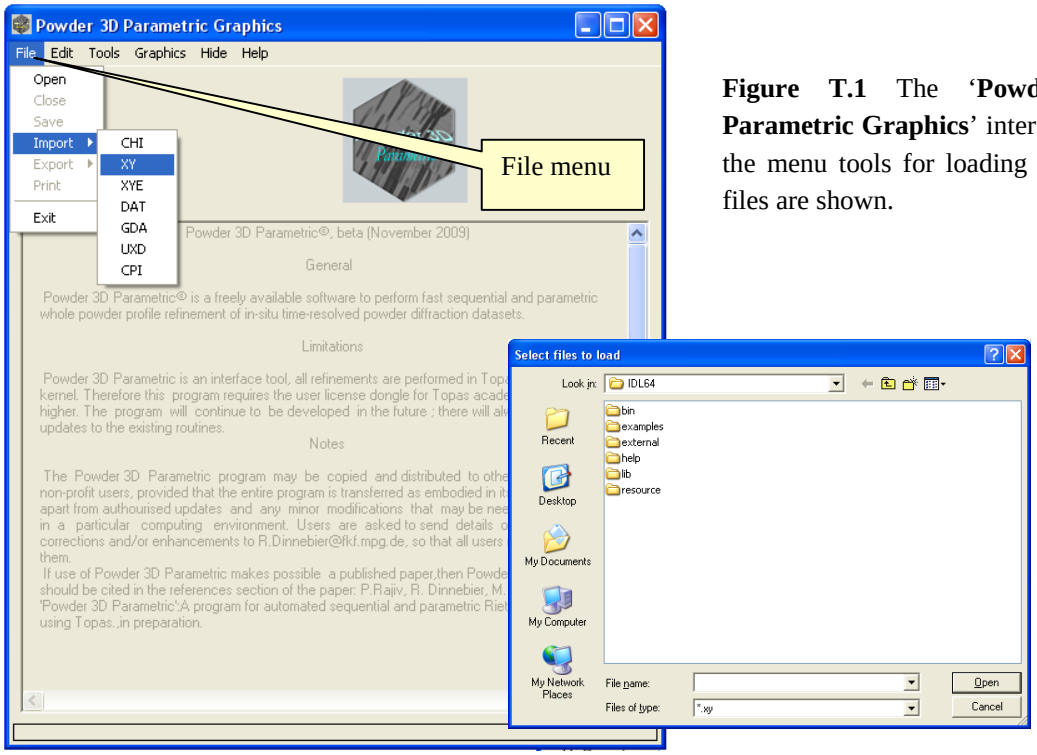

Figure T.1 The '**Powder 3D Parametric Graphics**' interface and the menu tools for loading the data files are shown.

T2.2. View loaded files (Step 2)

1 After loading the data, some information about the number of files, their location etc., will be displayed in the '**Database information**' GUI (Figure T.2 inner picture). Click '**OK**' to proceed further.

2 The 2θ vs I plot of the first file (in the 2D dataset) will appear on the '**Graphics**' tab of the '**Powder 3D Parametric Graphics**' interface (plotted in Figure T.2).

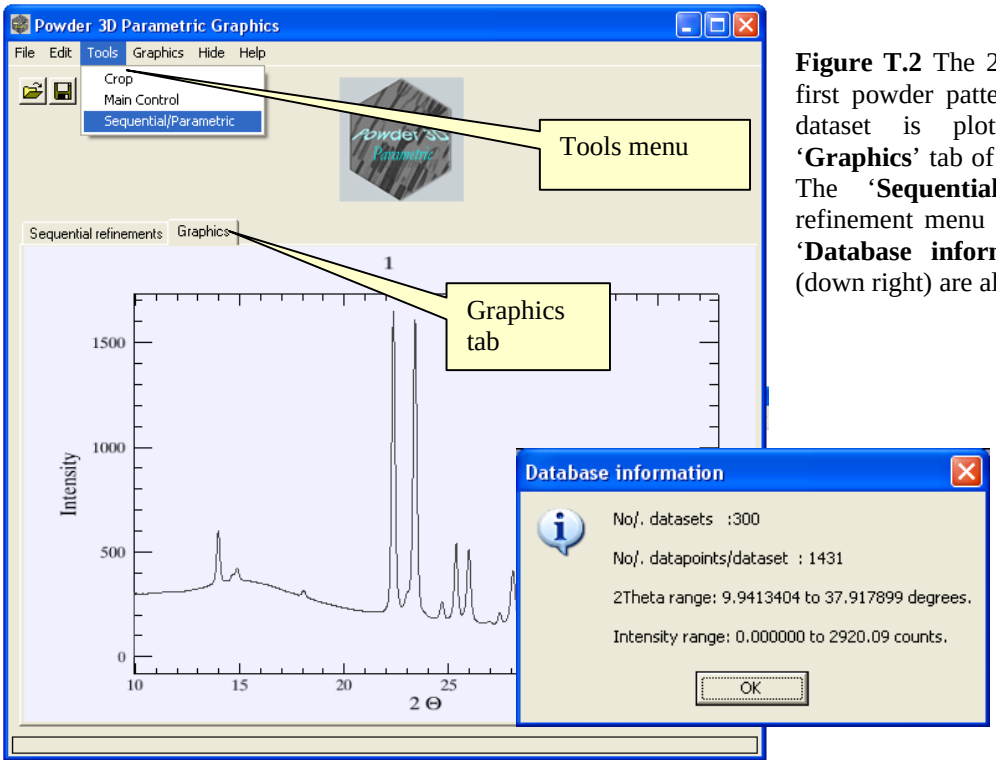

Figure T.2 The 2θ vs I of the first powder pattern in the 2D dataset is plotted in the '**Graphics**' tab of the interface. The '**Sequential/Parametric'** refinement menu (top left) and '**Database information**' GUI (down right) are also shown.

3 Now, click on the '**Tools**' menu (Figure T.2) and select the option '**Sequential/Parametric**'. A new interface with the title '**Basic information**' will appear (see Figure T.3).

T2.3. Basic experimental information (Step 3)

1 In the '**Basic information**' window (Figure T.3), use the drop-down menu '**External variable**' to choose the external variable (e.g., Temperature) on which the experiment has been performed**.** (The default abscissa name for plotting the graphics is '**Pattern No**').

2 Enter the range of external variable in the text boxes '**External variable Range**', e.g., Temperature **From** 300 K **To** 800 K. (Make sure that the units are correct).

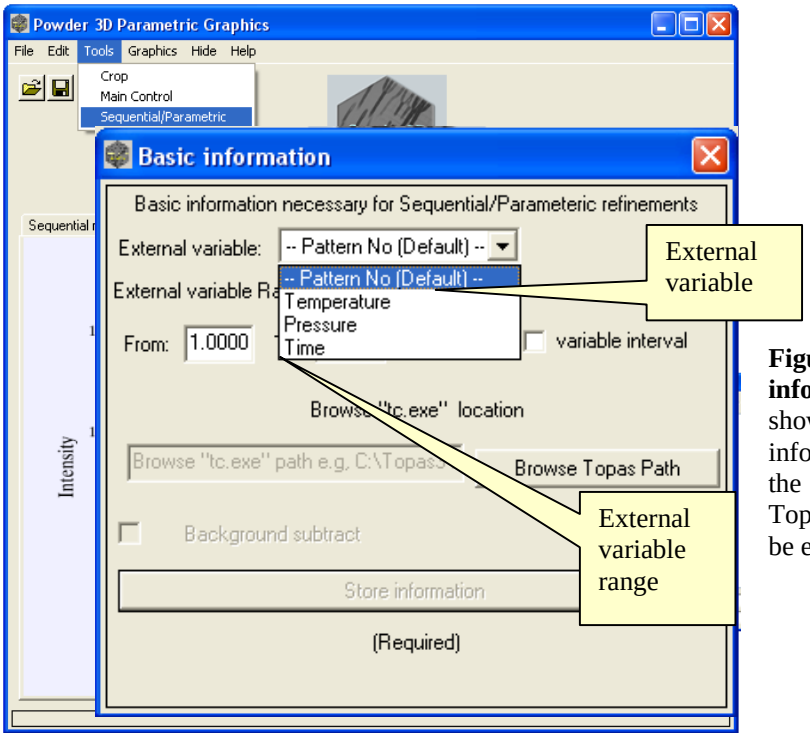

Figure T.3 'Basic information' window is shown. The experimental information (external variable, the measurement range and Topas executable path), must be entered here.

3 If the measurements are made at variable (uneven) intervals (as in case of some high pressure experiments) then select '**variable interval**' checkbox, to expand the '**Basic information**' window (Figure T.4).

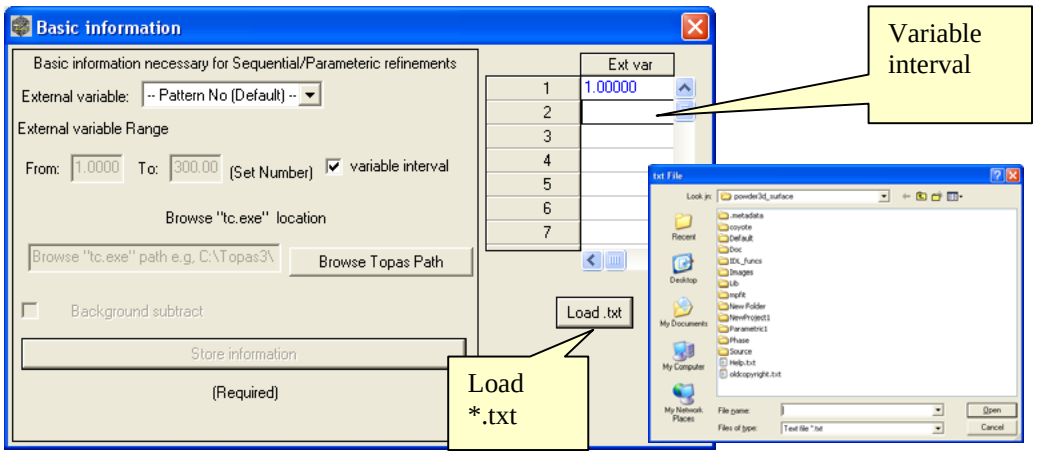

Figure T.4 Variable interval 'extension' interface.

4 The variable measurement intervals can either be entered manually in a table provided (‘**Ext var**’ in Figure T.4) or can be loaded from an ASCII file (‘*.txt’) by clicking the button ‘**Load. txt**’ (Figure T.4). (The external variables must be entered as a list in succeeding lines in the prepared *.txt file)

T2.4. Topas (tc.exe) path (Step 4)

1 After entering the external variable information, browse the location of the file ‘tc.exe’ by prompting the ‘**Browse Topas Path**’ button (Figure T.5). Locate the file ‘tc.exe’ (Topas launch mode executable) and click ‘**Open**’ in ‘**Topas .exe Location**’ window. By default the ‘tc.exe’ file will be located in the Topas working directory (e.g., D:\Topas4-1 or C:\ Topas3).

2 Important: It is obligatory to give the correct path of the ‘tc.exe’ file for performing sequential and parametric refinements.

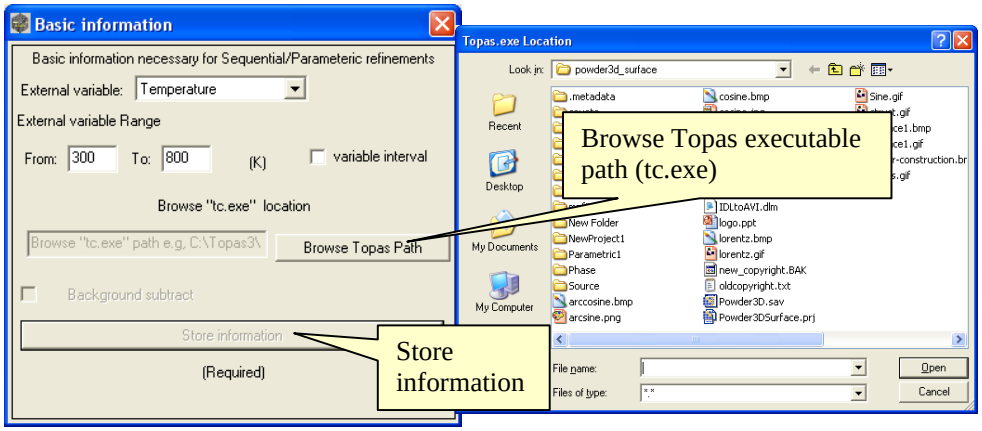

Figure T.5 Topas executable (tc.exe) path.

3 After locating the ‘tc.exe’ file, make sure that all the information is correctly entered and then click on the ‘**Store information**’ button (Figure T.5) to save them. The saved information can be modified at anytime in the ‘**Edit’** menu of the ‘**Powder 3D Parametric Graphics**’ interface. **Edit**>**WPPF Options**> **External variables / Topas path** (section F2.3).

4 Prompting the '**Store information**' button opens the '**Topas input file builder**' interface (Figure T.6, right). This GUI contains several tabs where the Topas keywords necessary to build an input file (*'*.inp'* file) can be loaded.

T2.5. Topas input file builder (Step 5)

1 After '**Topas input file builder**' interface (Figure T.6, right) pops up, depending upon the nature of phase transitions (isothermal or non-isothermal), the user must check either the '**No transition points (Whole range)**' button or click one of the '**Transition points**' buttons (Figure T.6).

2 One of these options must be selected at this point in order to proceed with the sequential and/or parametric refinements. (Read the detailed explanation in sections T3 and T4 before using one of the options Case 1 or Case 2 in this section).

3 **Case 1:** The datasets used in the chapters 4 and 5, are measured under non-isothermal conditions. Here the phase transitions are sharp, clear, visible and quicker with respect to the time axis. In such experiments (see Figures 5.1 to 5.4 in chapter 5) the structural phases and the overlapped parts (or the coexisting phases) are more often treated or refined (WPPF) independently[1]. Therefore the '**Transition points**' routines[2] must be used for separating the powder patterns that belongs to phases from the overlapped regions. (In simple terms: Use this option if the user wants the phases to be treated and refined independently).

4 **Case 2:** In cases of isothermal measurements explained in chapter 6 and other quantitative phase studies, (where there are no 'visible' phase transitions or the phase transitions are continuous and there are symmetrical relationships between the decayed parent phase and newly formed phase) the '**No transition points (Whole range)**' (Figure T.6) option must be selected. (See Figures 6.1 in chapter 6). (In simple terms: Use this option if the user wants to refine all the loaded patterns sequentially).

[1] During the WPPF analysis the overlapped parts of the dataset can either be refined or ignored, depending upon the property of the material studied
[2] This routine has been explained in chapters 4 and 5; will be also demonstrated in section T 3.

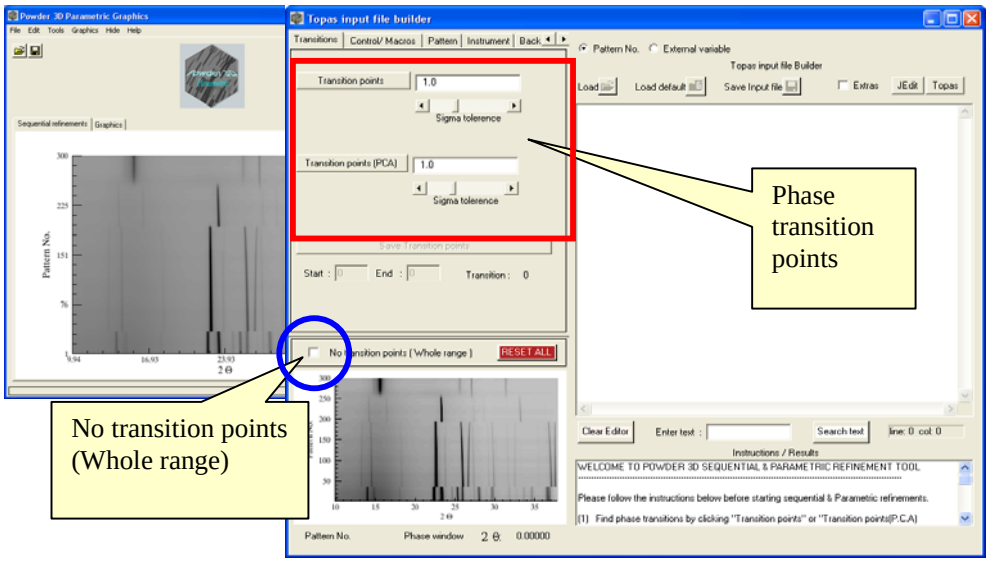

Figure T.6 The '**Topas input file builder'** (right) pops up after storing the experimental information. '**Transition points**' (red framed) and '**No transition points (Whole range)**' (circled in blue) checkbox are highlighted. Depending upon the nature and number of phase transitions, the user must prompt one of the buttons before proceeding with the sequential/parametric refinements.

T3. Phase transition points (Case 1)

T3.1. Determination

1 The phase transition points can be determined using the 'sequential correlations vector' (chapter 4) by clicking the '**Transition points**' button (Figure T.7).

2 The transition points determined by the program will be shown as lines (colored blue) in the '**Sequential refinements**' tab of the '**Powder 3D Parametric Graphics**' interface (Figure T.7). These lines can be moved manually to correct the inaccuracies (if any) in the positions of the transition points determined from the program.

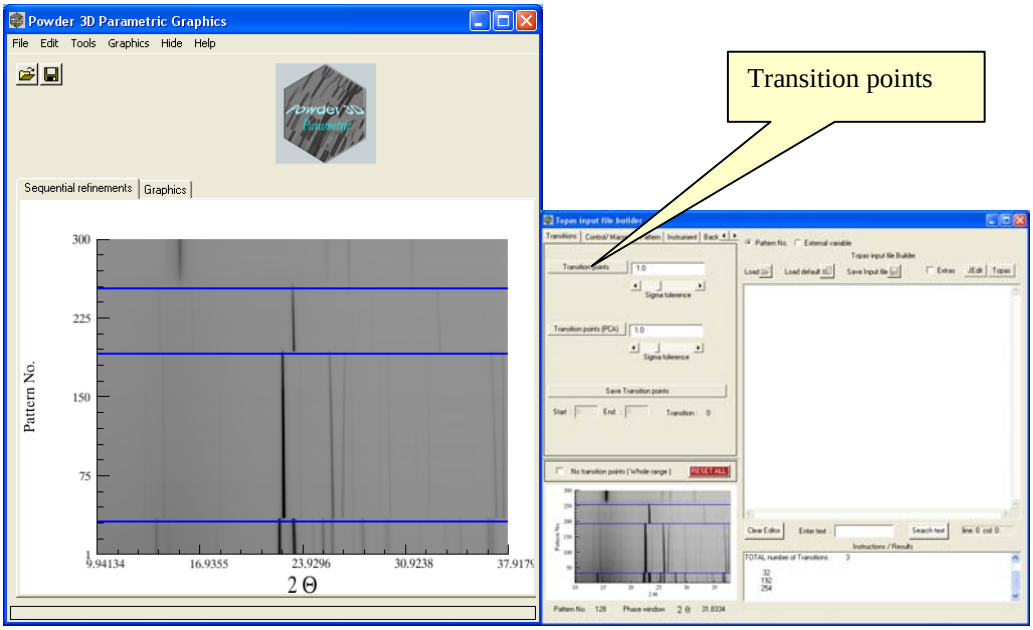

Figure T.7 The phase transition points are determined by clicking one of the '**Transition points**' button. The phase transition points (in this case transition temperature) found are shown as lines (colored blue) in the **Powder 3D Parametric Graphics** window.

T3.2. Error in Phase transition points determination

If the program fails to determine the correct number of phase transitions, one of the following three actions can be performed.

1 The threshold of the 'sequential correlations vector' can be changed by prompting the '**Sigma tolerance**' slider in the '**Topas input file builder**' GUI (Figure T.8).

2 Principal Component Analysis (PCA) button (**Transition points (PCA)**) can be used to determine the phase transition points. The Eigen values[3] of the powder patterns intensities determined from the PCA are plotted in Figure T.9; these values will be used to cluster the patterns.

[3] Eigen values of one of the dimensions are plotted in Figure T.9.

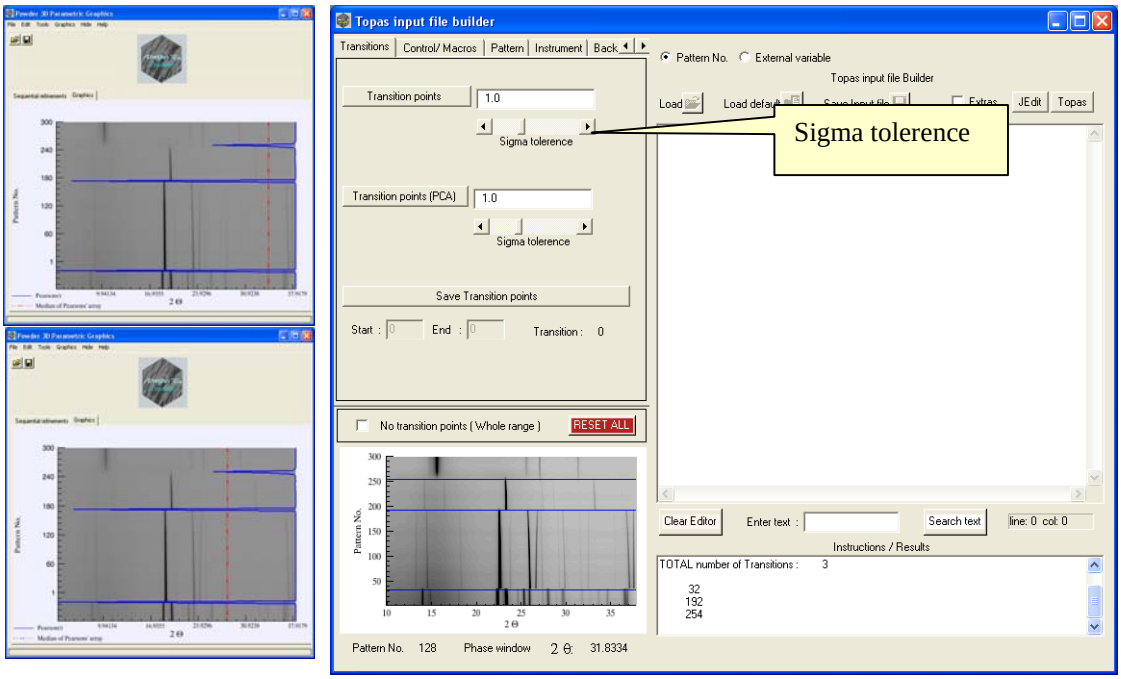

Figure T.8 The phase transition points for two different thresholds (the red dotted vertical lines in the two small figures at left) of the sequential correlations vector are shown.

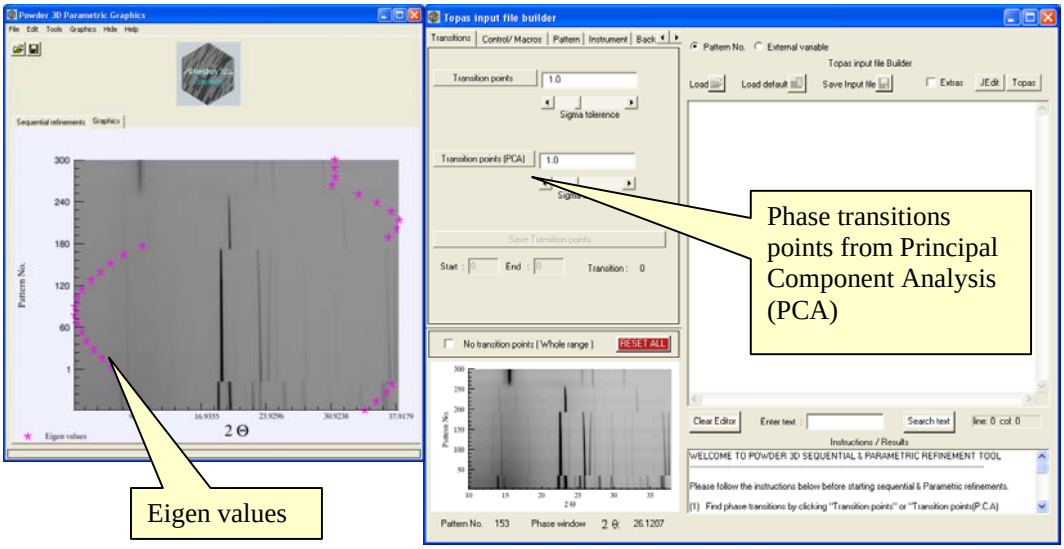

Figure T.9 The graphics related to the determination of phase transition points using Principal Component Analysis are shown. One of the sets of Eigen values of the patterns are plotted in the '**Powder 3D Parametric Graphics'** interface.

3 Manually add/remove the phase transition points by right clicking in the '**Powder 3D Parametric Graphics'** interface (Figure T.10).

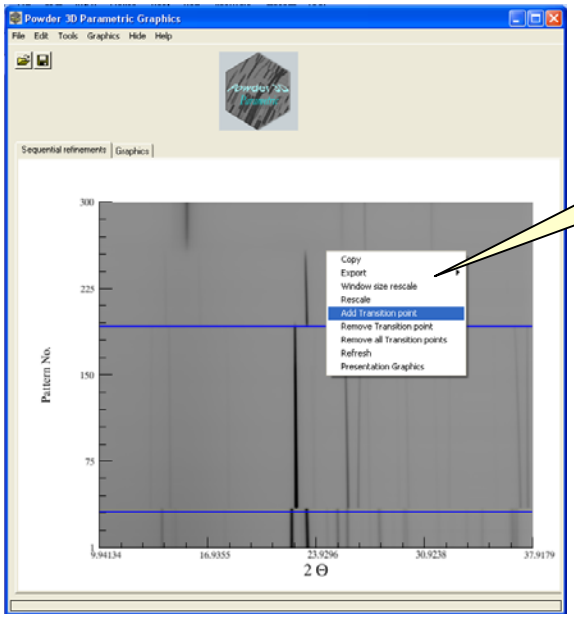

Figure T.10 Manual addition or removal of the phase transition points.

T3.3. Saving phase transitions

1 After confirming the number of phase transition, they must be saved by clicking on the '**Save Transition points**' button. (If an incorrect number of phases has been saved by mistake, the user can go back to the previous step by clicking the '**RESET ALL**' button!)

2 The event of saving the transition points causes two changes in the GUIs. First the blue colored lines in '**Powder 3D Parametric Graphics**' interface (Figure T.7 to Figure T.9) are converted into yellow 'hatches'. They can be used to mask the overlapped phases (Figure T.11). The width of these hatches can be manually modified to redefine the overlapped (multiple) phases.

3 Depending upon the nature of the transition and need of the user, the (hatched) overlapped parts can be refined separately or can be ignored.

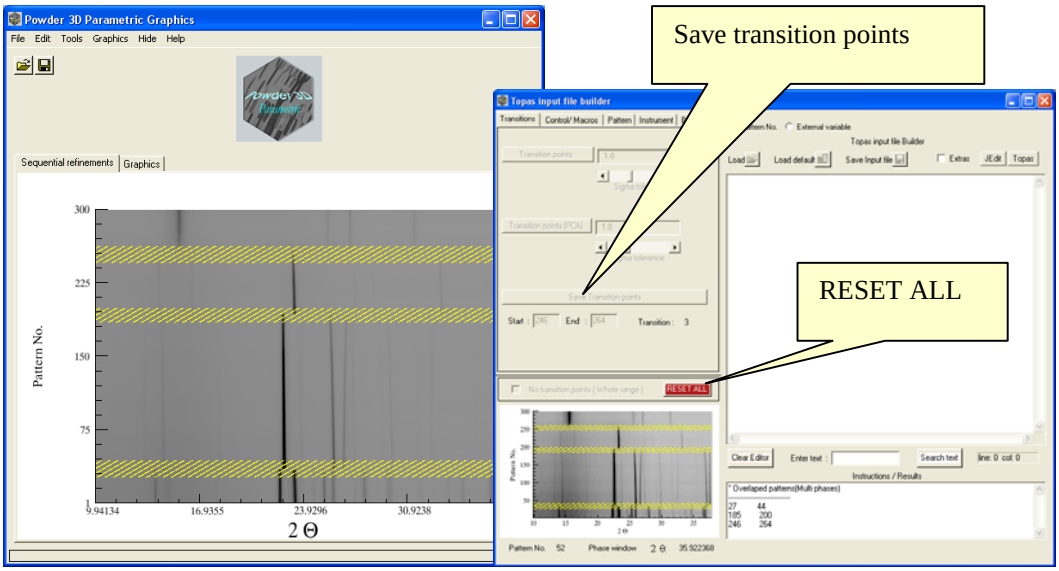

Figure T.11 Saving the phase transition points.

4 The zoom window of the '**Topas input file builder'** shown in Figure T.12 can be used to fine-tune the widths of the overlapped phases.

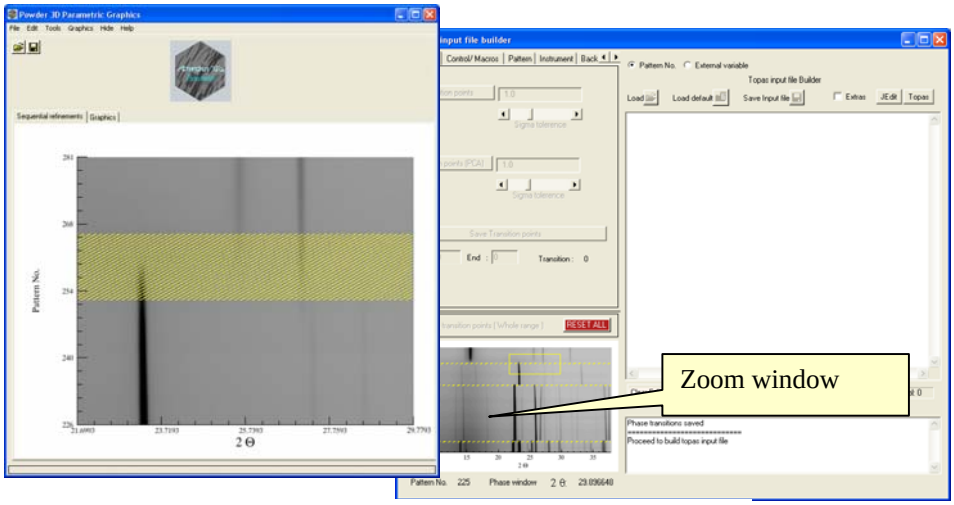

Figure T.12 Zooming the overlapped region.

5 The second event that occurs after saving the transition points is the increase of the number of tab windows in the '**Topas input file builder**' GUI from 'm' to 'm+n+1'.

where, 'm' = 5 (number of original tabs, **Control/Macro, Background, etc.**)

'n' = the number of phase transitions + number of overlapped parts. (See for example Figure T.13. In this case there are 3 phases + 1 decomposition + 3 overlapped, totally 7)
'1' is an extra tab created in which the sequential refinements can be started (Figure T.18).

6 The 'phase' part (**.phs* file in chapter 3) of the Topas input files for all the identified phases and overlapped regions (if necessary) can be independently prepared in these ('n') tabs (see Figure F.14).

7 The default names of these tabs are **Range1**, **Range2**,..etc and **Overlapped1**, **Overlapped2**.., etc. The names of these phases and overlapped regions can be modified in **Edit>WPPF Options>Range names** (section F2.3).

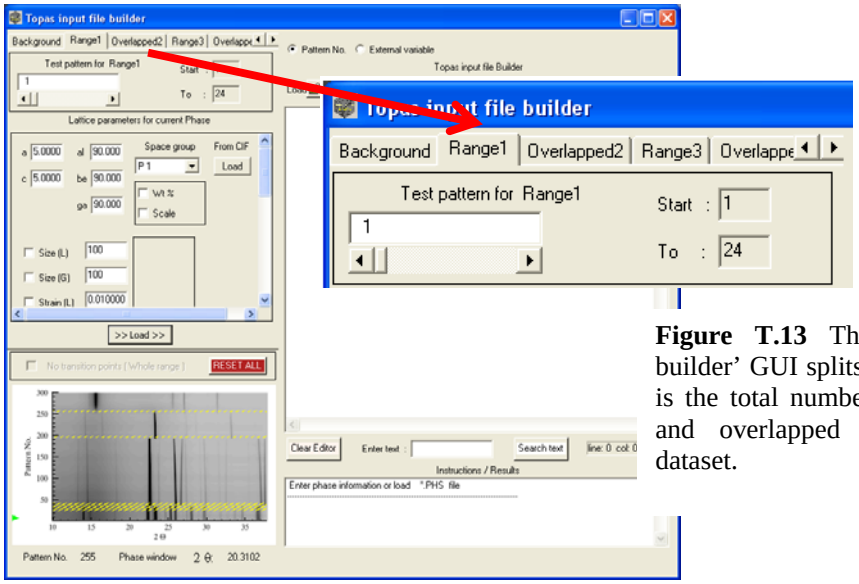

Figure T.13 The 'Topas input file builder' GUI splits to 'n' tabs, where 'n' is the total number of phase transitions and overlapped regions in the 2D dataset.

T4. No transition points (Case2)

1 The **'No Transition points (whole range)**' option simply assumes that the 2D dataset doesn't contain any transition, a single phase mixture or isothermal transition (as explained in chapter 6).

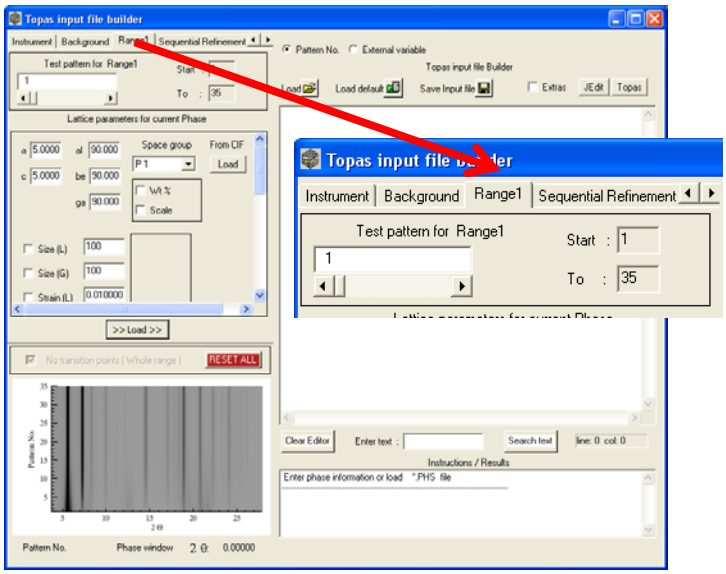

Figure T.14 A new phase tab with the default name '**Range1**' is created in the '**Topas input file builder**' after the choosing the '**No Transition points (whole range)**' option.

2 Selecting '**No Transition points (whole range)**' (Figure T.6) option automatically saves the number of phases and creates one new 'phase tab' in the '**Topas input file builder**' with the default name '**Range1**' (Figure T.14).

3 In this tab the 'phase' part (**.phs* file in chapter 3) of the Topas input files for the identified phase '**Range1**' can be independently built.

T5. A simple sequential refinement

In this section, the procedure for performing sequential WPPD (LeBail fit) of the high temperature α-Ag_3VO_4 (Dinnebier *et al.*, 2007) using the program is explained.

T5.1. Using the 'Topas input file builder'

1 The powder patterns to be refined must be first loaded and the basic experimental information must be entered as explained in sections T2.1 to T2.4.

2 The specimen used in the current illustration has been measured under non-isothermal conditions. Therefore the phase transition points must be determined (as instructed in 'Case 1' in section T3.1) and they must be saved (section T3.3).

3 The next step is to prepare one input file for doing a test 'LeBail' fit. The Topas keywords that make up the required test input file can be loaded using various widget gadgets provided at various tabs of the '**Topas input file builder'**.

4 In Figure T.15, one of the tabs (the '**Control/Macro**' tab) of '**Topas input file builder'** is shown. The parameters associated with the '**Control/Macro**' tab (e.g. *'iter'*, *'convolution_step'*, *'r_wp'*, etc.) can be loaded to the plain text editor by prompting the corresponding gadgets.

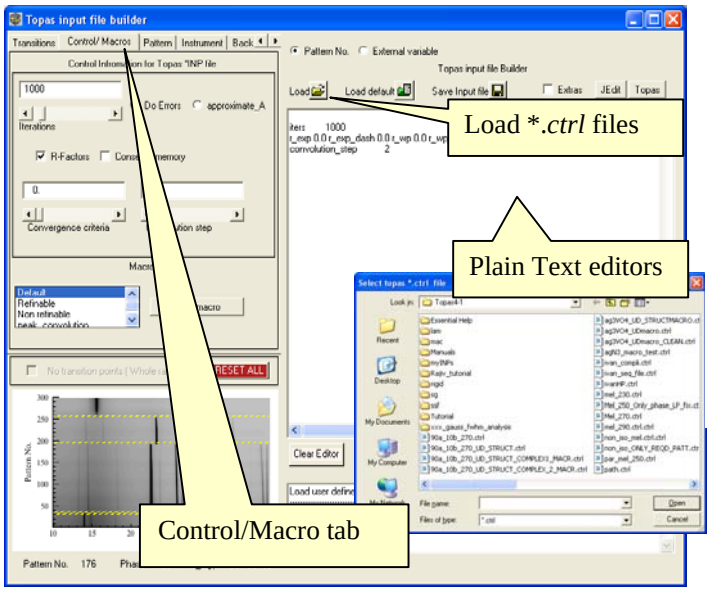

Figure T.15 Control/Macro tab is highlighted. The control parameters e.g. '*iter*', '*convolution_step*', '*r_wp*' etc can be loaded to the text editor. The inner picture is the GUI to '**Load**' the prepared '**.ctrl*' file.

5 In a similar way the Topas keywords associated with the powder pattern (e.g., '*start_X*', '*finish_X*' etc.) and the keywords related to a structural phase (e.g., '*al*', '*weight_percent*') can be loaded from the **Pattern** and Phase tabs of '**Topas input file builder'** respectively (Figure T.16).

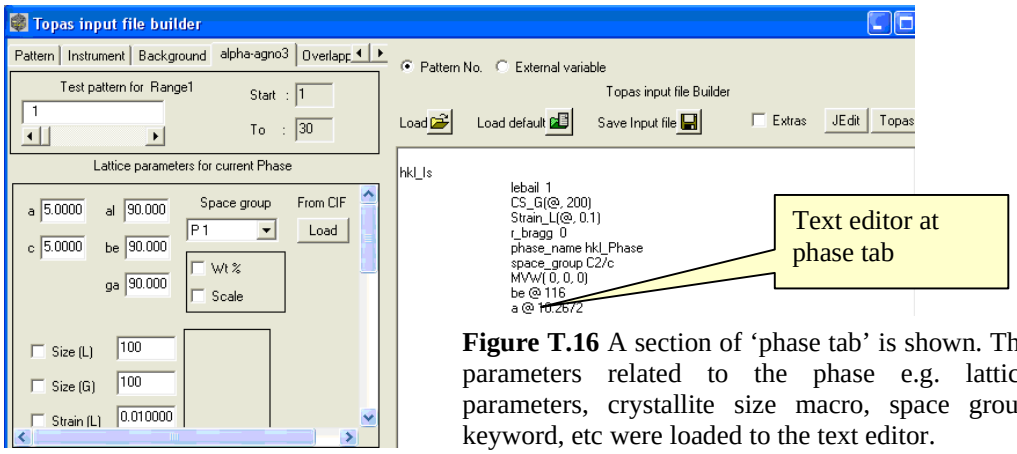

Figure T.16 A section of 'phase tab' is shown. The parameters related to the phase e.g. lattice parameters, crystallite size macro, space group keyword, etc were loaded to the text editor.

6 These keywords (associated with **Control/Macro**, **Pattern** tabs etc.) can also be placed into the text editor by loading an ASCII file (with extensions '**.ctrl*' '**.patt*' or '**.phs*' etc.) containing the set of required keywords (Figure T.15). This file has to be manually prepared beforehand by the user and must be loaded to the text editor by using '**Load**' button (Figure T.15).

7 Alternatively, all the required keywords can also be typed manually by the user in the text editor!

T5.2. What if the input file required for the test refinement is already available?

If the input file required to refine a dataset has already been prepared by the user (or the user doesn't want to use the widget tools provided by the program), then the 'phase' part of the file must be copied to the editor of the corresponding 'phase' tab (Figure T.16). All the other 'common' keywords (e.g., *start_X* or *LP_factor*) must be placed to the text editor in one of the other tabs. The 'phase' part of the file starts from the keyword '*str*' or the macro '*STR*' or '*hkl_Is*' to the *end of file*.

```
xdd D:\RAJIV\Guinier_data\Topas\READABLE\Ag3VO4\0001.xy
r_wp 2.441967259 r_wp_dash 3.453943704

iters 1000
        bkg @ 0 0 0 0 0 0 0 0 0 0 0 0
        Zero_Error(@, 0)
        LP_Factor( 90)
        convolution_step 2
        Rp 100
        Rs 100
        lam
                ymin_on_ymax  0.0001
                la  1 lo  1.12058 lh  0.00001
        x_calculation_step 0.02

        hkl_Is
                lebail  1
                CS_G(@, 200)
                Strain_L(@, 0.1)
                r_bragg  0
                phase_name hkl_Phase
                space_group C2/c
                MVW( 0, 0, 0)
                be @ 116
                a @ 10.2672
                b @ 4.9814
                c @ 10.224
```

Figure T.17 The input file used in section 5.2 is shown. The 'common' part of the input file is typed in red. The 'phase' part of the file is typed in blue.

The input file used in section T5.1 is shown in Figure T.17. The common part of the input file (typed red in Figure T.17) can be placed to a text editor in any one of the tabs in '**Topas input file builder'** (e.g., '**Pattern**', '**Instrument**', '**Background**', '**Control/Macro**' etc, Figure T.15). The phase part of the file (typed blue in Figure T.17) must be entered necessarily in the 'phase' tab (in Figure T.16).

1 After loading all the Topas keywords that make up the required input file, the user must goto the '**Sequential Refinement**' tab (the last tab window in the '**Topas input file builder'** (Figure T.18)). The names of all the detected phases and overlapped parts will be listed (Figure T.18, framed in green) in this tab.

2 The final Topas '*inp*' file will be loaded in the text editor in the '**Sequential Refinement**' tab after selecting the name of the phase to be refined (see Figure

T.18, framed in green). The loaded input file cannot be edited in this tab (Figure T.18); the keywords can be edited only in their text editors in their respective editors in the common tabs and can be reloaded in the '**Sequential Refinement**' tab.

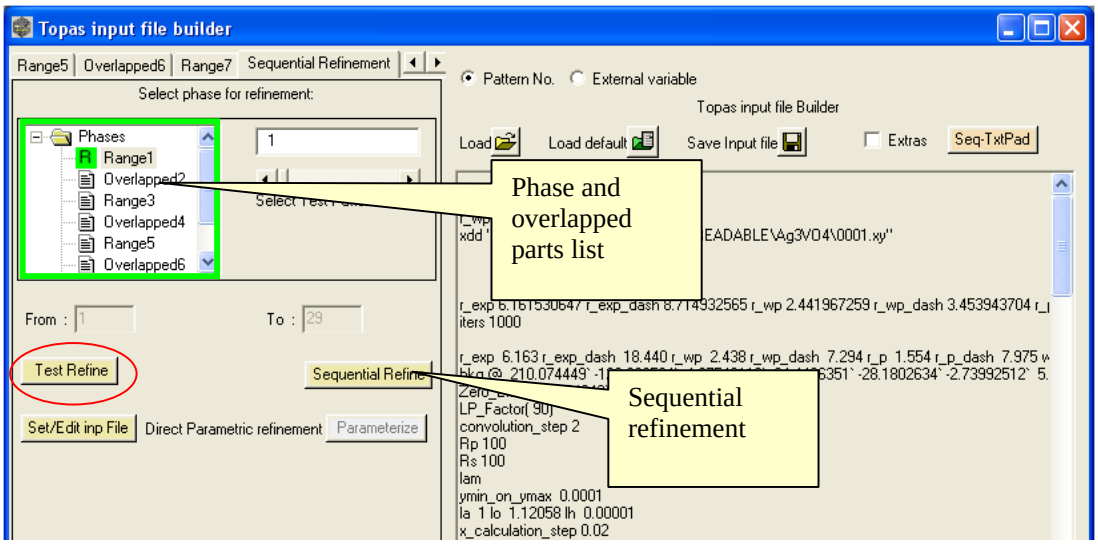

Figure T.18 '**Sequential Refinement**' tab is shown. The list of phases and overlapped parts of Ag_3VO_4 with their default names are highlighted in green frame. The '**Test refine**' button (section T5.3) is circled in red.

T5.3. Test refinement

Before following the instructions in this section (from step 1) please first read step 6.

1 The phase to be refined must first be selected by the user from the list (in this example the user must select the phase '**alpha-agno3'** see in Figure T.20). This event will load the input file for the selected phase into the editor (cannot be edited). The test refinement can be started by prompting the **'Test Refine'** button (Figure T.20).

2 After performing the test refinement, its results will be displayed in a separate window ('**Refinement Converged alpha-agno3**' in Figure T.19). This GUI will contain the convergence plot, the Topas *.*out* file, the list of refined variables of the selected ('**alpha-agno3')** phase.

3 Based on the convergence of the refinement, the user can decide whether to keep the results of test refinement or to redo the test refinement. (In particular, the user must decide whether the refined parameters can be used as starting values for the consecutive refinements or not).

4 If the user wants to redo the test refinement then he must click on the '**Ignore**' button and go back to common tabs to modify the keywords or parameters (if necessary).

5 If the user is satisfied with the results (the convergence and 'test.*out*' file) of the test refinement, he can proceed with sequential/parametric refinements by clicking on the '**Keep Parameters**' button. The label color of the refined phase will change to green and the letter 'R' will appear denoting that the 'test.*out*' file of test refinement has been saved and the saved file will be used for the sequential refinements (Figure T.20 framed red).

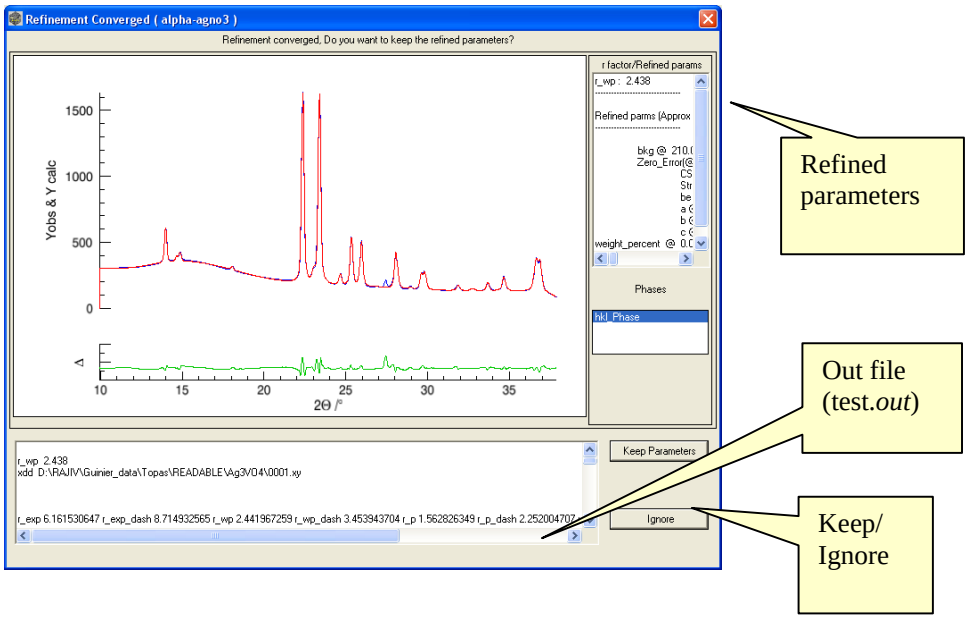

Figure T.19 The result of a test refinement is shown. The refined Topas 'test.*out*' file is loaded at the bottom. The refined parameters are listed in an editor at the right side.

6 Important: The user must be aware of the variables that will be used in parametric refinement and accordingly their refinement flags must be set in the input file used in the test refinement. For example (1) if the user wants to study the reaction kinetics of the specimen then the Topas variable '*scale*' must be set refinable in the test refinement. (2) If the user wants to study the thermal expansion of a compound,

then the corresponding lattice parameters must be set refinable in the test refinement.

7 After the successful test refinement, the sequential refinements can be started by prompting the button '**Sequential Refine**' in Figure T.18. This action will popup another confirmation GUI ('**Please store parameter names...**' in Figure T.20) which lists the names of the sequentially (and parametrically) refinable variables.

8 At this point the user must recheck if all the parameters set refinable in the test refinement have been extracted and displayed correctly in this window (Figure T.20), as the refinement flags of these parameters cannot be altered anymore after this instant. (Optionally, the refinable variables can also be given names. For example the lattice parameter '*c*' can be named as *'chkl_Phase'* with, *'hkl_Phase'* representing the default extension (see Figure T.20). The new names of the parameters will be listed in the text space '**Parameter names**' after confirming the entered names with the '**Generate/Show**' button. These names will be used to tag the refinable variables in parametric refinement (see Figure T.21)).

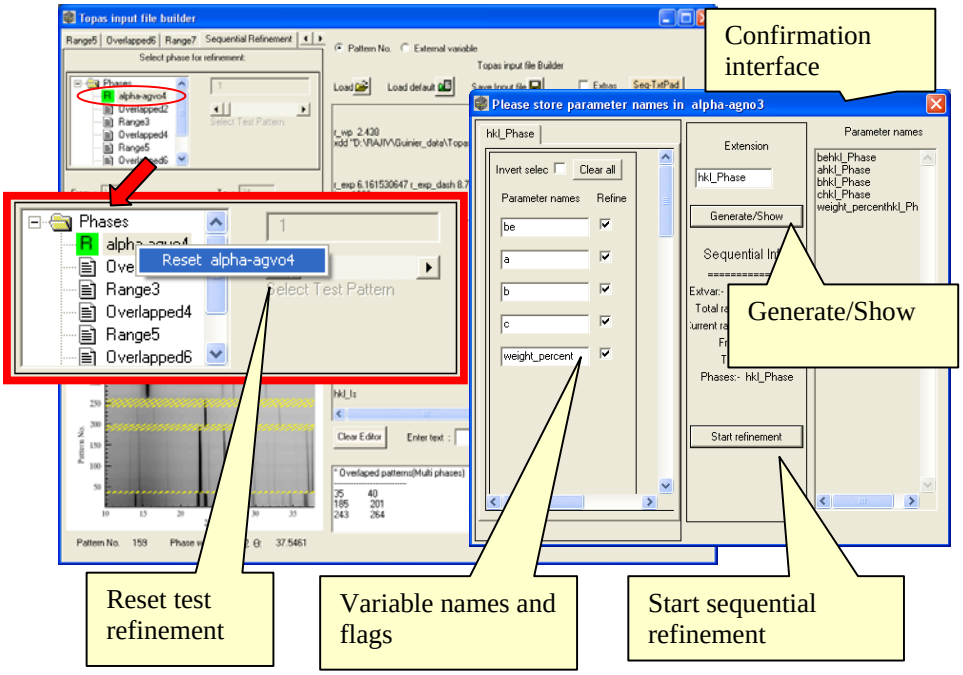

Figure T.20 The sequential refinement tab is highlighted. The 'Confirmation interface' that pops up before starting the sequential refinement is shown in the inner picture (right). The user must confirm the names of the variables and their refinements flags in this interface. To redo a test refinement, the user must right click on the name of the phase to be refined and reset it ('R' and green color disappears after resetting).

9 The modifications of the refinement flags of the variables or the inclusion of a new parameter must be done in various parts of the '**.inp*' file (e.g. the **phase, pattern** tabs etc.).

10 The test refinement of the modified input file can be started only after resetting the phase that is modified. (Figure T.20 indicated by red arrow).

T5.4. Start sequential refinement

1 The sequential refinements can be started by clicking the button '**Start refinement**' (in 'Confirmation interface' GUI in Figure T.20). The program will prepare and execute all the input files needed for the sequential refinements.

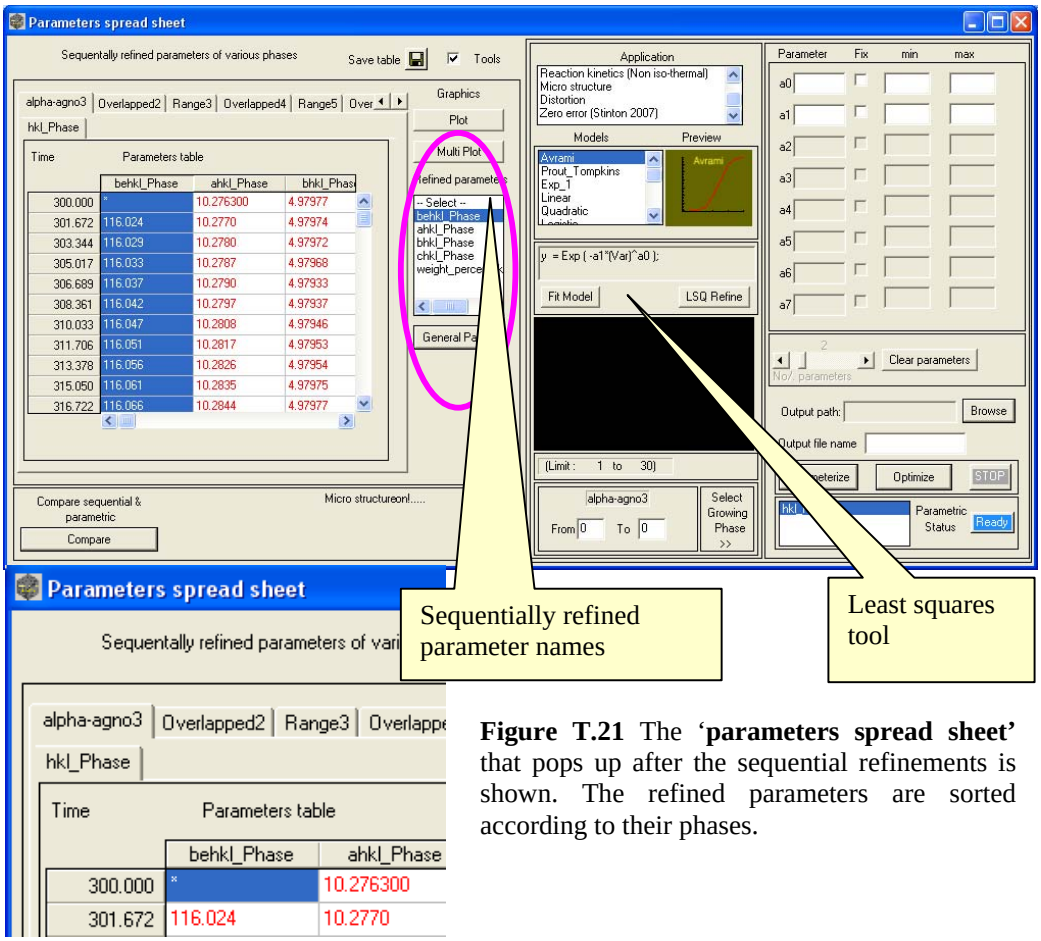

Figure T.21 The '**parameters spread sheet**' that pops up after the sequential refinements is shown. The refined parameters are sorted according to their phases.

2 After the completion of the sequential refinements, a spread sheet (see section F4.4) containing the refined parameters and several options for parametrization will pop up (Figure T.21).

3 The sequentially refined variables are sorted according to their phases (Figure T.21, bottom picture) and listed in this spread sheet. The variation of refined parameters with respect to external variables can be studied, by plotting them simultaneously against the external variable.

4 The 'least squares' tool supplied by the program can also be used to model these variables.

T6. Parametric Refinement

Depending on the requirement of the user, the variables can be parameterized in two ways; 'General parameterization' and 'Application parameterization'. These modes will be explained in the following sections.

T6.1. General Parameterization

In 'General parameterization' mode depends completely on the need of the user. This mode is used to parameterize any variable that is sequentially refined using a model provided by the program or by any user defined equation.

As an example, consider the sequential refinements performed in section T 5.4 (Figure T.21). The sequentially refined lattice parameters of the monoclinic '**alpha-agno3'** phase are listed in Figure T.21 (circled in pink). To parameterize one of the variables, the following steps must be performed.

1 The name of the variable to be parameterized must be selected from the '**Refined parameters**' list (Figure T.22). (For example the lattice parameter '*c*' '*chkl_Phase*' in Figure T.22 can be selected).

2 The '**.out'* file generated in the parametric refinement must be given a valid name and its location must be selected using the '**Browse**' button (circled in pink in Figure T.22). (It is recommended that the '**.out'* file is saved in the Topas working directory).

3 The correct range of patterns used in parametric refinement must be entered in their respective fields. (‘**From’** and ‘**To’** in Figure T.22., circled in blue).

4 An appropriate model of the variable must be selected from the list ‘**Models**’ (Figure T.22., circled brown)

5 The parametric refinement can be started by prompting the ‘**General Param**’ (Figure T.22., circled yellow) button.

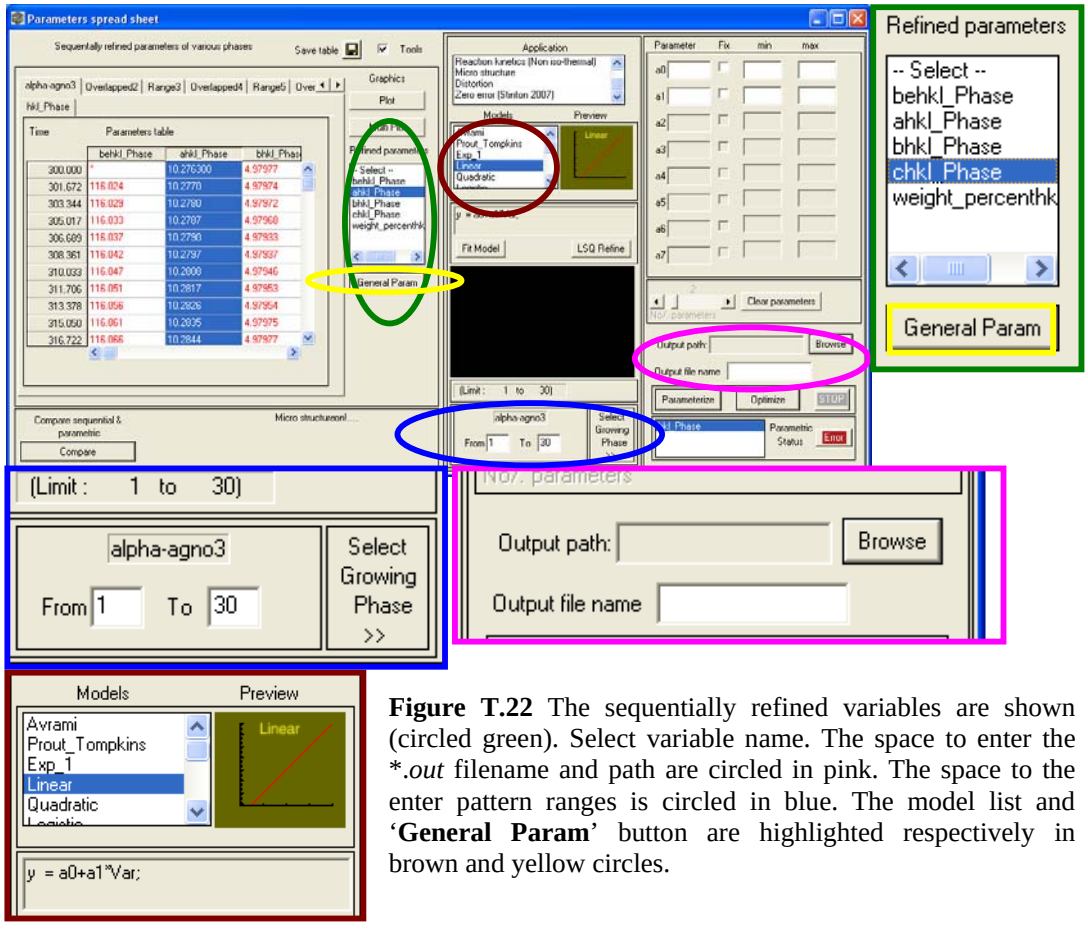

Figure T.22 The sequentially refined variables are shown (circled green). Select variable name. The space to enter the **.out* filename and path are circled in pink. The space to the enter pattern ranges is circled in blue. The model list and ‘**General Param**’ button are highlighted respectively in brown and yellow circles.

6 After clicking ‘**General Param**’ button, a confirmation window containing all relevant information about the refinement will appear (shown in Figure T.23).

7 To proceed with parametric refinement, the ‘**Start refinement**’ (Figure T.23 circled in yellow) option must be prompted. For modifications, ‘**Cancel/Modify**’ (Figure

T.23 circled in red) button must be clicked and the procedure must be started from step 1.

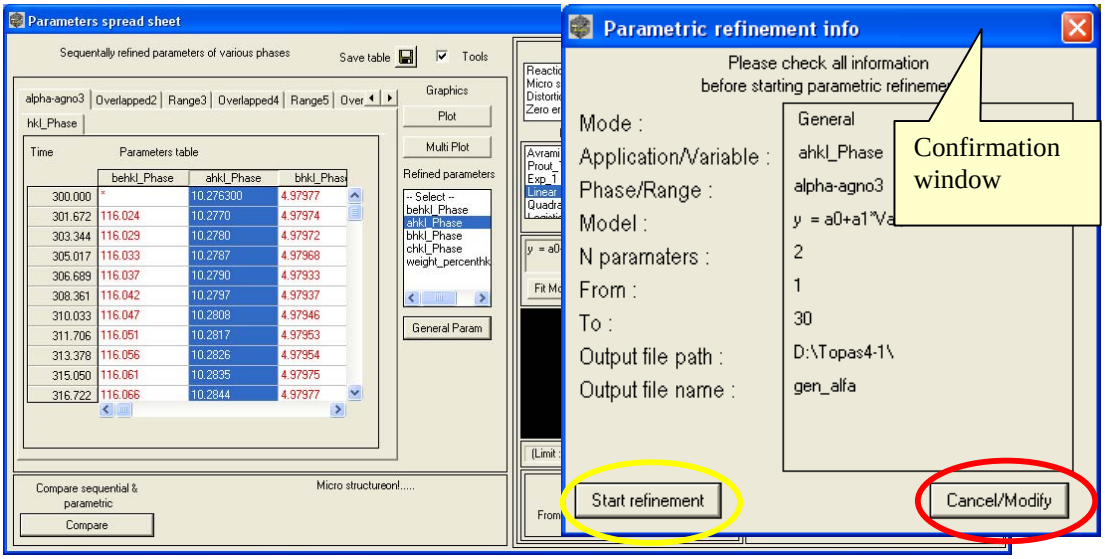

Figure T.23 The confirmation window that appears before proceeding with the parametric refinement is shown. To start parametric refinement click on '**Start refinement**' (circled in yellow). To make any modification click '**Cancel/Modify**' (circled in red) and start from step 1.

- The set of parameters '*c*' obtained in sequential and parametric fit are compared in the '**Sequential refinements**' tab of the '**Powder 3D Parametric Graphics**' interface (Figure T.24). The variable '*c*' is parameterized with a linear function.

- The comparison plot (Figure T.24) can be scaled using the options provided in the '**Plot Options**' GUI.

- The status and the success of the refinement are indicated by colors of '**Parametric Status**' button in Figure T.24 (red circled). This button can be clicked to get the detailed status of the parameterization as in the confirmation window in Figure T.23.

- The weighted residuals (*r_wp*) of the refinements are displayed at the '**Instruction/Results'** text box of the '**Topas input file builder'** (Figure T.25).

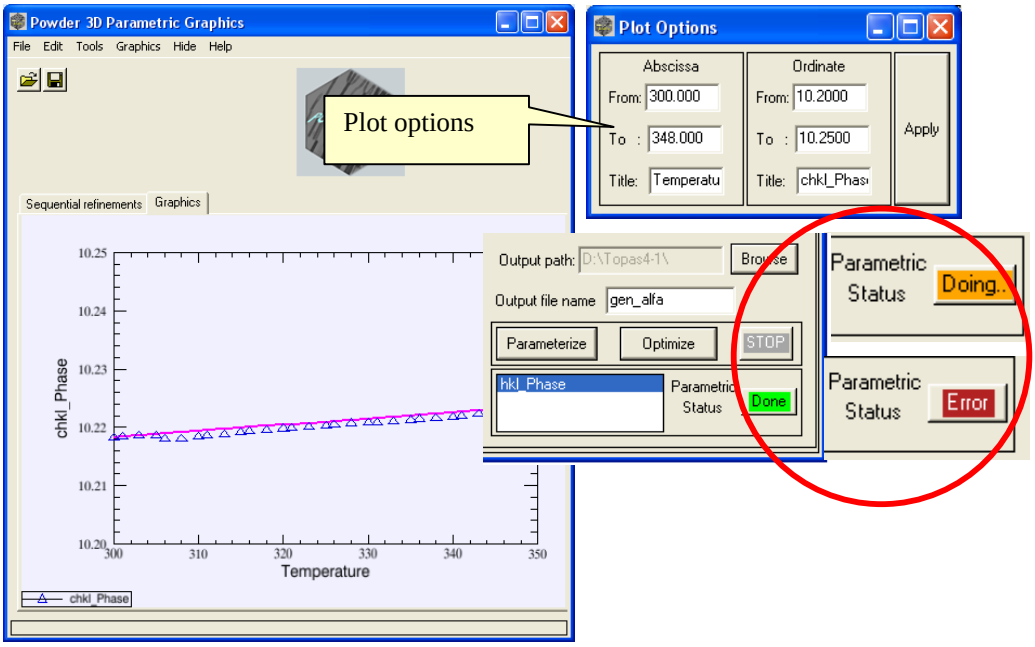

Figure T.24 Comparison of parameter '*c*' obtained in sequential (blue triangle) and parametric (pink line) refinements are shown in '**main graphics window**'. The plots can be scaled using the '**Plot Options**' GUI. The refinement status is indicated by various colors (the red circle).

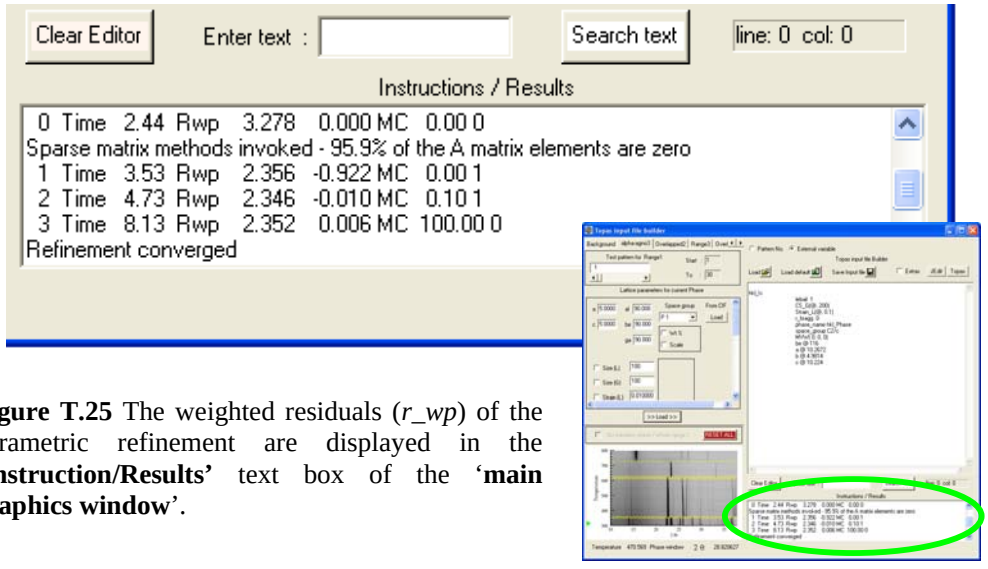

Figure T.25 The weighted residuals (*r_wp*) of the parametric refinement are displayed in the '**Instruction/Results'** text box of the '**main graphics window**'.

T6.2. Application parameterization

The program provides some predefined application modules such as, '**Reaction kinetics**', '**Zero error**' and '**Micro structure**' etc. These modules have unique scientific purposes; some of them are discussed in detail in chapters 6 and 7. The procedure to execute one of these applications (reaction kinetics) is illustrated in this section.

T6.2.1. Reaction kinetics

The goal of the '**Reaction kinetics**' module of the program is to use the parametric Rietveld refinement method to extract the reaction rate constant and reaction order[4] of a specimen from its time dependent XRPD datasets. For the demonstration purpose, the test dataset of one of the mixtures of CUPC (Chapter 6) will be used in this tutorial.
To get the Avrami parameters ('n' and 'k') from parametric Rietveld refinement, the instructions given below must be followed:

T6.2.1.1. Sequential refinements

1 The data files must be loaded first (see the procedures explained in section T2.1 of this manual)

2 The sample dataset used in this illustration are measured isothermally (in dependence on time). Therefore, they belong to 'No transition points case 2' explained in section T4 (also see Figure 6.1(a) in chapter 6). The '**No transition points (Whole range)'** checkbox **in** '**Topas input file builder'** must be selected**.**

3 The set of input instructions to do one test refinement must be placed into the editor in one of the following ways explained in T5.1 or section T5.2. (Depending upon the availability of the input file).

4 The test refinement must be performed as explained in the section T5.3. (For kinetic analysis, the parameters '*scale*' and /or '*weight_percent*' must be refined in the test refinement).

[4] The Avrami parameters 'n' and 'k' (see explanations in chapter 6)

5 The sequential refinements can be started as explained in the section T5.4. The '**Parameters spread sheet**' obtained after sequential refinements of the sample dataset is shown in Figure T.26.

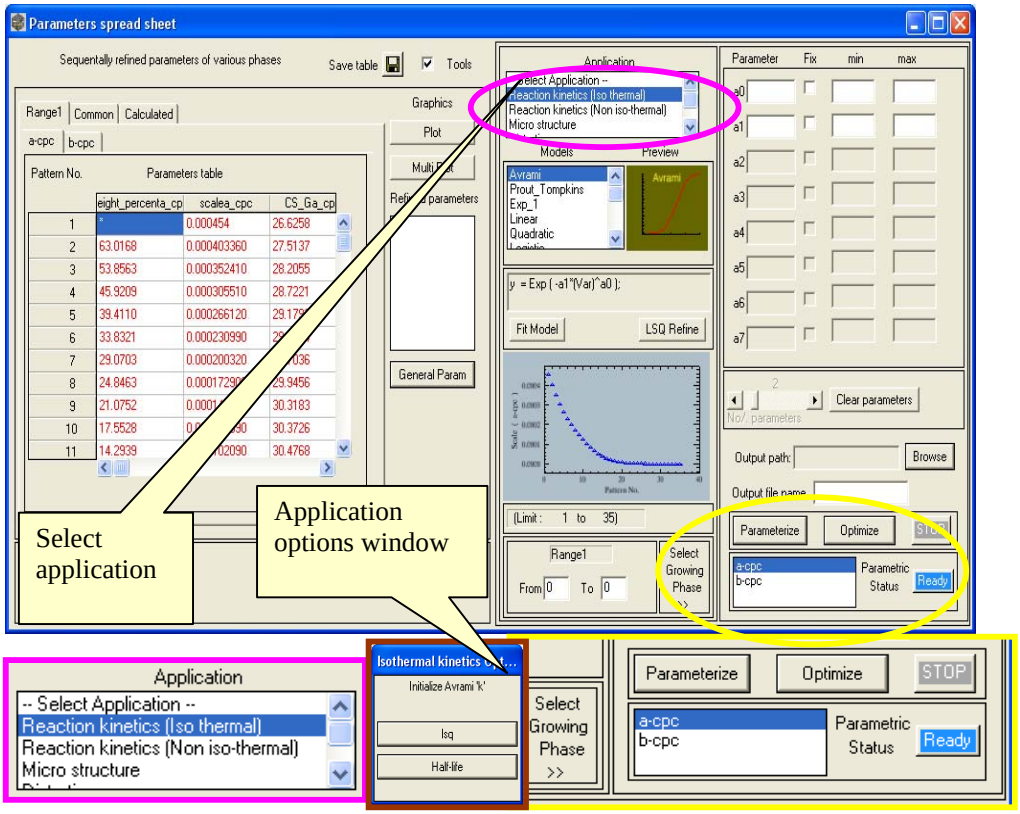

Figure T.26 The '**Parameter spread sheet**' obtained after sequential refinements of the sample CUPC dataset in '**Reaction kinetics**' module is shown. The 'Application option window' (framed in brown) is unique for each application. The '**Application'** name, '**Parameterize**' buttons are highlighted in pink and yellow colors respectively.

T6.2.1.2. Parametric refinements

1 To proceed with parametric refinement (in Reaction kinetics), the name of the application must be selected first ('**Application**' in Figure T.26, circled in pink). Depending upon the experiment type, '**Reaction kinetics (Iso thermal)**' (the present case), or '**Reaction kinetics (Non iso-thermal)**' must be selected (see the list in Figure T.26).

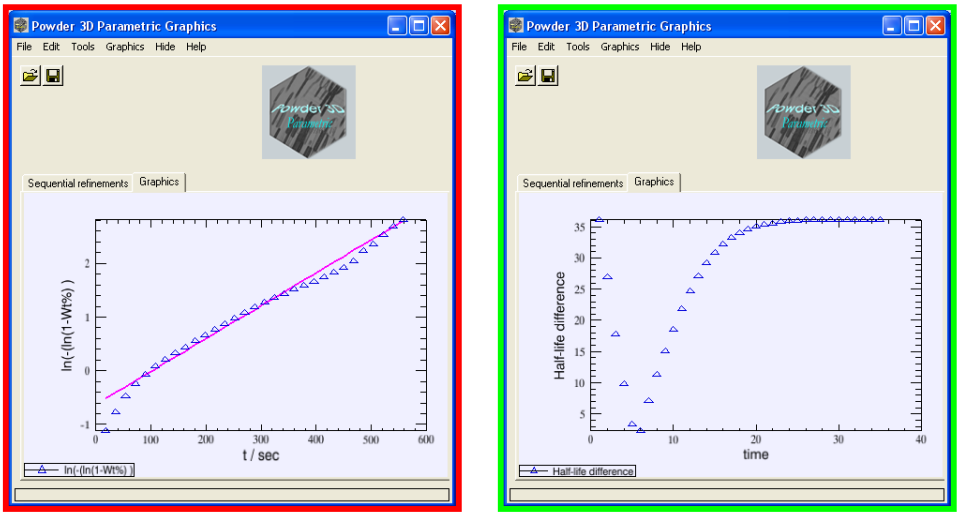

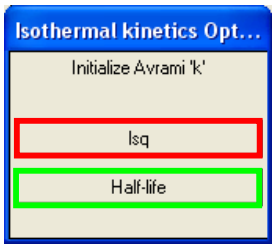

Figure T.27 The starting values for the Avrami parameter 'k' is found by making a linear fit to the growing weight fraction (framed in red). The parameter 'k' is also initialized with the half-life of the decaying phase (see chapter 6). The standard deviations of the half-life of decay of the decaying phase are plotted in this figure (framed green).

2 When an application is selected, the corresponding '**Options window**' will popup (brown framed in Figure T.26). The '**Reaction kinetics options window**' has two widget buttons '**lsq**' and '**Half-life**'. These two buttons are used for initializing the Avrami parameter 'k'. The '**lsq**' performs a general least squares fit to the linearized weight fraction of the growing phase. The '**Half-life**' button finds the half life of decay of the vanishing phase (see also chapter 6), from which the approximate value of 'k' is estimated. Before using these two options, make sure that the growing phase is correctly selected ('**Select Growing Phase >>**' in Figure T.26)

3 The linear least squares fit to the weight fractions of the growing phase and the standard deviations of the half-life of the decaying phase are plotted in Figure T.27. One of them can be used to get the starting values for the parameter 'k'. Note: Physically meaningful starting value of the parameter 'k' is required for the successful parametric refinement of datasets with higher fluctuation (see chapter 6).

4 To proceed further the growing phase must be selected (see step 2 and also Figure T.26 circled in yellow).

5 The instructions in section T6.1 from steps 2, 3 and 4 must be followed. (The default and best model for this analysis is '**Avrami**').

6 '**Parameterize**' button shown in Figure T.26 (framed in yellow) (NOT '**General Param**'!) must be prompted for starting the refinement. A confirmation window as shown in Figure T.23 will popup. The information shown in this window must be rechecked and then the refinement can be started by clicking '**Start refinement**' (Figure T.23).

7 The results of parametric refinement are shown in Figure T.28. The Avrami parameters obtained from parametric refinement are highlighted in Figure T.28.

8 The results will also be updated in '**Instruction/Results'** text box of the '**Topas input file builder'** (Figure T.25)

9 The global weighted residuals (*r_wp*) obtained in the parametric refinements are plotted in Figure T.29. Their shape can be used to select the correct pattern range and redo parametric refinements (as explained in chapter 6).

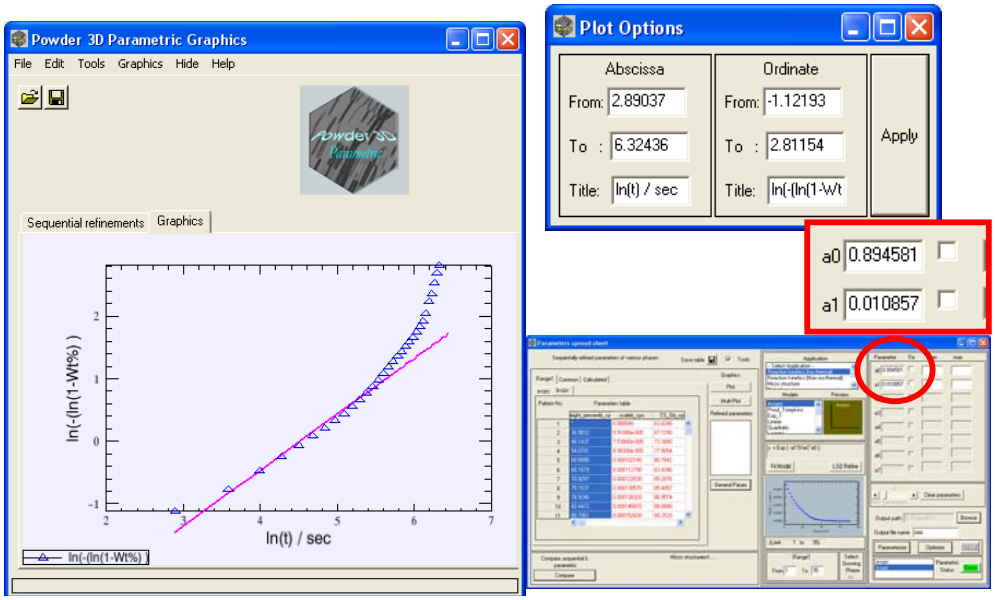

Figure T.28 The results of sequential and parametric refinements associated with the '**Reaction kinetics**' module are shown. The refined parameters are highlighted with the red circle. The default coefficient names are a0, a1,.., etc The coefficients a0 and a1 represent the Avrami parameters 'n' and 'k' respectively.

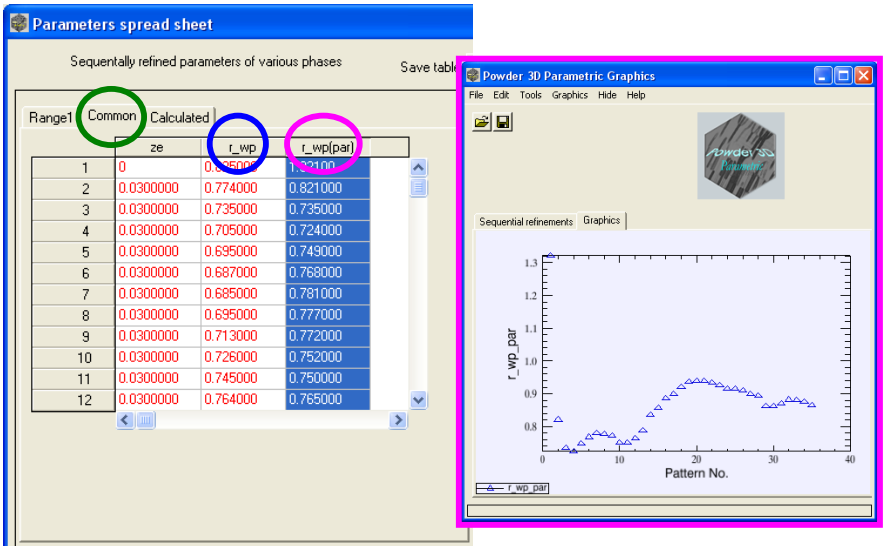

Figure T.29 The weighted residuals (*r_wp*) of sequential/parametric refinements are shown in the **Common** parameters tab (circled in green). The weighted residuals of parametric refinement (pink circled) are plotted on the right picture.

T6.2.1.3. User defined equation

Instead of Avrami model, general user equations can also be used to parameterize the scale factor.

1 The model name '**User_defined**' has to be selected from the model list '**Models**' (in Figure T.30).

2 The model equation must be entered in the field provided (Figure T.30). (Note that the syntax for these equations must be identical to that of the Topas macro language).

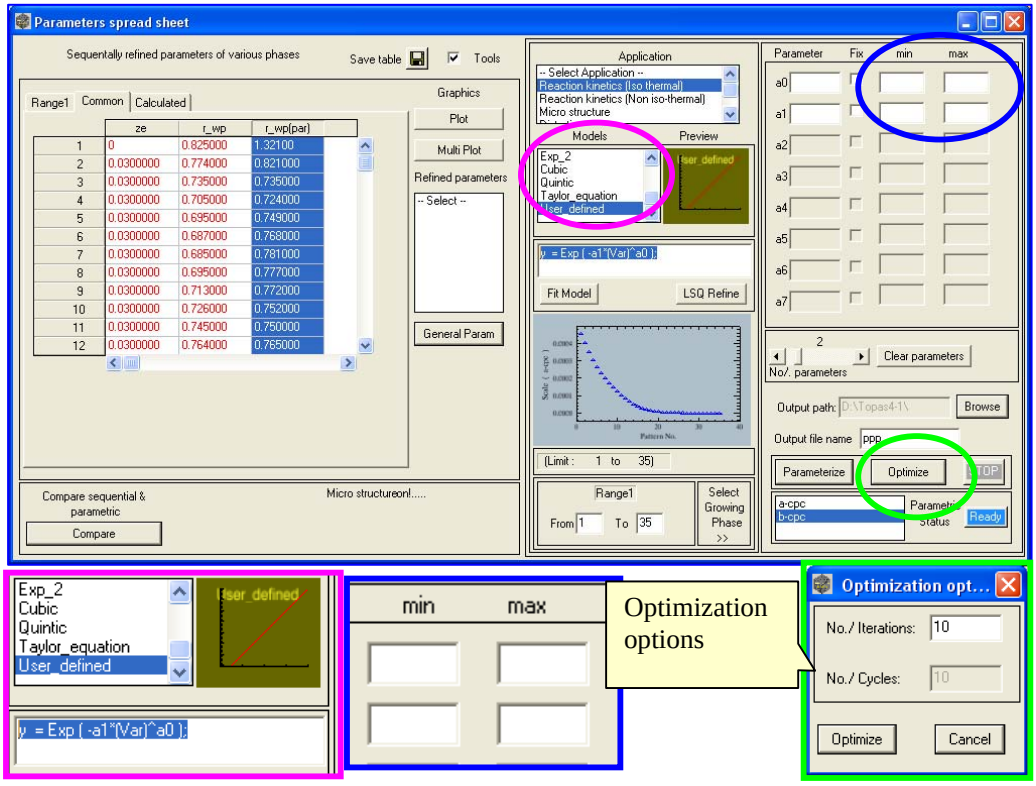

Figure T.30 The option '**User_defined**' must be selected from the list first (circled in pink). The user defined equation of the parameter (in the present case scale factor) can be introduced in the text box (framed in pink). The '**min**' and '**max**' text boxes (blue framed) can be used to limit the refinable parameters. The options for global optimization are also shown ('**Optimization options**' GUI).

3 Similar to Topas macro language, semicolon (;) must be used as the terminating statement. The default model coefficient names are a0, a1, a2...etc and the default name to represent the independent variable 'x' is '**Var**'. (For example use the equation '**y = a0+a1*Var;**' to parameterize the scale factor with a linear model).

4 To do parametric refinement, the steps (from step 2) in section T6.2.1.2 must be followed.

T6.2.1.4. 'Min' –'Max' and global optimization of variables

The '**min**' and '**max**' fields (highlighted in blue frame' in Figure T.30) are identical to the Topas keywords '*min*' and '*max*' used for constraining the refinable variables. The '**Optimize**' button (high lighted in green frame in Figure T.30) can be used to perform global optimization of the refined variables. To do global optimization of the variables follow the two steps below.

1 The '**Optimize**' button must be prompted. The number of iterations for global optimization must be entered in a new interface ('**Optimization options**') that appears (the default number of iterations is 10).

2 The '**Optimize**' button in the '**Optimization options**' window must be clicked to start the global optimization. Part of the input file used in global optimization is shown in Figure T.31.

```
iters          10
out_prm_vals_on_convergence Filename.txt

continue_after_convergence
chi2_convergence_criteria 0.0001
prm  a1  0.00717`val_on_continue = Val + Rand ( 0.000000, 0.000000  );
```

Figure T.31 A part of the Topas input file used in the 'Global optimization' is shown. The variable 'a1' is optimized here.

T7. Some exceptions in the input file syntax

While creating the input file for the test refinement, the user must follow certain 'syntax' restrictions imposed by 'Powder 3D parametric'. These restrictions are made in order to improve the success of some of the 'keyword-search' algorithms used in the program.
The syntax restrictions are listed and explained in detail in this section.

1 While entering the Topas statements (especially 'str', 'hkl_Is' and the macro 'STR') in any of the text editors in the **Topas input file builder**, make sure that all the statements are entered in succeeding lines and not in the same line (see Figure T.32 for explanation).

```
str
CS_G(, 25.10749_0.33412)
Strain_L(, 2.62461_0.07480)
prm a0 =11.5;
.
.
.
str   CS_G(, 25.10749_0.33412)
Strain_L(, 2.62461_0.07480) prm a0 =11.5;
.
.
.
r_bragg  0.354
scale    0.2434
phase_name "Struct"
cell_mass  919

r_bragg  0.354  scale  0.2434 phase_name "Struct" cell_mass  919
```

Figure T.32 The statements recognized by Topas launch mode and 'Powder 3D Parametric' are colored blue. The statements recognized only by Topas launch mode kernel are colored red.

Although Topas can read and execute multiple statements entered in a single line (shown in Figure T.32 as in red letters), the program 'Powder 3D parametric' can recognize only the statements that are entered in consecutive lines (letters colored blue in Figure T.32).

2 In the test input file, the Topas-keyword parameters to be refined must be marked with the '@' symbol (as explained in the Topas technical reference, Coelho, 2007) and the variables of the macros to be refined must be given valid names.

For example, to refine the lattice parameter '*a*', the statement '*a @ 5.5*' must be used. To refine a macro variable e.g., the Gaussian component of crystallite size, the macro must be entered as *CS_G (cs1, 25.108)* (*cs1* is the variable name) and not as *CS_G (@ , 25.108).*

```
macro PS {@} macro BGR { @ } macro REF{ @ }
macro GENERAL { Zero_Error(PS, -0.01178) convolution_step 2
Simple_Axial_Model(PS, 1.68310)
lam ymin_on_ymax 0.001 la  1 lo  0.41592 lh  5e-006 x_calculation_step 0.01}
prm a0  8.76946  prm a1  8.38397
macro AAA(P){A0 + a1 P }

bkg BGR  1169.13181`  301.835586` -196.058595` -30.5271779`  14.570048`
GENERAL
str
. . .
Cubic(PS 4.5)
site As1 num_posns  4 x REF  0.15` y REF  0.402` z REF  0.13` occ As  1 beq
=B1

macro GENERAL {
Zero_Error (@, -0.01178)
convolution_step 2
Simple_Axial_Model(@, 1.68310)
 lam
 ymin_on_ymax 0.001
 la  1 lo  0.41592 lh  5e-006
 x_calculation_step 0.01
}
prm a0  8.76946
prm a1  8.38397
macro AAA(P){A0 + a1 P }
bkg @1169.13181`  301.835586` -196.058595` -30.5271779`  14.570048`
GENERAL
str
. . .
Cubic(@ 4.5)
site As1 num_posns  4 x @ 0.15` y @ 0.402` z @  0.13` occ As  1 beq =B1
```

Figure T.33 Extravagant use of macros is highlighted by the yellow marker. They must be replaced by '@' marked by blue. The texts colored in red must be modified in order to be read by the program 'Powder 3D Parametric'.

3 The structure of input file used in the test refinement must be maintained as simple as possible. The user defined macros for instance can be introduced in an input file only if there is a need for it or only if the number of statements that it contains is at

least greater than 3. An example of the extravagant usage of the macros ‘PS’, ‘BGR’ and ‘REF’ are shown in Figure T.33 (marked in yellow). These macros have a single character ‘@’ as their contents. Instead of using macros for a single character, the character (‘@’) itself can be directly used at the required places in the input file. The program cannot correctly recognize these macros of these types (‘PS’, ‘BGR’ and ‘REF’) and neither interpret their contents, but it will display an error message. In contrast to the macros (‘PS’, ‘BGR’ and ‘REF’) the macro named ‘GENERAL’ (in Figure T.33) is a sensible way of collecting the common parameters together; can be used at various places in the input file and the program will easily recognize its contents.

4 If the user wants to redo sequential refinements, the input files ‘test1.inp’, ‘test2.inp’,...,‘testN.inp’ etc (default file names) created by the program in the previous set of refinements must be deleted before restarting sequential refinements. (They will be saved generally in the location e.g., D:\Topas4-1 or C:\Topas3, depending upon where the ‘tc.exe’ file is located).

Part II

GUI descriptions and functionalities

F1. 'Powder 3D' to 'Powder 3D Parametric'

The program 'Powder 3D parametric' has originally been developed with the aim to be affixed as an application module to the data reduction software 'Powder 3D' (Hinrichsen *et al*., 2006). During the course of the development, some complexities in the flow of the program and allocation of the run time virtual memory have been encountered. These difficulties have led to us to build an independent sequential/parametric refinement tool with the name 'Powder 3D parametric'.

Although the program 'Powder 3D Parametric' is independent of 'Powder 3D' and had been developed independently, some of the basic functionalities[5] of 'Powder 3D' have been retained in the '**Powder 3D Parametric Graphics**' interface of the new program 'Powder 3D parametric'.

In this section, the functionalities of the important widget tools and GUIs of 'Powder 3D Parametric' and also the functionalities of the components retained from 'Powder 3D' are described. The tools retained from the program 'Powder 3D' are explicitly referred by the name of the concerned author.

F2. Powder 3D Parametric Graphics interface

The '**Powder 3D Parametric Graphics**' interface (shown in Figure F.1) is used mainly for importing data files, exporting data as image files and for graphical data visualization. This window will pop up after the program is executed. Some of the functions (the '**File'** menu, '**Load**', '**Save**', '**Main control**' and '**Graphics menu**') of this GUI have been retained from 'Powder 3D' (Hinrichsen *et al*., 2006).

[5] Some widget tools (load, save tools) and graphical layouts (2D, 3D plots)

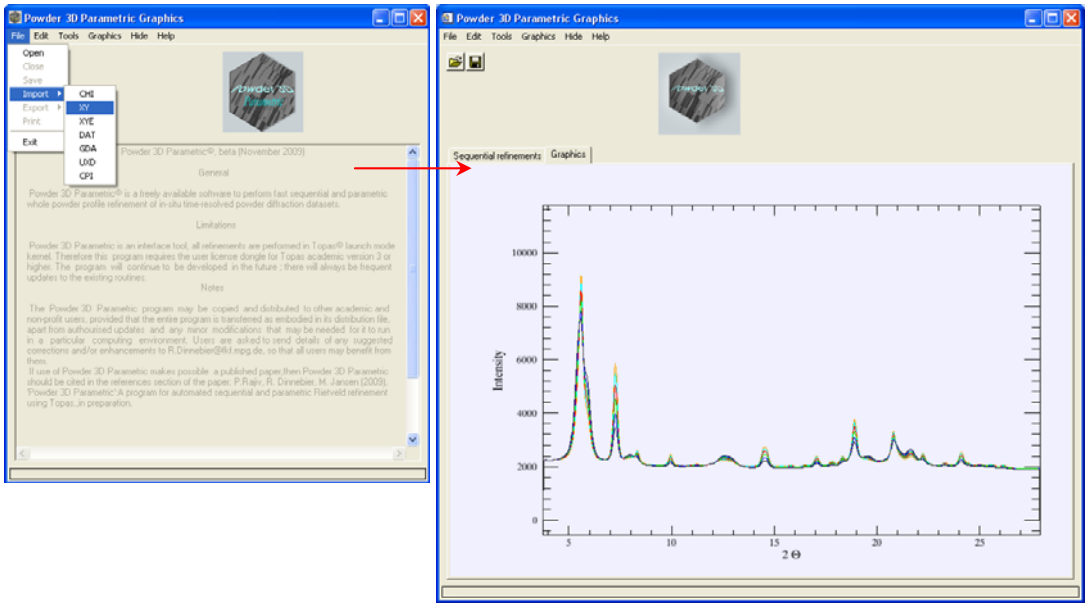

Figure F.1 The main graphics window '**Powder 3D Parametric Graphics**' that pops up after executing the file 'Powder3D Parametric.sav' is shown. Left: without loading the dataset Right: After loading the data set.

F2.1. Load, Save buttons and Graphic window tabs

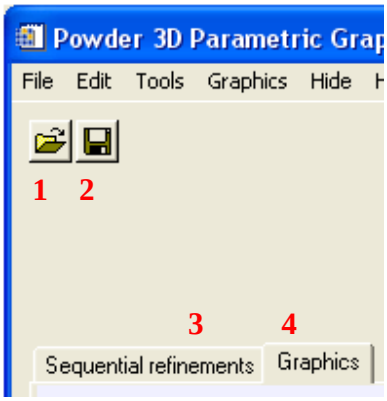

Figure F.2

1 **Load:** To load a saved *.3dp file.
2 **Save: Shortcut t**o save the current work as *.3dp file.
3 **Sequential refinements:** Graphics related to sequential refinements, phase transitions will be displayed here.
4 **Graphics:** General presentation graphics (2D, 3D plots, filters), parametric refinement graphics, etc., will be displayed here.

F2.2 File menu

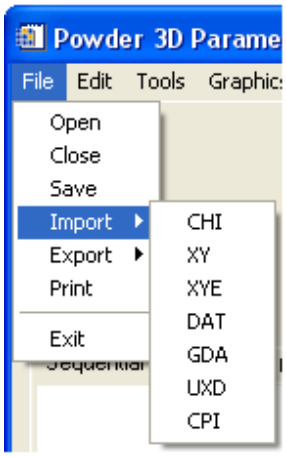

Figure F.3

Import: XRPD data files of formats '*.chi','*.xy', *.xye','*.dat','*.gda','*.uxd', '*.cpi' are loaded here.
Export: To export the contents of current graphics window to an image file.
Save: To save work as *.3dp file.
Print: To print the image in current graphic tab.
Exit: Exit program.

F2.3 Edit menu

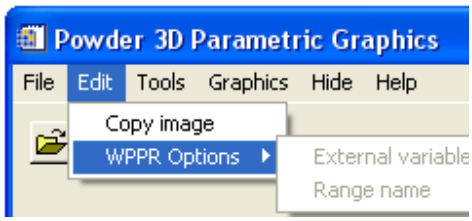

Figure F.4

Copy image: To export the contents of current graphics window to an image file.

WPPR options: Sequential refinement options.
External variable/Topas path: Pops up '**Basic information'** window.
Range names: Modify phase names.

The '**External variable/Topas path**' and '**Range names'** will be explained in the following sections.

F2.3.1 External variable/Topas path

This GUI is used to modify the external variable name, range and path of the Topas executable (tc.exe) (see tutorials section T2.3, Basic experimental information (Step 3)).

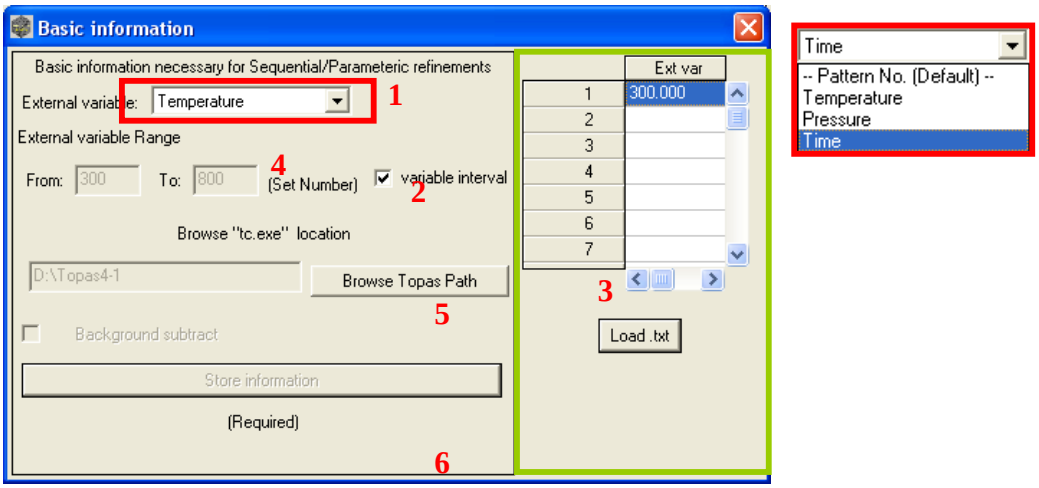

Figure F.5

1 **External variable:** To choose the external variable name from a list.

2 **Variable interval:** In case of non-uniform measurement step (e.g. high pressure measurements) this option can be checked. Selecting this option opens up the main '**Basic information**' window (framed in green) where the measurement temperature/pressure can be entered.

3 **Ext var:** They can be also loaded if they are in the form of a text file.

4 **From To:** To enter the range of measurements temperature /pressure/time etc.

5 **Browse Topas Path:** To browse tc.exe path.

6 **Store information:** Used for storing the entered information.

F2.3.2 Range names

Figure F.6

The range/phase names (explained in tutorials sections T3 and T4) can be modified here.

F2.4 Tools menu

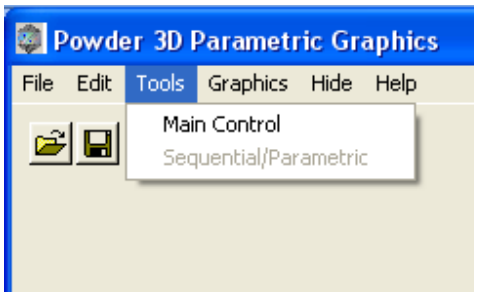

Figure F.7

Main control: Opens a GUI that provides some graphics options.

Sequential/Parametric: Opens up '**Basic information**' GUI followed by Topas input file builder.

The 'Main control' and Sequential/Parametric tools are explained in the following section.

F2.4.1 Main controls

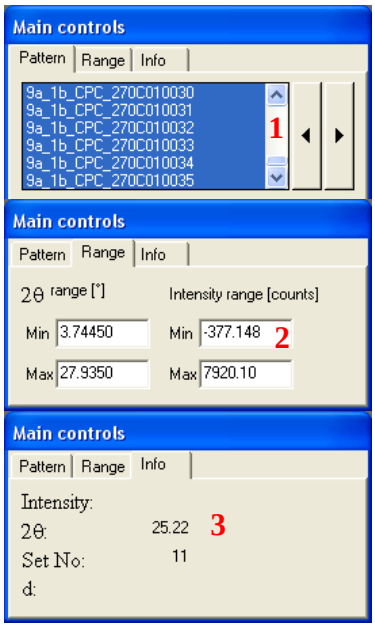

Figure F.8

1 **Pattern:** The 'Main control' tool (used in the program 'Powder 3D') can be used to plot single/multiple patterns.

2 **Range:** The range of the plot (2θ and intensity) can be set.

3 **Info:** It shows the mouse position when placed on the plot in the graphics window.

F2.4.2 Sequential/ Parametric

Prompting this option will open up the '**Basic information** 'GUI (explained in section F2.3.1). After entering all the necessary information the '**Store information**' button (Figure F.5) must be pressed, which will open the '**Topas input file builder**' (also see section T2.3, T2.4 of the tutorial). The '**Topas input file builder**' GUI is explained in detail in section F2.3 of this manual.

F2.5 Graphics menu

Figure F.9

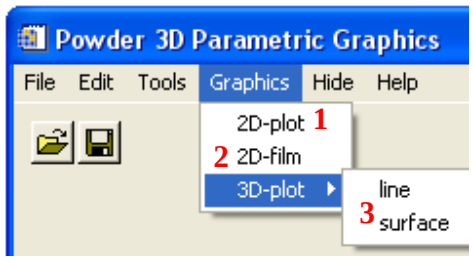

1 The '**Graphics**' tool (used in the program 'Powder 3D') can be used for plotting a single pattern (2θ vs I) (Figure F.1 and F.6).

2 **2D-film**: Chapter 5 (Simulated heating Guinier film plot).

3 An example for 3D (line) plot is shown in Figure F.9.

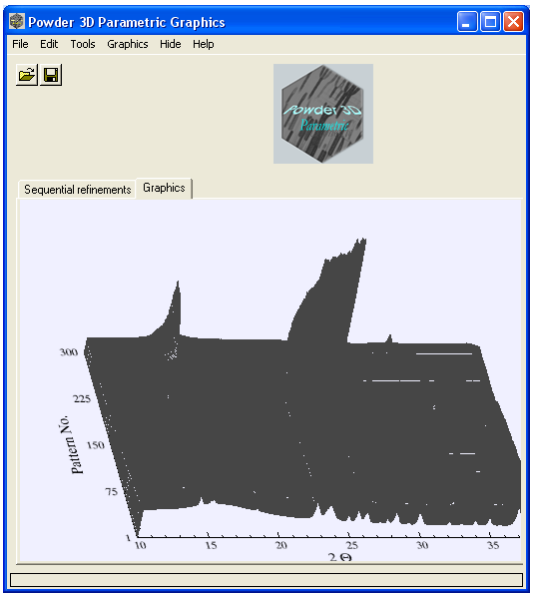

Figure F.10

3D line plot of Ag_3VO_4 dataset (Dinnebier *et al.*, 2007).

F2.6 Hide menu

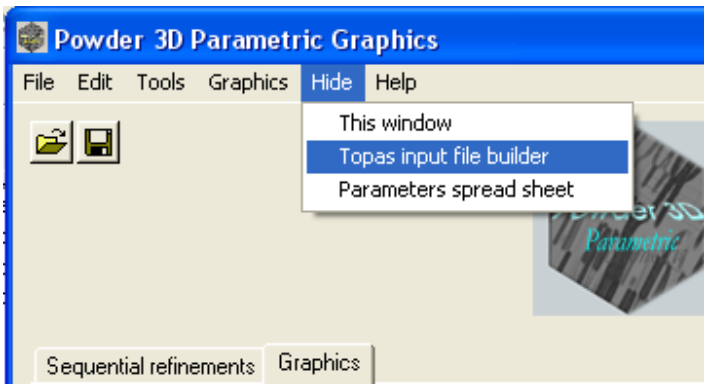

Figure F.11

This menu is meant to temporarily hide some GUIs which the user doesn't want to work with. The windows '**main graphics window**' or '**Topas input file builder'** or '**Parameters spread sheet**' can be selected and hid.

F2.7 Help menu

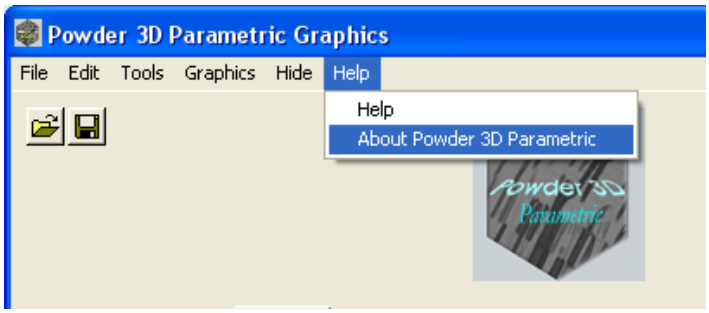

Figure F.12

This menu is used to open the user's manual and some information about the program.

F3 Topas input file builder

In this section some of the important features and tools of the '**Topas input file builder**' (Figure T.6 in tutorials) are explained. The '**Transitions'** tab and several other tab windows used in the '**Topas input file builder**' will be described individually in this section.

F3.1 'Transitions' tab

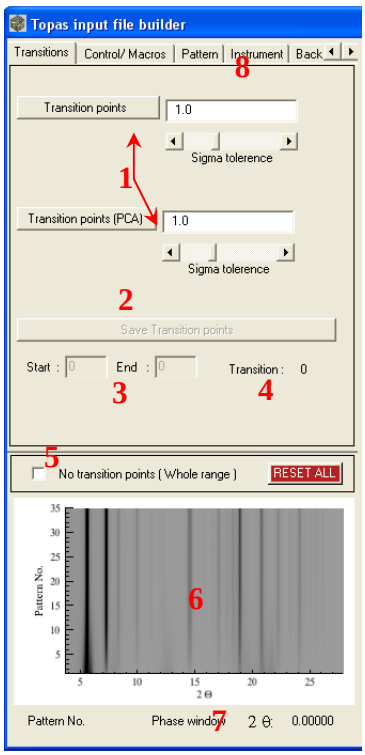

Figure F.13

1. **Transition points:** Phase transitions can be found (by correlations coefficient and principal component analysis).
2. **Save Transition points:** To save phase transition points.
3. **Start-End:** Shows the starting and ending pattern numbers of a phase.
4. **Transition:** Shows the phase index.
5. **No transition points (Whole range):** Choose all the patterns for sequential refinement (assumes that the compound has 1 phase, see tutorial section T4).
6. **Zoom window:** The 2D plots of '**main graphics window**' can be zoomed.
7. Display mouse cursor position
8. **Tabs:** Various tab windows to construct parts of Topas input file.

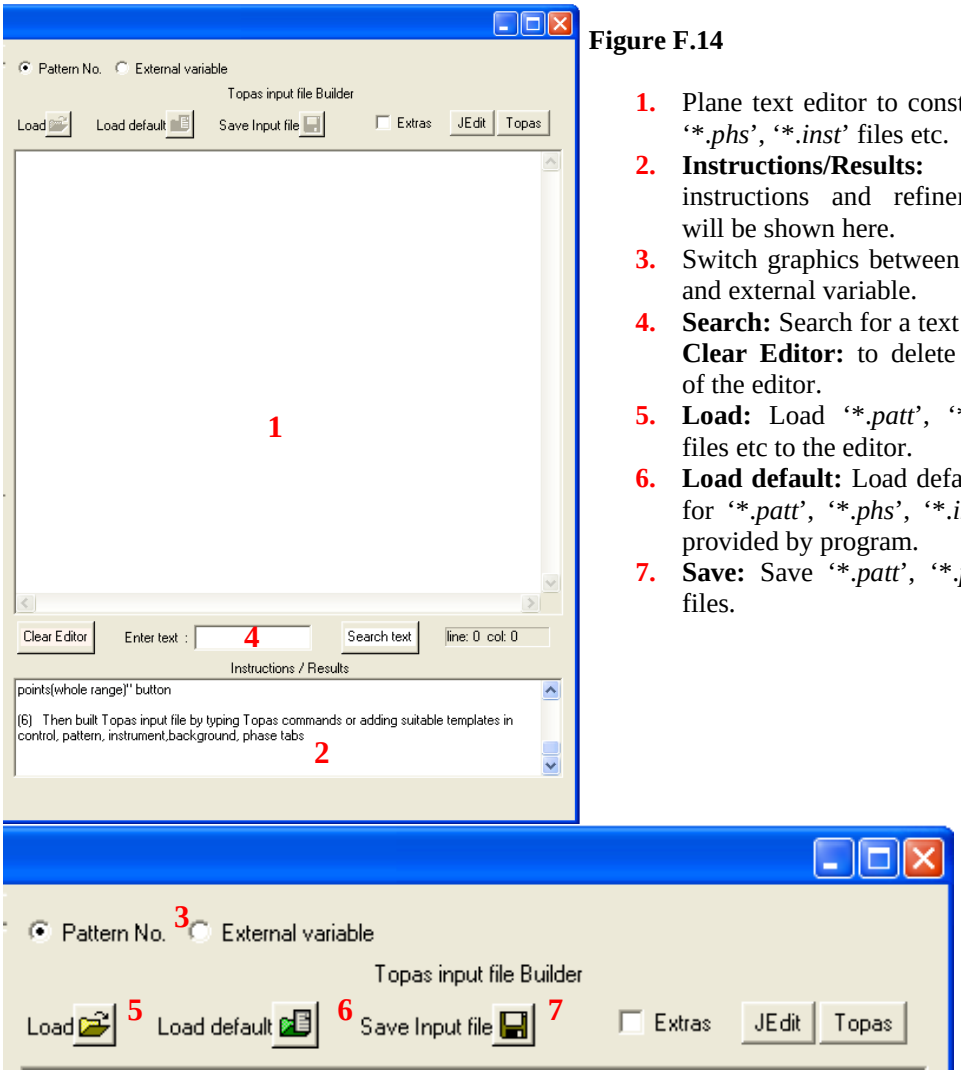

Figure F.14

1. Plane text editor to construct '**.patt*', '**.phs*', '**.inst*' files etc.
2. **Instructions/Results:** Stepwise instructions and refinement results will be shown here.
3. Switch graphics between 'Patten No.' and external variable.
4. **Search:** Search for a text in the editor. **Clear Editor:** to delete the contents of the editor.
5. **Load:** Load '**.patt*', '**.phs*', '*inst*' files etc to the editor.
6. **Load default:** Load default templates for '**.patt*', '**.phs*', '**.inst*' files etc provided by program.
7. **Save:** Save '**.patt*', '**.phs*', '**.inst*' files.

F3.2 Topas input file building tabs

The functions of the **Control/Macro**, **Pattern**, **Instrument**, **Background** and **Phase** tab windows will be illustrated in this section. In each of these tab windows, the Topas keywords associated with control parameters (in **Control/Macro** tab), powder pattern information (in **Pattern** tab), the instrumental information (in **Instrument** tab), the background intensity information (in **Background** tab) and the phase information (in **Phase** tab) can be loaded in to their text editor; the respective '**.ctrl*', '**.patt*', '**.inst*', '**.bkg*', and '**.phs*' files can be prepared.

F2.3.2.1 Control/Macro tab

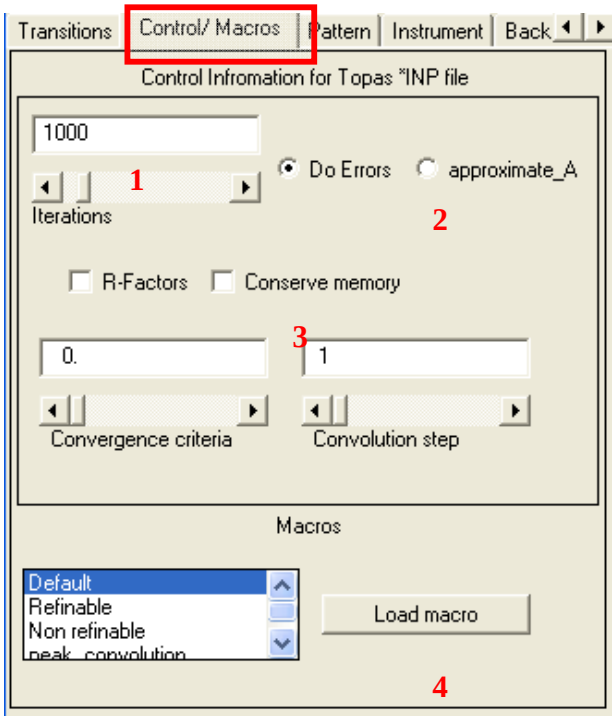

Figure F.15

1 **Iterations:** Topas command '*iter*'.
2 **Do Errors:** Topas commands '*do_errors*'/'*approximate_A*'.
3 Related Topas 'control' commands.
4 **Load macro:** Appends the selected macro template to the '**.ctrl*' part of the '**.inp*' file.

F2.3.2.2 Pattern tab

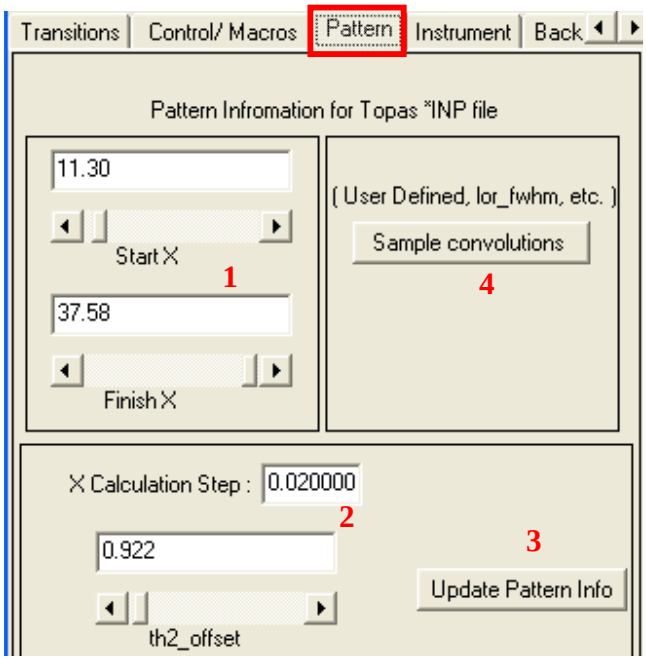

Figure F.16

1 Topas command '*start_X*' and '*finish_X*'.
2 '*X_calculation_step*' and two theta correction.
3 **Update Pattern Info:** Update all 'patten' information.
4 The **sample convolutions** opens another GUI (see Figure F.18).

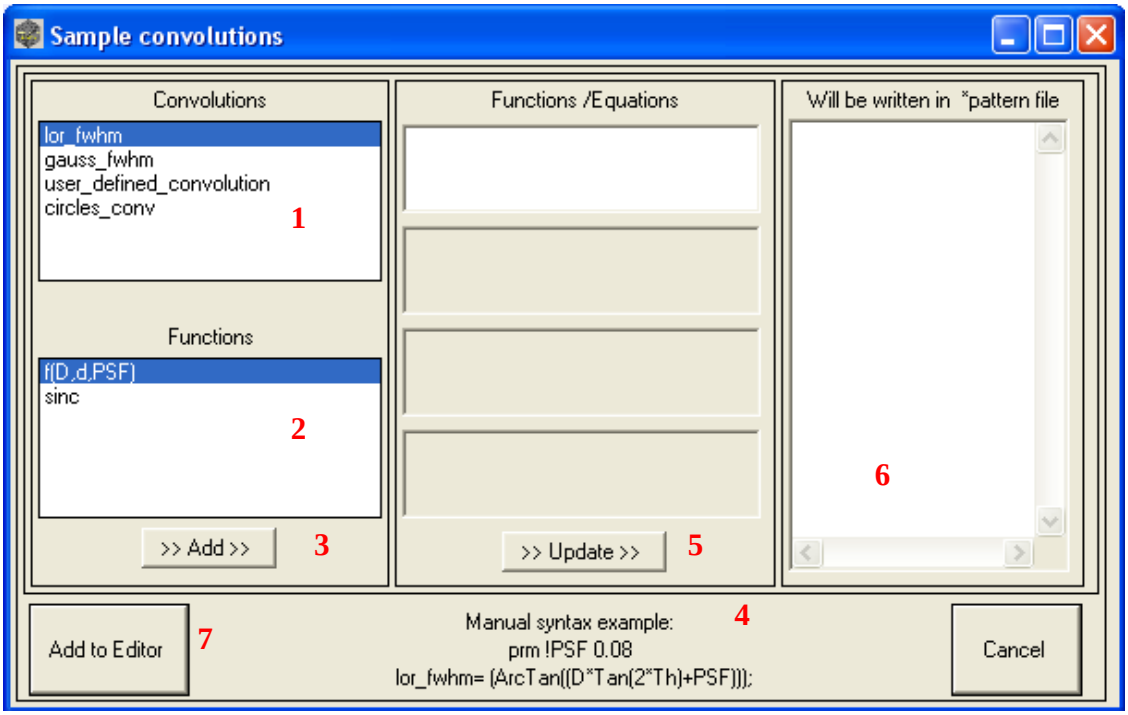

Figure F.17

1 **Convolutions:** Select convolutions.
2 **Functions:** Select general convolution functions.
3 Combine them.
4 The syntax for user defined convolutions.
5 Click '**>>Update>>**' to enter the selected convolutions to be updated in the text editor (**6**).
6 The selected convolutions to be updated here.
7 Click '**Add to Editor**' to append all the selected convolutions to the '*Pattern*' tab of the Topas editor.

F2.3.2.3 Instrument tab

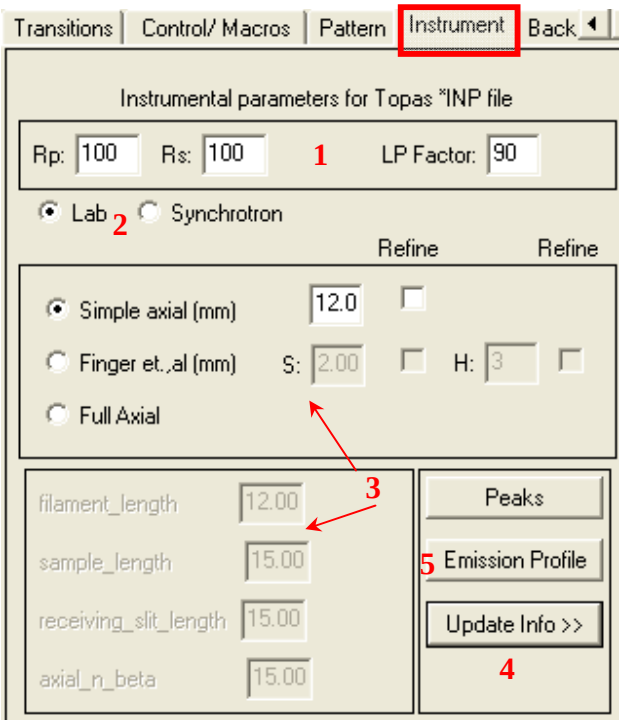

Figure F.18

1. Basic **Instrument** parameters.
2. **Lab/synchrotron:** Select between lab/synchrotron data.
3. Asymmetry models.
4. **Update Info>>**: Update all instrumental' information.
5. Upload **Emission Profile** (see Figure F.20).

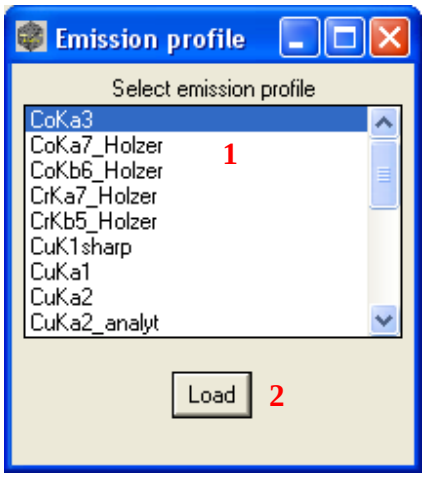

Figure F.19

1. Select **Emission profile**. Refer Topas users manual, (Coelho, 2007) for details.
2. **Load** the emission profile statement to the editor.

F2.3.2.4 Background tab

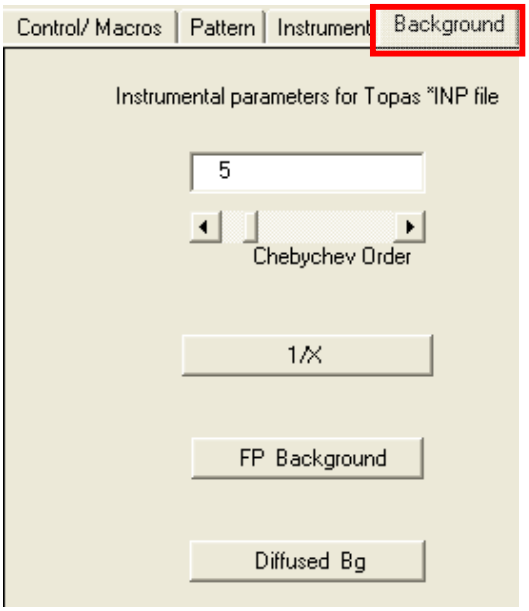

Figure F.20

Select the Topas keywords necessary to describe the **background** of a powder pattern.

F2.3.2.5 Phase tab

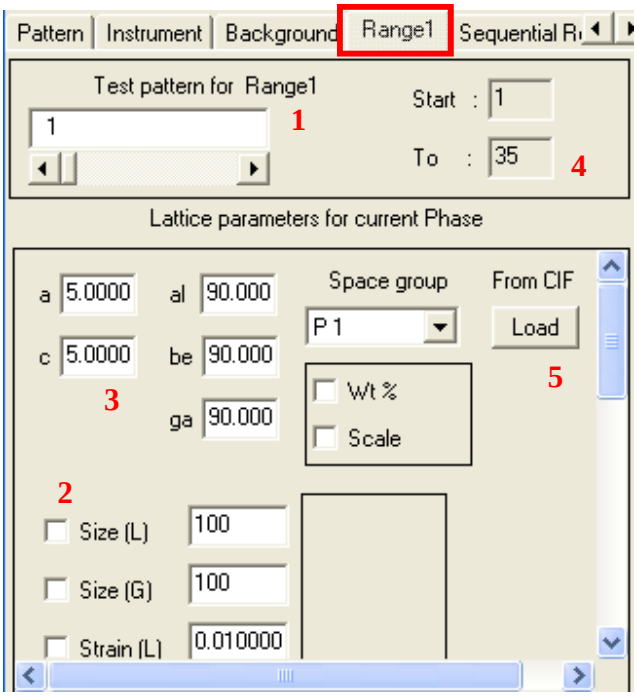

Figure F.21

1 Select the test pattern in current phase.
2 Size/strain parameters.
3 Lattice parameters.
4 Start/end pattern number.
5 Load structure from 'CIF' file.

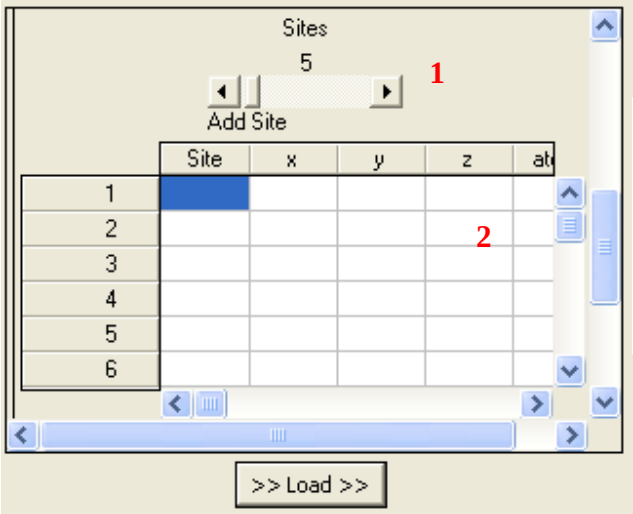

Figure F.22

1 **Add Site:** Select the number of atomic sites.
2 **Site:** Atom sites.

F2.3.2.6 Phase tab

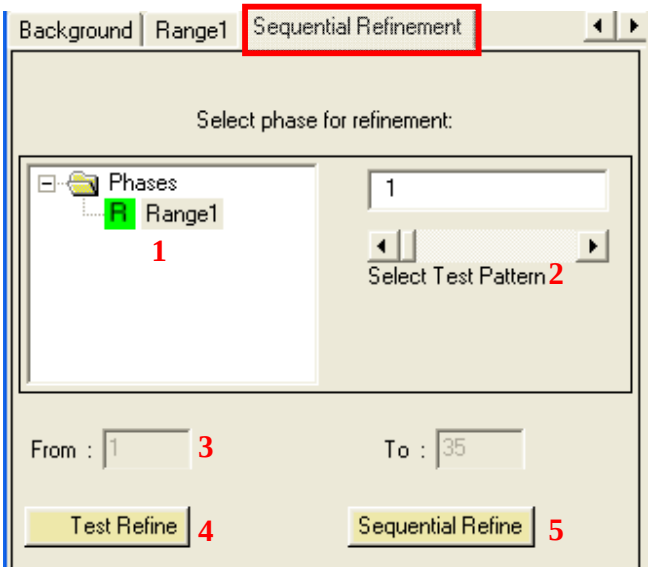

Figure F.23

1 **Range:** Select the phase to be (test) refined.
2 **Select Test Pattern:** Select the pattern index from which the sequential refinements must be started.
3 **From-To:** Pattern ranges in the selected phase.
4 **Test Refine:** Do test refinement (see section T5.3 of the tutorial).
5 **Sequential Refine:** Do sequential refinement (see section T5.4 of the tutorial).

F4 Parameters spreadsheet

The sequentially refined parameters are displayed in a worksheet (Figure F.25). The functionalities of various tools in this GUI will be discussed in this section.

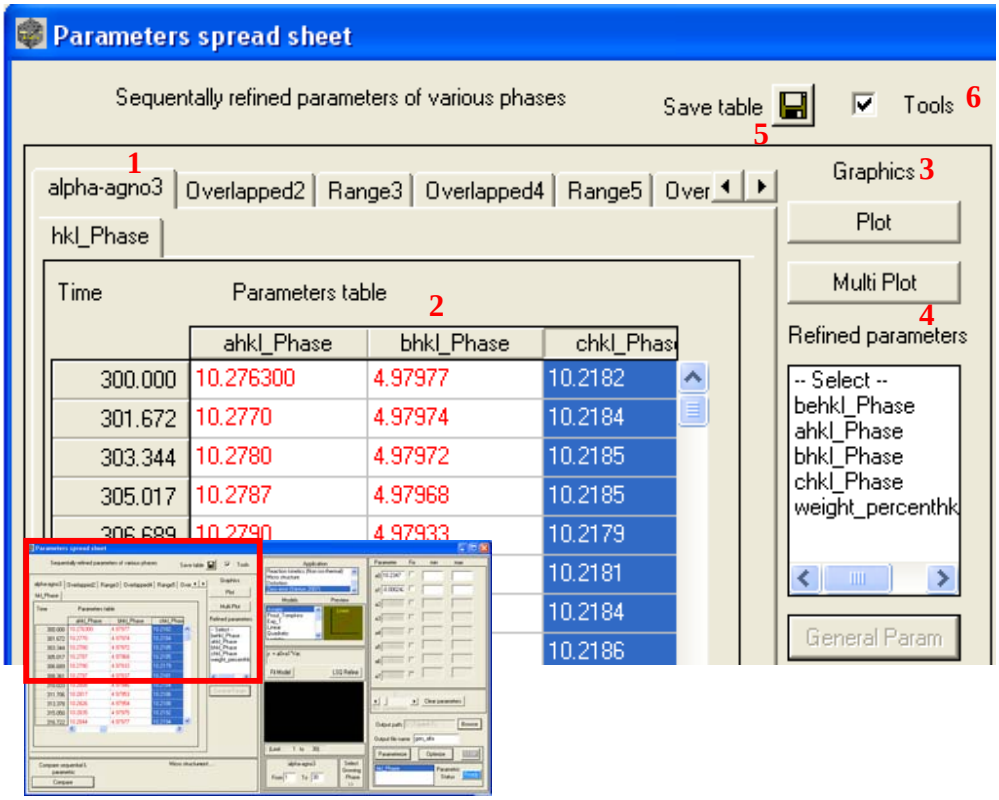

Figure F.24

1 Several tabs are created (proportional to the number of phases and overlaps)
2 **Parameters table:** The refined parameters are placed here in their respective tabs.
3 **Graphics:** Plot and Multi plot the selected parameters.
4 **Refined parameters:** List of sequentially refined parameters (see section T6.1 in the tutorial).
5 **Save table:** Save refined parameters as an ASCII file.
6 **Tools:** Opens the tools menu (Figure F. 26).

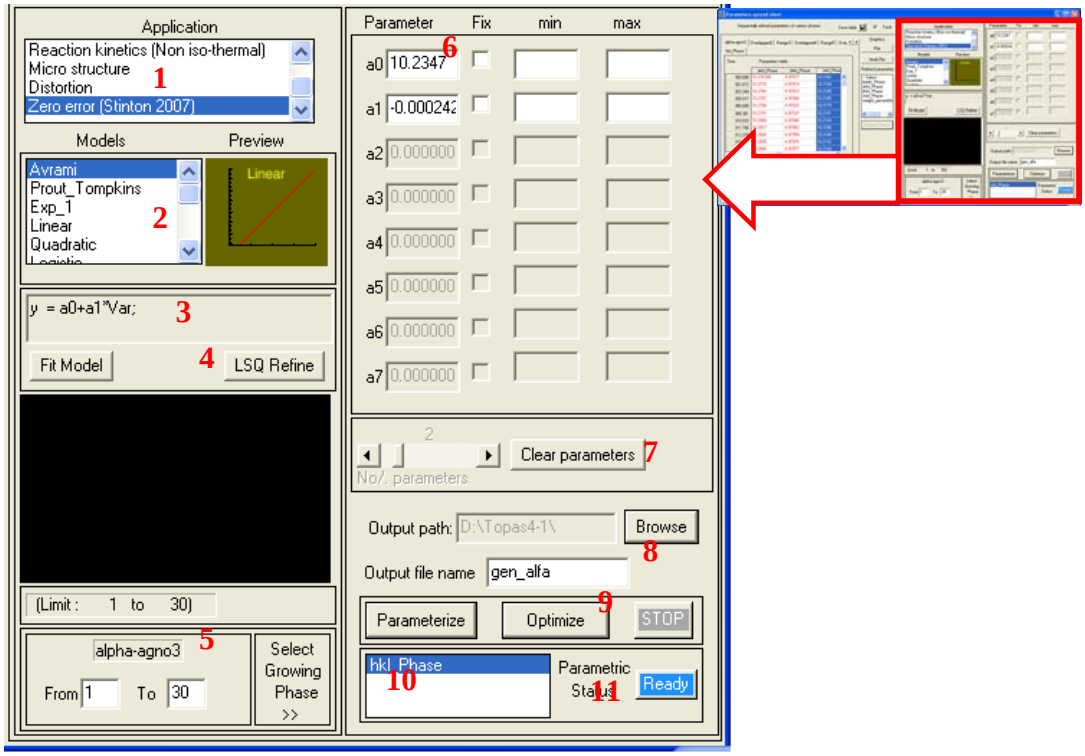

Figure F.25

1 **Application:** Select application module (section T6.2 of tutorial).
2 **Models:** Select the parametric refinement model (the corresponding plot is drawn at the right '**Preview**').
3 Space for 'User defined equation'.
4 **Fit Model/LSQ Refine**: Perform least squared refinements.
5 **Limit:** Range of patterns to be parameterized.
6 **a0,a1,..,**etc**:** Refined coefficients (in parametric refinement, global optimization and also least squared refinements).
7 **Clear parameters** and select number of parameters (**No/. parameters**).
8 **Out put file name** and **Output path:** Topas '*out*' file name and path.
9 Parametrization and global optimization.
10 Select the decaying/growing phase (section T6.2).
11 **Ready:** Status of parametric refinement.

Part III

Additional routines

A1. Graphics for sequential refinement

The observed, calculated and the difference in intensities of the sequentially refined powder patterns can be plotted by selecting '>>**Graphics**>>**sequential-Plot**' in the Powder 3D Parametric Graphics window.

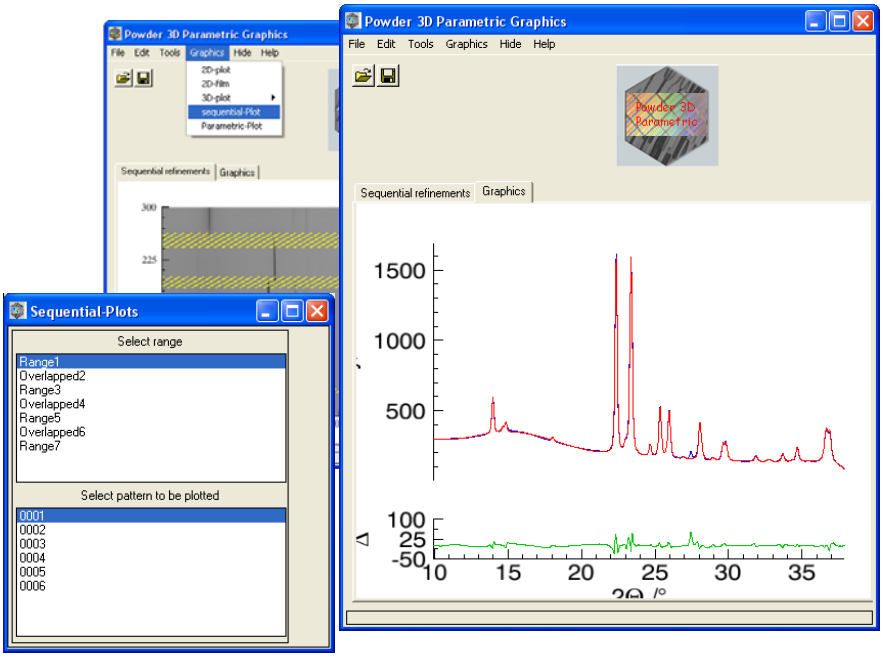

Figure A.1 The observed, calculated and the difference in intensities of the sequentially LeBail refined powder pattern of α-Ag_3VO_4 are drawn.

A2. Input file maker for Sequential and Parametric refinements

Some new sets of routines (will be called 'Inp maker') have been implemented in the program for performing the sequential refinements and also for creating the input file required for parametric refinement. These routines work independent of the flow of the main program (i.e., the procedures explained in the tutorials section) and cannot provide any graphical support (Figure A3 and Figure A4). These routines require that the 'test' input file required for the refinements is already at hand.

The 'Inp maker' can be started by selecting '**Extras**' and clicking on '**InpMaker**' in the Topas input builder (Figure A2).

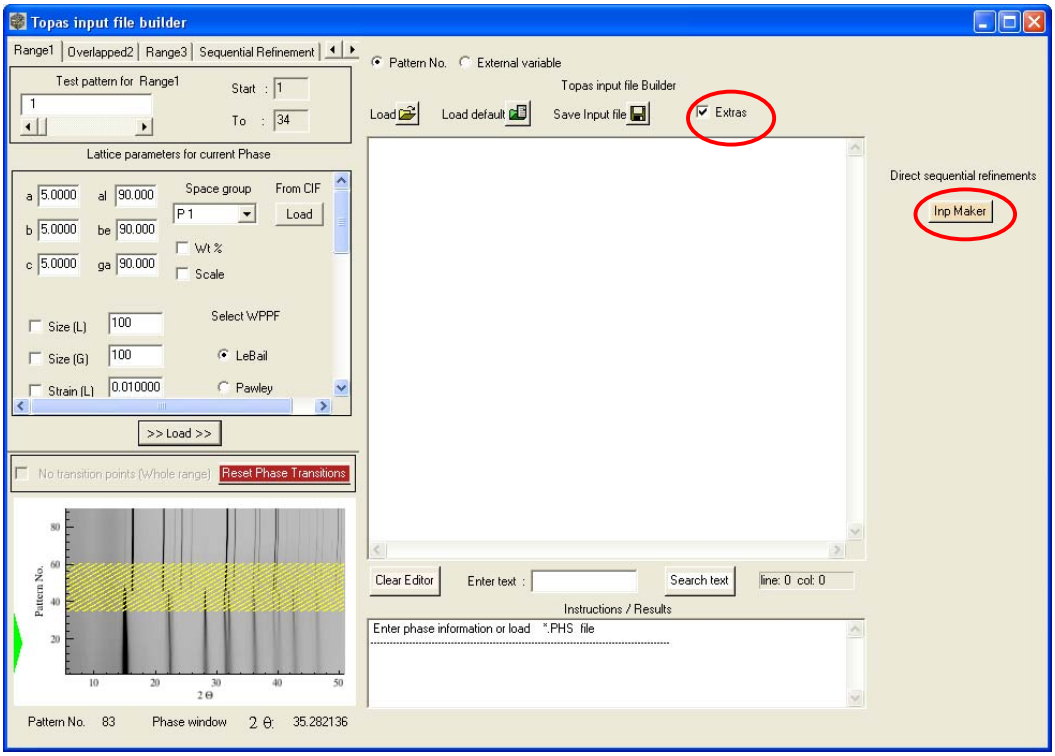

Figure A.2 Start '**Powder 3D Parametric Topas *.inp maker**' by selecting '**Extras**' and clicking on '**InpMaker**' (circled in red).

The '**Load**' and '**Browse Topas path**' (Figure A.3 circled red) buttons must be prompted to load the data location and Topas path, similar to section T 2.1. Using '**Sequential**

refinements' button (Figure A.3 circled green), the manually prepared 'test' input file can be loaded and executed.

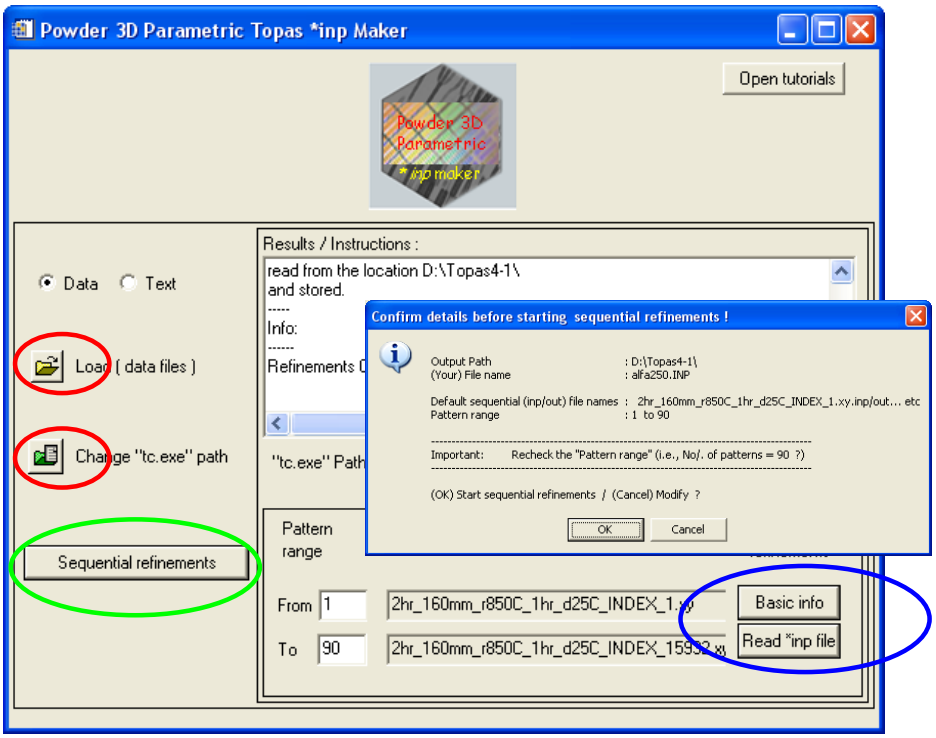

Figure A.3 '**Powder 3D Parametric Topas *.inp maker**' GUI is shown. The inner picture is the confirmation window that appears before proceeding with sequential refinements.

The 'OUT' macro of Topas can be made use in the 'test' input file in such a way that the sequentially refined parameters are stored in the form of a table in a '*.txt' file. After executing all the input files sequentially, the refined parameters table can be easily analyzed using the commercial programs that offer facilities to analyze data using worksheets (Microsoft Excel, 2010).

The instructions to prepare the input file required for parametric refinement are as given below.

- '**Basic info**' button (Figure A.3 circled blue) must be prompted to load the basic experimental information (similar to section T 2.3).

- '**Read *.inp file**' button (Figure F.3 circled blue) must be prompted to load the prepared 'test' input file.

- After selecting the 'test' input file an interface similar to the 'parameters spreadsheet' (section F 4) will pop up (Figure A.4).

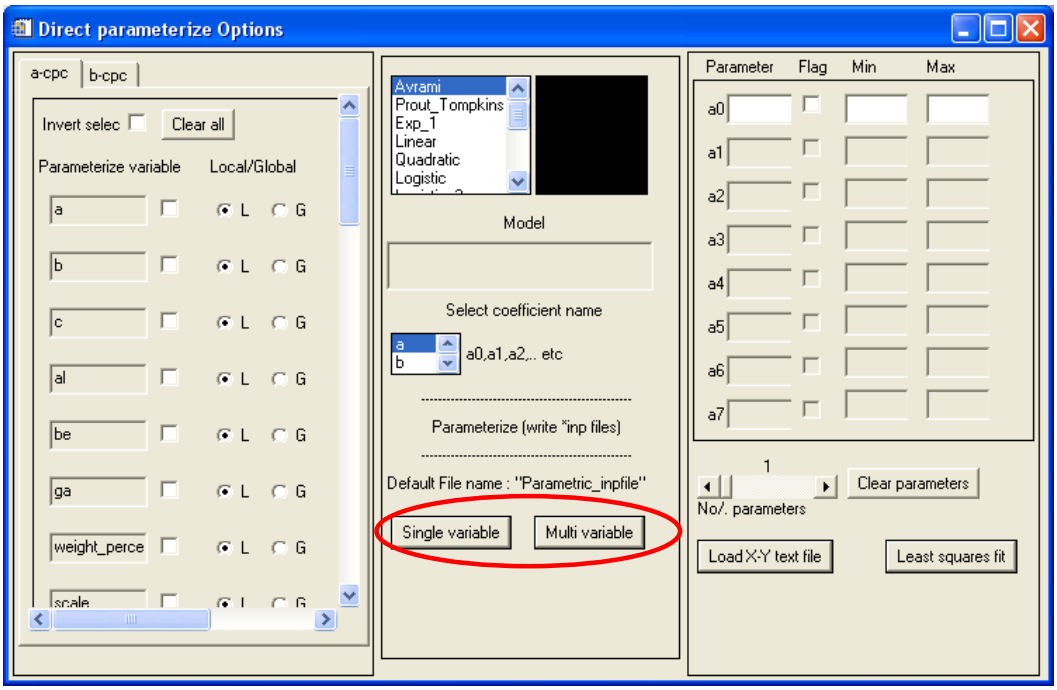

Figure A.4 The parametric refinement options as provided by '**Powder 3D Parametric Topas *.inp maker**'.

Any refinable parameter can be selected from the list and can be parameterized (Figure A.4). (The detailed procedure is similar to the one explained in section T 6.1). Options for parameterizing multiple variables are also provided in the interface. This interface can only prepare the input file necessary for the parametric refinement; the prepared file can be executed by the user in Topas GUI mode.

Supplementary information

Topas input files

The Topas input files used in some applications of parametric Rietveld refinements in chapters 6 and 7 and in the tutorials are presented in this section.

A. Topas input file used in the 'test' Rietveld refinement of CUPC (90% α and 10% β at 270 K)

```
' # CUPC at (90% alpha 10% beta at 270
xdd D:\Dinnebier1107\a_CPC\90%alpha_10%beta_270\Daten\9a_1b_CPC_270C010001.xy
prm !D  98.48031
prm !PSF  0.08
prm !d  0.24032
prm !mix  0.50909 min 0.0 max 1.0
gauss_fwhm = (1-mix) (ArcTan((D*Tan(2*Th)+PSF+d*(1/Cos(2*Th)))/D)-(2*Th))/Deg + 0.000001;
lor_fwhm  =  (mix) (ArcTan((D*Tan(2*Th)+PSF+d*(1/Cos(2*Th)))/D)-(2*Th))/Deg + 0.000001;
User_Defined_Dependence_Convolution(circles_conv, 1/Tan(Th) ,, -0.00559 =0;)

do_errors

bkg @ 2000.31576`_0.991286267 -154.789347`_1.32789819  41.9161118`_1.17502874 -42.5934438`_1.11460528 -15.4704793`_1.21647327

    start_X  3.5
    finish_X  39.0
    Zero_Error(@, 0.03)
    LP_Factor( 90)
    convolution_step 2
    Rp 100
    Rs 100
    lam
        ymin_on_ymax  0.0001
        la  1 lo  1.238879 lh  1e-006
    x_calculation_step 0.02

str     '# For alpha CUPC
        CS_G(CSg1, 26.62579`_0.23397)
        CS_L(CSl1, 26.62579`_0.23397)

        r_bragg  0.177506733
        phase_name a-cpc
        cell_mass  576.081_0.000
        cell_volume  608.6226_0.0000
        weight_percent w1  72.206_0.157
        scale @  0.0004544034`_0.0000014359
        space_group P-1
        Phase_LAC_1_on_cm( 41.08137_0.00000)
        Phase_Density_g_on_cm3( 1.57175_0.00000)


        a   @   3.85081
        b   @   13.03808
        c   @   12.20957
        al  @   89.05154
        be  @   96.74084
        ga  @   89.28388
```

```
50
51          site Cu41  x  0.00000_0.00000 y  0.00000_0.00000 z  0.00000_0.00000 occ Cu 1 beq !b1  6.5871_0.4149
52          site N4    x -0.06134_0.00000 y  0.13770_0.00000 z -0.07459_0.00000 occ N 1  beq !b1  6.5871_0.4149
53          site N10   x  0.26224_0.00000 y  0.06352_0.00000 z  0.13203_0.00000 occ N 1  beq !b1  6.5871_0.4149
54          site C2    x -0.23041_0.00000 y  0.15738_0.00000 z -0.17708_0.00000 occ C 1  beq !b1  6.5871_0.4149
55          site C5    x  0.05908_0.00000 y  0.22740_0.00000 z -0.03130_0.00000 occ C 1  beq !b1  6.5871_0.4149
56          site C11   x  0.40029_0.00000 y  0.01280_0.00000 z  0.22564_0.00000 occ C 1  beq !b1  6.5871_0.4149
57          site C12   x  0.33275_0.00000 y  0.16468_0.00000 z  0.14344_0.00000 occ C 1  beq !b1  6.5871_0.4149
58          site C1    x -0.21854_0.00000 y  0.26263_0.00000 z -0.20043_0.00000 occ C 1  beq !b1  6.5871_0.4149
59          site C3    x -0.03523_0.00000 y  0.30730_0.00000 z -0.10822_0.00000 occ C 1  beq !b1  6.5871_0.4149
60          site N39   x  0.24064_0.00000 y  0.24077_0.00000 z  0.06888_0.00000 occ N 1  beq !b1  6.5871_0.4149
61          site C13   x  0.56410_0.00000 y  0.08313_0.00000 z  0.29934_0.00000 occ C 1  beq !b1  6.5871_0.4149
62          site N38   x  0.38720_0.00000 y -0.08875_0.00000 z  0.24723_0.00000 occ N 1  beq !b1  6.5871_0.4149
63          site C14   x  0.52132_0.00000 y  0.17948_0.00000 z  0.24723_0.00000 occ C 1  beq !b1  6.5871_0.4149
64          site C6    x -0.35216_0.00000 y  0.32287_0.00000 z -0.29424_0.00000 occ C 1  beq !b1  6.5871_0.4149
65          site C8    x  0.02402_0.00000 y  0.41418_0.00000 z -0.10490_0.00000 occ C 1  beq !b1  6.5871_0.4149
66          site C15   x  0.74580_0.00000 y  0.07091_0.00000 z  0.40692_0.00000 occ C 1  beq !b1  6.5871_0.4149
67          site C17   x  0.65832_0.00000 y  0.26850_0.00000 z  0.30020_0.00000 occ C 1  beq !b1  6.5871_0.4149
68          site C7    x -0.29490_0.00000 y  0.43013_0.00000 z -0.29216_0.00000 occ C 1  beq !b1  6.5871_0.4149
69          site H42   x -0.48743_0.00000 y  0.29003_0.00000 z -0.36231_0.00000 occ H 1  beq !b1  6.5871_0.4149
70          site C9    x -0.10829_0.00000 y  0.47559_0.00000 z -0.19828_0.00000 occ C 1  beq !b1  6.5871_0.4149
71          site H44   x  0.15937_0.00000 y  0.44676_0.00000 z -0.03669_0.00000 occ H 1  beq !b1  6.5871_0.4149
72          site C16   x  0.88456_0.00000 y  0.15941_0.00000 z  0.46105_0.00000 occ C 1  beq !b1  6.5871_0.4149
73          site H46   x  0.77706_0.00000 y -0.00016_0.00000 z  0.44519_0.00000 occ H 1  beq !b1  6.5871_0.4149
74          site C18   x  0.84115_0.00000 y  0.25751_0.00000 z  0.40808_0.00000 occ C 1  beq !b1  6.5871_0.4149
75          site H48   x  0.62687_0.00000 y  0.33951_0.00000 z  0.26184_0.00000 occ H 1  beq !b1  6.5871_0.4149
76          site H43   x -0.38954_0.00000 y  0.47546_0.00000 z -0.35936_0.00000 occ H 1  beq !b1  6.5871_0.4149
77          site H45   x -0.06851_0.00000 y  0.55344_0.00000 z -0.19780_0.00000 occ H 1  beq !b1  6.5871_0.4149
78          site H47   x  1.01757_0.00000 y  0.15245_0.00000 z  0.53924_0.00000 occ H 1  beq !b1  6.5871_0.4149
79          site H49   x  0.94303_0.00000 y  0.32109_0.00000 z  0.44823_0.00000 occ H 1  beq !b1  6.5871_0.4149
80
81
82  rigid
83    z_matrix Cu41
84    z_matrix N4    Cu41 =1.9983;
85    z_matrix N10   Cu41 =1.9968; N4  90.162
86    z_matrix C2    N4  =1.3600; Cu41 125.894      N10  -180
87    z_matrix C5    N4  =1.3559; Cu41 125.622      C2    180
88    z_matrix C11   N10 =1.3601; Cu41 125.851     N4   -180
89    z_matrix C12   N10 =1.3560; Cu41 125.694     C11   180
90    z_matrix C1    C2  =1.3993; N4  109.123     Cu41  180
91    z_matrix C3    C5  =1.4061; N4  108.943      Cu41 -180
92    z_matrix N39   C5  =1.3508; N4  126.948      C3    180
93    z_matrix C13   C11 =1.3989; N10 109.176      Cu41  180
94    z_matrix N38   C11 =1.3484; N10 127.018      C13  -180
95    z_matrix C14   C12 =1.4021; N10 108.925      Cu41 -180
96    z_matrix C6    C1  =1.4196; C2  132.099      N4    180
97    z_matrix C8    C3  =1.4154; C5  132.063      N4    180
98    z_matrix C15   C13 =1.4195; C11 132.067      N10  -180
99    z_matrix C17   C14 =1.4156; C12 132.123      N10   180
100   z_matrix C7    C6  =1.4186; C1  118.280    C2    180
101   z_matrix H42   C6  =1.0302; C1  121.233    C7    180
102   z_matrix C9    C8  =1.4226; C3  118.274    C5    180
103   z_matrix H44   C8  =1.0300; C3  120.944    C9    180
104   z_matrix C16   C15 =1.4183; C13 118.281      C11   180
105   z_matrix H46   C15 =1.0301; C13 121.268      C16  -180
106   z_matrix C18   C17 =1.4229; C14 118.305      C12  -180
107   z_matrix H48   C17 =1.0299; C14 121.016      C18  -180
108   z_matrix H43   C7  =1.0313; C6  119.666      C1    180
109   z_matrix H45   C9  =1.0285; C8  119.691    C3   -180
110   z_matrix H47   C16 =1.0311; C15 119.686      C13   180
111   z_matrix H49   C18 =1.0285; C17 119.716      C14  -180
112
113
114           rotate  -47.22794 min  -67  max   -38    qa 1 operate_on_points "C* H* N* "
115           rotate -235.68848 min -253  max  -223    qb 1 operate_on_points "C* H* N* "
116           rotate   42.40869 min  37 max    67  qc 1 operate_on_points "C* H* N* "
117
```

```
str  '# beta CUPC
    CS_G(CSg2, 63.82397`_2.30224)
    CS_L(CSl2, 63.82397`_2.30224)
        Strain_L(L2, 0.77455`_0.03632)
        r_bragg 0.388072433
        phase_name b-cpc
        cell_mass  1152.162_0.000
        cell_volume  1218.8981_0.0000
        weight_percent w2  27.794_0.157

        scale @ 0.0000436690`_0.0000003337
        space_group P21/c
        Phase_LAC_1_on_cm( 41.02566_0.00000)
        Phase_Density_g_on_cm3( 1.56962_0.00000)



        a  @  14.80445
        b  @  4.82199
        c  @  19.91594

        be  @  120.98190

        site Cu41  x  0.00000_0.00000 y  0.00000_0.00000 z  0.00000_0.00000 occ Cu 1 beq  !b2  6.2259_0.1290
        site N4   x  0.07258_0.00000 y -0.21635_0.00000 z  0.09977_0.00000 occ N 1 beq  !b2  6.2259_0.1290
        site N10  x  0.13462_0.00000 y  0.19596_0.00000 z  0.03052_0.00000 occ N 1 beq  !b2  6.2259_0.1290
        site C2   x  0.02715_0.00000 y -0.41046_0.00000 z  0.12259_0.00000 occ C 1 beq  !b2  6.2259_0.1290
        site C5   x  0.17568_0.00000 y -0.19403_0.00000 z  0.15620_0.00000 occ C 1 beq  !b2  6.2259_0.1290
        site C11  x  0.14808_0.00000 y  0.39318_0.00000 z -0.01240_0.00000 occ C 1 beq  !b2  6.2259_0.1290
        site C12  x  0.22817_0.00000 y  0.15467_0.00000 z  0.09765_0.00000 occ C 1 beq  !b2  6.2259_0.1290
        site C1   x  0.10307_0.00000 y -0.51602_0.00000 z  0.19571_0.00000 occ C 1 beq  !b2  6.2259_0.1290
        site C3   x  0.19736_0.00000 y -0.37934_0.00000 z  0.21723_0.00000 occ C 1 beq  !b2  6.2259_0.1290
        site N39  x  0.24801_0.00000 y -0.02414_0.00000 z  0.15588_0.00000 occ N 1 beq  !b2  6.2259_0.1290
        site C13  x  0.25308_0.00000 y  0.48134_0.00000 z  0.02815_0.00000 occ C 1 beq  !b2  6.2259_0.1290
        site N38  x  0.07425_0.00000 y  0.49336_0.00000 z -0.08286_0.00000 occ N 1 beq  !b2  6.2259_0.1290
        site C14  x  0.30391_0.00000 y  0.33010_0.00000 z  0.09795_0.00000 occ C 1 beq  !b2  6.2259_0.1290
        site C6   x  0.09765_0.00000 y -0.71938_0.00000 z  0.24506_0.00000 occ C 1 beq  !b2  6.2259_0.1290
        site C8   x  0.29089_0.00000 y -0.43849_0.00000 z  0.28897_0.00000 occ C 1 beq  !b2  6.2259_0.1290
        site C15  x  0.30800_0.00000 y  0.67996_0.00000 z  0.00988_0.00000 occ C 1 beq  !b2  6.2259_0.1290
        site C17  x  0.41233_0.00000 y  0.37006_0.00000 z  0.15302_0.00000 occ C 1 beq  !b2  6.2259_0.1290
        site C7   x  0.19075_0.00000 y -0.78097_0.00000 z  0.31717_0.00000 occ C 1 beq  !b2  6.2259_0.1290
        site H42  x  0.02816_0.00000 y -0.82036_0.00000 z  0.22926_0.00000 occ H 1 beq  !b2  6.2259_0.1290
        site C9   x  0.28672_0.00000 y -0.64181_0.00000 z  0.33907_0.00000 occ C 1 beq  !b2  6.2259_0.1290
        site H44  x  0.36024_0.00000 y -0.33711_0.00000 z  0.30458_0.00000 occ H 1 beq  !b2  6.2259_0.1290
        site C16  x  0.41667_0.00000 y  0.72229_0.00000 z  0.06450_0.00000 occ C 1 beq  !b2  6.2259_0.1290
        site H46  x  0.27040_0.00000 y  0.79122_0.00000 z -0.04159_0.00000 occ H 1 beq  !b2  6.2259_0.1290
        site C18  x  0.46848_0.00000 y  0.56846_0.00000 z  0.13556_0.00000 occ C 1 beq  !b2  6.2259_0.1290
        site H48  x  0.44982_0.00000 y  0.25868_0.00000 z  0.20446_0.00000 occ H 1 beq  !b2  6.2259_0.1290
        site H43  x  0.18873_0.00000 y -0.92797_0.00000 z  0.35399_0.00000 occ H 1 beq  !b2  6.2259_0.1290
        site H45  x  0.35368_0.00000 y -0.68833_0.00000 z  0.39150_0.00000 occ H 1 beq  !b2  6.2259_0.1290
        site H47  x  0.45822_0.00000 y  0.86548_0.00000 z  0.05252_0.00000 occ H 1 beq  !b2  6.2259_0.1290
        site H49  x  0.54731_0.00000 y  0.60111_0.00000 z  0.17468_0.00000 occ H 1 beq  !b2  6.2259`_0.1290

```

```
rigid
  z_matrix Cu41
  z_matrix N4    Cu41 =1.9983;
  z_matrix N10   Cu41 =1.9968; N4  90.162
  z_matrix C2    N4  =1.3600; Cu41 125.894      N10  -180
  z_matrix C5    N4  =1.3559; Cu41 125.622      C2    180
  z_matrix C11   N10 =1.3601; Cu41 125.851     N4   -180
  z_matrix C12   N10 =1.3560; Cu41 125.694     C11   180
  z_matrix C1    C2  =1.3993; N4  109.123     Cu41  180
  z_matrix C3    C5  =1.4061; N4  108.943      Cu41 -180
  z_matrix N39   C5  =1.3508; N4  126.948      C3    180
  z_matrix C13   C11 =1.3989; N10 109.176      Cu41  180
  z_matrix N38   C11 =1.3484; N10 127.018      C13  -180
  z_matrix C14   C12 =1.4021; N10 108.925      Cu41 -180
  z_matrix C6    C1  =1.4196; C2  132.099      N4    180
  z_matrix C8    C3  =1.4154; C5  132.063      N4    180
  z_matrix C15   C13 =1.4195; C11 132.067      N10  -180
  z_matrix C17   C14 =1.4156; C12 132.123      N10   180
  z_matrix C7    C6  =1.4186; C1  118.280   C2    180
  z_matrix H42   C6  =1.0302; C1  121.233   C7    180
  z_matrix C9    C8  =1.4226; C3  118.274   C5    180
  z_matrix H44   C8  =1.0300; C3  120.944   C9    180
  z_matrix C16   C15 =1.4183; C13 118.281      C11   180
  z_matrix H46   C15 =1.0301; C13 121.268      C16  -180
  z_matrix C18   C17 =1.4229; C14 118.305      C12  -180
  z_matrix H48   C17 =1.0299; C14 121.016      C18  -180
  z_matrix H43   C7  =1.0313; C6  119.666      C1    180
  z_matrix H45   C9  =1.0285; C8  119.691   C3   -180
  z_matrix H47   C16 =1.0311; C15 119.686      C13   180
  z_matrix H49   C18 =1.0285; C17 119.716      C14  -180


        rotate   -222.81660 min  -237 max   -207   qa 1 operate_on_points "C* H* N* "
        rotate   -199.01401 min  -214 max   -184   qb 1 operate_on_points "C* H* N* "
        rotate   28.83002 min  13  max   43   qc 1 operate_on_points "C* H* N* "
```

B. Topas input file used in the 'test' Rietveld refinement of CUPC (ε to β transition at 320K)

```
'# e-CUPC  at 320K
xdd "D:\RAJIV\melanie\Refinements\epsilon_CPC_320\Daten\e_CPC_320C010001.xy"
    prm  !D   98.48031
    prm  !PSF  0.08
    prm  !d    0.24032
    prm  !mix  0.50909 min 0.0 max 1.0
     gauss_fwhm = (1-mix) (ArcTan((D*Tan(2*Th)+PSF+d*(1/Cos(2*Th)))/D)-(2*Th))/Deg + 0.000001;
     lor_fwhm   =  (mix) (ArcTan((D*Tan(2*Th)+PSF+d*(1/Cos(2*Th)))/D)-(2*Th))/Deg + 0.000001;
     User_Defined_Dependence_Convolution(circles_conv, 1/Tan(Th) ,, -0.00559 max =0;)

do_errors

bkg @ 2019.6233`_0.873698663 -117.649371`_1.34052978  1.71355827`_1.2545307 -22.4460919`_1.19736329 -24.7393414`_1.22851055  24.2182737`

      start_X  3.5
      finish_X  39.0
      Zero_Error(@, 0.03)
      LP_Factor( 90)
      convolution_step 2
      Rp 100
      Rs 100
      lam
           ymin_on_ymax  0.0001
           la  1 lo  1.238879 lh  1e-006
      x_calculation_step 0.02

str
           CS_G(csg1, 55.16906_0.67034)
           Strain_L(sl1, 0.87783_0.01911)
           r_bragg  0.222464891
           phase_name e-CPC
           cell_mass  1152.162_0.000
           cell_volume  1257.1077_0.0000
           weight_percent w1  95.917_0.104

           scale @ 0.0001603023`_0.0000002319
           space_group P21/c
           Phase_LAC_1_on_cm( 39.77869_0.00000)
           Phase_Density_g_on_cm3( 1.52191_0.00000)


           a  @  5.05397_0.00101
           b  @    23.18984_0.00110
           c  @    10.76604_0.00067

           be @     94.93645_0.01783
```

```
         site Cu41  x 0.00000_0.00000 y 0.00000_0.00000 z 0.00000_0.00000 occ Cu 1 beq !b1  8.7379_0.1829
         site N4   x -0.04431_0.00000 y 0.07195_0.00000 z -0.10181_0.00000 occ N 1 beq !b1  8.7379_0.1829
         site N10   x 0.27323_0.00000 y -0.02827_0.00000 z -0.10881_0.00000 occ N 1 beq !b1  8.7379_0.1829
         site C2   x -0.21267_0.00000 y 0.11614_0.00000 z -0.08223_0.00000 occ C 1 beq !b1  8.7379_0.1829
         site C5   x 0.08893_0.00000 y 0.08490_0.00000 z -0.20226_0.00000 occ C 1 beq !b1  8.7379_0.1829
         site C11   x 0.40624_0.00000 y -0.07919_0.00000 z -0.09588_0.00000 occ C 1 beq !b1  8.7379_0.1829
         site C12   x 0.35749_0.00000 y 0.00014_0.00000 z -0.20820_0.00000 occ C 1 beq !b1  8.7379_0.1829
         site C1   x -0.18715_0.00000 y 0.15871_0.00000 z -0.17255_0.00000 occ C 1 beq !b1  8.7379_0.1829
         site C3   x 0.00387_0.00000 y 0.13906_0.00000 z -0.24883_0.00000 occ C 1 beq !b1  8.7379_0.1829
         site N39   x 0.27417_0.00000 y 0.05221_0.00000 z -0.25206_0.00000 occ N 1 beq !b1  8.7379_0.1829
         site C13   x 0.58086_0.00000 y -0.08373_0.00000 z -0.18942_0.00000 occ C 1 beq !b1  8.7379_0.1829
         site N38   x 0.37996_0.00000 y -0.11992_0.00000 z -0.00839_0.00000 occ N 1 beq !b1  8.7379_0.1829
         site C14   x 0.55000_0.00000 y -0.03341_0.00000 z -0.26068_0.00000 occ C 1 beq !b1  8.7379_0.1829
         site C6   x -0.31447_0.00000 y 0.21278_0.00000 z -0.19436_0.00000 occ C 1 beq !b1  8.7379_0.1829
         site C8   x 0.07749_0.00000 y 0.17231_0.00000 z -0.35060_0.00000 occ C 1 beq !b1  8.7379_0.1829
         site C15   x 0.76295_0.00000 y -0.12739_0.00000 z -0.21790_0.00000 occ C 1 beq !b1  8.7379_0.1829
         site C17   x 0.69991_0.00000 y -0.02426_0.00000 z -0.36410_0.00000 occ C 1 beq !b1  8.7379_0.1829
         site C7   x -0.24281_0.00000 y 0.24660_0.00000 z -0.29602_0.00000 occ C 1 beq !b1  8.7379_0.1829
         site H42   x -0.45541_0.00000 y 0.22732_0.00000 z -0.13817_0.00000 occ H 1 beq !b1  8.7379_0.1829
         site C9   x -0.04835_0.00000 y 0.22659_0.00000 z -0.37366_0.00000 occ C 1 beq !b1  8.7379_0.1829
         site H44   x 0.21849_0.00000 y 0.15763_0.00000 z -0.40659_0.00000 occ H 1 beq !b1  8.7379_0.1829
         site C16   x 0.91456_0.00000 y -0.11884_0.00000 z -0.32126_0.00000 occ C 1 beq !b1  8.7379_0.1829
         site H46   x 0.78541_0.00000 y -0.16445_0.00000 z -0.16527_0.00000 occ H 1 beq !b1  8.7379_0.1829
         site C18   x 0.88329_0.00000 y -0.06764_0.00000 z -0.39385_0.00000 occ C 1 beq !b1  8.7379_0.1829
         site H48   x 0.67725_0.00000 y 0.01280_0.00000 z -0.41664_0.00000 occ H 1 beq !b1  8.7379_0.1829
         site H43   x -0.33264_0.00000 y 0.28603_0.00000 z -0.31368_0.00000 occ H 1 beq !b1  8.7379_0.1829
         site H45   x 0.00187_0.00000 y 0.25152_0.00000 z -0.44707_0.00000 occ H 1 beq !b1  8.7379_0.1829
         site H47   x 1.04811_0.00000 y -0.14996_0.00000 z -0.34377_0.00000 occ H 1 beq !b1  8.7379_0.1829
         site H49   x 0.99444_0.00000 y -0.06197_0.00000 z -0.46857_0.00000 occ H 1 beq !b1  8.7379_0.1829



rigid
  z_matrix Cu41
  z_matrix N4    Cu41 =1.9983;
  z_matrix N10   Cu41 =1.9968; N4  90.162
  z_matrix C2    N4  =1.3600; Cu41 125.894      N10  -180
  z_matrix C5    N4  =1.3559; Cu41 125.622      C2   180
  z_matrix C11   N10 =1.3601; Cu41 125.851     N4   -180
  z_matrix C12   N10 =1.3560; Cu41 125.694     C11  180
  z_matrix C1    C2  =1.3993; N4  109.123     Cu41  180
  z_matrix C3    C5  =1.4061; N4  108.943       Cu41 -180
  z_matrix N39   C5  =1.3508; N4  126.948       C3   180
  z_matrix C13   C11 =1.3989; N10 109.176       Cu41  180
  z_matrix N38   C11 =1.3484; N10 127.018       C13  -180
  z_matrix C14   C12 =1.4021; N10 108.925       Cu41 -180
  z_matrix C6    C1  =1.4196; C2  132.099       N4   180
  z_matrix C8    C3  =1.4154; C5  132.063       N4   180
  z_matrix C15   C13 =1.4195; C11 132.067       N10  -180
  z_matrix C17   C14 =1.4156; C12 132.123     | N10  180
  z_matrix C7    C6  =1.4186; C1  118.280    C2   180
  z_matrix H42   C6  =1.0302; C1  121.233    C7   180
  z_matrix C9    C8  =1.4226; C3  118.274    C5   180
  z_matrix H44   C8  =1.0300; C3  120.944    C9   180
  z_matrix C16   C15 =1.4183; C13 118.281       C11  180
  z_matrix H46   C15 =1.0301; C13 121.268       C16  -180
  z_matrix C18   C17 =1.4229; C14 118.305       C12  -180
  z_matrix H48   C17 =1.0299; C14 121.016       C18  -180
  z_matrix H43   C7  =1.0313; C6  119.666       C1   180
  z_matrix H45   C9  =1.0285; C8  119.691    C3   -180
  z_matrix H47   C16 =1.0311; C15 119.686       C13  180
  z_matrix H49   C18 =1.0285; C17 119.716       C14  -180


         rotate  -224.98853_0.05913 qa 1 operate_on_points "C* H* N* "
         rotate  -45.30489_0.03357 qb 1 operate_on_points "C* H* N* "
         rotate  154.67390_0.05857 qc 1 operate_on_points "C* H* N* "
```

```
str
        CS_G(csg2, 34.22706)
        Strain_L(sl2, 0.39254)
        r_bragg 0.463582373
        phase_name b-cpc
        cell_mass  1152.162_0.000
        cell_volume  1226.6284_0.0000
        weight_percent w3  4.083_0.104

        scale @ 0.0000069935`_0.0000001965
        space_group P21/c
        Phase_LAC_1_on_cm( 40.76711_0.00000)
        Phase_Density_g_on_cm3( 1.55973_0.00000)

        Out(w3, "      Anteil_b:\    %11.5f","     error:\t%11.5f\n")

        a   @   14.94935_0.01255
        b   @   4.80864_0.00335
        c   @   20.08674_0.01240

        be  @   121.84361_0.07707



         site Cu41  x  0.00000_0.00000 y  0.00000_0.00000 z  0.00000_0.00000 occ Cu 1  beq !b1   8.7379_0.1829
         site N4    x  0.07402_0.00000 y -0.21479_0.00000 z  0.10022_0.00000 occ N 1  beq !b1   8.7379_0.1829
         site N10   x  0.13410_0.00000 y  0.19585_0.00000 z  0.03038_0.00000 occ N 1  beq !b1   8.7379_0.1829
         site C2    x  0.02946_0.00000 y -0.40822_0.00000 z  0.12329_0.00000 occ C 1  beq !b1   8.7379_0.1829
         site C5    x  0.17741_0.00000 y -0.19191_0.00000 z  0.15675_0.00000 occ C 1  beq !b1   8.7379_0.1829
         site C11   x  0.14655_0.00000 y  0.39217_0.00000 z -0.01284_0.00000 occ C 1  beq !b1   8.7379_0.1829
         site C12   x  0.22824_0.00000 y  0.15538_0.00000 z  0.09770_0.00000 occ C 1  beq !b1   8.7379_0.1829
         site C1    x  0.10624_0.00000 y -0.51275_0.00000 z  0.19668_0.00000 occ C 1  beq !b1   8.7379_0.1829
         site C3    x  0.20017_0.00000 y -0.37615_0.00000 z  0.21811_0.00000 occ C 1  beq !b1   8.7379_0.1829
         site N39   x  0.24911_0.00000 y -0.02241_0.00000 z  0.15625_0.00000 occ N 1  beq !b1   8.7379_0.1829
         site C13   x  0.25149_0.00000 y  0.48057_0.00000 z  0.02770_0.00000 occ C 1  beq !b1   8.7379_0.1829
         site N38   x  0.07190_0.00000 y  0.49136_0.00000 z -0.08356_0.00000 occ N 1  beq !b1   8.7379_0.1829
         site C14   x  0.30333_0.00000 y  0.33042_0.00000 z  0.09782_0.00000 occ C 1  beq !b1   8.7379_0.1829
         site C6    x  0.10190_0.00000 y -0.71513_0.00000 z  0.24636_0.00000 occ C 1  beq !b1   8.7379_0.1829
         site C8    x  0.29439_0.00000 y -0.43439_0.00000 z  0.29007_0.00000 occ C 1  beq !b1   8.7379_0.1829
         site C15   x  0.30556_0.00000 y  0.67855_0.00000 z  0.00919_0.00000 occ C 1  beq !b1   8.7379_0.1829
         site C17   x  0.41196_0.00000 y  0.37088_0.00000 z  0.15297_0.00000 occ C 1  beq !b1   8.7379_0.1829
         site C7    x  0.19569_0.00000 y -0.77580_0.00000 z  0.31869_0.00000 occ C 1  beq !b1   8.7379_0.1829
         site H42   x  0.03267_0.00000 y -0.81606_0.00000 z  0.23063_0.00000 occ H 1  beq !b1   8.7379_0.1829
         site C9    x  0.29129_0.00000 y -0.63672_0.00000 z  0.34048_0.00000 occ C 1  beq !b1   8.7379_0.1829
         site H44   x  0.36346_0.00000 y -0.33308_0.00000 z  0.30560_0.00000 occ H 1  beq !b1   8.7379_0.1829
         site C16   x  0.41443_0.00000 y  0.72137_0.00000 z  0.06388_0.00000 occ C 1  beq !b1   8.7379_0.1829
         site H46   x  0.26721_0.00000 y  0.78901_0.00000 z -0.04251_0.00000 occ H 1  beq !b1   8.7379_0.1829
         site C18   x  0.46726_0.00000 y  0.56865_0.00000 z  0.13526_0.00000 occ C 1  beq !b1   8.7379_0.1829
         site H48   x  0.45019_0.00000 y  0.26030_0.00000 z  0.20464_0.00000 occ H 1  beq !b1   8.7379_0.1829
         site H43   x  0.19444_0.00000 y -0.92208_0.00000 z  0.35574_0.00000 occ H 1  beq !b1   8.7379_0.1829
         site H45   x  0.35876_0.00000 y -0.68257_0.00000 z  0.39309_0.00000 occ H 1  beq !b1   8.7379_0.1829
         site H47   x  0.45538_0.00000 y  0.86411_0.00000 z  0.05173_0.00000 occ H 1  beq !b1   8.7379_0.1829
         site H49   x  0.54623_0.00000 y  0.60165_0.00000 z  0.17443_0.00000 occ H 1  beq !b1   8.7379_0.1829
```

```
173
174
175  rigid
176    z_matrix Cu41
177    z_matrix N4    Cu41 =1.9983;
178    z_matrix N10   Cu41 =1.9968; N4  90.162
179    z_matrix C2    N4  =1.3600; Cu41 125.894      N10  -180
180    z_matrix C5    N4  =1.3559; Cu41 125.622      C2   180
181    z_matrix C11   N10 =1.3601; Cu41 125.851      N4   -180
182    z_matrix C12   N10 =1.3560; Cu41 125.694      C11  180
183    z_matrix C1    C2  =1.3993; N4  109.123      Cu41  180
184    z_matrix C3    C5  =1.4061; N4  108.943      Cu41  -180
185    z_matrix N39   C5  =1.3508; N4  126.948      C3   180
186    z_matrix C13   C11 =1.3989; N10 109.176      Cu41  180
187    z_matrix N38   C11 =1.3484; N10 127.018      C13  -180
188    z_matrix C14   C12 =1.4021; N10 108.925      Cu41  -180
189    z_matrix C6    C1  =1.4196; C2  132.099      N4   180
190    z_matrix C8    C3  =1.4154; C5  132.063      N4   180
191    z_matrix C15   C13 =1.4195; C11 132.067      N10  -180
192    z_matrix C17   C14 =1.4156; C12 132.123      N10  180
193    z_matrix C7    C6  =1.4186; C1  118.280   C2   180
194    z_matrix H42   C6  =1.0302; C1  121.233   C7   180
195    z_matrix C9    C8  =1.4226; C3  118.274   C5   180
196    z_matrix H44   C8  =1.0300; C3  120.944   C9   180
197    z_matrix C16   C15 =1.4183; C13 118.281      C11  180
198    z_matrix H46   C15 =1.0301; C13 121.268      C16  -180
199    z_matrix C18   C17 =1.4229; C14 118.305      C12  -180
200    z_matrix H48   C17 =1.0299; C14 121.016      C18  -180
201    z_matrix H43   C7  =1.0313; C6  119.666      C1   180
202    z_matrix H45   C9  =1.0285; C8  119.691   C3   -180
203    z_matrix H47   C16 =1.0311; C15 119.686      C13  180
204    z_matrix H49   C18 =1.0285; C17 119.716      C14  -180
205
206
207            rotate   -222.81660 min  -237 max   -207   qa 1 operate_on_points "C* H* N* "
208            rotate   -199.01401 min  -214 max   -184   qb 1 operate_on_points "C* H* N* "
209            rotate   28.83002 min  13  max   43   qc 1 operate_on_points "C* H* N* "
```

C. Topas input file used in the 'test' Rietveld refinement of TiO_2 (anatase to rutile transition)

```
/* Anatase to rutile "irreversible " transformmation 298K (25°C)  to 1123K (850°C)
   rate up 6.875  and rate down 13.75 */
xdd "D:\RAJIV\Guinier_data\Topas\READABLE\TiO2\2hr_160mm_r850C_1hr_d25C_INDEX_1.xy"

    iters 1000000
    chi2_convergence_criteria 0.0000001
    bkg @ 1259.38645 21.62238 163.4 43.02 -35.00767 -214.74 77.31 14.41 21.74 1.6817 -78.92
    start_X  10
    LP_Factor(90)
    Zero_Error(@, -0.005142)
    convolution_step 2

    Rp 217.5
    Rs 217.5
    Simple_Axial_Model(@, 8.57571)
    Cylindrical_2Th_Correction(@, 1.4965)
    lam
        ymin_on_ymax  0.0001
        la  1 lo  0.921 lh  1e-005
        x_calculation_step 0.0221739

    str   '## For TiO2 anatase phase
        CS_G(csg1, 37.54192)
        Strain_L(s1, 0.0001)

        local p1 0.03938 min 0.0001
        spherical_harmonics_hkl sh1
        sh_order 6
        lor_fwhm = sh1 p1/Cos(Th);

        r_bragg  0.70176
        phase_name "Anatyse"
        MVW( 319.5157299, 140.3473963, 27.20576129)

        scale @ 0.00108
        space_group I41/amdS

        Phase_LAC_1_on_cm( 138.79)
        Phase_Density_g_on_cm3( 3.78)

        a @ 3.81
        b @ 3.81
        c @ 9.63

        site Ti1 num_posns 4 x =0; :   0 y =0; : 0 z  =0; : 0 occ Ti+4  1 beq  2.0623
        site O1 num_posns  8 x =0; :   0 y =0; : 0 z  0.2081   occ O-2   1 beq  2.2656
```

```
49      str  '## For Rutile phase
50           CS_G(csg2, 36.3182)
51           Strain_L(sl2, 0.0001)
52
53           local p2 0.0258 min 0.0001
54           spherical_harmonics_hkl sh2
55           sh_order 6
56           lor_fwhm = sh2 p2/Cos(Th);
57           'lor_fwhm = sh2 /Cos(Th);
58
59           r_bragg 1.090164
60           phase_name "Rutile"
61           MVW( 159.7578649, 64.419, 72.84)
62           scale @ 0.01272
63           space_group P42/mnm
64           Phase_LAC_1_on_cm( 151.09)
65           Phase_Density_g_on_cm3( 4.118)
66
67           a @ 4.463881
68           b @ 4.463881
69           c @ 2.99365
70
71           site Ti1 num_posns  2 x =0; : 0 y =0; : 0  z =0; : 0 occ Ti+4  1 beq  1.7481
72           site O1  num_posns  4 x  0.30499  y  0.30499  z =0; : 0 occ O-2  1 beq  1.8656
```

D. Topas input file used in the 'test' LeBail refinement of Ag_3VO_4

```
'# Ag3Vo4 at high temperatures Le Bail fit
r_exp 6.161530647 r_exp_dash 8.714932565 r_wp 2.441967259 r_wp_dash 3.453943704 r_p 1.562826349 r_p_dash 2.252004707
iters 1000
xdd D:\RAJIV\Guinier_data\Topas\READABLE\Ag3VO4\0001.xy
    r_exp 0 r_exp_dash 0 r_wp 0 r_wp_dash 0 r_p 0 r_p_dash 0 weighted_Durbin_Watson 0 gof 0
    bkg @ 0 0 0 0 0 0 0 0 0 0
    Zero_Error(@, 0)
    LP_Factor( 90)
    convolution_step 2
    Rp 100
    Rs 100
    lam
        ymin_on_ymax  0.0001
        la  1 lo  1.12058 lh  0.00001
    x_calculation_step 0.02

    hkl_ls
        lebail  1
        CS_G(cs1, 200)
        Strain_L(sl1, 0.1)
        r_bragg  0
        phase_name hkl_Phase
        space_group C2/c
        MVW( 0, 0, 0)
        be @ 116
        a @ 10.2672
        b @ 4.9814
        c @ 10.224
```

E. Part of the input file used in the parameterization of Rietveld weight fraction of CUPC

Part of the input file used in the parameterization of Rietveld weight fraction of α-CUPC is presented.

```
prm !ma_cpc 576.081_0.000
prm !va_cpc 608.622576_0.000
prm !mb_cpc 1152.162_0.000
prm !vb_cpc 1218.89808_0.000


prm scaleb_126 0.00012203`_0.00      min 1e-11 max 1
prm scaleb_144 0.00013057`_0.00      min 1e-11 max 1
prm scaleb_162 0.00013832`_0.00      min 1e-11 max 1
prm scaleb_180 0.00014587`_0.00      min 1e-11 max 1
prm scaleb_198 0.00015283`_0.00      min 1e-11 max 1


prm !t_126   126.000
prm !t_144   144.000
prm !t_162   162.000
prm !t_180   180.000
prm !t_198   198.000


xdd D:\RAJIV\melanie\Refinements\90%alpha_10%beta_270\Daten\9a_1b_CPC_270C010007.xy
bkg @  2020.58452`_0.790388369 -135.676894`_1.09598642  36.3601782`_0.986828908 -40.706404`_0.934419164 -5.
information

str
prm scalea_126= - ( scaleb_126*mb_cpc*vb_cpc)/( ma_cpc*va_cpc*(1- 1/Exp(-((a1*t_126)^a0))));:0.00020032`_0.0
scale  = scalea_126;:  0.00020032`_0.0

CS_G(CS1126_000a_cpc , 29.70357`_0.44705)
Strain_L(L1126_000a_cpc , 1.77218`_0.05784)
```

F. The 'structure' part of the parametric refinement input file of TiO_2 anatase

```
str
   out "Pars0.txt"  append
   gauss_fwhm  = (a0 + a1*t_298_000+ a2*t_298_000^2+ a3*t_298_000^3);
   local fwhm02 = Get(gauss_fwhm);
   local siz02 = 0.1 Rad Lam/ (Cos(Th) (fwhm02));
   local  siz08  1.39078`_LIMIT_MIN_0.0001 min .0001 max 5
   Strain_L( siz08 , 0.00010`_LIMIT_MIN_0.0001 )
   local p1  0.34107` min 0.0001
   spherical_harmonics_hkl sh100
   sh_order  6 load sh_Cij_prm {
   y00   !sh1_c00  1.00000
   y20   sh1_c20  -0.54450`
   y40   sh1_c40  -0.11372`
   y44p  sh1_c44p  0.00591`
   y60   sh1_c60   0.00415`
   y64p  sh1_c64p -0.03766`
   }
   lor_fwhm = sh100 p1/Cos(Th);
   r_bragg  1.47407857
   phase_name "Anatyse"
   MVW( 319.5157299, 140.3473963, 27.20576129)
   scale @ 0.0074711286`
   space_group I41/amdS
   Phase_LAC_1_on_cm( 141.60616`)
   Phase_Density_g_on_cm3( 3.87523`)
  a @ 3.79442`
  b @ 3.79394`
  c @ 9.51060`
  site Ti1 num_posns 4 x =0;:0.00000 y =0;:0.00000 z =0;:0.00000 occ Ti+4 1 beq 2.0623
  site O1 num_posns 8 x =0; :0.00000 y =0;:0.00000 z 0.2081 occ O-2 1 beq 2.2656
  cell_mass  319.516
  cell_volume  136.91268`
  weight_percent  @ 97.793`
  Out(Get(a),"%11.7f \t" )
  Out(Get(b),"%11.7f \t" )
  Out(Get(c),"%11.7f \t" )
  Out(Get(weight_percent),"%11.7f \t" )
  Out(Get(scale),"%11.7f \t" )
  Out(siz02 , " %11.7f \t")
  Out(fwhm02 , " %11.7f \t")
  Out(siz08 , "%11.7f \n")
```

References

Abdullah, M., 1990, On a robust correlation coefficient, *The Statistician.* **39:**455-460.

Albinati, A., and Willis, B. T. M., 1982, The Rietveld Method in Neut ron and X-ray Powder Diffraction, *J. Appl. Cryst* **15:**361-374.

ANKA, Angströmquelle Karlsruhe, Karlsruhe, pp. Synchrotron source.

Audebrand, N., and Louër, D., 2004, The microstructure of nanocrystalline powders from line profile analysis, *Materials Science Forum* **443-444:**71-76.

Avrami, M., 1939, Kinetics of phase change I. General theory, *J. Chem Phys.* **7:**1103-1112.

Avrami, M., 1941, Granulation, phase change, and microstructure kinetics of phase change. III, *J. Chem. Phys* **9:**177–184.

Azzalini, A., 1985, A class of distributions which includes the normal ones, *Scand J Statist.* **12:**171-178.

Balzar, D., 1999, "Voigt-Function Model in Diffraction Line-Broadening Analysis" in Defect and Microstructure Analysis from Diffraction (International Union of Crystallography Monographs on Crystallography No. 10) (R. L. Snyder, H. J. Bunge, and J. Fiala, eds.), Oxford University Press, New York.

Barr, G., Dong, W., and Gilmore, C. J., 2004, High-throughput powder diffraction II. Applications of clustering methods and multivariate data analysis., *J. Appl. Crystallogr*. **37:**243-252.

Bilderback, D. H., Elleaume, P., and Weckert, E., 2005, Review of third and next generation synchrotron light sources, *J. Phys. B: At. Mol. Opt. Phys.* **38:** S773–S797.

Bish, D. L., and Howard, S. A., 1988, Quantitative Phase Analysis Using the Rietveld Method, *J. Appl. Cryst* **21:**86-91.

Bragg, W. L., 1913, The diffraction of short electromagnetic waves by a crystal,

Proceedings of the Cambridge Philosophical Society **17:**43-57.

Brückner, S., 2000, Estimation of the background in powder diffraction patterns through a robust smoothing procedure, *J. Appl. Crystallogr.* **33:**977-979.

Bruker-Axs, 1960, Germany.

Caglioti, G., Paoletti, A., and Ricci, F. P., 1958, Choice of collimators for a crystal spectrometer for neutron diffraction, *Nucl. Instrum.* **3:**223-228.

Chernyshev, V. V., 2001, Structure detrmination from powder diffraction, *Russian Chemical Bulletin, International Edition* **50**(12)**:**2273-2292.

Chung, D. D. L., Haven, P. W. D., Arnold, H., and Ghosh, D., 1993, X ray diffraction at elevated temperatures, Vch, New York.

Coelho, A. A., 2007, TOPAS academic version 4.1, Coelho Software, Brisbane.

Cullity, B. D., and Stock, S. R., 2001, Elements of X-ray diffraction, Prentice Hall, New Jersy.

David, W. I. F., Leoni, M., and Scardi, P., 2010, Domain size analysis in the Rietveld method, *Materials Science Forum* **651:**187-200.

David, W. I. F., Shankland, K., Streek, J. v. d., Pidcock, E., Motherwell, W. D. S., and Cole, J. C., 2006, DASH: A program for crystal structure determination from powder diffraction data, *J. Appl. Crystallogr.* **39:**910-915.

Debye, P., and Scherrer, P., 1916, Interferenzen an regellos orientierten Teilchen im Röentgenlicht, *Physikalische Zeitschrift* **17:**277-283.

Dickerson, M. B., Pathak, K., Sandhage, K. H., Snyder, R. L., Balachandran, U., Ma, B., Blaugher, R. D., and Bhattacharya, R. N., 2002, Applications of 2D detectors in X-ray analysis, *JCPDS-International Centre for Diffraction Data 2002, Advances in X-ray Analysis.* **45**.

Dinnebier, R. E., 2007, MgBr2.H2O Laboratory measurement, Max Planck Institute for Solid State Research, Stuttgart.

Dinnebier, R. E., 2010, (P. Rajiv, ed.), Stuttgart.

Dinnebier, R. E., and Billinge, S. J. L., 2008, Powder Diffraction Theory and Practice, RSC, Cambridge.

Dinnebier, R. E., Kowalevsky, A., Reichert, H., and Jansen, M., 2007, Polymorphism of Ag_3VO_4, *Z. Krist* **222:**420–426.

Dinnebier, R. E., Vensky, S., Jansen, M., and Hanson, J. C., 2005, Crystal structures and topological aspects of the high-temperature phases and decomposition products of the alkali-metal oxalates M2[C2O4] (M=K, Rb, Cs), *Chem. Eur. J* **11:**1119-1129.

Evans, J. S. O., and Evans, I. R., 2004, Beyond classical applications of powder diffraction, *Chemical Society Reviews.* **33:**539-547.

Farjas, J., and Roura, P., 2006, Modification of the Kolmogorov-Johnson-Mehl-Avrami rate equation for non-isothermal experiments and its analytical solution, *Acta Materialia* **54:**5573-5579.

Fitch, A. N., 2007, Applications of high-resolution powder X-ray diffraction, *Solid State Phenomena* **130:**7-14.

Gilmore, C. J., Barr, G., and Paisley, J., 2004, High-throughput powder diffraction. I. A new approach to qualitative and quantitative powder diffraction pattern analysis using full pattern profiles, *J. Appl. Crystallogr.* **37:**658-664.

Gonzalez, R. M., Edwards, T. E., Lorbiecke, T. D., Winburn, R. S., and Webster, J. R., 2003, Advances in X-ray Analysis- Analysis of Geologic materials using Rietveld quantitative X-ray diffraction, *International Centre for Diffraction Data* **43**.

Halasz, I., Dinnebier, R. E., and Angel, R., 2010, Parametric Rietveld refinement for the evaluation of powder diffraction patterns collected as a function of pressure, *J. Appl. Crystallogr.* **43:**504-510.

Hammond, R., Pencheva, K., Roberts, K. J., Mouginb, P., and Wilkinson, D., 2005, An examination of the thermal expansion of urea using high-resolution variable-temperature X-ray powder diffraction, *J. Appl. Crystallogr.* **38:**1038–1039.

Harris, K. D. M., and Tremayne, M., 1996, Crystal Structure Determination from Powder Diffraction Data, *Chem. Mater.* **8:**2554-2570.

Hill, R. J., and Howard, C. J., 1987, Quantitative phase analysis from neutron powder diffraction data using the Rietveld method, *J. Appl. Crystallogr.* **20:**467-474.

Hill, R. J., Tsambourakis, G., and Madsen, I. C., 1993, Improved Petrological Modal Analyses from X-ray Powder Diffraction Data by use of the Rietveld Method I. Selected Igneous, Volcanic, and Metamorphic Rocks, *Journal of Pctrototy* **34**(5)**:**847-900.

Hinrichsen, B., 2008, **Two-dimensional X-ray powder diffraction**, in: *Geo and biological science*, University of Stuttgart, Stuttgart, pp. 159.

Hinrichsen, B., Dinnebier, R. E., and Jansen, M., 2006, Powder3D: An easy to use program for data reduction and graphical presentation of large numbers of powder diffraction patterns, *Z. Krist* **23:**231-236.

Horn, D., and Gottlieb, A., 2002, Algorithm for data clustering in pattern recognition problems based on quantum mechanics, *Phys Rev lett.* **88:**0187021- 0187024.

Horn, M., Schwerdtfeger, C. F., and Meagher, E. P., 1972, Refinement of the structure of anatase at several temperatures, *Zeitschrift für Kristallographie.* **Bd. 136:**273-281.

Hummer, D. R., Heaney, P. J., and Post, J. E., 2007, Thermal expansion of anatase and rutile between 300 and 575 K using synchrotron powder X-ray diffraction, *Powder Diffraction* **22**(4)**:**352-357.

Iordanova, R., Lefterova, E., Uzunuv, I., Dimitriev, Y., and Klissurski, D., 2002, "Nonisothermal crystallisation kinetics of V2O5-MoO3-Bi2O3 glasses", *J. Therm. Anal. Calorim.* **70:** 393–404.

ITT, 2009, IDL version 6.4, in: *ITT visual information solutions*.

IUPAC, 1997, IUPAC Compendium of Chemical Terminology.

Jagtap, N., Bhagwat, M., Awati, P., and Ramaswamy, V., 2005, Characterization of nanocrystalline anatase titania: an in situ HTXRD study, *Thermochimica Acta* **427:**37-41.

Jain, A. K., Duin, R. P. W., and Mao, J., 2000, Statistical pattern recognition: A review, *IEEE transactions on pattern analysis and machine intelligence* **22:**4-37.

Jarque, C. M., and Bera, A. K., 1980, Efficient tests for normality, homoscedasticity and serial independence of regression residuals, *Economics Letters.* **6:**255-259.

Kapoor, K., Lahiri, D., Rao, S. V. R., Sanyal, T., and B.P.Kashyap, 2004, X-ray diffraction line profile analysis for defect study in Zr–2.5% Nb material, *Bull Mater Sci* **27**(1)**:**59-67.

Kennedy, J. A., and Clark, S. M., 1996, A general method for the analysis of non isothermal kinetic data, *Materials Science Forum* **228-231:**423-430.

Langford, J. I., and Lou¨erz, D., 1996, Powder diffraction, *Rep. Prog. Phys.* **59:**131–234.

Larson, A. C., and Dreele, R. B. V., 1994, General Structure Analysis System (GSAS), in: *Los Alamos National Laboratory Report LAUR*, pp. 86-748.

LeBail, A., 2005, Whole powder pattern decomposition methods and applications:A retrospection, *Powder diffraction* **20**(4)**:**316-326.

LeBail, A., Duroy, H., and Fourquet, J. L., 1988, Ab-initio structure determination of LiSbWO6 by X-ray powder diffraction, *Mat. Res. Bull* **23:**447-452.

Liang, J.-J., and Hawthrone, F. C., 1994, Characterization of fine-grained mixtures of rock-forming minerals by Rietveld structure refinement Olivine+Pyroxene, *The Canadian Mineralogist* **32:**541-552.

Malek, J., and Mitsuhashi, T., 2000, Testing method for the Johnson-Mehl-Avrami Equation in kinetic analysis of crystallization processes, *J. Am. Ceram. Soc* **83**(8)**:**2103-2105.

Massüger, L. A., 2007, Experimental Extension of the Texture Method for Structure Solution of Polycrystalline Materials, ETH Zurich, Zurich, pp. 100.

Microsoft, 2010, Excel.

Monecke, T., S.Koehler, R.Kleeberg, and Herzig, P. M., 2001, Quantitative phase-analysis by the Rietveld method using X-ray powder-diffraction data: Applications to the study of Alteration halos associated with volcanic-rock-hosted massive sulfide deposits, *The Canadian Mineralogist* **39:**1617-1633.

Mukherjee, A. K., 2007, Ab-initio crystal structure determination fromX-ray powder diffraction data, *Journal of the Indian Institute of Science* **87**(2).

Müller, M., 2011, Parametric Rietveld refinement of structural phase transition of CuInSe2., *In preparation*.

Müller, M., Dinnebier, R. E., Ali, N. Z., Campbell, B. J., and Jansen, M., 2010a, Direct access to the order parameter: parameterized symmetry modes and rigid body movements as a function of temperature, *Materials Science Forum* **651:**79-95.

Müller, M., Dinnebier, R. E., Jansen, M., Wiedemann, S., and Plueg, C., 2010b, The influence of temperature, additives and polymorphic form on the kinetics of the phase transformations of copper phthalocyanine, *Dyes and Pigments* **85:**152-161.

Müller, M., Dinnebier, R. E., Jansen, M., Wiedemann, S., and Plüg, C., 2009, Kinetic analysis of the phase transformation from α to β-copper phthalocyanine: A case study for sequential and parametric Rietveld refinements., *Powder Diffraction* **24**(3)**:**191-199.

Norby, P., 1996, In situ time resolved synchrotron powder diffraction studies of

syntheses and chemical reactions., *Materials Science Forum* **228-231:**147-152.

NSLS, National Synchrotron Light Source, New York.

Öztuna, D., Elhan, A. H., and Tüccar, E., 2006, Investigation of four different normality tests in terms of type 1 errror rate and power under different distributions, *Turk J Med Sci* **36:**171-176.

Parise, J. B., Cahill, C. L., and Lee, Y., 2000, Dynamic powder crystallography with synchrotron X-ray source, *The Canadian Mineralogist* **38:**777-800.

Pawley, G. S., 1981, Unit-cell refinement from powder diffraction scans, *J. Appl. Crystallogr.*
14:357-361.

Pecharsky, V., and Zavilij, P., 2003, Fundamentals of powder diffraction and structural characterization of materials, Kluwer, Dordrecht.

Press, W. H., Teukolsky, S. A., Vetterling, W. T., and Flannery, B. P., 2002, Numerical recipes in C, Cambridge university press.

Rajiv, P., Dinnebier, R. E., and Jansen, M., 2009, Automatic determination of phase transition points in in situ X-ray powder diffraction experiments, *Powder Diffraction* **24**(1)**:**8-16.

Rajiv, P., Dinnebier, R. E., and Jansen, M., 2010, "Powder 3D Parametric"- A program for automated sequential and parametric Rietveld refinement using Topas, *Materials Science Forum* **651:**97-104.

Rajiv, P., Hinrichsen, B., Dinnebier, R. E., Joswig, M., and Jansen, M., 2007, Automatic calibration of powder diffraction experiments using 2D-detectors, *Powder Diffraction* **22:**3-19.

Raudsepp, M., Pani, E., and Kern, A., 2002, Powder Diffraction in Mining and Minerals, *Commission on powder diffraction International union of crystallography* **27:**10-12.

Rietveld, H. M., 1967, Line profiles of neutron powder-diffraction peaks for structure refinement, *Acta Crystallogr* **22:**151.

Rietveld, H. M., 1969, A profile refinement method for nuclear and magnetic structures, *J. Appl. Crystallogr.* **2:** 65-71.

Rius, J., Miravitlles, C., Gies, H., and Amigo, J. M., 1999, A tangent formula derived from Patterson-function arguments. VI. Structure solution from powder patterns with systematic overlap, *J. Appl. Cryst* **32:**89-97.

Rodriguez-Carvajal, J., 1990, FULLPROF: A Program for Rietveld Refinement and Pattern Matching Analysis, in: *Abstracts of the Satellite Meeting on Powder Diffraction of the XV Congress of the IUCr,* Toulouse, France, pp. 127.

Scardi, P., and Dinnebier, R. E., 2010, Extending the reach of powder diffraction modelling by user defined macros, *Materials Science Forum* **650**.

Scardi, P., Dong, Y. H., and Leoni, M., 2001, Line profile analysis in the Rietveld method and whole powder pattern fitting, *Materials Science Forum* **378-381:**132-141.

Schmidt, C. L., Dinnebier, R. E., and Jansen, M., 2009, Phase transition and thermal decomposition of silver isocyanate (AgNCO), *Solid State Sciences* **11:**1107–1113.

Schorr, S., and Geandier, G., 2006, In situ investigation of the temperature dependent structural phase transition in CuInSe2 by synchrotron radiation, *Cryst. Res. Technol* **41**(5)**:**450- 457.

Seul, M., O'Gorman, L., and Sammon, M. J., 2000, Practical algorithms for image analysis- description, examples and code, Cambridge university press.

Sietronics, 1978, Canberra, Australia.

Smith, S. W., 2003, Digital signal processing, Newnes publication, New York.

Stinton, G. W., and Evans, J. S. O., 2007, Parametric Rietveld refinement, *J. Appl. Crystallogr.* **40:**87-95.

Sugimoto, K., Dinnebier, R. E., and Hanson, J. C., 2007, Structures of three dehydration products of bischofite from in situ synchrotron powder diffraction data (MgCl2.nH2O; n = 1, 2, 4), *Acta Crystallogr B.* **63:**235–242.

Toraya, H., 1989, Whole powder pattern decomposition method, *The Rigaku Journal* **6**(2)**:**28-34.

Winburn, R. S., 2003, Advances in X-ray Analysis, **46**.

Xua, D., and Redman-Furey, N., 2007, Statistical cluster analysis of pharmaceutical solvents, *International Journal of Pharmaceutics.* **339:**175–188.

Young, R. A., 1991, The Rietveld method, Oxford university press, New York.

List of Tables and Figures

List of Tables

List of Figures

List of Figures in Users manual

Abbreviations and conventions

ASCII	American Standard Code for Information and Interchange
EM	Electro Magnetic
ESD	Estimated Standard Deviation
FWHM	Full Width at Half Maximum
GUI	Graphical User Interface
PCA	Principal Components Analysis
WPPF	Whole Powder Pattern (or Profile) Fit
WPPD	Whole Powder Pattern (or Profile) Decomposition
WPPR	Whole Powder Pattern (or Profile) Refinement
XRD	X-Ray Diffraction
XRPD	X-Ray Powder Diffraction
r	Pearson's correlations coefficient
r_wp	Weighted residual profile
r_wp_dash	Weighted residual profile (background subtracted)
ρ	Spearman's coefficient

τ	Kendall's coefficient
Sequential correlations vector	Correlations coefficients of the powder patterns measured at subsequent instants of external variables.
2D dataset	Powder patterns collected as a function of external variables.
Phase	Crystalline phase
Phase	Phase of an interfering wave

Curriculum vitae

General

Name:	Rajiv Paneerselvam
Date of birth:	10th January 1978
Place of birth:	Madurai, India.

Education

Jul 2006 - Feb 2011:	PhD student in crystallography at Max-Planck-Institute for Solid State Research Stuttgart, Germany. Advisors: Prof. Dr. Robert. E. Dinnebier Prof. Dr. Manfred Joswig
Oct 2004 - Jun 2006:	Master of Science in Physics from University of Stuttgart, Germany. Thesis title: Automatic calibration of powder diffraction experiments using two-dimensional detectors. Advisors: Prof. Dr. Robert. E. Dinnebier Prof. Dr. Manfred Joswig.
Jun 1996 - Jun 2001:	Physics studies at Madras Christian College, Tambaram, Chennai 600059, India. (Affiliated to University of Madras 600005, Chennai, India.)
Mar 1996:	(High school) M.V.M.M.M Higher secondary School, Dindigul-624004, India.

Important publications

- Automated parametric Rietveld refinement: Applications in the extraction of reaction kinetics and micro structural information: P. Rajiv, R. E. Dinnebier, M. Joswig and M. Jansen (**2010** *in preparation*).

- "Powder 3D Parametric"- A program for automated sequential and parametric Rietveld refinement using Topas: P. Rajiv, R. E. Dinnebier and M. Jansen. *Materials Science Forum*, 651, 97-104 **(2010)**.

- Automatic determination of phase transition points in *in situ* X-ray powder diffraction experiments: P. Rajiv, R. E. Dinnebier and M. Jansen. *Powder Diffraction*, 24, 1, 8-16 **(2009)**.

- Automatic calibration of powder diffraction experiments using two-dimensional detectors: P. Rajiv, B. Hinrichsen, R. E. Dinnebier, M. Joswig and M. Jansen. *Powder Diffraction*, 22**,** 1**,** 3-19 **(2007)**.

Poster presentations

- Towards 'automated sequential/parametric refinement of *in situ* XRPD data', P. Rajiv, B. Hinrichsen, R. E. Dinnebier, M. Joswig and M. Jansen. *Annual conference of the German society for crystallography* (*Deutsche gesellschaft für kristallographie*), Erlangen, **(2008)**.

- Determination of phase boundaries in *in situ* X-ray powder diffraction experiments, P. Rajiv, B. Hinrichsen, R. E. Dinnebier, M. Joswig and M. Jansen. *Annual conference of the German society for crystallography* (*Deutsche gesellschaft für kristallographie*), Bremen, **(2007)**.

Other qualifications and experiences

- Post graduate Diploma in Business administration (PGDBA) in Annamalai University India (through correspondence) (Jun 2001 - May 2002).

- Basic knowledge in objected oriented programming (Obtained a certificate of excellence in C & C++ from SSI –India in the year 2001).

Acknowledgements

I express my deep gratitude to Prof. Dr. Robert E. Dinnebier for providing me an excellent opportunity to work in his group. Thanks for his guidance, encouragement, freedom and for the wonderful atmosphere he provided in his group throughout the period of my stay at the MPI. I thank him for the topic I was provided with.

I am indebted to Prof. Dr. Manfred Joswig for accepting me as his student. Thanks for the constant encouragement, scientific discussions and for many valuable ideas he provided from my initial days in Stuttgart (M.Sc) until my Ph.D thesis. I also thank all the members of the Dept. of Geophysics University of Stuttgart for their cooperation.

I thank Prof. H.W. Reinhardt for being one of my examiners and Jun. Prof. O. Röhrle for being the chair of my examination committee; I also thank all other associated members of the Faculty of Civil and Environmental Engineering Uni-Stuttgart.

I am extremely grateful to Prof. Dr. Dr. h. c. Martin Jansen for providing space at MPI and for letting me to be a part of his department. Thanks also for the numerous opportunities he provided to take part in many scientific seminars, conferences, meetings and workshops and also for the chances he gave to make use of the scientific resources and instruments at the institute. I also express my thankfulness to all the members of Dept. Jansen. The Max Planck society is gratefully acknowledged for the financial support it provided during my stay.

I thank Prof. Dr. John.S.O. Evans (University of Durham U.K) for the valuable discussions and his ideas, also for offering the 'BCA Powder diffraction course-2008'. (Thanks to Dr. Amber Thompson-Durham for being my tutor in 'BCA structural analysis school 2007').

A special thanks to Dipl.min. Melanie Müller for supporting me initially in handling Topas input files, for correcting the mistakes in my thesis and for translating the German summary and abstract of my thesis (Thomas Pilz and Andreas Bach also). The current members of X-ray group:Christine, Oksana, Prasad, Naveed, Frank (also the former members Kuni, Zuev, Ergün, John and my old friends in Stuttgart, Edward..) are acknowledged for the atmosphere they provided. Thanks to Dr.rer.nat. Bernd Hinrichsen (BASF) for the initial support and guidance he provided in understanding IDL and C.

The following members of the faculty of Physics Madras Christian College, Chennai- India are gratefully acknowledged: Dr. R. Manickkavachagam, Dr. S.I.A. Philomin Raj, Dr. J.F. Rajasekaran, Dr. P. Chandran, Dr. P. Samuel Cornelius (Mathematics). I thank Dr.rer.nat Deepak Samuel (TIFR, Mumbai) for his constant personal and scientific support during my initial days in Germany. Finally, I express my thankfulness to my family members (my mother and brother) and my love to all my brothers and sisters for their constant support.

Declaration

Hiermit versichere ich an Eides statt, dass ich diese Dissertation unter Verwendung der angegebenen Hilfsmittel selbstständig angefertigt und bisher noch keinen Promotionsversuch unternommen habe.

Stuttgart, den , 1.8.2011

Rajiv Paneerselvam